

Longitudinal-Transverse Separation of Deep-Inelastic Scattering at low Q^2 on Nucleons and Nuclei

VRIJE UNIVERSITEIT

**Longitudinal-Transverse Separation of Deep-Inelastic
Scattering at low Q^2 on Nucleons and Nuclei**

ACADEMISCH PROEFSCHRIFT

ter verkrijging van de graad van doctor aan
de Vrije Universiteit Amsterdam,
op gezag van de rector magnificus
prof.dr. T. Sminia,
in het openbaar te verdedigen
ten overstaan van de promotiecommissie
van de faculteit der Exacte Wetenschappen
op maandag 6 december 2004 om 10.45 uur
in de aula van de universiteit,
De Boelelaan 1105

door

Vladas Tvaskis

geboren te New Voronez, USSR

promotor: prof.dr.ing. J.F.J. van den Brand
copromotor: dr. H.P. Blok

Contents

1	Introduction	1
2	Theory	5
2.1	Kinematics	5
2.2	Deep-Inelastic Scattering	6
2.3	The Quark Parton Model	10
2.4	Quantum Chromodynamics	11
2.5	Power Corrections	13
2.5.1	Target Mass Correction	13
2.5.2	Higher Twist Effects	13
2.6	Physics at low Q^2	14
2.7	Nuclear Effects in the Structure Functions	17
2.7.1	x Rescaling	18
2.7.2	Pion Enhancement Model	18
2.7.3	Q^2 Rescaling Model	19
2.7.4	Nucleon Swelling	19
2.7.5	Cluster Model	19
2.7.6	Vector Meson Dominance Model	20
2.7.7	Partonic Fusion	21
2.8	Ratio of the Longitudinal to Transverse Virtual-Photon Cross Sections	22
2.9	Models for F_2 and R	24
2.9.1	Parametrization of F_2 for Hydrogen	24
2.9.2	Parametrization of F_2 for Deuterium	25
2.9.3	Parametrization of the Cross Section for $A > 2$ Targets	26
2.9.4	Parametrization of the Function R	28
2.10	Radiative Corrections	28
3	Experimental Apparatus	31
3.1	Accelerator	32
3.1.1	Beam Position Measurement	33
3.1.2	Beam Energy Measurements	34
3.1.3	Beam Current Monitors	35
3.1.4	Beam Rastering System	35

3.2	Targets and Scattering Chamber	36
3.2.1	Cryotarget Ladder	37
3.2.2	Solid Targets Ladder	37
3.3	High Momentum Spectrometer	38
3.4	HMS detector package	40
3.4.1	Drift Chambers	41
3.4.2	Hodoscopes	42
3.4.3	Čerenkov Detector	43
3.4.4	Lead-Glass Calorimeter	45
3.5	Trigger system and Data acquisition	46
4	Data Analysis	49
4.1	Event Reconstruction	50
4.1.1	Tracking	50
4.1.2	Target Quantities	58
4.2	Detector Calibration	60
4.2.1	Drift Chamber Calibration	60
4.2.2	Gas Čerenkov Counter Calibration	61
4.2.3	Lead Glass Calorimeter Calibration	62
4.2.4	Determination of the Offsets in E , θ and E'	64
4.3	Identification of Good Events	65
4.3.1	Particle Identification	66
4.3.2	Charge Symmetric Background	66
4.3.3	Pion contamination	67
4.3.4	Background from the Target Walls	69
4.4	Deadtimes	70
4.4.1	Electronic Deadtime	71
4.4.2	Computer Deadtime	72
4.5	Efficiencies	72
4.5.1	Trigger Efficiency	73
4.5.2	Tracking Efficiency	75
4.5.3	Čerenkov Efficiency	76
4.5.4	Calorimeter Efficiency	79
4.6	Target Density Correction	81
4.7	Acceptance Function	83
4.8	Extraction of the Cross Section	87
4.9	Bin Centering Correction	87
4.10	Calculation of the Radiative Corrections	88
4.11	Extraction of R and F_2	92
4.12	Iteration procedure	93
4.13	Systematic Uncertainty	94

5 Results	97
5.1 σ_{exp}/σ_{MC} for ${}^1H(e, e)$	97
5.2 Cross Sections	98
5.3 Averaging Data and Calculation of the Uncertainty due to the α^2 Term	104
5.3.1 Averaging Data	104
5.3.2 Calculation of the Uncertainty due to the α^2 Term	105
5.4 Results for F_2 , F_1 and R for Hydrogen	107
5.4.1 Results for F_1 and F_2 from the Rosenbluth Separation Method	109
5.4.2 R for Hydrogen	109
5.4.3 Results for F_2 from a Model Dependent Method	112
5.5 Results for F_2 , F_1 and R for Deuterium	114
5.5.1 Results for F_1 and F_2 from the Rosenbluth Separation Method	114
5.5.2 R for Deuterium	118
5.5.3 Results for F_2 from a Model Dependent Method	120
5.6 Results for F_2 , F_1 and R for Carbon, Copper and Gold	120
5.6.1 Results for F_1 and F_2 from the Rosenbluth Separation Method for Carbon, Copper and Gold	120
5.6.2 R for Carbon, Copper and Gold	122
5.6.3 Results for F_2 from a Model Dependent Method for Carbon, Copper and Gold	126
5.7 The Ratios σ_D/σ_H , F_2^D/F_2^H and R^D/R^H	127
5.7.1 x Dependence of σ^D/σ^H	130
5.7.2 Q^2 Dependence of σ^D/σ^H	132
5.7.3 Ratio of the Structure Functions F_2^D/F_2^H	135
5.7.4 The Ratio R^D/R^H	135
5.8 The Ratios σ_A/σ_D , F_2^A/F_2^D and R^A/R^D	136
5.8.1 Ratio of the Cross Sections σ^A/σ^D	137
5.8.2 Ratio of the Structure Functions F_2^A/F_2^D	138
5.8.3 The Ratio R^A/R^D	139
6 Summary and Conclusions	141
7 Samenvatting	145
A Tables of F_2, F_1 and R	149
B Tables of the Cross Section Ratios	163
C Tables of the Ratios of the Structure Functions and R	167
Bibliography	169
Acknowledgements	175

Chapter 1

Introduction

Since the early experiments at SLAC, which discovered the nucleon substructure and led to the development of the quark parton model [1], deep inelastic scattering (DIS) has been the most powerful tool to investigate the partonic substructure of the nucleon. After about 30 years of experiments with electron and muon beams the nucleon structure function $F_2(x, Q^2)$ is known with high precision over about four orders of magnitude in x and Q^2 [2]. In the region of $Q^2 > 1 \text{ (GeV/c)}^2$ the results of the DIS measurements are interpreted in terms of partons (quarks and gluons). The theoretical framework is provided in this case by perturbative Quantum Chromo Dynamics (pQCD), which includes scaling violations, as described by the Dokshitzer-Gribov-Lipatov-Altarelli-Parisi (DGLAP) equations [3, 4, 5]. The description starts to fail when Q^2 becomes of the order of 1 (GeV/c)^2 , where non-perturbative effects (higher-twist effects), which are still not fully understood [6], become important (non-pQCD). The sensitivity for order- n twist effects increases with decreasing Q^2 , since they include a factor $1/(Q^2)^n$ ($n \geq 1$) [7].

There is a great interest in the behaviour of the structure functions F_1 and F_2 in the transition from the pQCD to the non-pQCD region. This behaviour is hardly known since there are few data in this region, except for the transverse cross section σ_T at the photon point ($Q^2 = 0$). However, it is known that F_2 and R (the ratio of the longitudinal and transverse virtual-photon cross sections, which includes both F_2 and F_1 structure functions) should vanish in the limit $Q^2 \rightarrow 0$ as required by current conservation. This means that in the transition region, whose exact location is as yet unknown, the $1/(Q^2)^n$ higher-twist expansion should go over into a $(Q^2)^n$ expansion.

Measurements on a large number of nuclei have determined the A -dependence of the structure function $F_2(x, Q^2)$ (EMC effect) [8]. The discovery that the structure functions (and therefore the quark and gluon distributions) in nuclei are different from those in the nucleon, was a surprise because it showed that the nuclear environment influences the internal structure of the nucleon. The EMC effect is still not fully understood. Moreover, it is not inconceivable that an A -dependent effect also exists in the other structure function $F_1(x, Q^2)$ (or in R).

It has to be mentioned that even if one only wants to determine F_2^A/F_2^D , in most cases it is necessary to know R . The ratio of the structure functions F_2^A/F_2^D in two particular cases

will be identical to the ratio of the cross sections σ_A/σ_D , which follows from the equation

$$\frac{\sigma^A}{\sigma^D} = \frac{F_2^A(1 + \epsilon R_A)(1 + R_D)}{F_2^D(1 + R_A)(1 + \epsilon R_D)}, \quad (1.1)$$

where ϵ represents the virtual-photon polarization parameter. If the experimental data have been taken at $\epsilon = 1$ (experiments at high energy) or if $R_A = R_D$ then it follows that

$$\frac{\sigma^A}{\sigma^D} = \frac{F_2^A}{F_2^D}. \quad (1.2)$$

Little information exists about the behaviour of the function $R(x, Q^2)$. Data on $R(x, Q^2)$ on hydrogen are available in a limited x and Q^2 ($Q^2 > 1$ (GeV/c) 2) range only, and the typical error on R in these measurements is 0.1-0.2 [9]. Few measurements of R exist for deuterium and heavier nuclei.

The determination of R plus a possible A -dependence requires measurements of the cross section at the same (x, Q^2) , but at different ϵ . It means that at least two beam energies have to be used (Rosenbluth separation technique). In only a few experiments such measurements have actually been carried out.

A possible nuclear modification of the transverse-longitudinal ratio has been studied especially by the HERMES collaboration, albeit in an indirect way [10]. In 1999 the HERMES collaboration reported an unexpectedly large A -dependence of $R(x, Q^2)$ [11]. This finding generated considerable theoretical interest suggesting a possible role for quarks in the exchange of mesons. These results triggered the proposal for the experiment described in this thesis. After the completion of the present measurements, a reanalysis of the HERMES data on nitrogen and new data on krypton showed that the initially observed effect had to be largely attributed to photon showers in the edges of the detection equipment [12]. So as yet no evidence for nuclear effects has been found in the kinematic range of the existing measurements of $R(x, Q^2)$ ($Q^2 > 1$ (GeV/c) 2 and $x > 0.01$) [13], but it has to be mentioned that the error bars in these measurements are rather large.

Consequently, it is interesting to measure the structure function F_2 and R at low Q^2 on nucleons and nuclei for the following reasons:

- Study of their behaviour in the transition region from pQCD to non-pQCD. Study of the development of higher-twist effects, *e.g.*, the transition of the expansion $1/(Q^2)^n$ to the expansion $(Q^2)^n$.
- Study of the A -dependence of the structure functions and of R at low Q^2 .

As a result of this interest experiment *e99 – 118* was carried out in summer 2000 at Jefferson Laboratory (Newport News, VA, USA). Data were obtained at low x (0.007-0.55) and Q^2 (0.03-2.8 (GeV/c) 2) with 2.301, 3.419 and 5.648 GeV electron beams (at a current

of $I = 25 \mu\text{A}$) and the High-Momentum Spectrometer in Hall C. Data were taken at various scattering angles between 10° and 60° on the targets H, D, C, Al, Cu, and Au. The measured cross sections were used to perform a Rosenbluth separation in order to map out the x and Q^2 dependence of the F_1 and F_2 structure functions and of the ratio of the longitudinal and transverse virtual-photon cross sections.

The work described in this thesis is organised as follows. Theoretical aspects, including models of the A -dependence, are discussed in chapter 2. The experimental setup and analysis are discussed in chapters 3 and 4, respectively. The results of the experiment are presented and discussed in chapter 5. The conclusions are summarised in chapter 6.

Chapter 2

Theory

2.1 Kinematics

The general form of the lepton-nucleon scattering reaction can be denoted as

$$e(k) + N \rightarrow e'(k') + X , \quad (2.1)$$

where e and e' are the initial and final states of the charged lepton with four-momentum k ($k=(E, \vec{k})$) and k' ($k'=(E', \vec{k}')$), respectively, N is the target nucleon ($p = (M, 0)$), and X represents the final hadronic state as shown in Fig. 2.1. The energy transfer of the lepton to

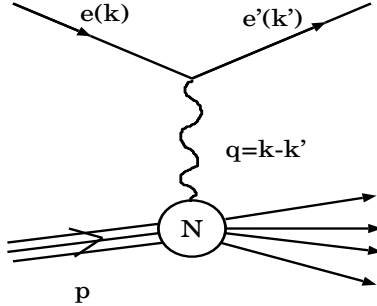


Figure 2.1: Lowest order Feynman diagram for inclusive lepton-nucleon scattering.

the target rest frame is given by

$$\nu = E - E' = \frac{p \cdot q}{M} , \quad (2.2)$$

which is the energy of the virtual photon γ^* . The negative squared mass of the virtual photon is given by

$$Q^2 \equiv -q^2 = 4EE' \sin^2(\theta/2) , \quad (2.3)$$

where θ is the angle between the initial and final directions of the lepton. Two dimensionless variables, the Bjorken scaling variable x and y , are expressed as

$$x = \frac{Q^2}{2p \cdot q} = \frac{Q^2}{2M\nu} , \quad (2.4)$$

where M is the mass of the proton, and

$$y = \frac{p \cdot q}{p \cdot k} = \frac{\nu}{E} , \quad (2.5)$$

where x can be interpreted as the fraction of the nucleon momentum carried by the struck parton, and y is the fraction of the beam energy transferred by the virtual photon. The total invariant mass squared of the hadronic system is

$$W^2 \equiv (p + q)^2 = M^2 + 2M\nu - Q^2 . \quad (2.6)$$

In case of elastic scattering $W^2 = M^2$ and hence $x = 1$.

2.2 Deep-Inelastic Scattering

The differential cross section for inclusive lepton nucleon scattering can be expressed as a function of the leptonic tensor $L^{\mu\nu}$ and the hadronic tensor $W_{\mu\nu}$, which describe respectively the electron and the hadron vertex in Fig. 2.1,

$$\frac{d^2\sigma}{d\Omega dE'} = \frac{\alpha^2}{Q^4} \frac{E'}{E} L^{\mu\nu} W_{\mu\nu} , \quad (2.7)$$

with α the fine structure constant. The leptonic tensor $L^{\mu\nu}$ [14] is completely calculable from QED. The hadronic tensor $W_{\mu\nu}$ [15] describes transitions to all possible final states. In case of an unpolarised target it includes an average over the initial spin states and a sum over all final spin states. The hadronic tensor $W_{\mu\nu}$ has to be parametrized because the structure of a hadron at present cannot be calculated from first principles in the perturbative Quantum Chromo Dynamics (pQCD). The general expression for the differential cross section can be written in the laboratory system as [14]

$$\frac{d^2\sigma}{d\Omega dE'} = \sigma_{Mott} \left[W_2(\nu, Q^2) + 2W_1(\nu, Q^2)\tan^2\frac{\theta}{2} \right], \quad (2.8)$$

where the Mott cross section σ_{Mott} is given by

$$\sigma_{Mott} = \frac{\alpha^2 \cos^2(\theta/2)}{4E^2 \sin^4(\theta/2)}, \quad (2.9)$$

and represents the cross section for elastic electron scattering from a spinless point charge. The two structure functions W_1 and W_2 contain the information about the structure of the nucleon and the final state, and have to be determined by experiment. Usually the two structure functions W_1 and W_2 are expressed in terms of the dimensionless functions, F_1 and F_2 as

$$F_1(x, Q^2) = MW_1(\nu, Q^2), \quad (2.10)$$

$$F_2(x, Q^2) = \nu W_2(\nu, Q^2). \quad (2.11)$$

Extensive measurements of the structure functions have been performed by many experiments. In Fig. 2.2 a compilation of the world data on the structure function F_2 of the proton is shown.

By the analogy to the expression for absorption of real photons the differential cross section can be expressed in terms of longitudinal (σ_L) and transverse (σ_T) virtual-photon cross sections as

$$\frac{d^2\sigma}{d\Omega dE'} = \Gamma \left[\sigma_T(x, Q^2) + \epsilon \sigma_L(x, Q^2) \right], \quad (2.12)$$

where Γ is the virtual photon flux

$$\Gamma = \frac{\alpha K}{2\pi^2 Q^2} \frac{E'}{E} \frac{1}{1-\epsilon} \quad (2.13)$$

with

$$K = \frac{2M\nu - Q^2}{2M}. \quad (2.14)$$

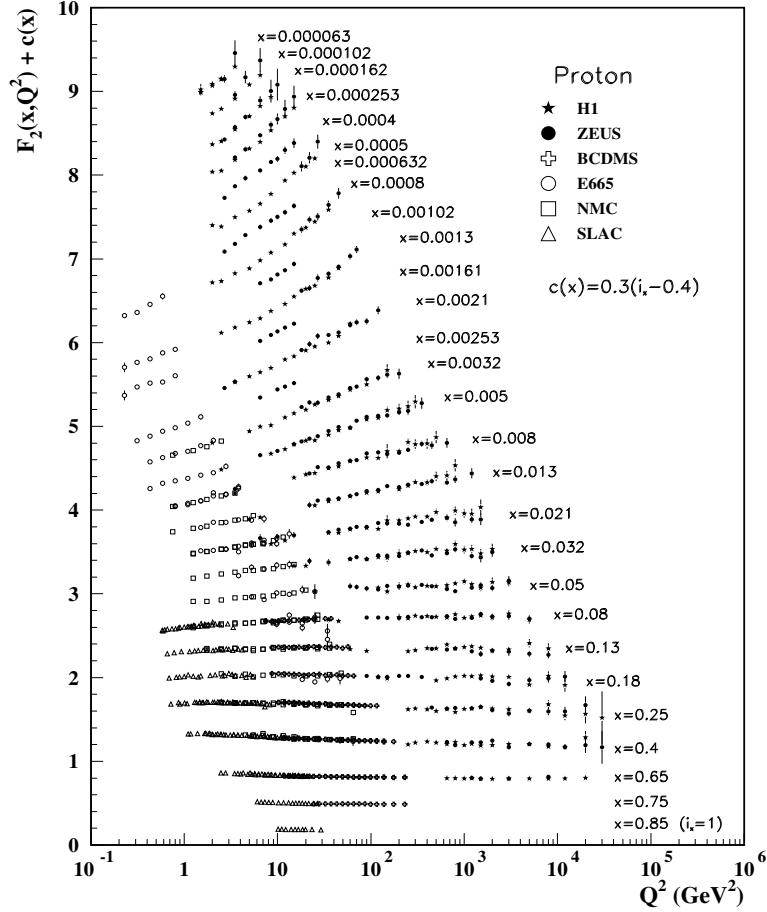


Figure 2.2: World data on the structure function $F_2(x, Q^2)$ of the proton from the Particle Data Group [2].

Here, the variable ϵ represents the virtual photon polarization parameter

$$\epsilon = \left[1 + 2 \left(1 + \frac{Q^2}{4M^2x^2} \right) \tan^2 \frac{\theta}{2} \right]^{-1}, \quad (2.15)$$

with $\epsilon = 0$ corresponding to a purely transverse polarization. The ratio of the longitudinal and transverse virtual-photon absorption cross sections is usually called R ;

$$R = \frac{\sigma_L}{\sigma_T}. \quad (2.16)$$

Data for R are shown in Fig. 2.3; see also Sect. 2.9.4.

The longitudinal and transverse virtual-photon cross sections are related to the structure functions $F_1(x, Q^2)$ and $F_2(x, Q^2)$ as follows,

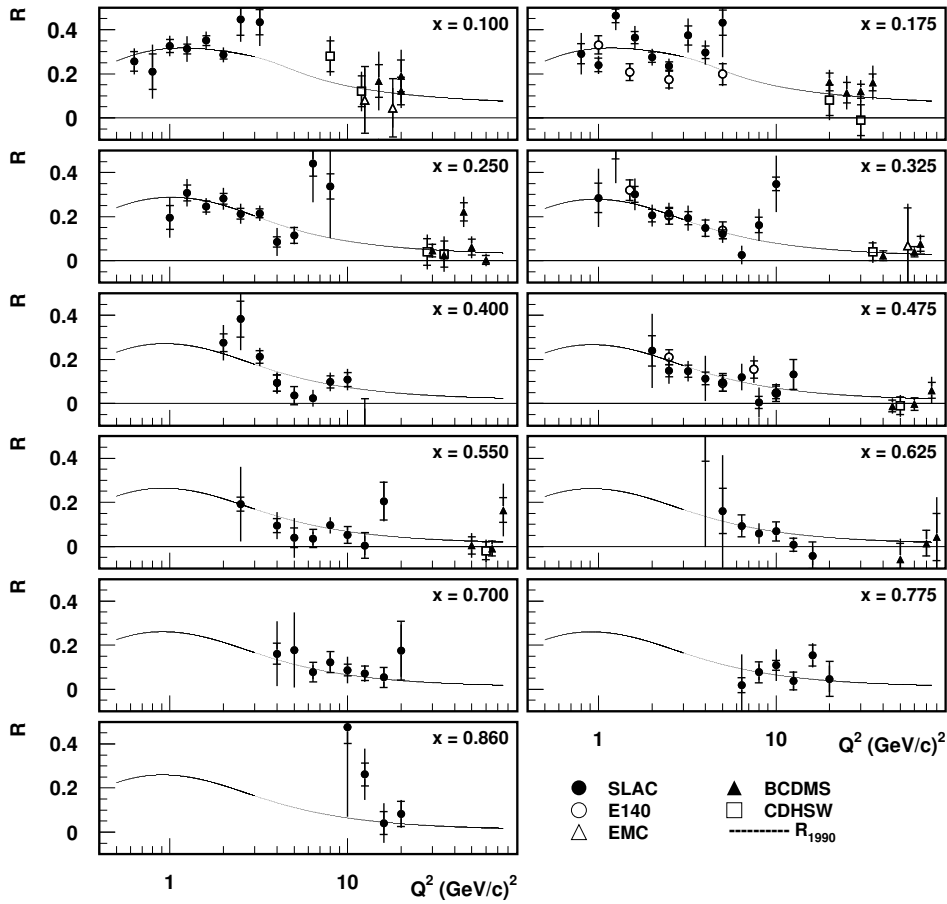


Figure 2.3: Combined hydrogen and deuterium data of R from Ref. [9]. The curve represents parametrization of the data R_{1990} , which is discussed in Sect. 2.9.4.

$$\sigma_T = \frac{4\pi^2\alpha}{KM} F_1 \quad (2.17)$$

and

$$\sigma_L = \frac{4\pi^2\alpha}{KM\nu} \left[\left(1 + \frac{\nu^2}{Q^2} \right) M F_2 - \nu F_1 \right] \equiv \frac{4\pi^2\alpha}{KM} \frac{1}{2x} F_L . \quad (2.18)$$

From Eq. (2.17) it can be seen that $F_1(x, Q^2)$ represents the transverse component of the cross section, while the structure function $F_2(x, Q^2)$, see Eq. (2.18), is a mixture of the transverse and longitudinal components. The structure functions F_1 and F_2 can be expressed in terms of σ_L and σ_T by the following formulas,

$$F_1 = \frac{MK}{4\pi^2\alpha} \sigma_T , \quad (2.19)$$

$$F_2 = \frac{\nu K(\sigma_L + \sigma_T)}{4\pi^2\alpha \left(1 + \frac{Q^2}{4M^2x^2}\right)} . \quad (2.20)$$

2.3 The Quark Parton Model

The early measurements of the nucleon structure functions showed that the structure functions F_1 and F_2 are approximately independent of Q^2 [16]. This behaviour has been discussed by Bjorken [17] and is now known as Bjorken scaling. This scaling phenomenon can be understood in the Quark Parton Model (QPM) [1], which assumes that the nucleon consists of pointlike constituents named partons (quarks). In this model the deep-inelastic electron-nucleon scattering is simply incoherent scattering from quasi-free pointlike quarks (with spin $\frac{1}{2}$) in the nucleon. In this model the two structure functions W_1 and W_2 can be expressed as a sum over all quark flavours as

$$MW_1(\nu, Q^2) \rightarrow F_1(x) = \frac{1}{2} \sum_i e_i^2 f_i(x) , \quad (2.21)$$

$$\nu W_2(\nu, Q^2) \rightarrow F_2(x) = x \sum_i e_i^2 f_i(x) = 2xF_1(x) , \quad (2.22)$$

where $f_i(x)$ is the momentum distribution of a quark with flavour i , and e_i is the charge of the quark (in units of the electron charge). The scaling variable x can be identified with the fractional momentum of the struck quark in the nucleon. Thus, F_2 contains information about the momentum distribution of the parton in the nucleon. The last part of Eq. (2.22) is known as the Callan-Gross relation. However, in reality scaling violations are observed, as shown in Fig. 2.2; see also Sect. 2.4.

According to Eq. (2.17), Eq. (2.18) and Eq. (2.22) R is given in the QPM by

$$R = \frac{4M^2x^2}{Q^2} . \quad (2.23)$$

Eq. (2.23) suggests that R is small at large Q^2 . This prediction of the QPM is in agreement with data [9, 18, 19, 20, 21], see Fig. 2.3, but the predicted quadratic reduction of R at small x is not observed in the data.

2.4 Quantum Chromodynamics

Part of the scaling violations at higher values of Q^2 in the QPM are explained by QCD in terms of gluon radiation.

Within QCD the QPM uses essentially the zeroth order term in the expansion in powers of α_s . The leading order terms (LO) are responsible for most of the observed scaling violations of the structure functions as shown in Fig. 2.4 (a, b, c). The first two diagrams (a, b) correspond

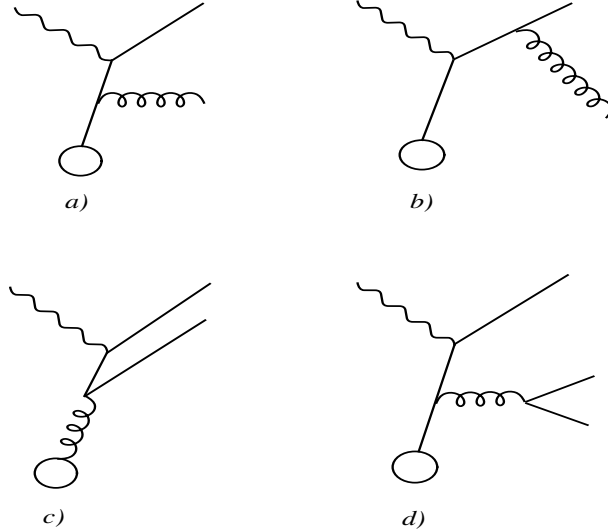


Figure 2.4: Leading order (LO) QCD corrections (a, b, c). Gluon bremsstrahlung diagram before (a) and after interaction (b). Coupling of virtual photon and gluon via quark-antiquark production (c). Example of the next-to-leading order correction (NLO) (d).

to gluon bremsstrahlung from the quark before or after the interaction. The virtual photon cannot couple directly to the gluon, but rather via the production of $q\bar{q}$ pairs as in Fig. 2.4 (c). The gluon bremsstrahlung diagrams can be visualised as a process in which a high x quark radiates a gluon, thus increasing the momentum fraction carried by gluons and decreasing that carried by quarks. Thus at large x , with increasing Q^2 , less of the nucleon momentum is carried by quarks and so F_2 decreases. The quark pair diagram is dominant at small x , where more gluons are available to create $q\bar{q}$ pairs. With increasing Q^2 more of the momentum is carried by sea quarks and that is why F_2 will increase. These trends are shown schematically in Fig. 2.5. Next-to-leading order corrections arise from diagrams like those shown in Fig. 2.4 (d).

The same effects can also be expressed in terms of changing spatial resolution of the virtual photon in deep inelastic scattering. According to QCD the virtual photon resolves a cloud of gluons and other quarks, as shown in Fig. 2.6. The number of quarks, that share the proton momentum, increases with Q^2 . This Q^2 dependence is calculable within QCD, and when the structure functions are known for a certain value of Q^2 , they can be evolved to

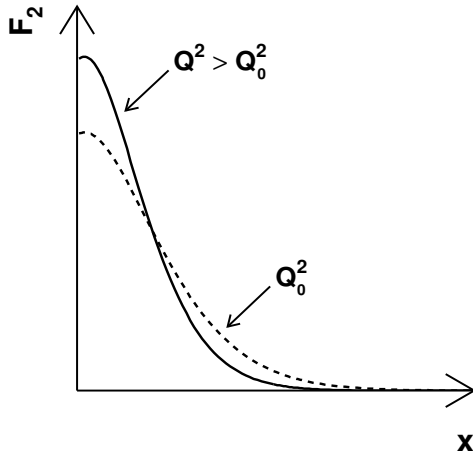


Figure 2.5: The schematic Q^2 dependence of the structure function F_2 .

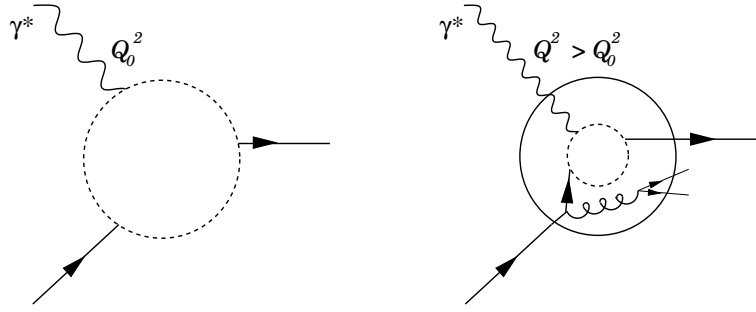


Figure 2.6: Schematic representation of the Q^2 dependence of the quark distributions.

other Q^2 values by using the Dokshitzer-Gribov-Lipatov-Altarelli-Parisi equations (DGLAP) [3, 4, 5].

At low values of Q^2 the wavelength of the virtual photon becomes so large that the quarks inside the nucleon are not fully resolved any longer. The lower limit of Q^2 at which the QPM is still applicable is not exactly known. However, comparison of the data [22] to QCD analyses suggests that Q^2 evolutions work well for Q^2 values as low as 0.3 (GeV/c)^2 . For lower Q^2 values other effects, such as those mentioned in Sect. 2.5, may be important.

Due to gluon radiation and creation of quark-antiquark pairs by gluons, quarks may carry transverse momentum. This then implies that the longitudinal cross section and hence R become non-zero.

2.5 Power Corrections

Additional corrections exist at low Q^2 which are needed in order to fully account for the scaling violations. These corrections are called power corrections and have a form $1/(Q^2)^n$. The operator product expansion (OPE) [23] is generally used to discuss these power corrections within the framework of QCD [24, 25].

2.5.1 Target Mass Correction

One type of power corrections to the structure function are target mass corrections, which arise from the non-vanishing mass M of the target hadron. QCD predictions have been derived under the assumption that the nucleon mass can be neglected when the energy transfer is high, which corresponds to high Q^2 . However, at low Q^2 this is no longer the case and correction terms have to be included [25]. By applying the target mass corrections directly to the structure functions, the measured structure functions $F_i(x, Q^2)$ can be related to corrected structure functions $F_i(\xi, Q^2)$ [26]. These corrected structure functions satisfy the DGLAP equations and depend on the Nachtmann scaling variable ξ [27], which is defined as

$$\xi = \frac{2x}{1 + \sqrt{1 + 4M^2x^2/Q^2}}. \quad (2.24)$$

It is to be noticed that $\xi \rightarrow x$ for high Q^2 . This is consistent with the QPM, which predicts that x is the correct scaling variable at large Q^2 .

2.5.2 Higher Twist Effects

The operator product expansion [23] yields the structure functions in inverse powers of Q^2 ,

$$F_2(x, Q^2) = \sum_{n=0}^{\infty} \frac{C_n(x, Q^2)}{(Q^2)^n}, \quad (2.25)$$

where the functions $C_n(x, Q^2)$ weakly depend (*i.e.*, logarithmically) on Q^2 . The various terms in this expansion are referred to as leading ($n = 0$) and higher ($n \geq 1$) twists. The *twist number* (t) is defined in such a way that the leading one is equal to two and higher ones correspond to consecutive even integers [6]. Thus the righthand side of the equation

$$F_2(x, Q^2) = x \sum_i e_i^2 \left[q_i(x, Q^2) + \bar{q}_i(x, Q^2) \right] \quad (2.26)$$

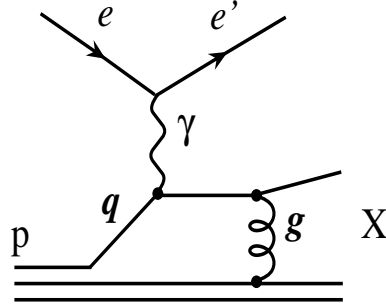


Figure 2.7: Example of the possible interactions between the struck quark and the spectator quarks. The depicted one gluon exchange represents a higher-twist correction that is not included in a LO approach.

corresponds to the leading twist contribution to F_2 . The higher twist operators correspond to interactions between the struck quark and the spectator quarks, as is shown in Fig. 2.7. The size of these terms in Eq. (2.25) cannot be easily calculated, since they depend on the unknown wave function of the bound-state quarks. By introducing a leading twist structure function, F_2^{LT} (leading twist contribution to F_2), the structure function F_2 is usually parametrized as [6]

$$F(x, Q^2) = F^{LT}(x, Q^2) \left(1 + \frac{C(x)}{Q^2} + \dots \right). \quad (2.27)$$

Here, the coefficient $C(x)$ characterises the strength of the twist-four term.

The need to modify the QCD-improved parton model by including higher twist contributions to the structure functions behaving as $1/(Q^2)^n$ ($n \geq 1$) is shown in Ref. [7]. For Q^2 larger than $1 (\text{GeV}/c)^2$ a QCD analysis [28] suggests that significant higher twist effects are needed in a next-to-leading order (NLO) calculation of F_2 and R in order to describe the data on both proton and deuterium targets. However, it has been shown by the same authors [29] that in a NNLO calculation a large fraction of the higher twist effects that have been observed at $Q^2 > 1 (\text{GeV}/c)^2$ disappear.

The higher twist corrections to the leading term in Eq. (2.26) cannot correctly describe the low Q^2 ($Q^2 < 1 (\text{GeV}/c)^2$) region, since the expansion, see Eq. (2.25) diverges for $Q^2 \rightarrow 0$, as illustrated in Fig. 2.8, and discussed in the next section.

2.6 Physics at low Q^2

In the region of high Q^2 the results of DIS measurements are interpreted in terms of partons (quarks and gluons). The theoretical framework is provided in this case by the QCD improved parton model. The description fails when Q^2 becomes of the order¹ of $1 (\text{GeV}/c)^2$, where

¹The lower limit of Q^2 at which the pQCD is still applicable is not exactly known.

non-perturbative effects become important (non-pQCD), which are still not fully understood [6]. However, within the general formalism it is possible to predict the behaviour of the structure functions $F_{1,2}$ and R at $Q^2 \rightarrow 0$.

The hadronic tensor $W_{\mu\nu}$ [15] is given by

$$W^{\mu\nu} = \frac{F_1(x, Q^2)}{M} \left(-g_{\mu\nu} + \frac{q^\mu q^\nu}{q^2} \right) + \frac{F_2(x, Q^2)}{M(p \cdot q)} \left(p_\mu - \frac{p \cdot q}{q^2} q^\mu \right) \left(p_\nu - \frac{p \cdot q}{q^2} q^\nu \right), \quad (2.28)$$

where M is the proton mass. The invariant quantity $p \cdot q$ is related to the energy transfer ν in the target rest frame as $p \cdot q = M\nu$.

In order to display the behaviour of the tensor $W^{\mu\nu}$ in the vicinity of $Q^2 = 0$, Eq. (2.28) can be rearranged in the form

$$W^{\mu\nu} = -\frac{F_1}{M} g^{\mu\nu} + \frac{F_2}{M(p \cdot q)} p^\mu p^\nu + \left(\frac{F_1}{M} + \frac{F_2 p \cdot q}{M q^2} \right) \frac{q^\mu q^\nu}{q^2} - \frac{F_2}{M} \frac{p^\mu q^\nu + p^\nu q^\mu}{q^2}. \quad (2.29)$$

The singularities for $Q^2 \rightarrow 0$ (third and fourth terms in Eq. (2.29)) cannot be real, as otherwise $W^{\mu\nu} \rightarrow \infty$. Therefore, the structure functions should obey the following relations in the limit $Q^2 \rightarrow 0$:

$$F_2 = O(Q^2) \quad (2.30)$$

$$\frac{F_1}{M} + \frac{F_2 p \cdot q}{M q^2} = O(Q^2). \quad (2.31)$$

Thus, the structure function F_2 must vanish in the limit $Q^2 \rightarrow 0$. An illustration of the behaviour of the structure function F_2 at low values of Q^2 is shown in Fig. 2.8.

Also, R vanishes when $Q^2 \rightarrow 0$. This follows from Eq. (2.30), Eq. (2.31) and Eq. (2.32).

$$R(x, Q^2) = \frac{\sigma_L}{\sigma_T} = \frac{(1 + Q^2/\nu^2) F_2}{2x F_1} - 1 = (1 + Q^2/\nu^2) (1 - O(Q^2)/F_1) - 1 = O(Q^2). \quad (2.32)$$

Models assuring a smooth transition from the scaling to the nonscaling region and applicable in a wide Q^2 interval are thus necessary for understanding the data and hence the underlying dynamics. This is possibly accomplished in the VMD model [30]. In this model the structure function F_2 is written as

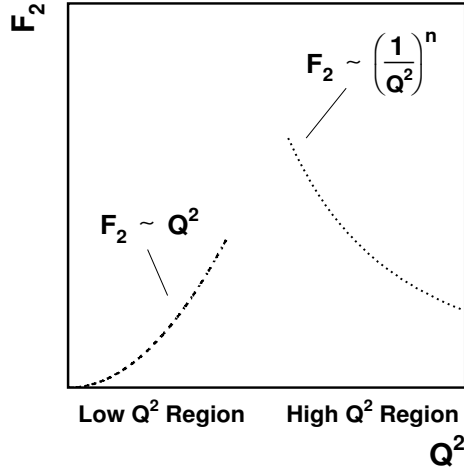


Figure 2.8: Illustration of the behaviour of the structure function F_2 at low values of Q^2 and the behaviour of F_2 as implied by higher twist effects. The LO term of F_2 at high Q^2 is not included.

$$F_2 = \frac{Q^2}{4\pi} \sum_V \frac{M_V^4 \sigma_V(s)}{\gamma_V^2 (Q^2 + M_V^2)^2}, \quad (2.33)$$

where the quantities $\sigma_V(s)$ are the vector-meson-nucleon total cross sections, M_V is the mass of the vector meson V , and γ_V^2 is related to the leptonic width of V . If only a finite number of vector mesons is included in Eq. (2.33), F_2 vanishes as $1/Q^2$ at large values of Q^2 . Therefore, it does not contain the leading twist term. Scaling can be introduced by including an infinite number of vector mesons in the sum. This version of the VMD model is called the generalized VMD model (GVMD) [31].

The longitudinal (σ_L) and transverse (σ_T) virtual-photon cross sections in this model are given by [30]

$$\sigma_T = \sum_V \frac{e^2}{f_V^2} \left(\frac{M_V^2}{M_V^2 + Q^2} \right)^2 \sigma_V^T, \quad (2.34)$$

$$\sigma_L = \sum_V \frac{e^2}{f_V^2} \frac{\xi_V(K) Q^2}{M_V^2} \left(\frac{K}{\nu} \right)^2 \left(\frac{M_V^2}{M_V^2 + Q^2} \right)^2 \sigma_V^T, \quad (2.35)$$

where σ_V^T is the total cross section of a transversely polarized vector particle. The ratio e/f_V is the vector-meson photon coupling, while K is equal to $\nu - Q^2/2m_p = (s - m_p^2)/2m_p$, where m_p is the mass of the proton and $s = w^2$. The factor $\xi_V(K)$ is introduced because the longitudinally polarized particle does not need to have the same cross section as a transverse one. Also, $\xi_V(K)$ is expected to be in the range $0 \leq \xi_V \leq 1$. So, according to Eq. (2.34) and Eq. (2.35) R is equal to

$$R = \sum_V \xi_V \frac{Q^2}{M_V^2} \left[1 - \frac{Q^2}{2m_p \nu} \right]^2. \quad (2.36)$$

According to Eq. (2.36) R varies as Q^2 at fixed ν/Q^2 (as long as $\xi(K)$ is slowly varying). In case of increasing Q^2 with the missing mass (or K) fixed, R first increases like Q^2 , goes through a maximum at $Q^2 = s - m_p^2$, and decreases like $1/Q^2$ as $Q^2 \rightarrow \infty$ [30]. In case of decreasing Q^2 according to Eq. (2.36) one finds $R \rightarrow 0$.

2.7 Nuclear Effects in the Structure Functions

In 1982 the EMC experiment at CERN discovered that the structure function F_2 depends on the mass number A of the target (A -dependence). This nuclear effect has been studied by comparing F_2 measured on bound nucleons in nucleus A and deuterium. Direct comparison with the structure function of the proton, strictly speaking the only free nucleon, is not appropriate in view of the fact that nuclei contain protons and neutrons in approximately equal numbers and that the proton and the neutron structure functions are different, especially at large x [8]. According to the expression from the QPM, Eq. (2.22), this difference implies that the quark distribution functions are different for a bound and a free nucleon.

In Fig. 2.9 the ratio F_2^A/F_2^D as a function of x is shown in a schematic way. The fact

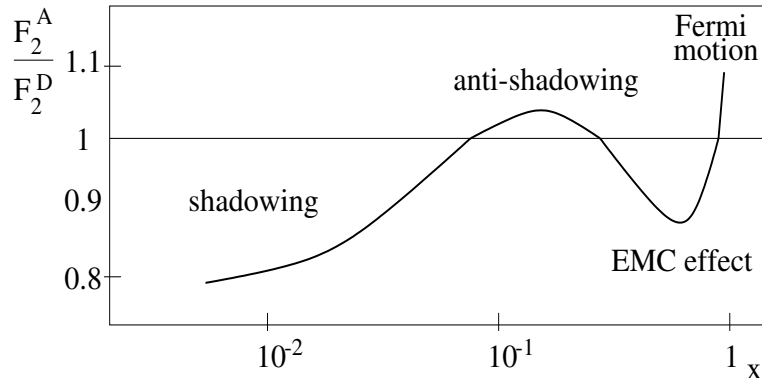


Figure 2.9: Schematic representation of the structure function ratio F_2^A/F_2^D .

that $F_2^A \neq F_2^D$ is referred to with different terms, depending on the region of x .

- For $x < 0.05 - 0.1$ the ratio F_2^A/F_2^D is smaller than unity. This is known as *shadowing*.
- For $x \approx 0.1 - 0.2$ the ratio is slightly larger than unity. This enhancement is called *anti-shadowing*.
- At $x \approx 0.2 - 0.8$ the ratio starts decreasing and reaches a minimum around $x = 0.6$ and then begins to rise again. This behaviour is called the EMC effect².
- For $x \gtrsim 0.8$ the ratio grows above unity. This is the *Fermi motion* region.

In this section several models that try to explain the observed ratio σ^A/σ^D are presented.

2.7.1 x Rescaling

The EMC effect can be explained by a model that assumes that the effective nucleon mass inside nuclei is lower than the free nucleon mass [32]. This causes a shift in the scaling variable x , see Eq. (2.4), towards higher values (*x rescaling*). In that case the bound-nucleon structure function F_2^A is approximated as

$$F_2^A(x, Q^2) \approx F_2^D(x/z, Q^2) , \quad (2.37)$$

where the variable z depends on the average one-nucleon separation energy (ϵ) and the mass of a free nucleon (m): $z \approx 1 - \frac{\epsilon}{m}$. It has been found [32] that in order to get agreement with the data in the region $x > 0.1$, the value of the separation energy (ϵ) has to be set to about 40 MeV.

2.7.2 Pion Enhancement Model

In the pion enhancement model the EMC effect is assumed to be due to an enhancement in the nucleus of the pion field associated with the nucleon-nucleon interaction [33, 34]. The structure function of a nucleon bound in a nucleus of mass number A is written as

$$F_2^A(x, Q^2) = \int_x f_N(z) F_2^N\left(\frac{x}{z}, Q^2\right) dz + \int_x f_\pi(y) F_2^\pi\left(\frac{x}{y}, Q^2\right) dy , \quad (2.38)$$

where the first integral represents the convolution of the free nucleon structure function F_2^N with the nucleon distribution function f_N inside the nucleus. Similarly, the second term is the convolution of the pion structure function F_2^π with the pion distribution function f_π in the nucleus. The assumption is made that the structure functions F_2^N and F_2^π are unaffected by the nuclear medium.

The presence of n_π^A pions in a nucleus A , carrying on average a fraction ϵ_π^A of the nuclear momentum per nucleon, reduces the momentum fraction carried by the nucleons to $\epsilon_N^A = 1$

²Usually, all nuclear effects together are called the EMC effect.

ϵ_π^A and gives rise to the EMC effect at large x . The model successfully describes the data in the range $0.1 < x < 0.8$ [33, 34].

In this model, the A dependence of the EMC effect can be reproduced by taking the pion density proportional to the nuclear density [35]. For $x < 0.1$, the ratio predicted by the model increases monotonically above unity due to the enhancement in the number of pions per nucleon (2 %, 9 %, 10 % and 12 % for D, Al, Fe, Au) required by the model. This enhancement, however, appears to be in contradiction with recent results of Drell-Yan experiments [36]. It has been shown [37] that if the parameters of the pion model are adjusted to be consistent with the Drell-Yan data, it would be able to account for less than 20 % of the EMC effect at $x > 0.4$.

2.7.3 Q^2 Rescaling Model

The rescaling model is formulated by Close, Roberts, Ross and Jaffe [38, 39, 40]. The idea of this model is that the quark confinement size in a nucleus is larger than that in a free nucleon. It suggests that the effective value of Q^2 may not be the same for a nucleus and for a nucleon,

$$F_2^A(x, Q^2) \approx F_2^D(x, \xi Q^2), \quad (2.39)$$

where ξ represents the amount by which Q^2 is rescaled inside the medium, *e.g.* $\xi > 1$. It turns out that Q^2 needs to be rescaled to higher values in order to obtain quark distributions which are different in bound [8].

At $Q^2 \approx 20$ (GeV/c)² the Fe/D data can be reproduced by this model with a value of the rescaling parameter $\xi \approx 2$. In the range of applicability of the model ($0.2 < x < 0.8$) the agreement with the data is good [41]. So far the model provides no explanation for the observed change of scale, only a framework for discussing it [8].

2.7.4 Nucleon Swelling

A small change of the nucleon radius, regardless of its origin, can lead to the EMC effect, as is shown in [42]. In case of an increased nucleon radius, the quark momentum distribution becomes compressed which leads to a smaller probability to find partons at large x , *e.g.* decreased F_2^A values. The resulting predictions are in reasonable agreement with the data for $x > 0.2$. It is found that the nucleon radius should be about 5-10 % larger in iron than in deuterium [41] in order to reproduce the EMC effect data. However, from other experiments (Quasi-elastic electron scattering) [43] such a large increase is not supported.

2.7.5 Cluster Model

In this model the assumption is made that a fraction of the valence quarks in the nucleus move quasi-freely inside enlarged bags, consisting of 6, 9 or more valence quark clusters. The possibility that clusters might explain the EMC effect has been mentioned first by Jaffe [44]. The momentum distribution of quarks in an i -quark cluster, $n_i(x)$ ($i=6,9,\dots$), is taken to be

$$xn_i(x) \sim x^{1/2}[1 - x/(i/3)]^{2(i-1)-1} \quad (2.40)$$

based on [45, 46]. It has been shown that with this model the EMC effect in Fe can be described by assuming that nucleons are subsumed into 6-quark or larger clusters with 30 % probability [47].

2.7.6 Vector Meson Dominance Model

For the low x ($x < 0.1$, shadowing) region the Vector Meson Dominance Model can be used in order to explain the behaviour of the ratio F_2^A/F_2^D .

High-energy photon induced reactions bear a remarkable resemblance to purely hadronic reactions, apart from a scale factor of about α in the cross section, where α is the electromagnetic coupling constant. This finds a simple interpretation in terms of the hadronic structure of the photon [31]. The physical photon can be viewed as fluctuating between a bare photon state, a set of electromagnetic states (e.g., e^+e^- pairs) and a superposition of hadronic states, with the same quantum numbers as the photon ($J^{PC} = 1^{--}$), so called vector mesons (ρ , ω , ϕ , ...). The probability for the photon to convert to a hadron is about α , where α is the electromagnetic coupling constant. This is the basis of the Vector Meson Dominance Model (VMD)³. It is clear then that within this model the photon - nucleus cross section must exhibit some of the characteristics of the hadron - nucleus interaction.

The total hadron - nucleus cross section σ_{hA} is known to be smaller than A times the total hadron - nucleus cross section σ_{hN} ($\sigma_{hA} < A\sigma_{hN}$). This is ascribed to the fact that the nucleons on the surface of the nucleus project their shadow onto the inner ones, which are thus not exposed to the full hadron beam intensity [8]. The photon interactions should thus also be shadowed in nuclei [48]. The size of the effect increases with the photon energy and with the nucleon mass number A [31].

According to the VMD the distance over which a photon behaves like a hadron can be written as

$$\Delta L_{\gamma(h)} = \frac{2\nu}{M_V^2 + Q^2} = \frac{1}{Mx} \frac{1}{1 + M_V^2/Q^2}, \quad (2.41)$$

where M_V is the mass of the vector meson the photon fluctuates into. The mean free path of the hadron in the nuclear medium is

$$L_h(M_V) = \frac{1}{n_0 \sigma(M_V)}, \quad (2.42)$$

³When heavier mass vector states are included in the VMD model, then that model is called Generalized Vector Meson Dominance Model (GVMD).

where n_0 is the nucleon density and $\sigma(M_V)$ is the cross section for interactions of the hadronic system of mass M_V with the nucleon. Necessary conditions for shadowing are that $\Delta L_{\gamma(h)} > L_h(M_V)$ and $R_A > L_h(M_V)$, with R_A the nuclear radius. So, shadowing will disappear at fixed ν , with increasing Q^2 because of the decrease of $\Delta L_{\gamma(h)}$. At fixed Q^2 shadowing will decrease with increasing x . Shadowing for the real photon ($Q^2 = 0$) will be a growing function of the photon energy.

Several types of VMD models exist: models that do not include the possibilities of interference between different vector states belonging to the photon are called *diagonal ones*. *Off - diagonal* models include these interference terms. Unfortunately, none of the VMD models makes explicit predictions for the very small x region ($x < 10^{-3}$). Comparison of the VMD with the data shows a reasonable agreement in the region $x > 0.01$ [8].

2.7.7 Partonic Fusion

This model also gives a possible explanation of the behaviour of the ratio F_2^A/F_2^D in the shadowing region.

In this model the scattering is considered in the Breit frame [49]. In this frame the energy of the virtual photon is zero and the momentum of the scattered parton is reversed by the collision. Using the uncertainty principle the localization of the parton carrying a fraction x of the nucleons momentum P_N can be written as $\Delta L \sim 1/P_i \sim 1/(xP_N)$. On the other hand, if R_N is the nucleon radius ($R_N \approx 1$ fm), then the nucleons are separated by a distance $\Delta L_N \sim 2R_N$ in the laboratory frame or $\Delta L_N \sim 2R_N(M/P_N)$ in the Breit frame. So, in case $\Delta L > \Delta L_N$ the partons belonging to different nucleons start to overlap. This condition is satisfied if $x < x_N = 1/(2R_N M) \approx 0.1$.

For x values smaller than $x_A = 1/(2R_A M) \approx x_N A^{-1/3}$ (R_A the nuclear radius) all partons from all nucleons overlap. Overlapping partons can interact and fuse, reducing the parton density at small x . The total momentum carried by the partons is not changed as a result of the fusion but is simply redistributed over different x regions. The depletion of low momentum partons due to the fusion process thus leads to an enhancement in the density of higher momentum partons, expected to be maximum around $x \approx x_N$.

Since in DIS the cross section is proportional to the parton distribution functions, the depletion of low x partons causes a depletion in the nuclear structure functions which starts somewhere below x_N and becomes maximal at $x \approx x_A$. Similarly the enhancement in the parton density at $x \approx x_N$ determines an increase (*anti - shadowing*) of the bound nucleon structure functions with respect to the free nucleon ones.

Other authors [50] elaborated on this approach, concentrating on the A dependence of the point where shadowing sets in. These authors observed that the average distance between one parton from a nucleon and another from a neighbouring nucleon is larger for nucleons at the surface of the nucleus than for nucleons well inside the nucleus. As a result of these surface versus volume effects, the onset of shadowing is seen to increase with A .

The comparison between this model approach and data gives a reasonable agreement in the region $x < 0.1$ [51, 52].

2.8 Ratio of the Longitudinal to Transverse Virtual-Photon Cross Sections

In order to calculate the ratio of the structure functions F_2^A/F_2^D from data, one needs information on $R(x, Q^2)$, which is the ratio of longitudinal to transverse virtual-photon absorption cross sections; $R = \sigma_L/\sigma_T$. This ratio enters the ratio of DIS cross section on two nuclei:

$$\frac{\sigma^A}{\sigma^D} = \frac{F_2^A(1 + \epsilon R_A)(1 + R_D)}{F_2^D(1 + R_A)(1 + \epsilon R_D)} . \quad (2.43)$$

In two particular cases knowledge of $R(x, Q^2)$ is not needed in order to calculate the ratio F_2^A/F_2^D . Firstly, when the data have been taken at $\epsilon = 1$, and in the second case when $R_A = R_D$. If either one of these cases is met, then

$$\frac{\sigma^A}{\sigma^D} = \frac{F_2^A}{F_2^D} . \quad (2.44)$$

The structure function F_2 can be expressed in terms of the longitudinal and transverse virtual photon absorption cross sections σ_L and σ_T ; see Eq. (2.20). A possible difference in the A dependence of these two components of the cross section can be studied by investigating the A dependence of R , the ratio of the longitudinal and transverse virtual photon absorption cross sections; see Eq. (2.16). Information on the A dependence of the longitudinal and transverse component separately could help in understanding the A dependence of F_2 .

Previous measurements of R (unlike F_2) showed that R does not seem to depend on A ; see Fig. 2.10, indicating that nuclear effects are equal⁴ for F_1 and F_2 . This has the important consequence that the structure function ratio F_2^A/F_2^D is identically equal to the cross section ratio σ^A/σ^D . It has to be mentioned that all previous measurements of R (for different targets) have been done at high values of Q^2 ($Q^2 \gtrsim 1$ (GeV/c)²) and have large errors [9]. For smaller values of ϵ the cross section is equal to F_2^A/F_2^D only if $R_A = R_D$. A difference between R_A and R_D will thus introduce an ϵ -dependence of σ_A/σ_D . Hence, measurements of σ_A/σ_D as a function of ϵ can be used to extract experimental information on R_A/R_D [13].

Experimentally, possible nuclear modifications of the transverse-longitudinal ratio $R(x, Q^2)$ have been studied most recently by the HERMES collaboration [10]. The large effect initially found was not confirmed by the neutrino data [55]. Moreover, a reanalysis of the HERMES data on ¹⁴N and new data on ⁸⁴Kr showed that the initially observed effect had to be largely attributed to photon showers in the edges of the detection equipment [12]. However, the discussion about a possible A -dependence of $R(x, Q^2)$ is not closed, as a modest enhancement of R is not excluded by the data. Several predictions exist about a possible A -dependence effect. It has been shown that nuclear mesons can contribute coherently to enhance the

⁴There are some weak indications that $R_A > R_D$.

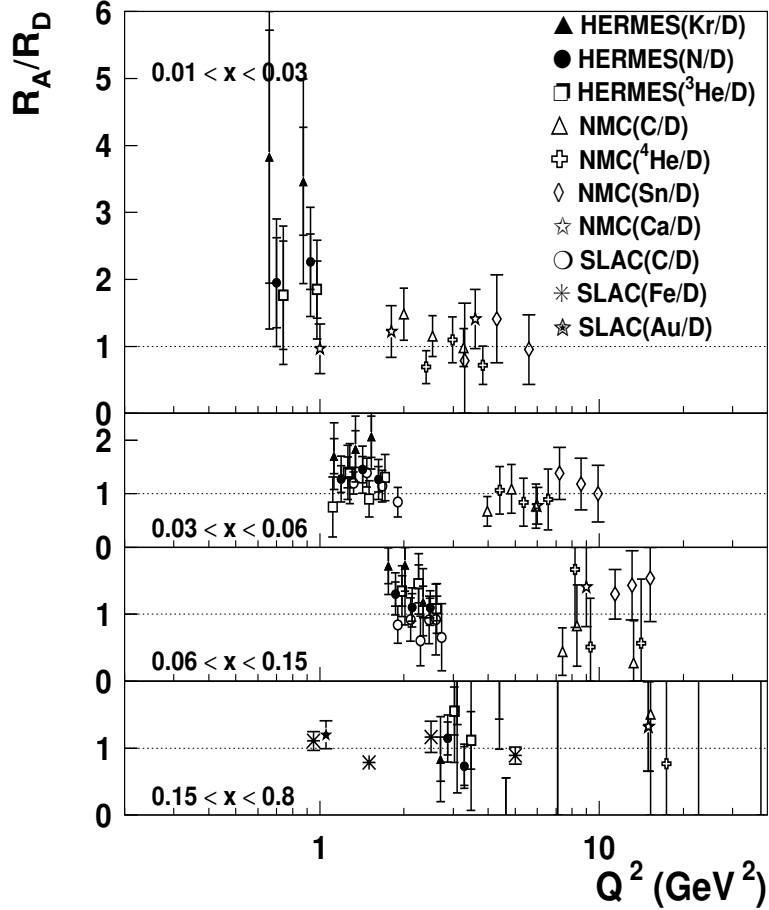


Figure 2.10: The ratio R_A/R_D for several nuclei with respect to deuterium as a function of Q^2 for four different x bins [13]. The closed symbols (nitrogen and krypton) are from the HERMES experiment [13]. The open triangles (carbon) and crosses (helium) have been derived from the NMC data by using Eq. (2.43). The SLAC [53] and NMC data [54] have been derived from published values of $\Delta R = R_A - R_D$ and a parametrization [9] for R_D .

electroproduction cross section on nuclei for longitudinal virtual photons at low Q^2 , while depleting the cross section for transverse virtual photons [56].

Alternatively, it has been shown that an A -dependence of $R(x, Q^2)$ may exist at high values of x and low values of Q^2 due to a mixture of the transverse and longitudinal structure functions [57], as shown in Fig. 2.11. The transverse structure function for a nucleus is described not only by the transverse one for the nucleon but also by the longitudinal one with the admixture coefficient $\vec{p}_{N\perp}^2/(2\tilde{p}_N^2)$. Here $\vec{p}_{N\perp}$ is the component of the nucleon momentum perpendicular to \vec{q} . The mixing arises from the fact that the nucleon momentum direction is not necessary along the virtual photon direction. Because the admixture is proportional to $\vec{p}_{N\perp}^2/(2\tilde{p}_N^2) \sim \vec{p}_{N\perp}^2/Q^2$, the modification effects are larger at small values of Q^2 . However, the

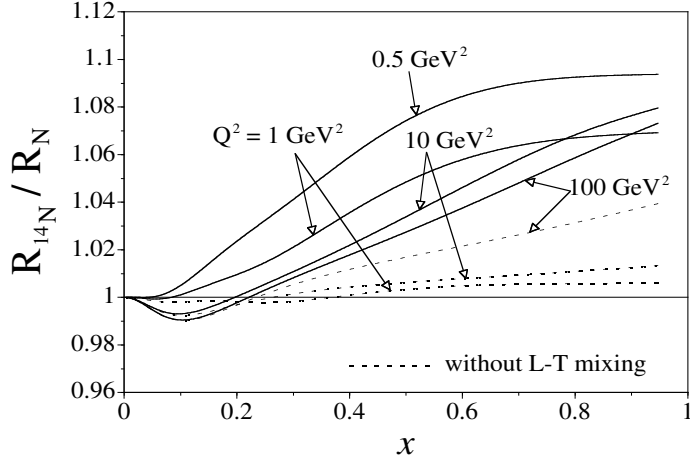


Figure 2.11: The nitrogen-nucleon ratio R_{14N}/R_N is shown at $Q^2 = 0.5, 1, 10$, and 100 (GeV/c) 2 . The solid curves are the full results and the dashed ones are obtained without admixture effects due to Fermi motion of the nucleon [58].

modification does not vanish even at $Q^2 = 100$ (GeV/c) 2 due to *Fermi-motion* and *binding* effects. Thus, the motion of the nucleon perpendicular to the direction of the virtual photon gives rise to a mixture of longitudinal and transverse structure functions in the nucleus [58].

2.9 Models for F_2 and R

In order to calculate radiative corrections and to carry out bin-centering corrections models are needed that parametrize F_2 and R . In this section all models used in the analysis are presented.

2.9.1 Parametrization of F_2 for Hydrogen

The parametrization *ALLM97* [59] has been used in order to obtain F_2 for hydrogen in the DIS region. This parametrization is based on a Regge motivated approach, similar to that used earlier by Donnachie and Landshoff [60], extended into a large Q^2 regime in a way compatible with QCD expectations. The data used to fit the parameters were all F_2 measurements available in 1997 together with the total photoproduction cross section data, which had been measured at that time up to center of mass energies of $W \approx 20$ GeV.

There are altogether 23 parameters to be determined from a fit to the data. The F_2 data can be converted to $\sigma_{tot}(\gamma^* p)$ by using Eq. (2.20),

$$\sigma_{tot}(\gamma^* p) \equiv \sigma_L + \sigma_T = \frac{4\pi\alpha^2}{Q^2(1-x)} \frac{Q^2 + 4m^2x^2}{Q^2} F_2(W^2, Q^2) . \quad (2.45)$$

The parametrization *ALLM97* describes the data well, both for real and virtual photons, as can be seen in Fig. 2.12.

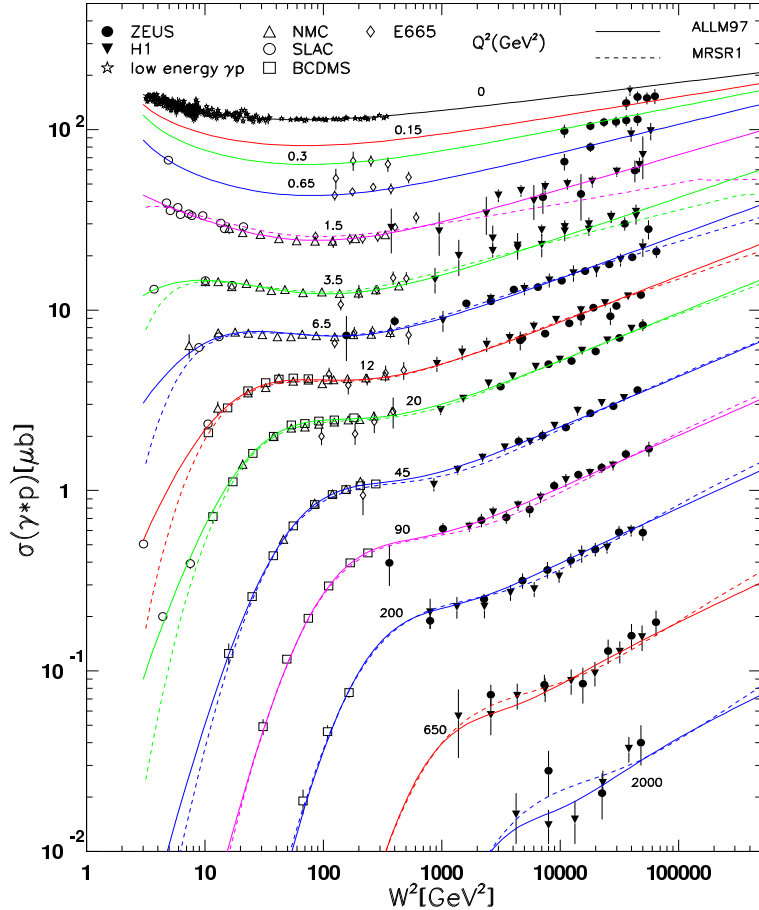


Figure 2.12: The total $\gamma^* p$ cross section as function of W^2 , for different Q^2 values. The curves correspond to the *ALLM97* parametrization (full curve) and those of the *MRSR1* one (dotted curve).

For the resonance region of hydrogen two models have been used. For values of $Q^2 > 0.3$ (GeV/c) 2 the so-called *h2model* has been used [61]. At values of $Q^2 < 0.5$ (GeV/c) 2 - the *ineft* model has been used [62]. These parametrizations have been joined linearly in the region $0.3 < Q^2 < 0.5$ (GeV/c) 2 . Both resonance models have been calculated up to $W^2 < 4.3$ GeV^2 and joined linearly to *ALLM97*, in the region $3.5 < W^2 < 4.3$ GeV^2 .

2.9.2 Parametrization of F_2 for Deuterium

Neglecting nuclear effects in deuterium, the deuterium structure function can be written as the sum of the proton and neutron structure functions,

$$F_2^D = F_2^p + F_2^n , \quad (2.46)$$

which can be rearranged into the form

$$F_2^D = F_2^p \left(\frac{F_2^n}{F_2^p} + 1 \right). \quad (2.47)$$

Using the parametrization of F_2^n/F_2^p [63] given by

$$\frac{F_2^n}{F_2^p} = 0.976 + x \left(-1.34 + x \left(1.319 + x(-2.133 + 1.533x) \right) \right), \quad (2.48)$$

and a parametrization for F_2^p , see Sect. 2.9.1, the deuterium structure function in the DIS region can be found.

In the resonance region ($W^2 < 4.3$ GeV 2) the model *d2model* has been used [64]. This resonance parametrization has been joined linearly to the DIS parametrization in the same way as it has been done for hydrogen.

2.9.3 Parametrization of the Cross Section for $A > 2$ Targets

In practice the ratio of the cross sections σ^A/σ^D is represented by the ratio of the normalized cross section for a hypothetical nucleus with an equal number $A/2$ of protons and neutrons to deuterium. Therefore, the data for nuclei with $N \neq Z$ have to be corrected for the excess neutrons, the so-called *non-isoscalarity* correction

$$\left(\frac{\sigma^A}{\sigma^D} \right) \Bigg/ \left(\frac{\sigma^A}{\sigma^D} \right)_{is} = \frac{\left(Z + N \frac{F_2^n}{F_2^p} \right)}{0.5A \left(1 + \frac{F_2^n}{F_2^p} \right)}. \quad (2.49)$$

The model values for $(\sigma^A/\sigma^D)_{is}$ are based on parametrizations of SLAC and NMC. At high x region ($x > 0.7$ for carbon, copper and gold, and $x > 0.25$ for aluminium) the parametrization for $\left(\frac{\sigma^A}{\sigma^D} \right)_{is}$ based on the SLAC data [65] has been used, see Fig. 2.13,

$$\left(\frac{\sigma^A}{\sigma^D} \right)_{is} = C(x) A^{\alpha(x)}, \quad (2.50)$$

where the functions $C(x)$ and $\alpha(x)$ have the following parametrizations:

$$\begin{aligned} \alpha(x) = & -0.070 + 2.189x - 24.667x^2 + 145.291x^3 \\ & -497.237x^4 + 1013.129x^5 - 1208.393x^6 \\ & +775.767x^7 - 205.872x^8, \end{aligned} \quad (2.51)$$

with

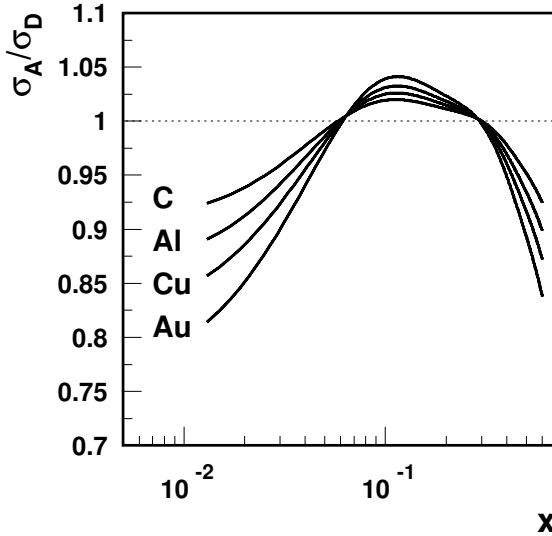


Figure 2.13: Parametrization of the ratio $\left(\frac{\sigma^A}{\sigma^D}\right)_{is}$ according to Ref. [65], for the nuclei used in experiment e99-118.

$$\ln C(x) = 0.017 + 0.018 \ln x + 0.005 (\ln x)^2 . \quad (2.52)$$

At low x the parametrizations based on NMC data [66, 67], have been used

$$\left(\frac{\sigma^A}{\sigma^D}\right)_{is} = \begin{cases} (0.9255 - 0.40x - 0.09873e^{(-27.714x)} + 0.2567x^{0.2465}) - 0.025 & \text{if } x < 0.7 \text{ (C)} \\ 0.825 - 0.46x - 0.19e^{(-21.8x)} + 0.34x^{-4.91}x^{5.0} & \text{if } x < 0.25 \text{ (Al)} \\ (1.026 - 0.56x - 0.34e^{(-45.7x)} + 0.26x^{(-4.41)}x^{5.0}) + 0.03 & \text{if } x < 0.7 \text{ (Cu)} \\ (0.970 - 1.433x - 0.334e^{(-54.53x)} + 1.074x^{0.711}) + 0.071 & \text{if } x < 0.7 \text{ (Au)} . \end{cases}$$

Using Eq. (2.49) and the parametrization of $(\sigma^A/\sigma^D)_{is}$ the model cross section for heavy targets is given by the following formula:

$$\sigma^A = \sigma^D \left(\frac{\sigma^A}{\sigma^D}\right)_{is} \left[\frac{\left(Z + N \frac{F_2^n}{F_2^p} \right)}{0.5A \left(1 + \frac{F_2^n}{F_2^p} \right)} \right] . \quad (2.53)$$

2.9.4 Parametrization of the Function R

In the first iteration of the data analysis, see Sect. 4.12, the parametrization R_{1990} [9] was used in order to describe R . This parametrization was made by Whitlow [9] by re-analysis of the SLAC combined proton and deuterium data for deep inelastic electron scattering. Also, the results from experiments E140 [18], EMC [19], BCDMS [20] and CDHSW [21], have been used as shown in Fig. 2.3. However, this parametrization is not working at low values of Q^2 where no data exist. In order to have a first approximation for R at low Q^2 , R is calculated as if $Q^2 = 0.35 \text{ (GeV/c)}^2$ for $Q^2 < 0.35 \text{ (GeV/c)}^2$. This allows to use the parametrization R_{1990} at low Q^2 .

This parametrization has been used in the first iteration for all targets, since no clear evidence for a deviation of R_A from R_D has been found until now [13] as shown in Fig. 2.10.

The parametrization R_{1990} violates the constraint at $Q^2 = 0$, see Eq. (2.32). Therefore, in later iterations another parametrization has been used, see Sect. 4.12.

2.10 Radiative Corrections

The differential cross section for electron-nucleon scattering, see Eq. (2.8), is written in the one photon exchange (OPE or Born) approximation, with the simplest picture shown in Fig. 2.1 (or in Fig. 2.14 (a)). This is the lowest order contributing process in α , the fine structure constant. Additional Feynman diagrams (higher order electromagnetic processes in α) contributing to the scattering are shown in Fig. 2.14 (b, c, d, e), which include vacuum polarization (creation of particle-antiparticle pairs), vertex processes (emission and reabsorption of virtual photons), and bremsstrahlung (emission of real photons in the field of the nucleon during interaction). Cross sections measured in electron scattering may have large contributions from those processes. In order to determine the differential (Born) cross section these other processes should be calculated and corrected for.

The radiative processes can be divided into two main categories. Internal effects occur at the scattering vertex. The internal effects include internal bremsstrahlung (emission of photons in the field of the nucleon during the scattering process), vacuum polarization, vertex processes, and multiple photon exchange.

External processes occur within the target material either before or after the primary scattering takes place. External processes include bremsstrahlung and ionization energy losses. These processes depend on the target thickness.

All processes described above will lead to energy changes of the incoming and/or the scattered electron (e or e'). When the *incoming* electron radiates a photon, its energy will decrease and the probability for the elastic scattering (or quasi-elastic) will increase. On the other hand the incoming electron could loose energy and still be involved in a deep inelastic scattering event. The various processes that can contribute to the data described in this thesis are shown in Fig. 2.15. The first two of these processes can be called background processes. The calculation and subtraction of the radiative contributions is discussed in detail in Sect. 4.10.

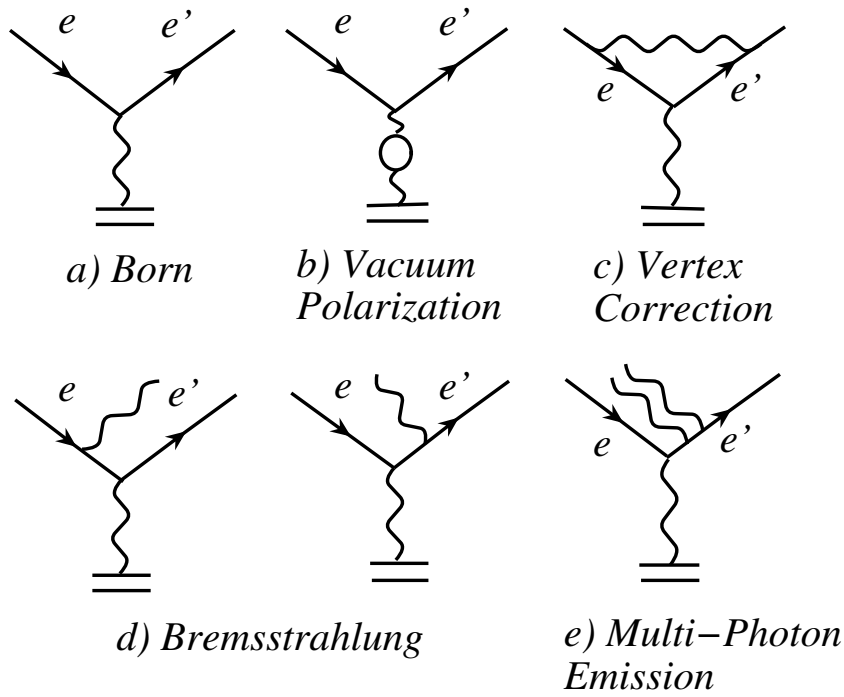


Figure 2.14: a) Lowest order Feynman diagram for inclusive lepton-nucleon scattering. b-e) Additional Feynman diagrams (higher order electromagnetic processes in α) contributing to the measured cross section.

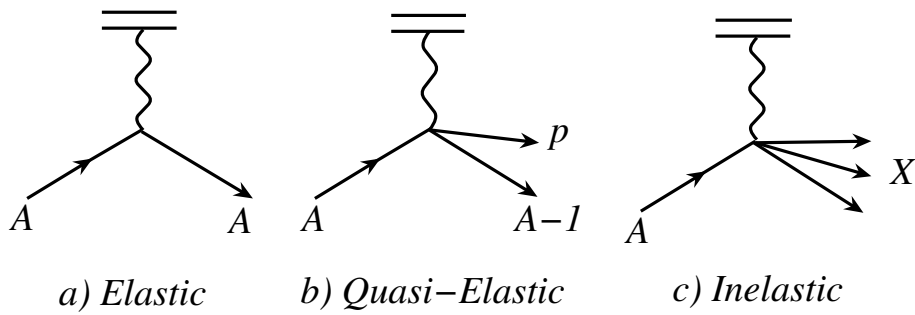


Figure 2.15: Schematic representation of the processes that can contribute to the data described in this thesis, see Sect. 4.10.

Chapter 3

Experimental Apparatus

The present experiment (e99-118) has been carried out in summer 2000 at Jefferson Laboratory (Newport News, VA, USA) with 2.301, 3.419 and 5.648 GeV electron beams ($I = 25 \mu\text{A}$) and the High-Momentum Spectrometer in hall C. Data have been taken at various scattering angles between 10 and 60 degrees on the targets LH_2 (liquid hydrogen), LD_2 (liquid deuterium), C, Al, Cu, Au. The kinematic coverage of experiment e99-118 is shown in Fig. 3.1 and is given in Table 3.1.

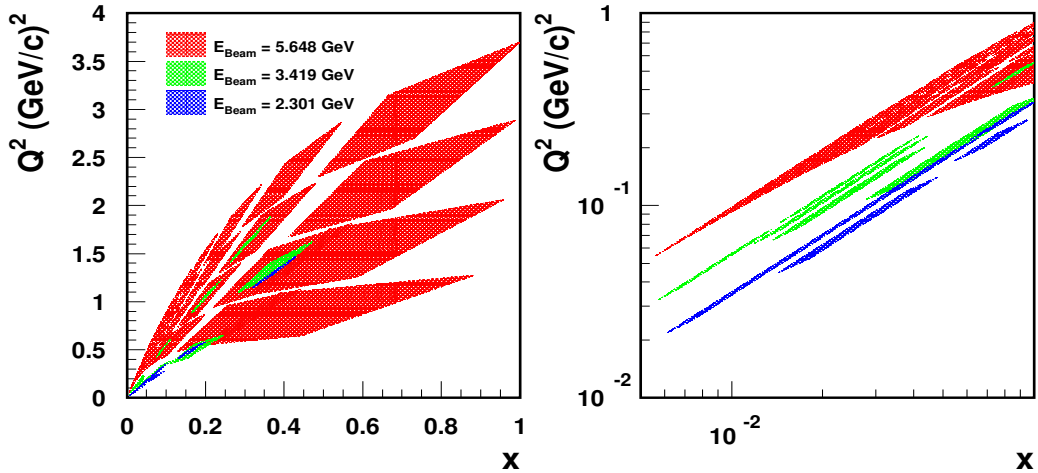


Figure 3.1: Left: kinematic coverage of experiment e99-118. Right: distribution of the low values of x and Q^2 of experiment e99-118.

E_{Beam} (GeV)	min E' (GeV)	max E' (GeV)	min θ (degree)	max θ (degree)
5.648	0.418	5.132	10.566	22.566
3.419	0.440	3.220	10.566	52.166
2.301	0.440	1.950	10.586	69.046

Table 3.1: Kinematic coverage of experiment e99-118. Columns 2,3 (4,5) give the minimum and maximum values of detected electron energy (E') and scattering angle (θ).

3.1 Accelerator

The experiment made use of the unpolarized, continuous-wave (100% duty factor) electron beam provided by CEBAF (Continuous Electron Beam Accelerator Facility). This accelerator is designed to deliver beam currents of up to a total of $200 \mu\text{A}$ to three experimental halls simultaneously. The accelerator produces short beam bunches at a repetition rate of 1497 MHz, which are in turn delivered to each of the three experimental halls (499 MHz per hall), resulting in a 2 ns bunch structure in each hall. The width of each bunch in the injector is typically 1 ps. The accelerator shown in Fig. 3.2, consists of an injector, two linear accelerators (Linacs), and two recirculation arcs. The electron beam is injected at 64.1 MeV

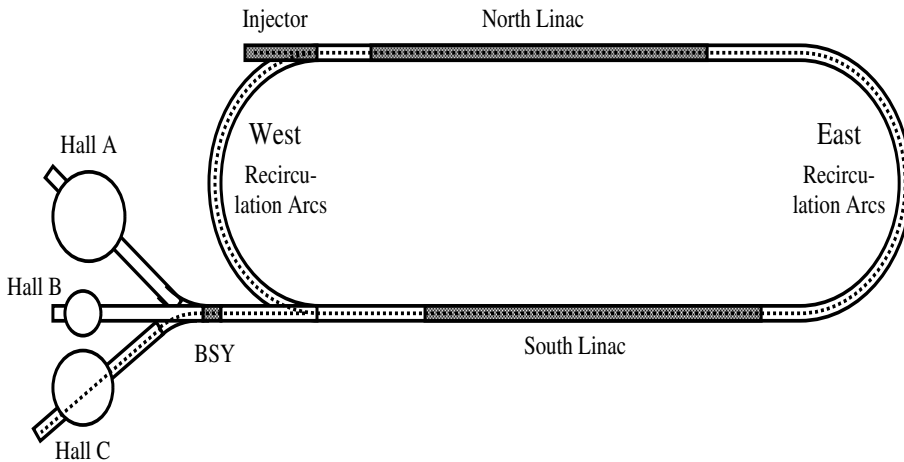


Figure 3.2: Schematic view of the CEBAF accelerator.

into the North Linac where it is accelerated up to 559.3 MeV. The beam then passes through the East Arc and enters the South Linac where it is accelerated an additional 559.3 MeV before passing through the West Arc for additional acceleration in the Linacs or entering the Beam Switch Yard (BSY). The beam from BSY can be extracted into any one of the three experimental halls. The beam can be recirculated through the Linacs up to five times, corresponding to beam energies of 1.1827, 2.3013, 3.4199, 4.5385 or 5.6571 GeV. The beams from different passes are recirculated together through the linacs but require different bending

fields in the arcs. For this purpose each arc consists of a vertical stack of separate arcs, each with different bending fields (five for the East Arc and four for the West Arc). Beams with different energies are separated at the end of the each linac, travel through the appropriate arc, and are recombined before passing through the next linac. The beam current delivered to Hall C is typically between 10 and 100 μA . The beam is delivered through a beam handling system (BHS) into Hall C (3C Arc), see Fig. 3.3. This BHS is equipped with a number of

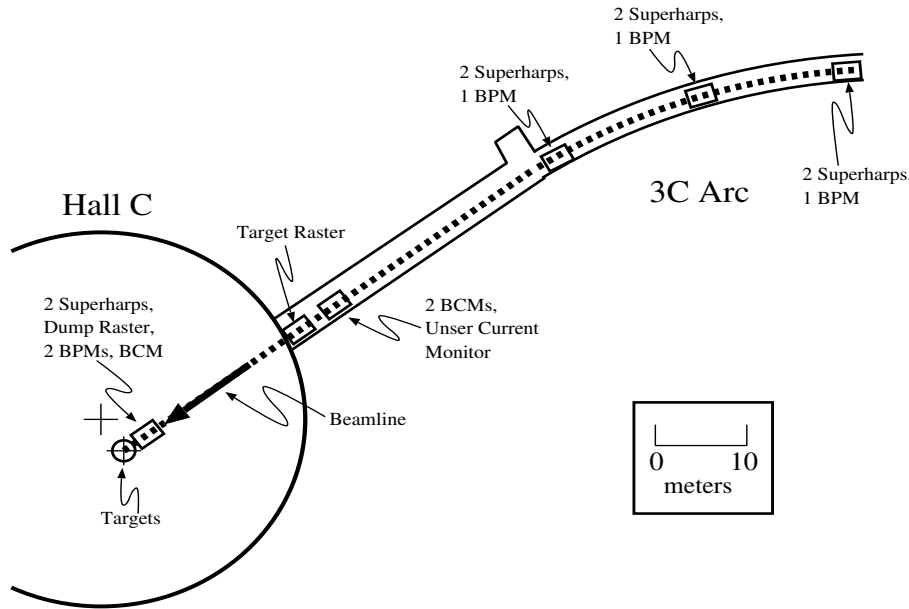


Figure 3.3: Schematic view of the beam handling system of the Hall C and its instrumentation.
For an explanation of the various items see text.

dipole, quadrupole and steering magnets to bend, focus and steer the beam onto the target. There are several monitors in the beamline to measure the position, profile and current of the beam.

3.1.1 Beam Position Measurement

So-called superharps make a destructive but extremely precise measurement of the beam position and profile. A superharp consists of three tungsten wires, two vertical that measure the horizontal beam profile and one horizontal wire that measures the vertical beam profile, mounted in a frame which is connected to an arm that can be moved in and out of the beam. Analog-to-Digital converters (ADCs) connected to each wire read the signals on the wires as the frame is moved in and out of the beam, while a position encoder determines where the wire intercepts the beam. With the position information and the ADC measurements the position and profile of the beam can be measured. More detailed information about the superharps can be found in Ref. [82].

The beam position is also measured with five Beam Position Monitors (BPMs) which

provide non-destructive beam position information along the beam line which are used during data taking; see Fig. 3.4. A BPM is a cavity containing two pairs of antennae perpendicular

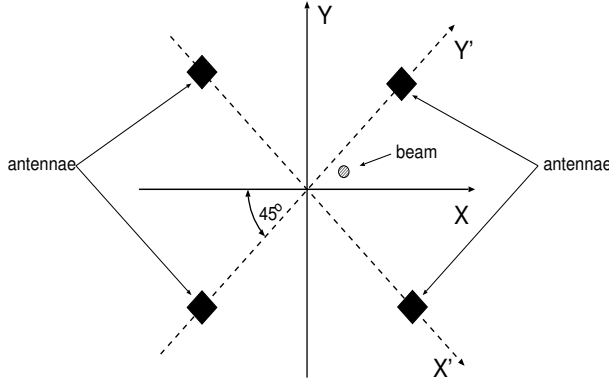


Figure 3.4: Diagram of the orientation of the BPM antennae.

to each other and inclined by $\pm 45^\circ$ with respect to the horizontal plane. When the beam passes through the cavity parallel to the symmetry axis both pairs of antennae pick up the frequency of the beam. Each antennae gives a signal proportional to the distance that the antennae is positioned from the beam. The beam position is derived from the difference over the sum of the signals from antennae on opposite sides of the beam. This method provides a position measurement independent of beam current. Since this is a position relative to the central axis of the beam line these measurements must be compared to the Superharps measurements to determine the absolute position of the beam during data taking. The final accuracy of the beam position measurements is ± 1.0 mm, with a relative position uncertainty of 0.1-0.2 mm. More detailed information about the BPMs can be found in Ref. [83].

3.1.2 Beam Energy Measurements

The electron beam energy is measured by using the magnets in the Hall C arc. For this measurement the focusing magnets in the arc are turned off and only bending magnets are used. With superharps the beam position is measured at the beginning, in the middle and at the end of the arc, and the position information is used to steer the beam to the central path. With precisely mapped fields of the dipoles the beam positions are used to determine the electron momentum from the equation

$$p = \frac{e}{\theta_{arc}} \int B dl , \quad (3.1)$$

where e is the electron charge, θ_{arc} is the bend angle of the arc (34.40°) and $\int B dl$ is the magnetic field integral. With this method the beam energy is determined with an uncertainty of $\delta p/p \approx 2 \times 10^{-4}$. More detailed information about this method can be found in Ref. [81]. The results are corrected later by another method discussed in Sect. 4.2.4.

3.1.3 Beam Current Monitors

The Hall C beam line has four devices installed to measure the beam current: three microwave cavity Beam Current Monitors (BCMs), and a parametric DC current transformer (Unser monitor).

The BCMs measure the integrated beam current in two second intervals, and their output voltage, as well as the output voltage of the Unser, is converted into frequency with a voltage-to-frequency converter, and read out by a scaler. A BCM consists of a cylindrical wave guide, mounted in the beam line so that the beam travels along the axis of the cylinder. The dimensions of the cylinder were selected so that the 499 MHz structure of the beam excites the 1497 MHz TM_{010} mode in the wave guide. The resonance frequency is picked up by wire loop antennae, and converted to a DC voltage through a RMS-to-DC converter. The cavities have a stable gain and offset, and a high signal/noise ratio, but cannot measure the absolute current, because the output power as a function of the measured beam current depends on the cavity impedance, quality factor, and the signal cable attenuation. The absolute calibration is done with the Unser monitor.

The Unser monitor is installed between BCM1 and BCM2. It cannot be used for charge measurements because it is sensitive to thermal fluctuations, resulting in large drifts in its zero-offset. However, because the gain is stable and well measured, the Unser monitor is used to calibrate the gain of the BCMs. More information about the Unser monitor can be found in Ref. [84].

During a calibration run the accelerator delivers beam to the hall in current steps lasting 2 minutes, first increasing up to the current at which data are taken, then decreasing, with equal time intervals of no beam in between the steps. During the beam off intervals the zero offsets of the Unser monitor and the BCMs are measured. During the beam-on intervals the gains of the BCMs and Unser are measured. Then the BCM gains are calibrated with the offset and well known gain of the Unser monitor.

The systematic error from the calibration procedure due to noise of the Unser monitor signal and uncertainty of the gain of the power meter signal used to measure the beam current signal from the BCM yields on overall absolute systematic uncertainty on the current of 0.2 μA .

3.1.4 Beam Rastering System

The electron beam generated at CEBAF is a high current beam with a small transverse size ($\leq 200 \mu\text{m}$ FWHM). It can deposit a large amount of power in the target. In order to prevent local boiling in the cryotargets the beam is rastered before striking the target. For that purpose the beamline is equipped with a pair of fast raster magnets, located 20 meters upstream of the target. The first set rasters the beam vertically and the second horizontally. The current driving the magnets is varied sinusoidally, at 17 kHz in the vertical direction, and 24.2 kHz in the horizontal direction. The frequencies are chosen to be different so that the beam motion does not form a stable (Lissajous) figure at the target, but it moves over a square area. The amplitude of the raster pattern on the target is $\pm 1.2 \text{ mm}$ in both directions

during the present experiment. However, the reduction in power density due to the rastering is not enough to avoid fluctuations of the cryogenic target density (see Sect. 4.6).

3.2 Targets and Scattering Chamber

The targets are located in a cylindrical aluminium scattering chamber, which is installed at the spectrometer pivot. The scattering chamber has an inner radius of 61.6 cm and a height of 150 cm. The beam exit windows are made of 0.4 mm and 0.2 mm thick aluminium foils on the sides of the HMS and SOS spectrometers, respectively. The scattering chamber has

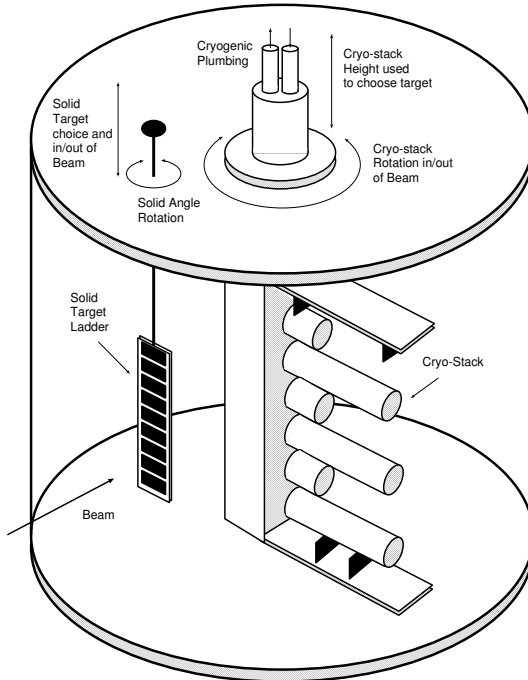


Figure 3.5: Hall C scattering chamber.

room for two target ladders, one for cryogenic targets and one for solid targets. The present experiment required both target ladders.

The solid target ladder contains two carbon, two copper and one gold targets. The two carbon targets (and the two copper targets) differ in thickness, see Table 3.3.

The cryogenic ladder contains hydrogen, deuterium and aluminium targets. In order to use the solid target the cryotarget ladder must be lifted fully out of the beam and rotated 90° so that it is out of the beam path and does not interfere with the spectrometer acceptance. Then, the solid target ladder can be inserted, as shown in Fig. 3.5. The solid targets can be lifted vertically to allow the cryotarget ladder to be rotated into the beam.

3.2.1 Cryotarget Ladder

The cryotarget ladder consists of three loops for circulating cryogenic liquids with two target cells each and two dummy (aluminium) targets, one at approximately 4 cm and one at approximately 15 cm in length (the 15 cm targets are not used in this experiment); see Fig. 3.6. Loop 1 contains liquid hydrogen (LH_2), cooled down to 19.0 K and held at a

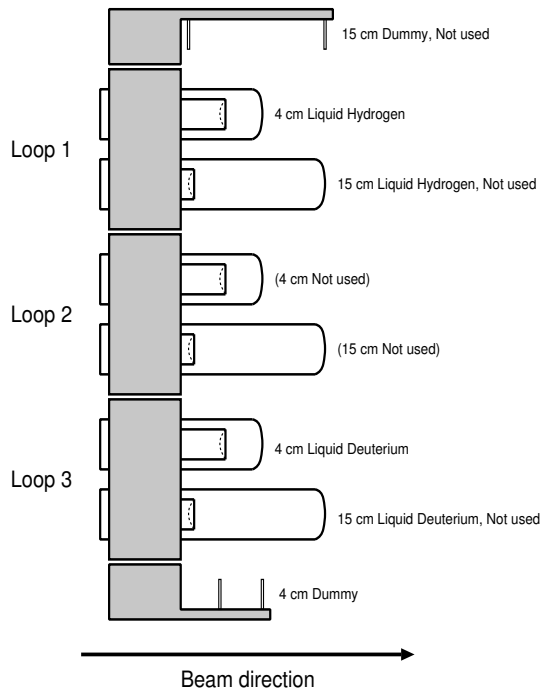


Figure 3.6: The cryotarget ladder.

density of $0.0723 \pm 0.0004 \text{ g/cm}^3$. The second loop is kept empty. The third loop contains liquid deuterium (LD_2), cooled to a temperature of 22.0 K and a density of $0.1670 \pm 0.001 \text{ g/cm}^3$. The target cells are made of 0.0127 cm aluminium. Each dummy target consists of two dummy endcaps to simulate an empty target for background measurements. The target windows are curved, therefore a change in beam position will change the effective target length. The thicknesses and radiation lengths of the targets in the cryotarget ladder are listed in Table 3.2.

3.2.2 Solid Targets Ladder

The solid target ladder system mounts to a port in the top of the scattering chamber directly above the target position; see Fig 3.5. An encoded linear-motion mechanism permits accurate, reproducible positioning of any of the five targets at beam height. The target ladder may also be rotated to any angle about the vertical motion axis. This is done to reduce the amount of target material that particles have to traverse in order to reach the spectrometer. For

Target	Thickness (g/cm ²)	Radiation Length (%)
4 cm LH ₂	0.2961 ± 0.0015	0.48
4 cm LD ₂	0.6840 ± 0.0039	0.56
Cell Walls (²⁷ Al)	0.0340 ± 0.0035	0.14
4 cm Dummy (²⁷ Al)	0.5071 ± 0.0017	2.11

Table 3.2: Thicknesses and radiation lengths of the targets in the cryotarget ladder. Cell walls represent entrance and exit foils.

in this experiment the solid target ladder is rotated by $20.3^\circ \pm 0.2^\circ$. The target is cooled by flowing water through a copper tube that is attached to the back of the target. The tube is shaped so that water flows past each target on all four sides; see Fig. 3.7. The thicknesses

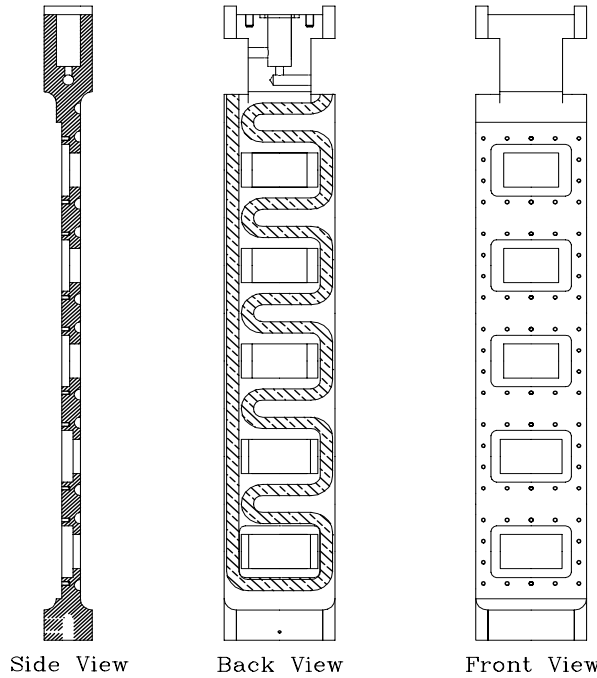


Figure 3.7: The solid target ladder.

and radiation lengths of the targets in the solid target ladder are listed in Table 3.3.

3.3 High Momentum Spectrometer

The standard detectors in Hall C at CEBAF are two magnetic spectrometers, the High Momentum Spectrometer (HMS) and the Short Orbit Spectrometer (SOS). Since only the HMS is used in this experiment the description of the spectrometers in HALL C is limited

Target	Thickness (g/cm ²)	Radiation Length (%)
Carbon (1% r.l.)	0.4519 ± 0.0013	1.06
Carbon (3% r.l.)	1.2454 ± 0.0025	2.96
Copper (2% r.l.)	0.2334 ± 0.0007	1.81
Copper (3% r.l.)	0.3462 ± 0.0013	2.69
Gold	0.2378 ± 0.0030	3.68

Table 3.3: Thicknesses and radiation lengths of the targets in the solid ladder.

to the HMS. The HMS can detect charged particles with a momentum up to 7.4 GeV/c.

Fig. 3.8 shows that the HMS consists of three quadrupole magnets (Q_1 , Q_2 , Q_3) followed by a dipole with a bend angle of 25° which brings the particles to a detector package. The

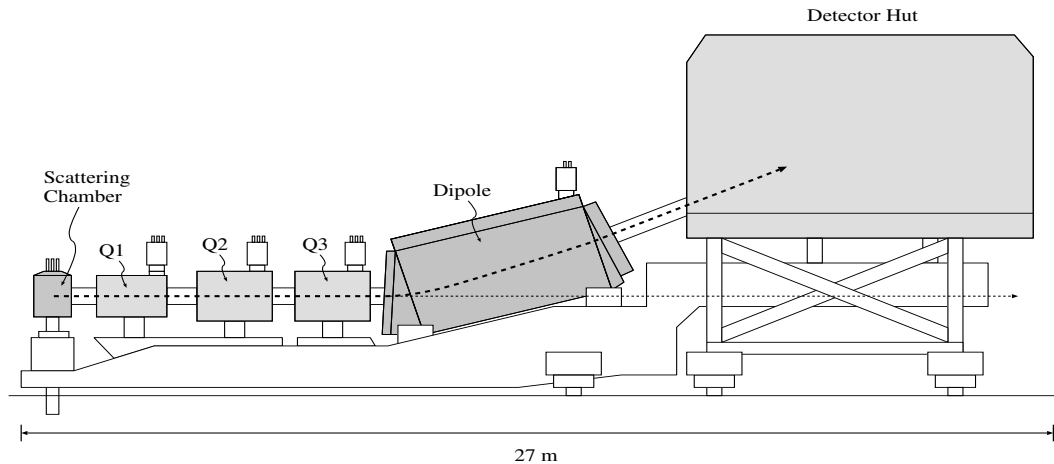


Figure 3.8: Schematic view of the High Momentum Spectrometer (HMS).

magnetic elements and the detector hut are mounted on a massive steel carriage which can be rotated in the horizontal plane to any angle between 10.5° and 80.0° relative to the beam axis. The magnetic fields of quadrupoles are tuned in point-to-point mode so that particles with the same momentum and position at target vertex are focused to the same point in the focal plane which is located between two drift chambers. The quadrupole magnets Q_1 and Q_3 focus in the dispersive direction, whereas Q_2 focuses in the non-dispersive direction, thus providing a large momentum bite, solid angle and extended target acceptance (acceptance for particles which scatter from a target extended along the beam line). The dipole is the dispersive element of the system and determines the central momentum of the spectrometer. The HMS characteristics are given in Table 3.4.

Parameter	Value
Maximum central momentum	7.4 GeV/c
Momentum acceptance	$\pm 10\%$
Momentum resolution	<0.1 %
Solid angle	6.7 msr
Scattering angle acceptance	± 27.5 mr
Out-of-plane angle acceptance	± 70 mr
Extended target acceptance	7 cm
Scattering angle resolution	1.0 mr
Out-of-plane angle resolution	2.0 mr

Table 3.4: HMS performance characteristics. The solid angle and angular acceptances are given for the HMS-100 tune.

3.4 HMS detector package

The detector package of the HMS consists of two drift chambers (DC1 and DC2), two sets of X-Y scintillator hodoscopes (S1X, S1Y and S2X, S2Y), a gas Čerenkov detector and a lead-glass calorimeter. A schematic view of the HMS detector package is shown in Fig. 3.9. A particle that enters the detector package first passes through one of the drift chambers.

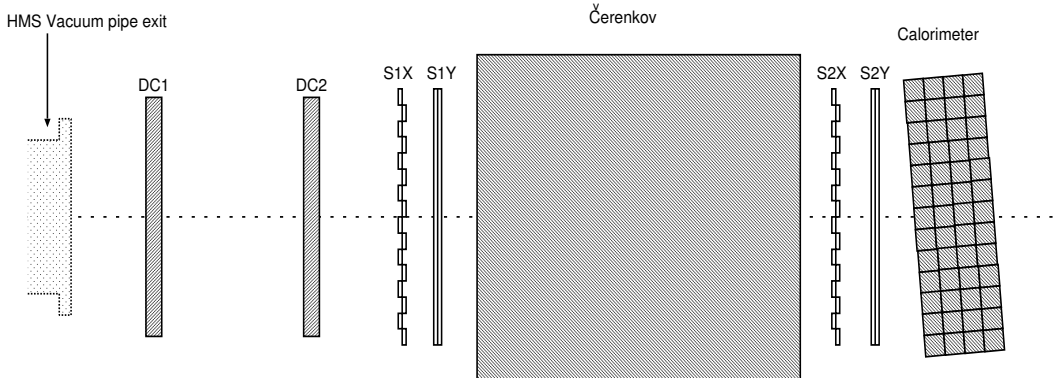


Figure 3.9: Schematic side view of the HMS detector package.

The drift chambers provide position and direction information, which is used by a tracking algorithm to determine the trajectory of the particle. After passing through the second drift chamber the particle enters the first pair of the scintillator hodoscopes which are part of the trigger for detector read-out. Then the particle passes through the gas Čerenkov detector which provides particle identification. Subsequently the particle enters the second pair of scintillator hodoscopes which like the first pair are part of the trigger. In addition, they allow to identify heavy particles through time-of-flight. Finally, the particle enters the calorimeter,

which provides further particle identification.

3.4.1 Drift Chambers

Two drift chambers are used in the HMS to determine particle trajectories through the spectrometer.

The drift chambers are spaced 81.2 cm apart, and each has an active area of about 113 cm (x) by 52 cm (y). They consist of six separate planes of sense wires (anodes) of 25 μm diameter gold-plated tungsten spaced 1.0 cm apart in a gas mixture of argon and ethane, and field wires (cathodes) of 150 μm gold-plated copper beryllium wires. The planes are spaced 1.8 cm apart. Between each sense wire is a field wire which is held at a negative potential (-1800 V to -2500 V). On both sides of the sense planes is an additional plane of field wires, held at the same negative potential. The planes are ordered X, Y, U, V, Y', X' as seen by incoming particles. The X and X' planes provide two measurements of position of the particles in the dispersive direction. The Y and Y' planes offer two measurements of position in the transverse direction and the U and V are rotated $\pm 15^\circ$ from the X (X') planes, see Fig. 3.10.

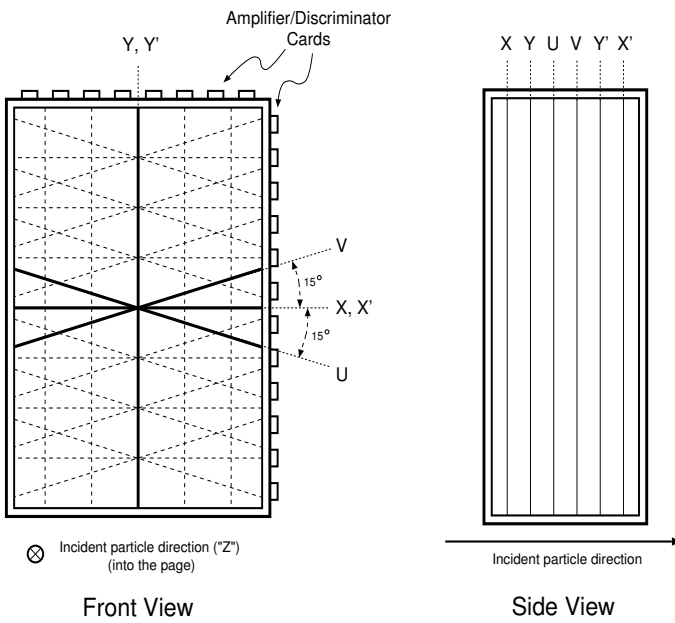


Figure 3.10: Schematic view of the HMS drift chamber showing the orientations of the six wire planes.

When a charged particle traverses the drift chamber it ionizes the gas mixture in the chamber. The ionized electrons then drift through the electric field generated by the chamber wires to the nearest sense wire and are detected. The drift time is used to determine the distance from the incoming particle to the sense wire. The time that it takes for the electrons to drift to the sense wire is proportional to the distance of the track from the sense wire.

The signals from each wire are amplified and discriminated on the cards attached directly to the drift chambers and then sent to the TDCs (Time-to-Digital Converters) located in the back of the detector hut. By detecting which wire sensed the particle and knowing the drift time (drift distance) from the TDCs, the position of the particle at each plane is determined by the tracking software with a resolution of approximately $280 \mu\text{m}$ per plane (see Sect. 4.1). The coordinate information from the drift chambers is used to determine the trajectory of the incoming particle through the spectrometer. More information about the HMS drift chambers can be found in Ref. [76].

3.4.2 Hodoscopes

The HMS has 4 hodoscopes, which provide the trigger for detector read-out and allow to identify heavy particles through time-of-flight (TOF). The TOF capability is not used in the present experiment. The hodoscopes are paired in two horizontal-vertical X-Y sets (S1X, S1Y and S2X, S2Y). The sets are separated by 220 cm. Each X hodoscope consists of 16 horizontally oriented scintillators (paddles), while the Y hodoscopes consist of 10 vertically oriented scintillators. The paddles of the X and Y hodoscopes are all 1 cm thick and 8 cm wide, but they have different length. The X paddles are 75.5 cm long, and the Y paddles are 120.5 cm long. Each scintillator paddle is wrapped in one layer of light-tight aluminium foil and two layers of Tedlar. At both ends of each paddle are Photomultiplier Tubes (PMTs) attached to the paddle through lucite light guides. The paddles are staggered in the beam direction with 0.5 cm overlap between the paddles to avoid gaps, see Fig. 3.11. When charged

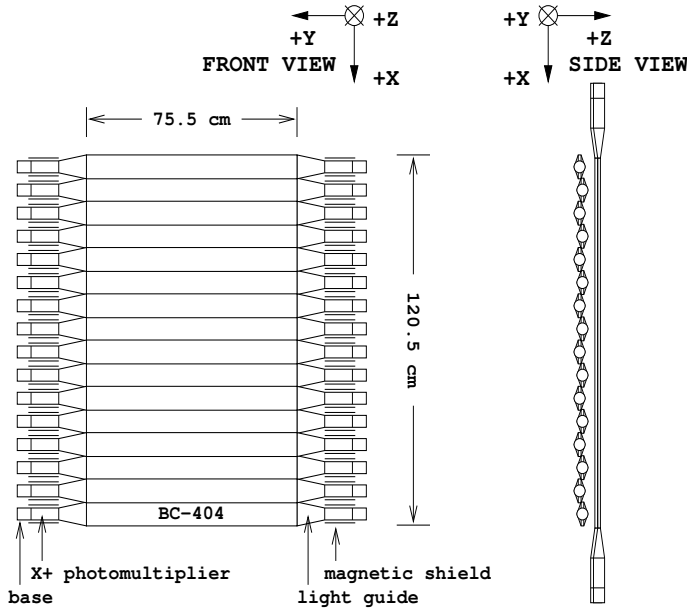


Figure 3.11: Hodoscope geometry.

particles pass through the paddles they excite the atoms. These atoms emit light as they

return to their ground state. The light is detected by PMTs at the ends of the paddles. The light that is not emitted along the length of the paddle is reflected internally through the scintillator and ultimately also detected by the PMTs.

The signal pulses from the PMTs are sent to the counting house where they run through the splitter, giving two signals with 1/3 and 2/3 of the amplitude of the original input signal. The smaller signal goes to Analog-to-Digital Converters (ADCs) that measure the integral of the signal. The other part of the signal is discriminated and one set of outputs is sent to TDCs (for timing information). The other set of outputs is sent into a logic module. The logic module first generates the logical OR of all the discriminated signals from the tubes on one side of a given plane, for example: $S1X+ \equiv (S1X1+ \text{ OR } S1X2+ \text{ OR } \dots \text{ OR } S1X16+)$. There are equivalent sets of signals for the “-” side of each plane. Then, these sets of signals are combined into six outputs:

a) $S1X \equiv (S1X+ \text{ AND } S1X-)$ and analogously for $S1Y$, $S2X$, $S2Y$. These four output logic signals indicate which of the hodoscope planes are active and make a new logic signal in case at least three of them have fired which is called SCIN.

b) The X-Y pairs are further combined to form $S1 \equiv (S1X \text{ OR } S1Y)$, and $S2 \equiv (S2X \text{ OR } S2Y)$. These signals indicate whether the pairs are active and make a logic signal called STOF.

These logical outputs are then sent to the main trigger logic and to the scalers to be recorded. A more detailed description of the hodoscopes can be found in Ref. [77].

3.4.3 Čerenkov Detector

The HMS gas Čerenkov detector provides particle identification by operating as a threshold detector.

It consists of a large cylindrical tank (diameter of 150 cm, length of 165 cm) situated in the middle of the detector stack between the hodoscope pairs S1 ($S1X$, $S1Y$) and S2 ($S2X$, $S2Y$), see Fig. 3.9. A pair of front reflecting spherical mirrors mounted vertically with 1 cm overlap at the rear of the detector is rotated over 15 degrees to focus the light on a pair of PMTs, see Fig. 3.12. The detector is filled with C_4F_{10} gas. The Čerenkov detector measures the light emitted when a charged particle travels through the gas with a velocity above the speed of light in the gas. This is known as Čerenkov radiation. The light will be emitted with an angle $\cos(\theta) = 1/n\beta$, where β is the velocity of the particle relative to the speed of light and n is the index of refraction of the material. If $n\beta < 1$ no light will be emitted. The light is reflected from focusing mirrors to PMTs, which generate a signal proportional to the number of Čerenkov photons. The gas (refraction of the material) is chosen such that electrons at the spectrometer momentum will emit Čerenkov radiation and pions will not. The refractive index of the gas is $n = 1.0006$ and this gives a pion threshold above 4 GeV/c and an electron threshold of about 15 MeV/c. The average measured signal from an electron is about 10 photoelectrons, see Fig. 3.13. However, it is still possible for a pion to be misidentified as an electron when it produces a knock-on δ electron that fires the Čerenkov detector, see Sect. 4.3.3.

The signals from each PMT are sent to the counting house where each signal is split in a

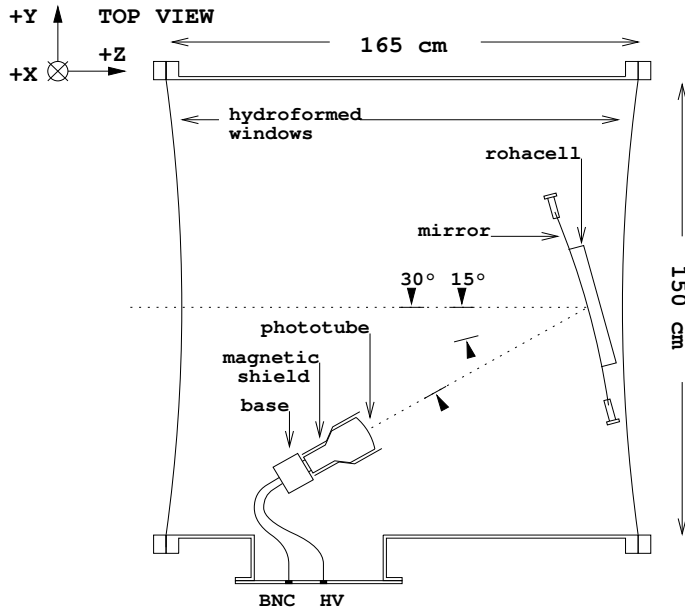


Figure 3.12: Čerenkov geometry.

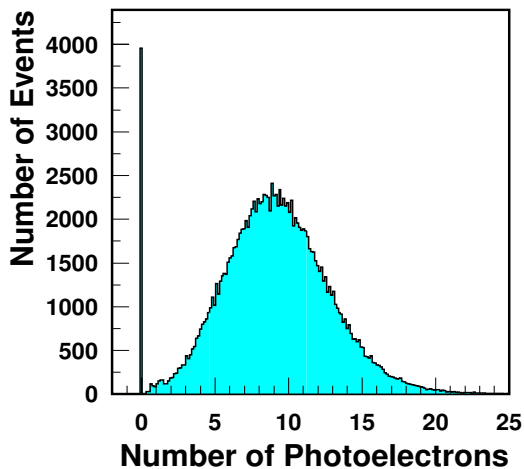


Figure 3.13: HMS Čerenkov spectrum. Most of the pions appear at zero photoelectrons.

fashion similar to the hodoscope signals. One pair of signals is sent to the ADC and the other pair is summed and put through the discriminator to give signals for the TDC and trigger logic (\tilde{C}). More information about the Čerenkov detector can be found in Ref. [77].

3.4.4 Lead-Glass Calorimeter

The HMS has a lead-glass calorimeter which is used to discriminate between electrons and pions.

Fig. 3.14 shows that the calorimeter consists of 52 TF1 type lead glass blocks $10\text{ cm} \times 10\text{ cm} \times 70\text{ cm}$, with a PMT on one end. The blocks are arranged in four layers with 13

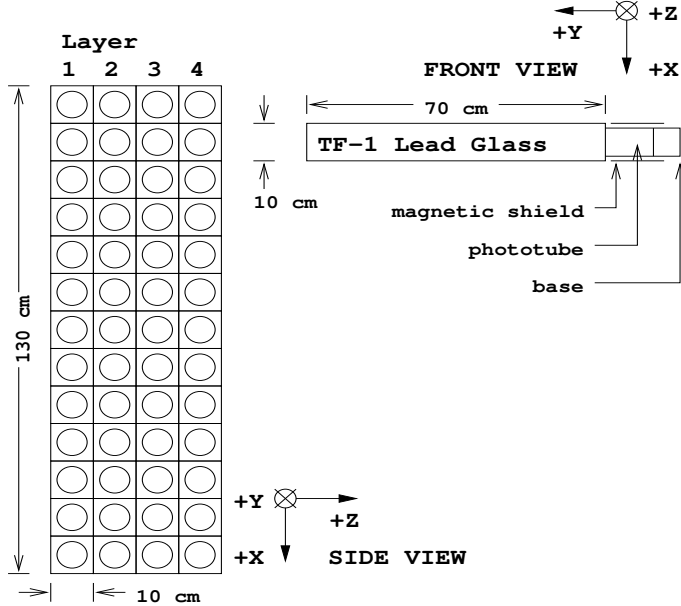


Figure 3.14: Calorimeter geometry.

blocks per layer, giving a total thickness of the calorimeter along the direction of particle motion of 16 radiation lengths. As shown in Fig. 3.9 the calorimeter is rotated over 5° with respect to the dispersive plane to prevent particles from passing in between the blocks. The calorimeter measures deposited energy of particles. Electrons interacting with matter radiate photons in the calorimeter, which in turn produce electron-positron pairs (when the photons are energetic enough). These pairs in turn also radiate photons and so a shower of particles (e^+, e^-, γ) is produced in the calorimeter. The charged particles produce Čerenkov radiation which is detected by photomultiplier tubes. The produced signal is proportional to the total track length of the particles in the calorimeter which is in turn proportional to the energy of the initial electron. Electrons (positrons) entering the calorimeter deposit their entire energy, and thus the ratio of deposited energy of electrons (positrons) in the calorimeter to the detected energy derived from the particle bending in the spectrometer is one, see Fig. 3.15.

Pions normally deposit about 300 MeV through ionization in the calorimeter so a peak in the E_{calo}/E' spectrum can be observed at $0.3\text{ GeV}/E'$. However, pions can have a charge-exchange reaction and produce a neutral pion, which in turn decays into two photons, the full energy of which will be deposited in the calorimeter. This leads to a high-energy tail for

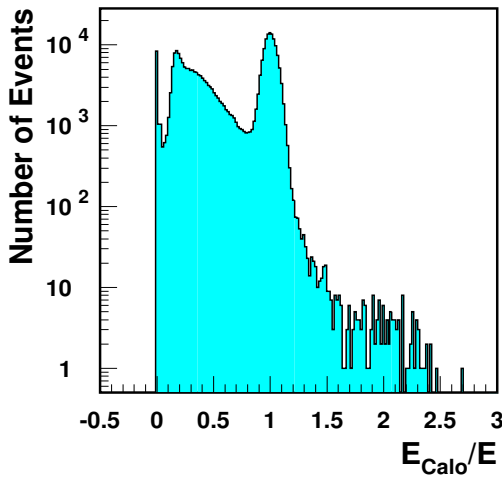


Figure 3.15: An example of the HMS calorimeter spectrum for LH_2 at 10.6° , $p = 1.846 \text{ GeV}/c$.

pions, which can result in pion misidentification.

The signals from the PMTs are sent to the counting house where they are split 50/50. One half is sent to the ADC and the other half to the linear modules to be summed. The sum in the first layer (PRSUM) and the sum of the entire calorimeter (SHSUM) are discriminated to give three logic signals for the trigger. High (PRHI) and low (PRLO) threshold on the energy in the first layer and the sum of all 52 signals is discriminated at single threshold (SHLO).

3.5 Trigger system and Data acquisition

The purpose of the single arm trigger logic is to generate a trigger signal when an electron or other particle arrives. The trigger logic is shown in Fig. 3.16. Charged particles passing through the spectrometer produce triggers in one or more detectors described earlier. Certain combinations of these triggers are used to form the pretrigger. An electron trigger (ELREAL) can be produced in two ways:

- 1) The low - level electron trigger (ELLO) requires a Čerenkov signal (\check{C}), plus at least two out of three of the following conditions: a) at least one of the two scintillator layers of each hodoscopes has fired ($\text{STOF} \equiv \text{S1 AND S2}$). b) at least three of the four scintillator layers of both hodoscopes have fired (SCIN). c) There is a (PRLO) signal from calorimeter.
- 2) A high - level electron trigger (ELHI) requires that all of the following signals are present: a) The (SCIN) signal. b) The (PRHI) signal from the calorimeter. c) The (SHLO) signal from the calorimeter. The high - level electron trigger (ELHI) does not use the Čerenkov

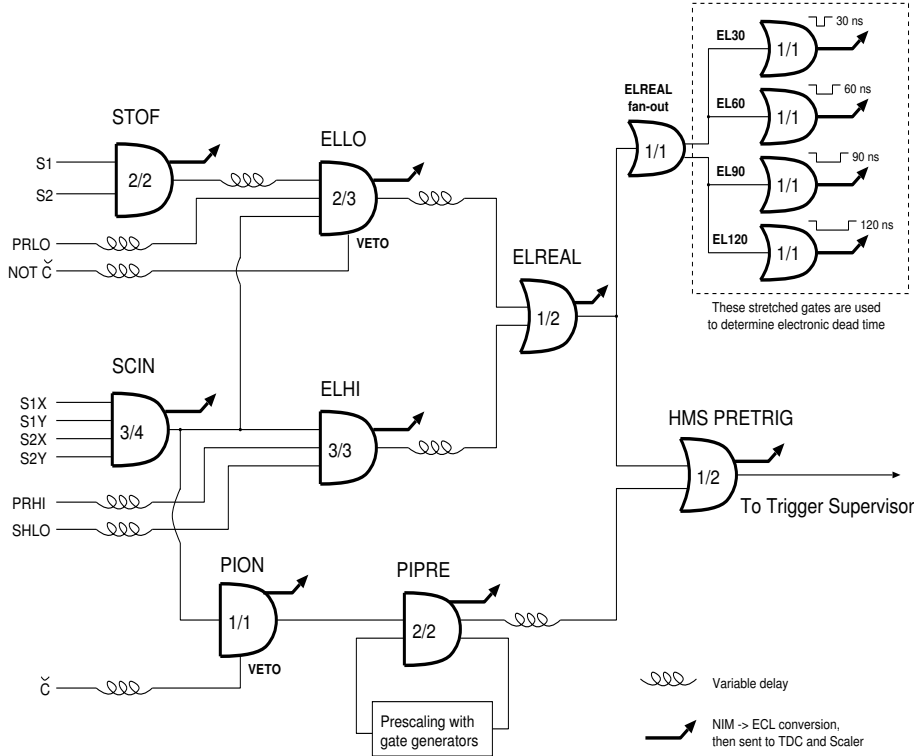


Figure 3.16: Schematics of the single arm trigger logic. Numbers like *e.g.* 2/3 inside the logic unit symbols indicate that two out of three inputs to the unit must receive a logic 1 in order for the unit produce an output.

signal.

The electron trigger (ELREAL) is (ELLO) OR (ELHI). The reason for using two electron triggers (ELLO) and (ELHI) is to reduce the trigger inefficiency and to provide the most efficient electron-hadron separation by the Čerenkov and the calorimeter detectors.

There is an additional pion trigger (PION) which requires the (SCIN) signal, and no Čerenkov signal (\check{C}). The (PION) signal is then combined with a prescaling circuit to form (PIPREF), which ensures that a low-rate sample of pions is sent along to the data acquisition system. Two copies of (ELREAL) are generated: one is fanned out into four logic units with dead times set between 30 and 120 ns in order to allow a measurement of the electronic dead time and another (ELREAL) OR (PIPREF) forms the signal (PRETRIG), which is forwarded to the Trigger Supervisor (TS).

When a run is started first 1000 pedestal triggers are generated by (PED PRETRIG) and the data acquisition system records the read-outs from the ADCs. Then the data acquisition system begins to record physics events. When a physics event is signaled by (PRETRIG), the data acquisition system records the read-outs of the detectors ADCs and TDCs. The TS sets TS BUSY while the data acquisition system records the read-outs. After the data acquisition system has completed recording the event information, TS BUSY is set off to

allow for the next physics event. Both trigger and pretrigger signals are written into scalers providing information about the computer dead time. More detailed information about the Trigger Supervisor can be found in Ref. [78].

The data acquisition is handled by the CODA (CEBAF Online Data Acquisition) software package [80] running on a Hewlett-Packard workstation. Data for each run are written directly to disc and consist of three types of events: 1) detector information handled by the ADCs and TDCs, 2) scaler information, and 3) information from the EPICS database. The ADCs and TDCs are read-out for each event, while the scalers are read every 2 seconds. The EPICS database contains information such as magnet settings, beam position and target temperature and pressure. These quantities are read out every 30 seconds. More information about data acquisition can be found in Ref. [80].

Chapter 4

Data Analysis

The goal of the experiment is to measure the nuclear dependence of $R=\sigma_L/\sigma_T$ at low values of Q^2 . In order to achieve this, the cross section should be calculated from the raw data and the Rosenbluth separation should be done for the cross sections at the same values of (x, Q^2) but different ϵ , using the formula

$$\frac{d^2\sigma}{d\Omega dE'} = \Gamma(\sigma_T + \epsilon\sigma_L) . \quad (4.1)$$

The analysis of the raw data files has been done with the standard Hall C event reconstruction software plus some improvements, which have been made during this analysis.

To calculate the cross section correctly the following steps have to be taken:

- Event reconstruction.
- Detector calibrations.
- Particle identification.
- Determination of dead times (electronic, computer).
- Subtraction of background events.
- Determination of efficiencies (trigger, tracking, Čerenkov, calorimeter).
- Target density correction.
- Acceptance corrections.
- Bin Centering correction.
- Radiative corrections.
- Iteration procedure.

All these steps are described in this chapter. For some of these procedures the calculation of the experimental *Yield* is necessary,

$$Yield = \frac{PS \times N^{events}}{Charge \times Eff \times Live\;Times}, \quad (4.2)$$

where *Eff* includes the efficiencies of the Trigger, Tracking, Čerenkov and Calorimeter, *Charge* is the accumulated charge, *PS* is the prescale factor and the *Live Times* include the computer and electronic live times.

4.1 Event Reconstruction

One of the important and difficult parts in any experiment is the event reconstruction. From many possible tracks the real track should be chosen (reconstructed) as the correct one. A rate dependence (due to the track selection procedure) has been found during this analysis, which led to a detailed investigation of the track reconstruction procedure and a change in the tracking procedure code used in Hall C. In this section the old and the improved methods of the track reconstruction are discussed.

4.1.1 Tracking

The trajectory of a particle in the detection system is measured by two drift chambers, each with six planes (see Sect. 3.4.1). Using matrix elements to describe the transport through the spectrometer, the vertex at the target is then reconstructed from the focal plane coordinates (position and direction of the trajectory at the focal plane).

The position of the particle as it passes through a plane is measured by using the position of the wire that is hit and adding to it the drift distance of the electron from the ionized atom. If wires from a drift chamber have been hit more than 30 times for one trigger then no track will be determined. The drift distance is determined from the drift time, which is recorded as drift chamber TDC values. Small corrections are applied for the time required for the signal to propagate along the wire and differences in cable lengths between the chamber and the TDCs.

In each chamber there are only two planes Y and Y' that can give information about the transverse coordinate (information about the dispersive coordinate is given by the X, X', V and U planes). That is why in order to have information about the transverse coordinate of the track it is necessary to have a fired Y (Y') plane in each chamber. So, at least 5 out of 6 planes should be fired in each drift chamber.

The drift chamber hits (fired planes) are used to identify clusters of hits (space points) in each chamber. A space point is generated with information from hits in a pair of unlike planes (combo)¹. For the HMS, the X-Y, X-Y', X'-Y, X'-Y', U-Y, U-Y', V-Y, V-Y', U-V

¹Where unlike means that they can determine the position in both the dispersive and the transverse direction.

planes are considered unlike, but the wires of the X-U, X'-U, X-V, X'-V planes are too close to being parallel to accurately determine a space point. The tracking program takes the first combo and calls it a space point. Then if the second combo is within a certain range (space point criterion) of this space point then these two combos are united to one space point (X_{av}, Y_{av} coordinates). If the second combo is out of the range of the first space point then the program creates new space point. The same procedure is repeated for all combos in each drift chamber. Ideally, if all combos are within the range, then the program will create only one space point per drift chamber. The *space point criterion* is the radius of a circle within which the combos must lie in order to be considered part of the same space point.

All planes of a chamber contributing to a space point are used to determine a track through that chamber, called a stub. For each wire in a space point, the particle could pass the wire on the left or the right. To solve this left-right ambiguity, stubs are fitted using the wire information (2^6 stubs at maximum), and the stub with the best χ^2 is chosen. The χ^2 for the stub (track) is calculated with the formula,

$$\chi^2 = \frac{DC_{wc} - DC_{tc}}{\sigma_{DC}^2}, \quad (4.3)$$

where DC_{wc} and DC_{tc} are wire and track coordinates of the stub (track) and σ_{DC} is the wire chamber resolution for each plane.

The stubs from the two drift chambers that have positions and slopes (see below) such that they point to each other within certain criteria, are linked together to form a track. In case multiple tracks are possible each of these tracks is recorded along with the χ^2 of the fit, and the track with the lowest χ^2 is selected as the final track.

The *stub criteria* define the horizontal (X, X') and vertical (Y, Y') distance and slope ranges in which two stubs must lie to be considered part of the same track².

In a simple point of view it seems that the best way to find a true track is to set the criteria to a high value and select the track with the best χ^2 . In order to check this idea one run with a high rate has been analyzed. In Fig. 4.1. the number of electrons corrected by the tracking efficiency (see Sect. 4.5.2) versus cut on χ^2 is shown. The dependence of the cut on χ^2 is clearly seen. It is obvious that this dependence should not happen. The idea why eventually it happens is: due to selection of the wrong track³. The wrong track can have a better χ^2 , but it will be lost by the geometrical cuts (the cuts which define the geometrical range of the collimator) as is shown in Fig. 4.2, or the wrong track still could be within the geometrical range, but it could not find a cluster in the calorimeter and will be cut away by the PID cuts, see Sect. 4.3.1. Note, in the tracking algorithm a requirement on the latter has been already added: in case the tracking program creates more than one track, the track that hits a cluster in the calorimeter will be selected. In case more than one

²Since in the Hall C reconstruction software it has been assumed that $Y' = 0$ when fitting a stub, the Y' criterion is not effective.

³The track can be wrong due to incorrect stub combination or wrong due to wrong left-right ambiguity solution.

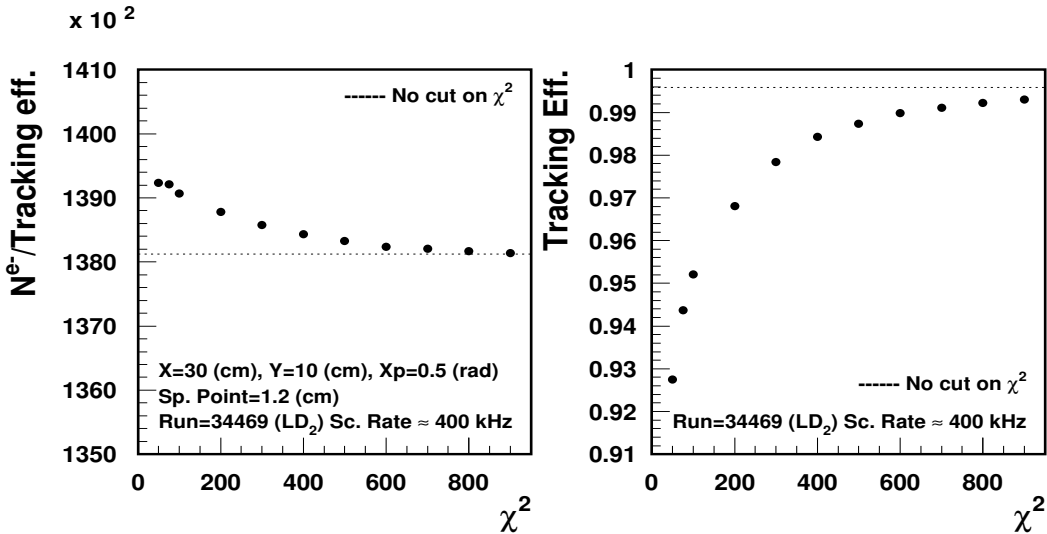


Figure 4.1: Left: χ^2 cut dependence for electrons. Right: the corresponding tracking efficiency for different cuts on χ^2 .

track hits a cluster, then the track with the best χ^2 is chosen. All previous and next plots are created with that condition. The difference between these two methods is about 0.3 % at 400 kHz. Unfortunately, as shown in Fig. 4.1 this condition is not enough for helping to find the correct track.

In order to find the best values for the stub and space point criteria the following method has been used. Four out of five criteria have been fixed at low values of the upper limits employed in the criteria and a run with a high rate is analyzed for different values of the unfixed criterion. The number of electrons corrected by the tracking efficiency versus the X stub criterion is shown in Fig. 4.3 (left). The other criteria are equal: $Y = 2\text{ cm}$, $X' = 0.2\text{ rad}$ and space point criterion equal to 0.7 cm. There is no requirement on Y' since it is forced to be zero. The behaviour of the tracking efficiency for different values of the X stub criterion is shown in Fig. 4.3 (right). The same checks have been done for other criteria (see Figs. 4.4-4.6). For the Y stub criterion an additional test has been done. In order to check how well the Y coordinate is determined for a track the following condition has been used: all Y planes should have fired; in case one of the Y planes has not fired, then this track is not used in the analysis⁴. Thus, the new requirement for a track is $2/2+3/4$ instead of $5/6$. The result is shown in Fig. 4.4 (left). From that figure it is clear that there is no difference between the yields that have been calculated with the $5/6$ or $2/2+3/4$ conditions and that is why always condition $5/6$ has been used. The tracking efficiency for $2/2+3/4$ condition is low, because the events which fired only one Y plane have been included in the tracking

⁴This track is corrected for by the tracking efficiency.

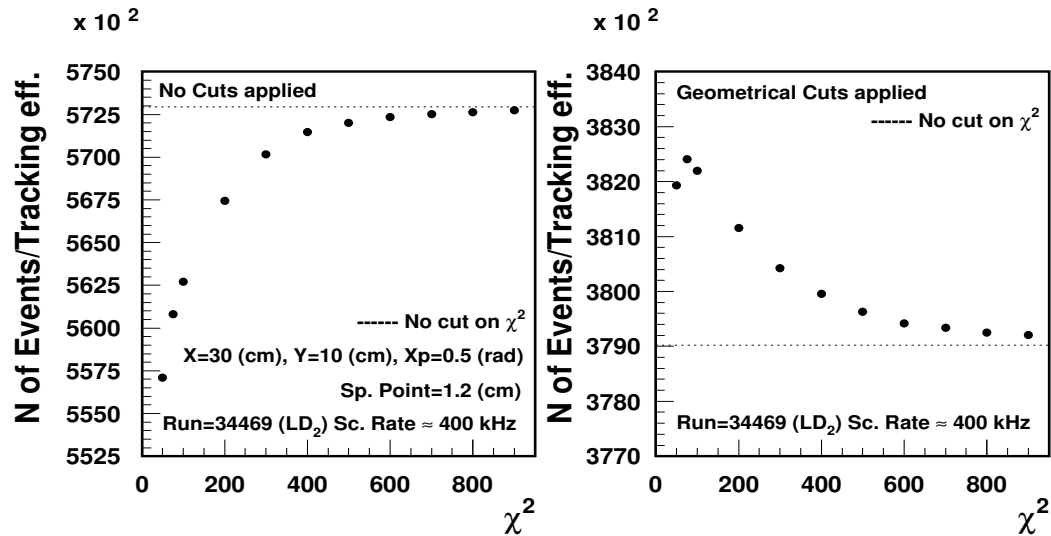


Figure 4.2: Left: χ^2 cut dependence for all events. Right: χ^2 cut dependence for events which passed the geometrical cuts. For these plots all criteria have been set to high values.

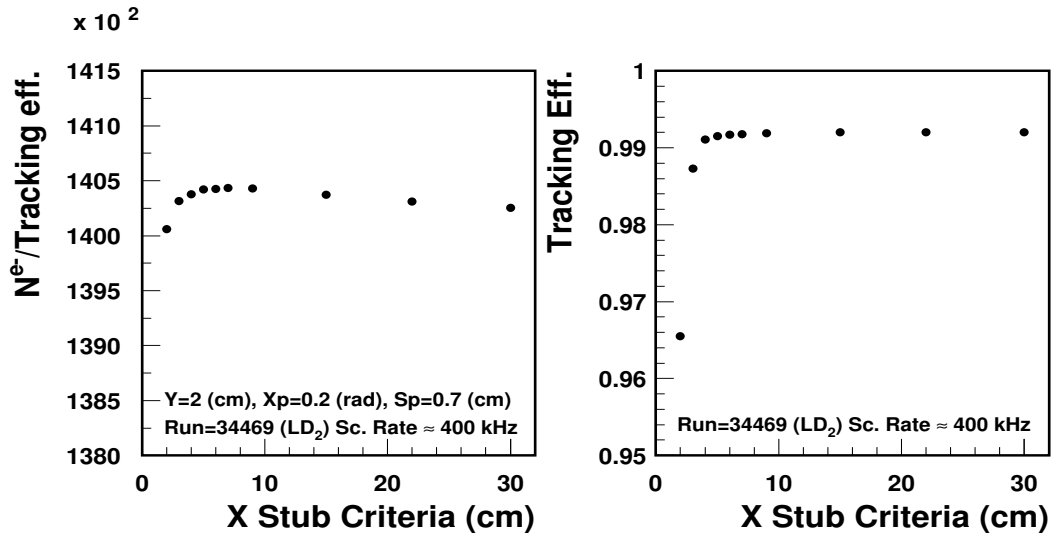


Figure 4.3: Left: dependence of the yield on the value of the X stub criterion. Right: the corresponding tracking efficiency.

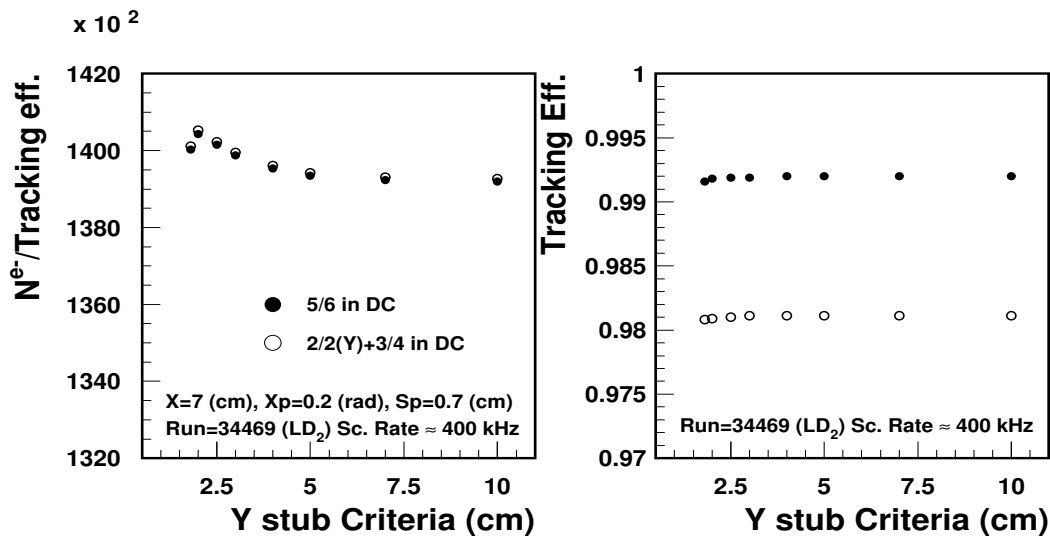


Figure 4.4: Left: dependence of the yield on the value of the Y stub criterion. Right: the corresponding tracking efficiency.

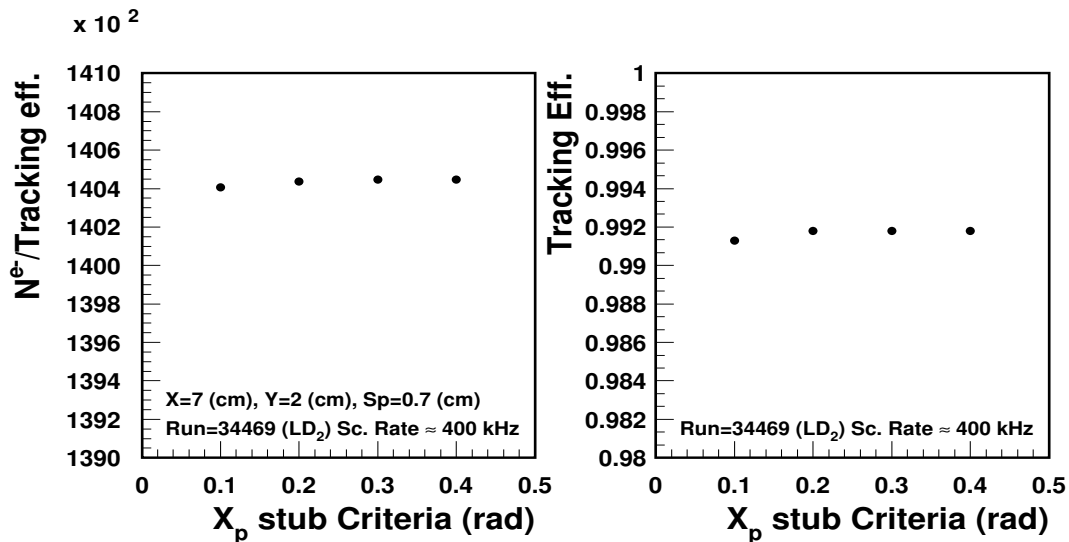


Figure 4.5: Left: dependence of the yield on the value of the X_p stub criterion. Right: the corresponding tracking efficiency.

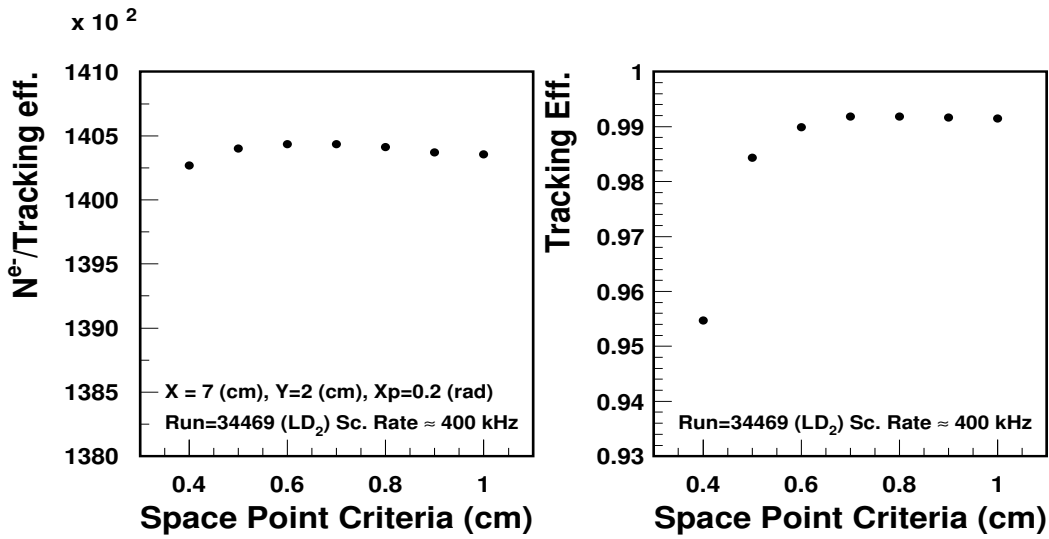


Figure 4.6: Left: dependence of the yield on the value of the Space Point criterion. Right: the corresponding tracking efficiency.

efficiency, see Fig. 4.4 (right).

As shown on all plots with different stub criteria the results (yields) are not stable. Therefore, three questions arise: 1) Why does the number of electrons corrected by the tracking efficiency depend on the stub criteria ? 2) What is the true value for the corrected number of electrons for the chosen run ? And finally 3) How to find the correct (real) track ?

In order to find the answers to these questions the special program *Single Event Display* has been used. That program allows to inspect the track selection procedure for each event. In Fig. 4.7 the track selection for one of the events is shown⁵. It is clear that the program has created two tracks that look similar in the side view, see Fig. 4.7 (left), but completely different in the top view, see Fig. 4.7 (right). The program selects the track with the best χ^2 from these two possible tracks, which is cut away after applying the geometrical cut (as it has been checked). Fortunately, the *Single Event Display* shows a new way to select the correct track in such case.

A real track should hit the scintillators, so instead of choosing the track with the best χ^2 , the nearest track to the fired 2Y scintillator bar should be chosen as the correct one (the preference is given to 2Y because it is the one farthest away from the drift chambers). In case two (or more) reconstructed tracks hit the same bar in the 2Y scintillator, the information from the 2X scintillator can be used. It is also possible that 2 (or more) tracks hit 2 (or more) different bars that have not fired. Then the preference is given to the track, which passed through the bar nearest to the fired bar. So, the new algorithm for track selection is:

⁵In order to better understand Fig. 4.7, see Fig. 3.9, Fig. 3.11 and Fig. 3.14.

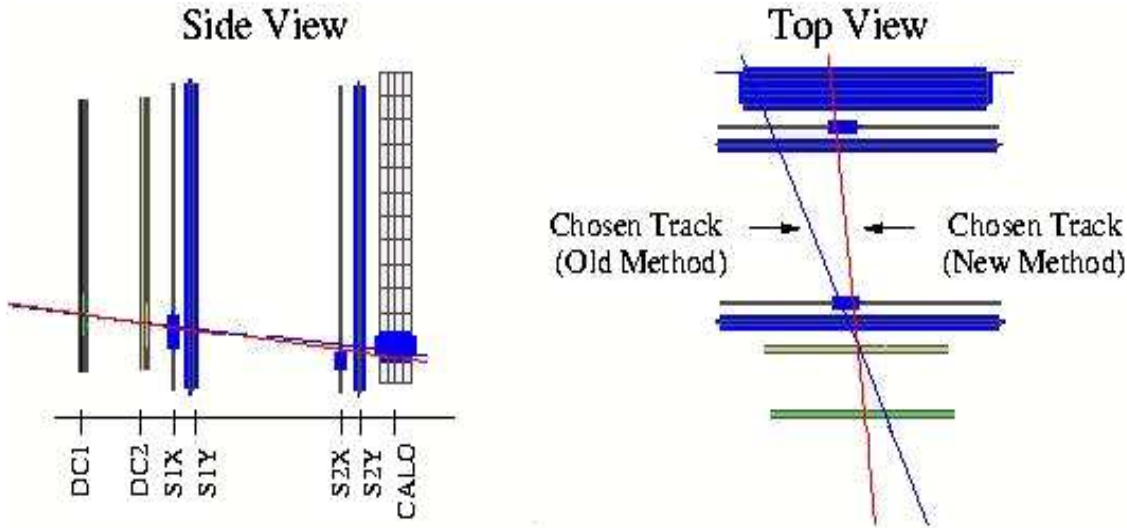


Figure 4.7: Track selection procedure in *Single Event Display*.

- If the program reconstructs only one track, then that track is used.
- If the program reconstructs two or more tracks then the track that hits the cluster in the calorimeter is used. In case two or more tracks hit the cluster in the calorimeter (or neither of them) then in order to select a correct track the following criteria are used.
- If the program reconstructs two or more tracks then the nearest track to the fired bar in 2Y is chosen.
- If two or more reconstructed tracks hit the same fired bar in 2Y then the track nearest to the fired bar in 2X is chosen.
- If two or more reconstructed tracks hit the same fired bar in 2Y and 2X then the track with the best χ^2 is chosen.

With the new method (algorithm) the program will select the other track, see Fig. 4.7 (New Method).

In order to check the new method of track selection the same run as before has been analyzed for different cuts on χ^2 . The new χ^2 dependence is shown in Fig. 4.8 for different stub criteria and different methods. For the new method two analyses have been done. Once, the stub criteria have been set to high values (the same values as were used in the old method) and once to low values. It is clear that with the new method of track selection there is hardly any difference when using different values for the criteria (as it should be!). However, the difference between the corrected number of electrons calculated with the old and new methods with the same stub criteria is about 1.7 %. Together with the 0.3 % discussed already above the total difference between the old and new methods is about 2 % at 400 kHz. The behaviour of the corrected electrons at low χ^2 is due to different χ^2 distribution for the sample of the

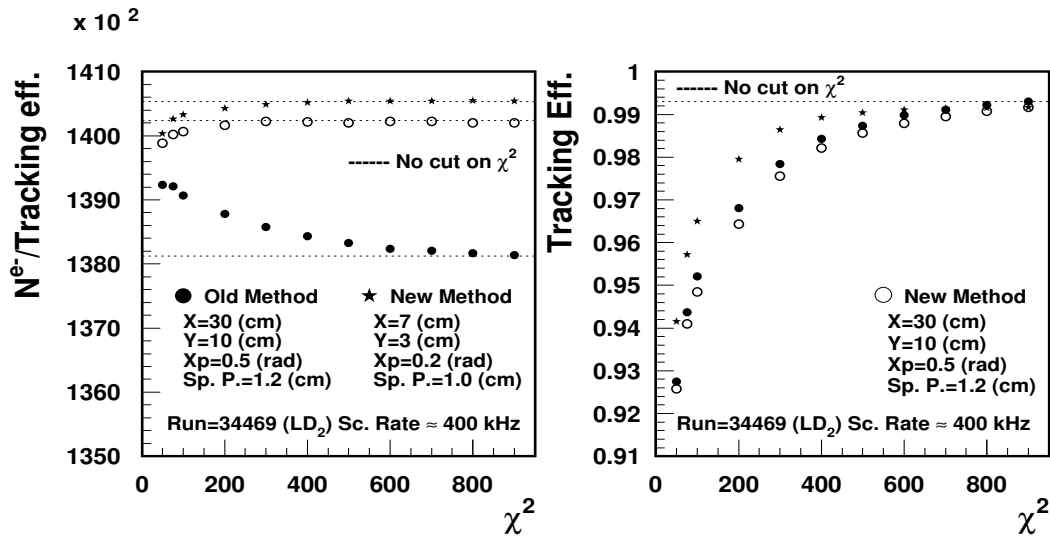


Figure 4.8: Left: χ^2 cut dependence of the number of corrected electrons calculated with the Old and New Methods. Right: the corresponding tracking efficiencies.

total electrons and the sample that is used for the tracking efficiency. During the analysis no cut on χ^2 is used. In Table 4.1 all tracking criteria used during this analysis are given.

Another parameter that should be investigated is the maximum number of reconstructed tracks. For all previous plots that number has been set equal to 10, which means that after this number has been reached the tracking routine stops making candidate tracks. However, in case that 3 stubs are produced in one chamber and 4 in the other one, then the maximum number of the candidate tracks will be 12, so two of these tracks will never be considered as a candidate, and it could lead to event loss. For that reason the same high rate run is analyzed with different maximum number of candidate tracks. The result is shown in Fig. 4.9 (left). The difference between the number of electrons corrected by the tracking efficiency with the maximum number of the reconstructed tracks 10 and 30 is about 0.006 %. On account of these results it has been decided to keep the value of the maximum number of reconstructed tracks at 10. In Fig. 4.9 (right) the behaviour of the tracking efficiency is shown. The tracking efficiency is independent from the maximum number of reconstructed tracks on the level of 10^{-4} .

In order to check all results described above two additional runs have been analysed: a low rate run and a high rate run of elastic scattering. The latter run is chosen because of the more localized distribution of events. The results from these two runs are similar as discussed above, which proves that presently employed new method has been properly chosen.

Parameters	HMS
Maximum number of Hits	30
Minimum number of Hits	5
Minimum Combos	5
Space Point Criterion (cm)	1
X stub Criterion (cm)	7
Y stub Criterion (cm)	3
X' stub Criterion (rad)	0.2

Table 4.1: Tracking algorithm parameters.

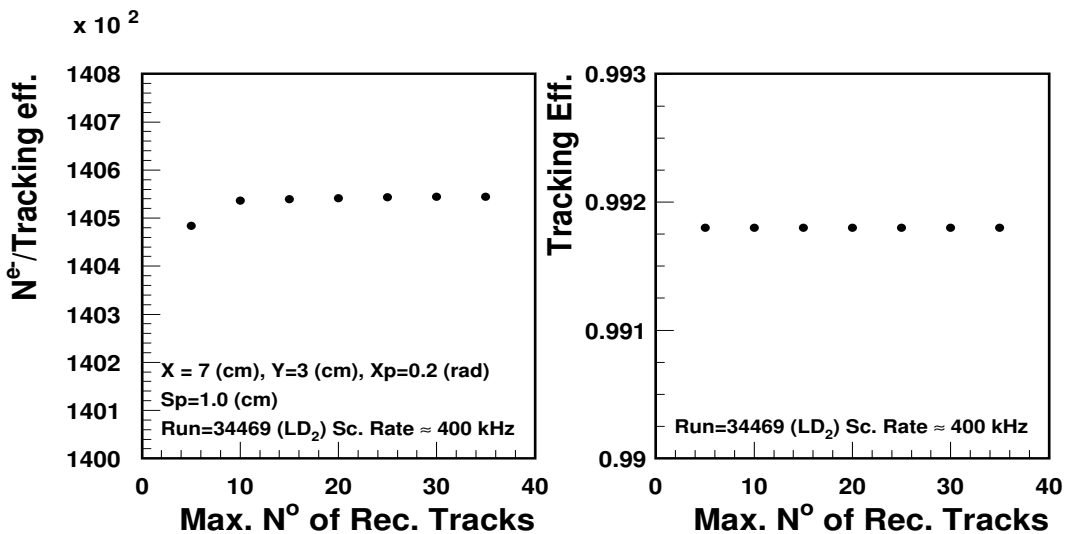


Figure 4.9: Left: dependence of the number of corrected electrons on the maximum number of reconstructed tracks. Right: the corresponding tracking efficiency.

4.1.2 Target Quantities

Once a particle has been tracked, its focal plane quantities are determined. The focal plane is located at an equal distance from both drift chambers. The focal plane quantities consist of x_{fp} and y_{fp} (the vertical and horizontal coordinates, respectively), and x'_{fp} and y'_{fp} (the vertical and horizontal trajectory slopes, respectively), see Fig. 4.10. The position angle combination (x_{fp}, x'_{fp}) describes the track in the dispersive plane of the spectrometer, while the other combination (y_{fp}, y'_{fp}) describes the track in the plane transverse to it.

The four focal plane quantities $x_{fp}, y_{fp}, x'_{fp}, y'_{fp}$ in combination with knowledge about the spectrometer optics define a particle trajectory through the spectrometer, which can be

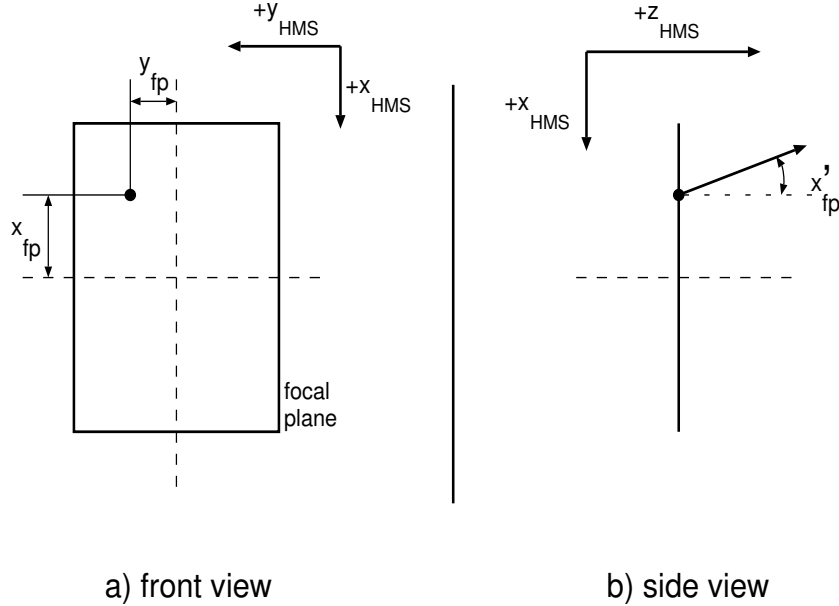


Figure 4.10: The focal plane quantities.

traced back to the reaction vertex in the target. The target quantities at the reaction vertex are reconstructed from the focal plane quantities through transformations of the form,

$$T_{tar} = \sum_{i,j,k,l} R_{i,j,k,l}^y (X_{fp})^i (Y_{fp})^j (X'_{fp})^k (Y'_{fp})^l , \quad 1 \leq i+j+k+l \leq N , \quad (4.4)$$

where $R_{i,j,k,l}^y$ is the *row* of the reconstruction matrix corresponding to target variable T_{tar} , and N the order of the expansion. Since four focal plane quantities are available, only four target quantities can be reconstructed. These are X'_{tar} , Y_{tar} , Y'_{tar} and δ , where the latter gives the particle momentum relative to the central momentum setting of the spectrometer, p_0 ,

$$\delta = \frac{p - p_0}{p_0} . \quad (4.5)$$

Note that since only four variables can be reconstructed, knowledge of the momentum through δ is chosen over knowledge of X_{tar} , as it is assumed that all events have a vertex with $X_{tar}=0$ (the vertical spread of the beam is neglected).

In order to check the matrix elements [88] to be used in the analysis of this experiment the following methods have been used: data were taken with a thin carbon target placed at position $X=0$, $Y=0$ in the beam, while the HMS collimator was replaced by the sieve slit, see Fig. 4.11. The sieve slit is attached to the front of the spectrometer. The sieve slit is

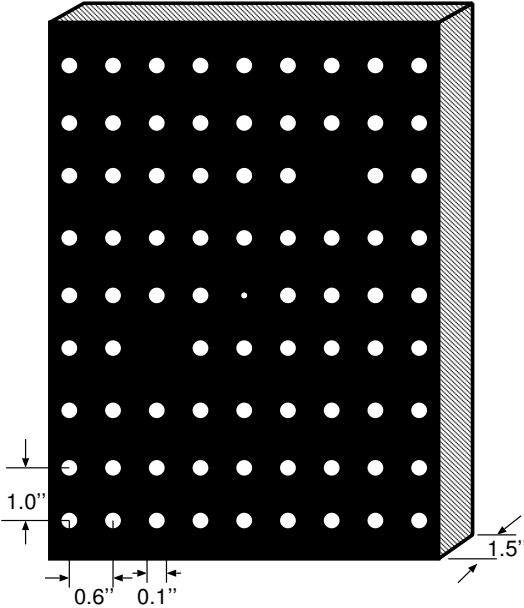


Figure 4.11: The HMS sieve slit. Two holes are missing to verify the sign of the angle reconstruction. The central hole is smaller than the others to measure the angular reconstruction resolution.

an array of holes with a smaller diameter hole in the center and two missing holes on the either side of this central hole. The missing holes provide information on the orientation of the sieve slit during the analysis.

Fig. 4.12 shows the reconstruction of the sieve slit holes in the vertical and the horizontal direction.

4.2 Detector Calibration

In order to achieve the best performance, the various detectors have to be calibrated. These calibrations included converting the drift chamber TDC values to drift distance, calibrating the gains of the Calorimeter and Čerenkov PMTs, *etc.*

4.2.1 Drift Chamber Calibration

The drift chambers provide information on the wires that were hit for each event, along with a TDC value for each hit. By using the hodoscopes to determine the time the particle passed through the focal plane (*i.e.* as a TDC *START*), the drift chamber TDC value (*STOP*) can be converted into a drift time. In order to determine the distance between the track and a wire the time-to-distance map is generated by the following procedure. The TDC values from all wires in a given plane have been taken for a large number of events (at least 50 k). This

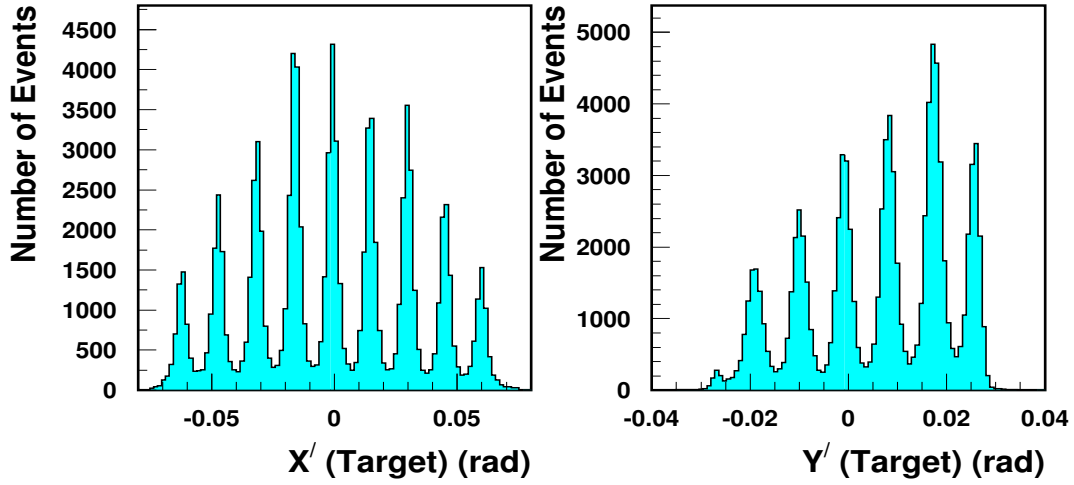


Figure 4.12: Reconstruction of the vertical (left) and horizontal (right) sieve slit hole patterns.

gives a drift time distribution $F(\tau)$. It is assumed that by averaging over all cells⁶ the drift position distribution is uniform. The distribution over a single cell is not uniform. However, when the cells are combined, the deviations from uniformity are so small that the effect on the drift distance reconstruction is on the order of $10 \mu\text{m}$, which is below the resolution of the chambers. After applying a loose cut on the TDC values to reject random or noise hits the drift distance is calculated by using the formula

$$D(t) = D_{max} \frac{\int_{t_{min}}^t F(\tau) d\tau}{\int_{t_{min}}^{t_{max}} F(\tau) d\tau}, \quad (4.6)$$

where t_{min} , t_{max} define the range of times to be included in the fit, $D(t)$ is the distance from the wire, D_{max} is the maximum possible distance (1/2 of the wire spacing, or 0.5 cm), $F(\tau)$ is the drift time distribution, and t is the time value from the TDC. A separate time-to-distance map is generated for each plane in the chambers. Fig. 4.13 shows the measured drift time distribution for one of the Y planes, along with the drift distance calculated from the drift time.

4.2.2 Gas Čerenkov Counter Calibration

The normalization of the signals from the gas Čerenkov detector is determined by measuring electrons in the spectrometer and converting the ADC signal to the number of the photo-

⁶A sense wire surrounded by field wires is called a cell.

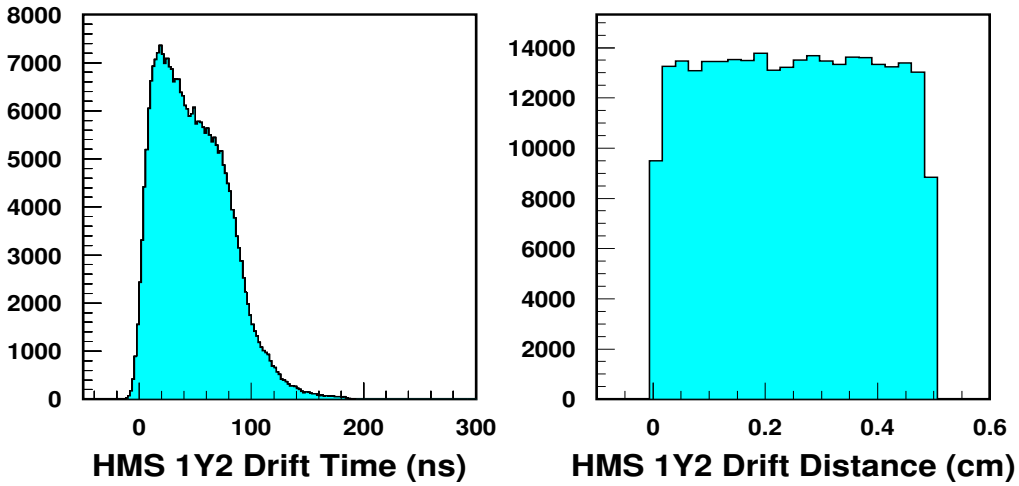


Figure 4.13: Drift time and drift distance spectra for the HMS drift chamber. The first and last bins only partially overlap the 0.5 cm region, and therefore contain less counts than the other bins. The drift time can be negative because the overall offset between the times measured by the drift chamber and the time measured by the hodoscope is not removed.

electrons detected. Electrons have been selected using the electromagnetic calorimeter. To transform the ADC signal to the number of the photoelectrons only one parameter is needed, the number of channels per photoelectron,

$$Tr = ADC_{1\gamma} - Pedestal , \quad (4.7)$$

where $ADC_{1\gamma}$ is the channel number where one photoelectron has been observed. Pedestal and single photoelectron peaks have been found by fitting the ADC distribution with Gaussian functions.

4.2.3 Lead Glass Calorimeter Calibration

To determine the energy deposited in the calorimeter, it is necessary to calibrate the gain of each module (lead glass block plus PMT), transform the measured ADC value into a deposited energy, and correct for attenuation in the lead glass block.

To provide a good calorimeter signal to the electronic trigger it is necessary to equalize the gain between modules. This has been done globally by adjusting the high voltages on the PMTs, so that blocks in each layer give about the same ADC signal. As the bottom blocks register higher energy electrons, their gain must be lower than for the top blocks, so that the

output ADC signals will be of the same size. This procedure has to be done using particles like the π , that deposit about the same amount of energy in each layer of the calorimeter.

To transform the measured ADC value into a deposited energy the following procedure has been applied: electrons, that have been selected using the Čerenkov detector, deposit their entire energy into the calorimeter. So, for each electron

$$\sum_i c_i A_i \approx E \quad (4.8)$$

should hold. Here i is the number of the block that has been hit, A_i is the signal from its ADC, c_i is its calibration constant, that transforms the measured ADC value into a deposited energy and E is the energy of the scattered electron. The calibration constants c_i for all blocks (totally 52 blocks, see Sect. 3.4.4) are found by minimizing the difference between the energy sum from the hit blocks and the energy of the scattered electron with respect to c_i . Attenuation in the lead glass leads to a variation of the signal with distance from the PMTs (because each block is read out on one end), so for each block a correction factor, based on the hit position is applied. To determine these corrections, only events that passed a high Čerenkov cut (electrons) have been used for the calibration.

After the blocks were calibrated and the measured energies corrected for attenuation, the resolution for the HMS calorimeter is $0.0793/\sqrt{E'}/\text{GeV}$ as shown in Fig. 4.14.

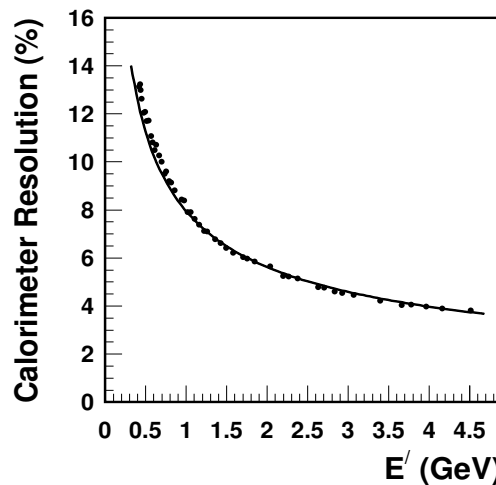


Figure 4.14: The experimental calorimeter resolution as a function of the scattered electron energy. The curve follows the expression $0.0793/\sqrt{E'}/\text{GeV}$.

4.2.4 Determination of the Offsets in E , θ and E' .

The nominal electron beam energy is determined during the experiment by the Hall C arc energy measurement using the superharps, as described in Sect. 3.1.2. The HMS central spectrometer momentum is obtained from the field to momentum conversion code for the HMS dipole and the nominal scattering angle is read from a scale observed by a remote TV camera. Possible small offsets in the beam energy (δE) as well as the offsets in the spectrometer central momentum ($\delta E'$) and scattering angle ($\delta\theta$) must be determined experimentally.

During the experiment several runs of elastic scattering on hydrogen have been taken at different E , θ and E' combinations. Analysis of these runs provides information about the experimental offsets δE , $\delta\theta$ and $\delta E'$. The expression for the total invariant mass squared in the virtual photon-nucleon system can be written in terms of E , θ and E' as

$$W^2 = M^2 + 2M(E - E') - 4EE'\sin^2(\theta/2) . \quad (4.9)$$

For scattering on hydrogen the value for W of the elastic peak should be the proton mass M , so the difference between the calculated value of W and the proton mass ($\Delta W^2 = W^2 - M^2$) must be due to offsets in E , θ and/or E' ,

$$\Delta W^2 = \frac{\partial W^2}{\partial E}\delta E + \frac{\partial W^2}{\partial E'}\delta E' + \frac{\partial W^2}{\partial \theta}\delta\theta , \quad (4.10)$$

with

$$\frac{\partial W^2}{\partial E} = 2M - 4E'\sin^2(\theta/2) , \quad (4.11)$$

$$\frac{\partial W^2}{\partial E'} = -2M - 4E\sin^2(\theta/2) , \quad (4.12)$$

$$\frac{\partial W^2}{\partial \theta} = -4EE'\sin(\theta/2)\cos(\theta/2) . \quad (4.13)$$

The values of ΔW^2 have been calculated⁷ for each elastic scattering run (totally 9 runs) for a certain set of values $(\delta E, \delta E', \delta\theta) = (0, 0, 0)$. Then the ΔW^2 has been minimized with respect to the values of $(\delta E, \delta E', \delta\theta)$ resulting in best estimates for the kinematic offsets as listed in Table 4.2.

The spectrometer momentum and scattering angle offsets have been constrained to be constant, assuming that the correction to the conversion of the field to momentum is constant, and the true HMS angle differs from the floor markers by a constant amount. These assumptions seem valid considering previous elastic scattering data.

E_n (GeV)	δE (%)	$\delta E'$ (%)	$\delta\theta$ (mrad)
5.648	-0.16	-0.21	-0.6
3.419	-0.02	-0.21	-0.6
2.301	-0.01	-0.21	-0.6

Table 4.2: Kinematic offsets obtained from the analysis of the elastic scattering.

For this experiment the experimental offsets are given in Table 4.2. In order to check the obtained kinematic offsets the new values of W have been calculated. The results are shown in Fig. 4.15.

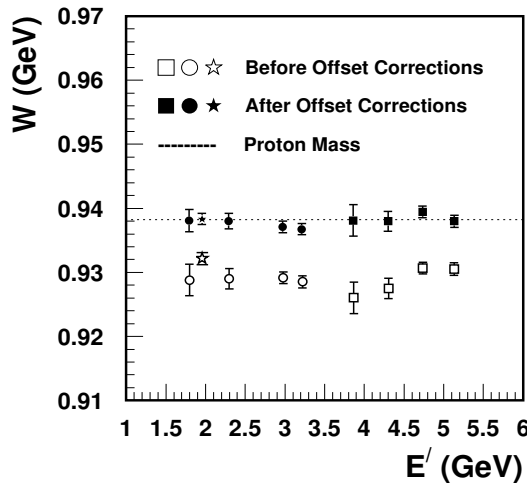


Figure 4.15: Computed W values for the elastic scattering on hydrogen before and after offset corrections.

The systematic uncertainties in the E , E' and θ measurements have been determined from the spread in the final values of W (using the results from the present and e94-110 experiments [87]) considering the values of the partial derivatives, see Eq. (4.10): $\delta E = 0.05\%$, $\delta E' = 0.06\%$, $\delta\theta = 0.2$ mrad.

4.3 Identification of Good Events

In order to achieve the main goal of the present experiment it is necessary to select only well identified electrons from the experimental data. In order to separate electrons from pions

⁷Before this procedure E and E' were corrected for energy loss in the target.

the Čerenkov and Calorimeter detectors are used. In addition to electrons the spectrometer detects negative hadrons, mostly pions. That is why it is important to choose such selection criteria (cuts) that help to identify clean electrons as efficiently as possible. Also, all kind of background electrons (charge symmetric background, background from target walls) should be subtracted and π contamination should be estimated.

4.3.1 Particle Identification

As has been mentioned in Sect. 3.4.3 the gas Čerenkov detector is used as a threshold detector. The mean Čerenkov signal for electrons is about 10 photoelectrons and in principle pions should give no Čerenkov signal, so pions appear at zero photoelectrons. A typical Čerenkov spectrum is shown in Fig. 3.13. In order to separate the electrons from the pions, in this analysis only events with more than 2 photoelectrons in the Čerenkov detector are used (these events are mostly electrons),

$$N_{\text{Cerenkov}} > 2 . \quad (4.14)$$

As has been explained in Sect. 3.4.4 electrons deposit their full energy in the calorimeter, so $E_{\text{calo}}/E' \approx 1$ (the pion peak is observed at about 0.3 GeV/ E' in the E_{calo}/E' spectrum), where E' is the energy of the detected particle. Therefore, the second criterion for the selection of the electrons has been chosen as

$$E_{\text{calo}}/E' > 0.7 . \quad (4.15)$$

In Fig. 4.16 the two-dimensional distribution of Čerenkov versus calorimeter response is shown. The solid lines show the cuts on the Čerenkov and calorimeter distributions (PID cuts).

4.3.2 Charge Symmetric Background

In the detected electron spectrum there is an unwanted real electron background coming from γ and π^0 particles produced in the target. The pions decay into photons, which can produce positron-electron pairs. These electrons will pass all PID cuts. Finally there are DIS electrons and electrons from the γ and π^0 : $e_{\text{total}}^- = e_{\text{dis}}^- + e_{\text{bg}}^-$. In order to subtract this background it is assumed that the number of background electrons is equal to the number of positrons $e_{\text{bg}}^- = e^+$ (that is why this background is called charge symmetric). The number of positrons can be measured by reversing the polarity of the spectrometer. The positron data have been taken at the same spectrometer settings (p, θ) as the electron data, and the ratio

$$R = \frac{Y^{e^-} - Y^{e^+}}{Y^{e^-}} , \quad (4.16)$$

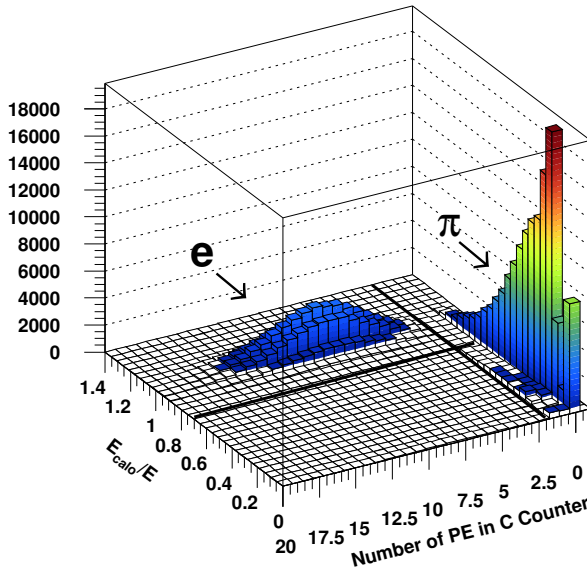


Figure 4.16: Particle identification

where Y^{e^-} is the yield for electrons and Y^{e^+} the yield for positrons, has been calculated for all beam energies, scattered electron energies and targets. The ratio R has been parametrized, as shown in Fig. 4.17, and the number of DIS electrons (for each target, angle, scattered electron energy and beam energy) has been corrected by these parametrizations (as a multiplicative factor) on a bin-by-bin basis in (E', θ) . The effect of this correction reaches 35 % at the smallest values of E' and the largest angles. The systematic uncertainty has been estimated as the deviation of the measured ratio R from the parametrization and is equal to 0.4 %.

4.3.3 Pion contamination

To identify electrons during the data analysis in this experiment two cuts have been applied on the calorimeter and Čerenkov distributions,

$$N_{\text{Čerenkov}} > 2 , \quad (4.17)$$

$$E_{\text{calo}}/E' > 0.7 . \quad (4.18)$$

However, after these cuts still some π background may be present.

Most of the pions do not produce any photoelectrons in the Čerenkov detector, but it is possible that pions generate knock-on electrons of high enough energy to emit Čerenkov light,

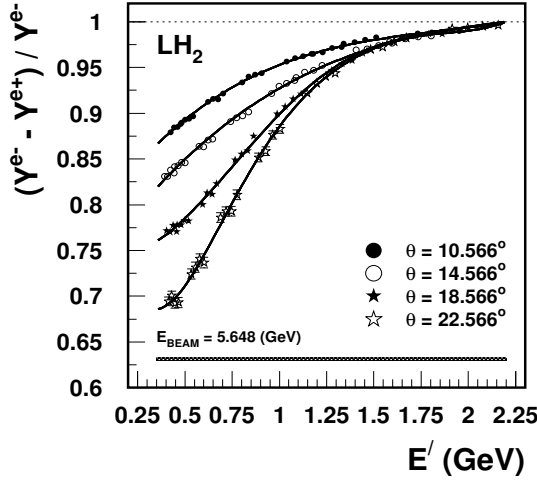


Figure 4.17: Multiplicative factor R for the cryo(hydrogen) at 5.648 GeV beam energy.

and these pions will pass the Čerenkov cut. Normally, pions in the calorimeter give a signal corresponding to their energy loss, which is about 0.3 GeV/ E' . The π background in the calorimeter presumably comes from pions that through a charge-exchange reaction produce a neutral pion which decays into two photons, and up to the full energy of the neutral pion can be deposited in the calorimeter. This leads to a high energy tail for pions that extends to $E_{cal}/E' = 1$.

However, if the cross sections for π^+ and π^- production are the same, then the number of pions remaining after the cuts in the negative polarity run will be canceled by the pions in the positive polarity run, when the correction for charge symmetric background is applied. Therefore, the ratio

$$R_\pi = \frac{Y^{\pi^-} - Y^{\pi^+}}{Y^{e^-}} \quad (4.19)$$

has been calculated in order to determine the pion contamination after subtracting the charge symmetric background.

The following method has been used to calculate this pion background

- 1) A calorimeter spectrum is created, with a cut $N_{Cerenkov} > 2$, as shown in Fig. 4.18. These are mainly electrons with some pion background.
- 2) A calorimeter spectrum is created, with a cut $N_{Cerenkov} < 2$, (see Fig. 4.18). This spectrum mainly contains pions, but also contains a tail from electrons as well.
- 3) The bin (bin_{max}) with maximum events is determined from distribution (2) (dashed lines), see Fig. 4.18.
- 4) The number of events with cut $N_{Cerenkov} > 2$ is determined in bin_{max} .

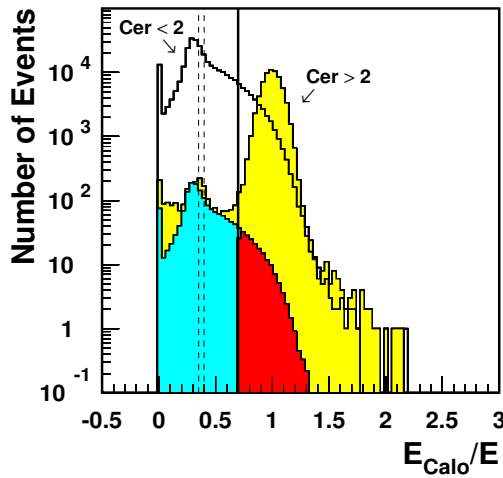


Figure 4.18: Calorimeter distributions for the LH₂ run ($E_{\text{Beam}} = 5.648 \text{ GeV}$) at 22.60° with different cuts used to calculate the pion contamination.

5) A normalization factor is calculated by using the formula:

$$\text{Norm}^{\text{factor}} = \frac{N(N_{\text{Cerenkov}} > 2)}{N(N_{\text{Cerenkov}} < 2)}. \quad (4.20)$$

7) The distribution, where the cut ($N_{\text{Cerenkov}} < 2$) is applied, is normalized by this factor (grey spectrum).

8) The cut ($E_{\text{calo}}/E' > 0.7$) is applied on distribution (7), and the number of pions is determined (dark grey spectrum).

The same procedure is used for all positive and negative polarity runs. (for all targets, angles and beam energies). According to this method the absolute value of R_π is always smaller than 0.003. Therefore, the pion contamination after subtraction of the charge symmetric background is negligible and the correction for the pion contamination has not been applied to the data.

4.3.4 Background from the Target Walls

As mentioned in Sect. 3.2.1 the cryotarget loops (which contain liquid hydrogen or deuterium) are made of aluminium. Hence, during the data taking on a cryotarget some of the incoming electrons scatter on the aluminium walls and create a background, which should be subtracted in order to get a clean sample of hydrogen or deuterium events. For that reason data on the aluminium dummy target have been taken at exactly the same kinematic settings (E, E', θ) as the hydrogen and deuterium data.

In order to subtract the aluminium background from the cryotarget data the following formula has been used

$$Y_{corrected} = Y_{Cryot.} - Y_{Alum.} \frac{T_{Walls}}{T_{Alum.}} \frac{R_{Alum.}^{ext}}{R_{Walls}^{ext}}, \quad (4.21)$$

where, Y are the yields for the cryo and aluminium dummy targets, T is the thickness of the aluminium walls in the cryotarget and aluminium dummy target, and R is the external radiative correction for the aluminium dummy target or the aluminium walls in the cryotarget⁸.

The yield for one of the hydrogen runs without aluminium background subtraction is shown in Fig. 4.19. In the same figure the yield for the target wall background and the corrected hydrogen yield are shown. The size of the background from the aluminium target

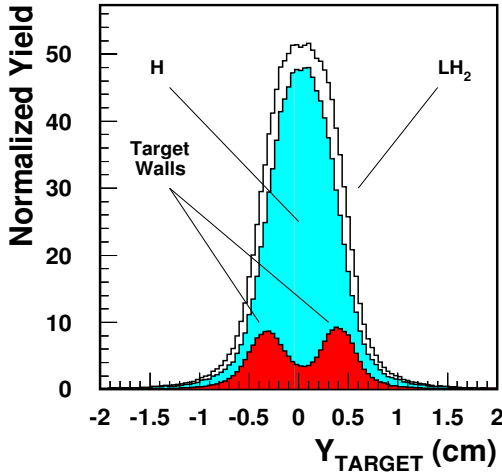


Figure 4.19: Normalized yield distributions for LH_2 , dummy and corrected sample of DIS events on hydrogen.

walls is generally about 18 %. The background has been calculated for each run and the subtraction has been done on a bin-by-bin basis in (E', θ) .

4.4 Deadtimes

During data taking, some events are not processed because the data acquisition or trigger electronics is busy while processing a previous event. These are termed dead-time losses and

⁸In order to simulate the effect of the hydrogen in the cryo target the effective radiation length of the front wall has been increased.

a correction for them must be applied when calculating yields or cross sections.

4.4.1 Electronic Deadtime

When two signals from different events try to activate the logic gate module within a short time, the later event is lost, if this event signal reaches the same module before the gate is closed after the first event. Such losses due to trigger electronics is called electronic dead time.

If the mean event rate is R , then the probability of finding n counts in a time t is given by the Poisson distribution

$$P(n) = \frac{(Rt)^n e^{-Rt}}{n!} . \quad (4.22)$$

The probability of zero events (live time) occurring in the interval t is thus $P(0) = e^{-Rt}$. For small Rt this can be approximated by $P(0) \approx 1 - Rt$. An event will be missed when it arrives within a time τ of an event accepted by the gate, where τ is the gate width of the logic signal. Therefore, the fraction of the measured events is equal to the probability that the time between events will be greater than τ

$$\frac{N_{\text{measured}}}{N_{\text{total}}} \approx 1 - R\tau . \quad (4.23)$$

In order to determine N_{total} , scalers with four different gate widths ($t=30, 60, 90, 120$ ns) have been used and the number of events recorded in each of them have been measured ($N_{30}, N_{60}, N_{90}, N_{120}$). A linear extrapolation back to zero gate width (using only gate widths $t = 60, 90, 120$) gives N_{total} . As the input to the scalers comes from a circuit that has a dead time which is more than 30 ns, scaler N_{30} does not lie on the linear extrapolation.

Ideally, these measurements of rates with different gate widths, should look like shown in Fig. 4.20 (left). Unfortunately, still unexplained effects were observed: the N_{60}, N_{90}, N_{120} scalers do not lie on a line as shown in Fig. 4.20 (right). The problem is still being investigated, perhaps it is due to cross talk in the electronic module.

This effect prevents determining the electronic dead time for this experiment in the usual way. It has been decided to use the average values of electronic dead times from previous experiments with an increased systematic uncertainty. The electronic dead time is taken to be $\tau = 40$ ns with a systematic uncertainty of 10 ns.

The electronic live time has been parametrized as a function of the pretrigger rate (1 - 40 ns × Pretrigger Rate (kHz)) and during the data analysis this parametrization has been used on a run-by-run basis.

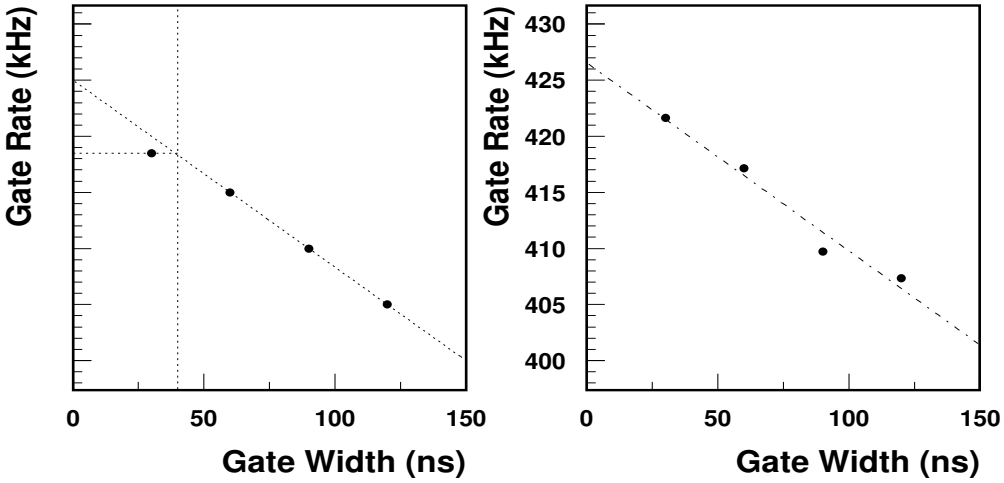


Figure 4.20: Left: expected behaviour of rates with different electronic trigger gate widths. Right: the behaviour of rates with different gate widths as found during the experiment.

4.4.2 Computer Deadtime

The other source of dead time is computer dead time. The computer dead time occurs as a result of the data acquisition computers being busy processing an event and not being available to process new events. In that case a new event is lost. Events recorded by the electronics have been logged as pretriggers. The pretriggers that have been processed successfully by the trigger supervisor are recorded as triggers. The ratio of triggers to pretriggers gives the computer live time, see Fig. 4.21.

$$L = \frac{N_{trigger}}{N_{pretrigger}} . \quad (4.24)$$

The computer live time is calculated for each run and applied on a run-by-run basis. The spread from the curve does not contribute to the systematic uncertainty because the parametrization is not used in the calculation of the cross section. The systematic uncertainty for the computer live time has been studied by comparing experimental yields at the same spectrometer kinematic setting but varying the prescale factors and therefore, computer live times [89]. These studies show that the yields agree within 0.2 %.

4.5 Efficiencies

During the data taking or data analysis some of the events are lost due to the following effects: 1) The trigger signal has not been generated (see Sect. 3.5). 2) The track could

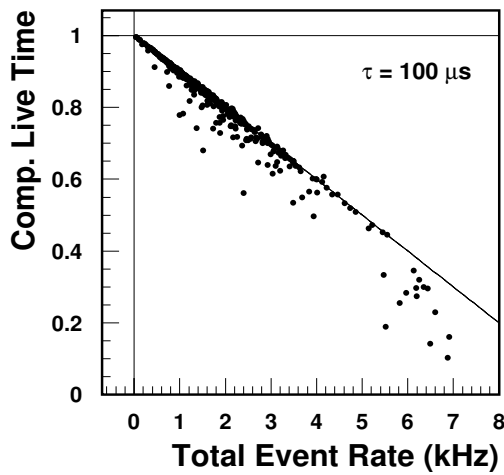


Figure 4.21: Computer live time as a function of the actual total trigger rate for all runs. The curve is from Eq. (4.23). The $100 \mu\text{s}$ is the time necessary to write the information from an event to the disk. The spread and deviations from the curve is due to network traffic.

not be reconstructed in the tracking procedure (see Sect. 4.1.1). 3) After using PID cuts on Čerenkov or calorimeter distributions (see Sect. 4.3.1) some of the otherwise valid events have been outside the cuts. In order to correct the cross section for these losses the efficiency for all these effects should be calculated.

4.5.1 Trigger Efficiency

Due to inefficiencies of the elements used for the triggers for the HMS spectrometer, as they were mentioned in Sect. 3.5, events can be lost. The schematic of the single arm trigger logic is shown in Fig. 3.16. It can be seen that the two electron triggers (low - level and high - level) are strongly correlated. For example, if the (SCIN) signal (at least three of the four scintillator layers of both hodoscopes have fired) is present for an event, there must also be a (STOF) signal (which requires one front panel and one back panel). If (PRHI) is present then there must also be a (PRLO) signal (high (PRHI) and low (PRLO) threshold on the energy in the first layer of the calorimeter). Thus, assuming that the Čerenkov signal (\check{C}) is always present the efficiency for the low - level electron trigger can be calculated as $\epsilon_{PRLO} \times \epsilon_{STOF}$. The small inefficiency of the Čerenkov is covered by the ELHI trigger which does not require the Čerenkov signal. If the calorimeter has an inefficiency, still an electron trigger could be produced if there is a (SCIN) signal. Accordingly the electron trigger efficiency for the HMS can be calculated (estimated) by the following formula

$$\epsilon_{trg} = \epsilon_{PRLO} \times \epsilon_{STOF} + (1 - \epsilon_{PRLO}) \times \epsilon_{3/4} . \quad (4.25)$$

The efficiency of each scintillator is determined by taking tracks that point to the center of the paddle, excluding the outer 0.5 cm of each paddle and determining how often each paddle fires. In order to prevent a tracking dependence of the calculation of the scintillator efficiency, which could happen if the track has been reconstructed slightly wrongly, the following conditions have been added: 1) the track should point to a cluster in the calorimeter and 2) if the paddle from the scintillator has not fired, where the track points, then the neighbouring paddles have been checked. If they fired, then this signal has been used in the determination of the scintillator efficiency. These modifications slightly increased the efficiency of the last two scintillators (2X) and (2Y) by 1.5 % and 3.2 %.

Also, an additional check has been done. If the paddle from the scintillator where the reconstructed track passed did not fire, all other paddles from this scintillator have been checked to verify whether another one fired. If any of them fired, then that signal has been used to determine the scintillator efficiency. This study showed that with this condition the scintillator 3/4 efficiency remains the same as with the conditions described above (only neighbouring paddles were checked). This check proved that the new conditions that have been added for the calculation of the scintillator 3/4 efficiency (see above) made this calculation completely independent of the tracking.

The scintillator 3/4 efficiency ($\epsilon_{3/4}$) has been calculated by summing over all possible combinations that would satisfy the 3/4 trigger

$$\epsilon_{3/4} = \prod_{i=1,4} \epsilon_i + \sum_{j=1,4} (1 - \epsilon_j) \prod_{i \neq j} \epsilon_i , \quad (4.26)$$

where i, j are the plane numbers and ϵ is the corresponding efficiency for each plane. The average scintillator 3/4 efficiency ($\epsilon_{3/4}$) is about 0.983.

The (PRLO) efficiency (ϵ_{PRLO}) has been calculated as the ratio of the events that have a (PRLO) signal and a signal from the Čerenkov over the events that have a signal from the Čerenkov,

$$\epsilon_{PRLO} = \frac{PRLO \& \check{C}ER > 0.5}{\check{C}ER > 0.5} . \quad (4.27)$$

The average (PRLO) efficiency is about 0.996.

The (STOF) efficiency (ϵ_{STOF}) has been calculated by using the efficiency of each scintillator ($\epsilon_1, \epsilon_2, \epsilon_3, \epsilon_4$,) by the following formula

$$\epsilon_{STOF} = \left(1 - (1 - \epsilon_1) * (1 - \epsilon_2)\right) \times \left(1 - (1 - \epsilon_3) * (1 - \epsilon_4)\right) . \quad (4.28)$$

The average (STOF) efficiency is about 0.997.

Finally, the total electron trigger efficiency for the HMS has been calculated by Eq. (4.25) and the result is shown in Fig. 4.22. The trigger efficiency is always higher than 0.996. The

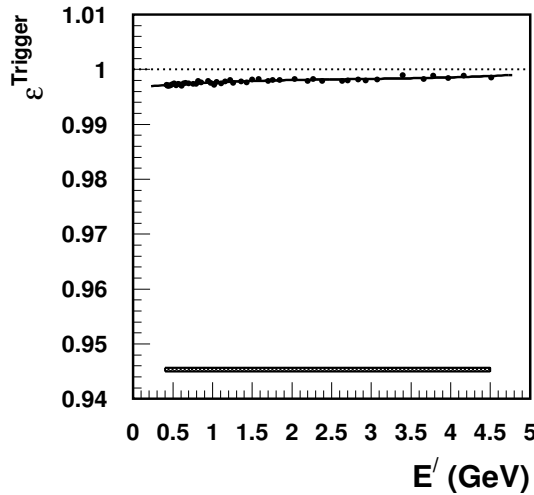


Figure 4.22: HMS electron trigger efficiency as a function of the scattered electron energy. The shaded error band indicates the size of the systematic uncertainty.

trigger efficiency has been parametrized as a function of the scattered electron energy and during the data analysis this parametrization has been used on a run-by-run basis. The systematic uncertainty is estimated as the spread of the measured trigger efficiency from the parametrization and is equal to 0.07 %.

4.5.2 Tracking Efficiency

There is a possibility that when a trigger occurs the tracking program cannot reconstruct a track. This may happen when there are too many fired wires in the drift chambers. If too many wires fired (as caused by a shower, yielding more than 30 fired wires for instance⁹) the chance of including a noise hit in the real track increases and it can prevent the tracking algorithm from finding a track.

In order to calculate the so-called fiducial tracking efficiency, the following procedure has been used. Only one of the central paddles in each scintillator plane should be hit. This defines the fiducial area, and guarantees that only one particle passed through both wire chambers within the central area of the spectrometer acceptance and should have been tracked. The fiducial area consists of paddles 5-12 in the X planes and 4-7 in the Y planes, as shown in Fig. 4.23. Particle identification cuts are used to select electrons. It is important

⁹It is a software cut on the tracking algorithm.

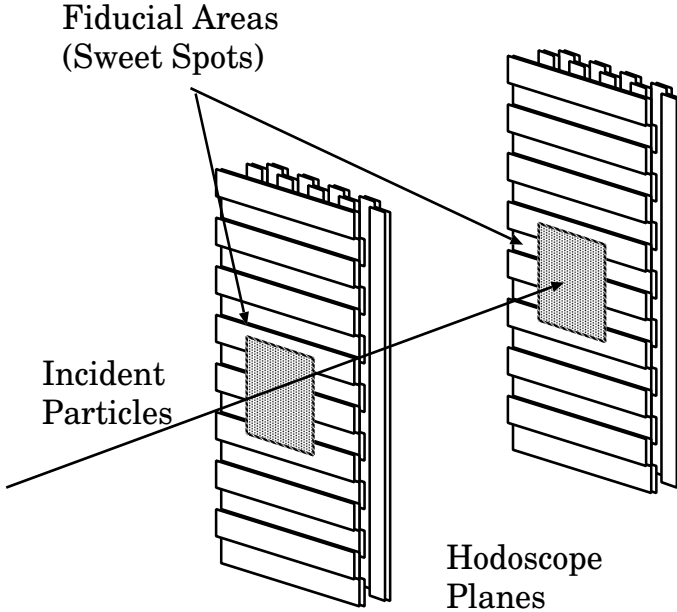


Figure 4.23: Illustration of the fiducial areas on the scintillator hodoscopes used for determination of the tracking efficiency.

to underline that for the calorimeter identification cut the total deposited energy has been used in order to prevent a dependence of the tracking on the calorimeter, see Sect. 4.5.4.

The tracking efficiency is calculated as the number of events for which a track has been found, divided by the number passing the mentioned criteria

$$\epsilon_{(tracking)} = \frac{TRG \& PID \& TR}{TRG \& PID}, \quad (4.29)$$

where TRG is the formed trigger, TR is the found track and PID represents the particle identification cut.

The tracking efficiency calculated for each run as a function of the scintillator (3/4) rate is shown in Fig. 4.24. The tracking efficiency has been parametrized as a function of the scintillator (3/4) rate and during the data analysis this parametrization has been used on a run-by-run basis. The systematic uncertainty is estimated as the spread of the measured tracking efficiency from the parametrization and is equal to 0.3 %.

4.5.3 Čerenkov Efficiency

As has been written in Sect. 4.3.1 the cut ($\text{Čerenkov} > 2$) is used on the Čerenkov spectrum in order to identify electrons. Some fraction of the electrons could be lost due to that cut. In order to determine how many electrons are lost it is important to have a clean sample of electrons (without pions) in the region $\text{Čerenkov} < 2$. Unfortunately, it is impossible to reach

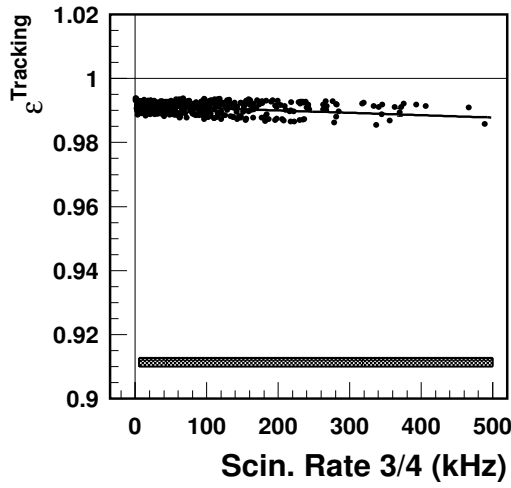


Figure 4.24: Tracking efficiency as a function of the scintillator (3/4) rate.

this directly with a cut on the calorimeter distribution only. For that reason two methods have been used for the determination of the Čerenkov efficiency:

The first method consists of analysing the elastic scattering runs. It is convenient to use these runs to determine the efficiency of the cut on the Čerenkov spectrum because an additional particle identification cut for electrons can be used, $0.65 \text{ GeV}^2 < W^2 < 1.15 \text{ GeV}^2$. The cut W^2 less than 1.15 GeV^2 has been chosen based on the π production threshold. In addition very tight cuts on the E_{calo}/E' spectrum have been used in order to minimize pion background and two particles (two clusters) on the calorimeter. In that case the Čerenkov efficiency can be calculated by the following formula

$$\epsilon_{cer} = \frac{N^{events}(0.9 < E_{calo}/E' < 1.1, 0.65 < W^2 < 1.15, \text{Cerenkov} > 2)}{N^{events}(0.9 < E_{calo}/E' < 1.1, 0.65 < W^2 < 1.15)} . \quad (4.30)$$

The results of this method are shown in Fig. 4.25 (left).

For the calculation of the Čerenkov efficiency at low E' the following method has been used: the Čerenkov efficiency which can be calculated by the following formula

$$\epsilon_{cer} = \frac{N^{events}(0.9 < E_{calo}/E' < 1.1, \text{Cerenkov} > 2)}{N^{events}(0.9 < E_{calo}/E' < 1.1)} , \quad (4.31)$$

will be higher for runs with low pion rate and lower for runs with high pion rate. So, the Čerenkov efficiency depends on the ratio π/e , which is proportional to

$$\pi/e = \frac{N^{events}(\text{Cerenkov} = 0)}{N^{events}(\text{Cerenkov} > 10)}, \quad (4.32)$$

where a very high cut on the Čerenkov spectrum has been used ($\text{Čerenkov} > 10$) in order to make a good selection of the electrons¹⁰. In that case the Čerenkov efficiency can be calculated for different runs with different pion rate and then extrapolated to $\pi/e = 0$, as it is shown in Fig. 4.25 (right). The same procedure has been used for runs at different E' .

The final result for the Čerenkov efficiency is shown in Fig. 4.25 (left). The two methods agree very well and cover the whole E' region.

For the first time it has been clearly seen that the Čerenkov efficiency¹¹ depends on E' . In order to investigate this dependence on E' two Čerenkov spectra for high and low energy

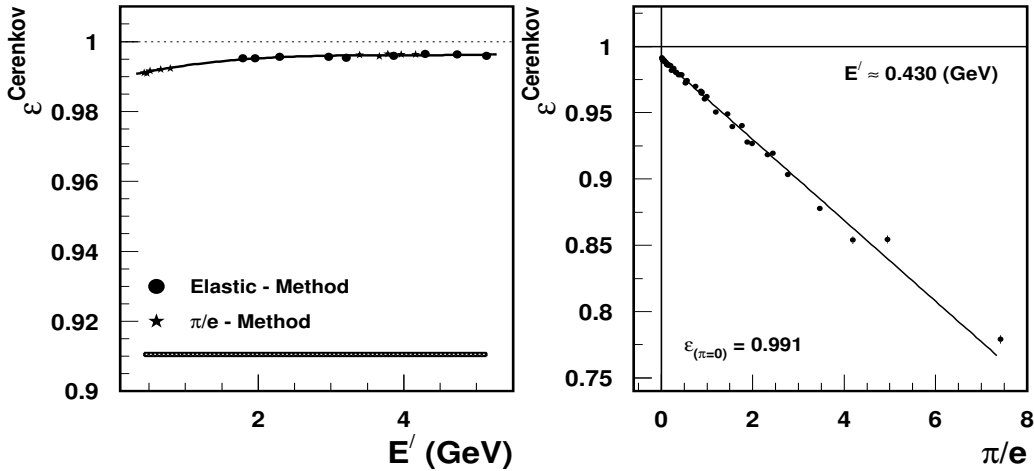


Figure 4.25: Left: the Čerenkov efficiency as a function of E' . Right: the Čerenkov efficiency as a function of the ratio π/e .

have been compared as shown in Fig. 4.26, which explains the behaviour of the Čerenkov efficiency. A tight cut ($0.9 < E_{calo}/E' < 1.1$) has been used in order to select electrons. The behaviour of the Čerenkov spectrum for different E' is not caused by the rate, because all data points in Fig. 4.25 (right) have a different rate and after correction for the π/e dependence the Čerenkov efficiency has been observed to be a constant as a function of rate. The reason of this behaviour of the Čerenkov spectrum for different E' is still not understood.

¹⁰This formula does not represent the real π/e ratio, because there are still some pions in the region $\text{Čerenkov} > 0$. Also many electrons will be thrown away by the $\text{Čerenkov} > 10$ cut. The goal is to have as clean as possible a sample of electrons and pions using only a cut on the Čerenkov spectrum.

¹¹It is the first time that the HMS Čerenkov efficiency has been determined at such a low E' .

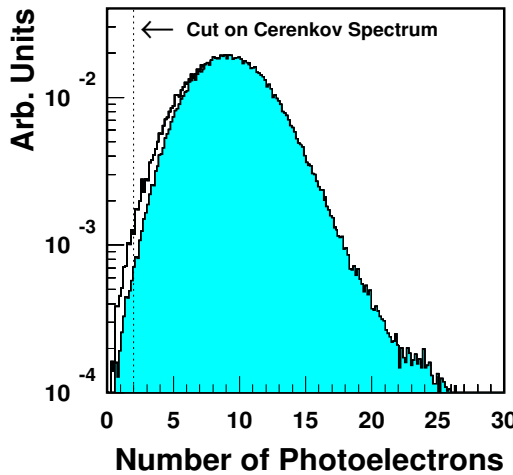


Figure 4.26: Čerenkov spectra for two different scattering energies: shaded spectrum - high E' value, open spectrum - low E' value.

The Čerenkov efficiency has been parametrized as function of the scattered electron energy (E') and during the data analysis this parametrization has been used on a run-by-run basis. The systematic uncertainty is estimated as the spread of the measured Čerenkov efficiency from the parametrization and is equal to 0.15 %.

4.5.4 Calorimeter Efficiency

During the analysis the cut $E_{calo}/E' > 0.7$ is used on the calorimeter spectrum to select electrons (see Sect. 4.3.1). It is important to know how many electrons are left below this cut. There are two types of signals of the electrons in the calorimeter spectrum below 0.7. There are electrons from the tail of the peak, see Fig. 3.15, and there are electrons for which the cluster is not found due to wrong tracking. The total calorimeter efficiency for electrons consists of two parts: an efficiency due to the cut on the calorimeter spectrum ϵ^{cut} (PID cut) and an efficiency due to wrong tracking ϵ^{wrong} ,

$$\epsilon_{cal}^{total} = \epsilon_{cal}^{cut} \times \epsilon_{cal}^{wrong}. \quad (4.33)$$

Besides electrons there are a lot of pions in the region $E_{calo}/E' < 0.7$ and therefore in order to calculate the calorimeter efficiency correctly the pions should be removed from the electron samples. In order to reduce pions as much as possible the cut on the Čerenkov spectrum is increased: Čerenkov > 10.

In order to calculate the ϵ^{wrong} efficiency the following method has been used: the electrons for which the cluster is not found in the calorimeter due to wrong tracking¹² appear in the calorimeter distribution near zero ($E_{calo}^{track}/E' \approx 0$). However, the value of the total deposited energy in the calorimeter normalized to the energy of the detected particle should still be about 1 ($E_{calo}^{total}/E' \approx 1$). Therefore, ϵ^{wrong} can be calculated as the ratio of electrons that can be identified with the cut $E_{calo}^{track}/E' > 0.7$ and $E_{calo}^{total}/E' > 0.7$. In addition special cuts should be applied in order to get rid of double clusters on the calorimeter. It can be done by using two requirements: the number of tracks should be equal to one, and only one paddle from each scintillator should be hit (this condition is needed because there are cases when there are a few hits in the paddles and two clusters in calorimeter, but there is only one track),

$$\epsilon_{cal}^{wrong} = \frac{N_{events}(E_{calo}^{track}/E' > 0.7, \text{Cerenkov} > 10)}{N_{events}(E_{calo}^{total}/E' > 0.7, \text{Cerenkov} > 10)}. \quad (4.34)$$

The ϵ^{wrong} efficiency at high scattered electron energy is very high and only decreases to 99 % at low E' .

In order to calculate the ϵ^{cut} efficiency the following method has been used: after applying a cut $\text{Čerenkov} > 10$ on the E_{calo}^{total}/E' spectrum the number of events left below the cut $E_{calo}^{total}/E' > 0.7$ becomes very small as shown in Fig. 4.27. It can be pions or electrons, or

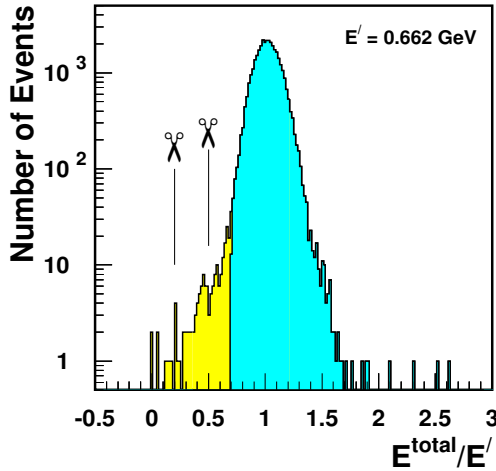


Figure 4.27: E_{calo}^{total}/E' spectrum after applying a cut $\text{Čerenkov} > 10$.

¹²The track is too far from the cluster.

both of them. For this reason the following formula has been used twice in order to calculate the ϵ^{cut} efficiency,

$$\epsilon_{cal}^{cut} = \frac{N_{events}(E_{calo}^{total}/E' > 0.7, Cerenkov > 10)}{N_{events}(E_{calo}^{total}/E' > 0.2 \text{ (or } > 0.5\text{)}, Cerenkov > 10)} . \quad (4.35)$$

First it has been used with a cut in the denominator $E_{calo}^{total}/E' > 0.2$ and then $E_{calo}^{total}/E' > 0.5$. In the first case the ϵ^{cut} efficiency has been probably underestimated and in the second case overestimated. The ϵ^{cut} efficiency has been calculated as the average of these two results. The difference between the two results has been taken as the systematic uncertainty.

The total calorimeter efficiency ϵ^{total} is shown in Fig. 4.28. The systematic uncertainty

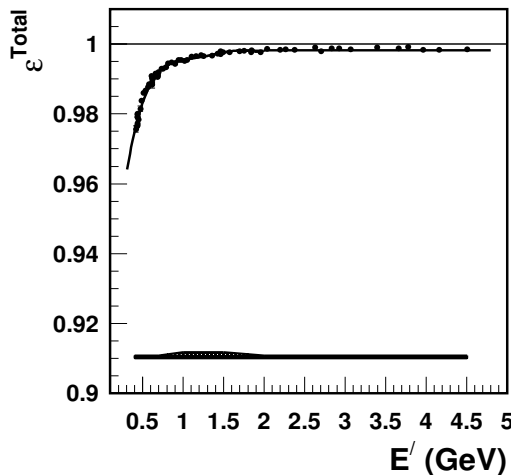


Figure 4.28: The total calorimeter efficiency (see text for detail) as a function of the scattered electron energy.

varies from 0.05 to 0.2 %. The calorimeter efficiency ϵ^{total} has been parametrized and that parametrization has been used during the analysis on a bin-by-bin basis in E' .

4.6 Target Density Correction

When the electron beam passes through the target it deposits energy and changes the temperature in the target along the beam. This temperature change does not influence the characteristics of the solid targets but, in the liquid targets it leads to a boiling effect: local changes in the target density. The boiling effect depends on the beam current, beam spot size, beam rastering size and the thermal properties of the target. In order to determine the

Target	E' (GeV)	θ (degree)	Slope in % per 100 μA
LH ₂	2.500	14.60	-4.2 +/- 0.7
LH ₂	2.271	18.60	-3.9 +/- 1.5
LD ₂	2.500	14.60	-4.1 +/- 0.9
LD ₂	2.271	18.60	-3.9 +/- 1.6

Table 4.3: Results obtained from the luminosity scan for the LH₂ and LD₂ targets.

dependence of the density on the current a few test runs have been taken on LH₂ and LD₂ with different beam currents: 15, 25, 35 and 45 μA (luminosity scan). The experimental yield has been calculated for each run and a linear extrapolation back to zero current (with normalization to unity) has been used to determine the current dependence of the target density, as shown in Fig. 4.29. The slope parameters are given in Table 4.3 for each target

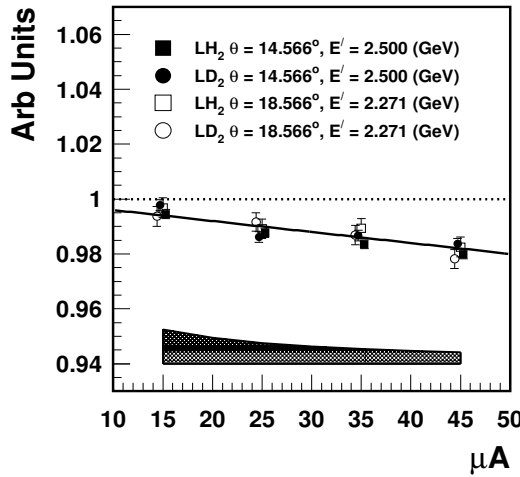


Figure 4.29: Luminosity scan for LH₂ and LD₂. The fit represents the correction factor for the density of the liquid targets due to the boiling effect.

and for several kinematic settings. As the slopes are equal within the error bars for both targets it has been decided to use a global fit (parametrization), which is shown in Fig. 4.29. The density correction for the liquid targets is 4.0 ± 0.3 % per 100 μA . This parametrization has been used on a run-by-run basis for the liquid targets. The maximum current that has been used during data taking is 25 μA , so the largest correction for the boiling effect on the liquid targets is 1.0 %.

The absolute systematic uncertainty in the BCM measurement in Fig. 4.29 has been

estimated to be $0.2 \mu\text{A}$.

4.7 Acceptance Function

For a fixed angle and momentum setting, the HMS measures data in a range of angles and momenta around the central values. Generally the acceptance is a function of the three target coordinates X, Y, Z and three spectrometer coordinates δ, X', Y' . The acceptance function of the spectrometer is written as a function of these six variables which represents the probability that a scattered particle coming from the point (X, Y, Z) , and with kinematics defined by (δ, X', Y') is detected. As the inclusive cross section does not depend on the target coordinates or the azimuthal angle, the acceptance function can be written as a function of only two variables (δ, θ) ¹³.

In first instance the acceptance function is just the bin width in δ times the geometrical solid angle for a certain θ bin. However, in some cases events could be lost due to inefficiencies or other limitations which requires to use an acceptance function.

Firstly, particles that passed the HMS entrance slit (collimator) may hit the vacuum chamber or other constructions within the spectrometer. This effect is very small for the range in δ and Y used in this experiment. Secondly, there will be an effect due to the finite resolution and non-perfect reconstruction of the spectrometer.

Due to resolution effects some events could appear after the reconstruction outside the collimator edges. In order to avoid losses because of this the collimator cuts in the analysis have been taken slightly larger than the actual size of the collimator,

$$\text{abs}(X'_{tar}) < 0.08 \text{ (rad)} , \quad (4.36)$$

$$\text{abs}(Y'_{tar}) < 0.04 \text{ (rad)} . \quad (4.37)$$

It has been verified that small changes of the values of these cuts do not affect the experimental yield. Due to the resolution effects and non-perfect reconstruction events could also move from one (δ, θ) bin to another one. When the bin is not located at the edge of the acceptance then some events could move away from that bin, but on the other hand events from other bins could move in. So, in that case the number of events in that bin will not change. Since the used acceptance in δ is well within the flat acceptance region the only real effect is in the θ dependence of the acceptance function near the edge. In practice only the inner 16 out of the 20 bins of the θ acceptance have been used. The acceptance function $A(\delta, \theta)$ has been calculated in a Monte Carlo (MC) program.

There are three main elements in the Monte Carlo simulation code: the event generator, the transport of the particles through the magnets, and the list of materials and apertures that cause multiple scattering or stop the particles. The initial coordinates are randomly

¹³The X' and Y' variables can be converted to the polar angle θ and the azimuthal angle ϕ .

generated along the target length, while the quantities δ , θ and ϕ are chosen randomly within their allowed limits. The particle is transported through the spectrometer to the detector hut using the computer program COSY Infinity [85], which models the magnetic part of the spectrometer, the magnet position, internal dimensions and magnet field maps. With this method a set of matrix elements is calculated up to order $N=5$, see Sect. 4.1.2. If the particle successfully traversed the spectrometer and the detector stack, it is considered a success and contributes to N_{success} . The spectrometer acceptance function can be written as,

$$\text{Acceptance}(\Delta\theta, \Delta\delta) = \frac{N_{\text{success}}}{N_{\text{gen}}} \Delta V , \quad (4.38)$$

where ΔV is the generation volume¹⁴ and N_{gen} is the number of generated events. The experimental data as well as the spectrometer acceptance function are binned into small bins in δ and θ . Each bin $N_{ij}(\delta_i, \theta_j)$ from the experimental data has been divided by the corresponding factor $MC_{(ij)} = \text{Acceptance}_{(ij)}$.

In order to check the Monte Carlo method, the following procedure has been used: Monte Carlo data have been generated using the cross section model, see Sect. 4.12, which has been used for the data analysis. All kind of corrections (dead times, efficiencies, target density, radiative corrections) have been used in the Monte Carlo. In addition the Monte Carlo results have been normalized by the charge and prescale factor. The result of this comparison for one of the runs is shown in Fig. 4.30. It shows that the experimental data and the Monte Carlo data are in good agreement at the selected HMS phase space of this experiment ($-8\% < \delta < 8\%$) and ($-32\text{ mrad} < (\theta - \theta_c) < 32\text{ mrad}$). The acceptance function has been used during the analysis on a bin-by-bin basis in (δ, θ) .

The systematic uncertainty of the MC has been studied by comparing the experimental data and MC with different position offsets on target, collimator, magnets and detector package. This comparison showed that the systematic uncertainty in MC is about 0.6 %.

A small δ dependent effect has been observed during this comparison, as shown in Fig. 4.31. It has been found that this effect is independent of target and kinematics (E, E', θ) .

One explanation of this δ dependence effect could be a small offset in the reconstruction of the target variable X'_{tar} as a function of δ , which would influence the acceptance through the X'_{tar} cut. In order to check this idea the same comparison as in Fig. 4.31 has been done for different regions of X'_{tar} . These calculations showed that the δ effect is independent from X'_{tar} . Furthermore, it has been estimated that unrealistically large errors in the determination of X'_{tar} would be needed to explain this effect.

A plausible explanation of the δ dependence effect is the following: the ratio which is shown in Fig. 4.31 is different for different δ regions due to a different δ bin widths, *i.e.*, the size of the δ_{exp} bins that have been used for the experimental data is not equal to the size of the δ_{MC} (δ_{real}) bins. This could happen if the calibration of δ is slightly in error, *i.e.*, δ_{exp} is not equal to δ_{real} , but is some function $h(\delta_{\text{real}})$. In that case the ratio, which is shown in Fig. 4.31 means, that $\Delta\delta_{\text{real}}/\Delta\delta_{\text{exp}} = f(\delta)$, where $f(\delta)$ is the curve, which is shown in Fig.

¹⁴The volume in which events have been generated.

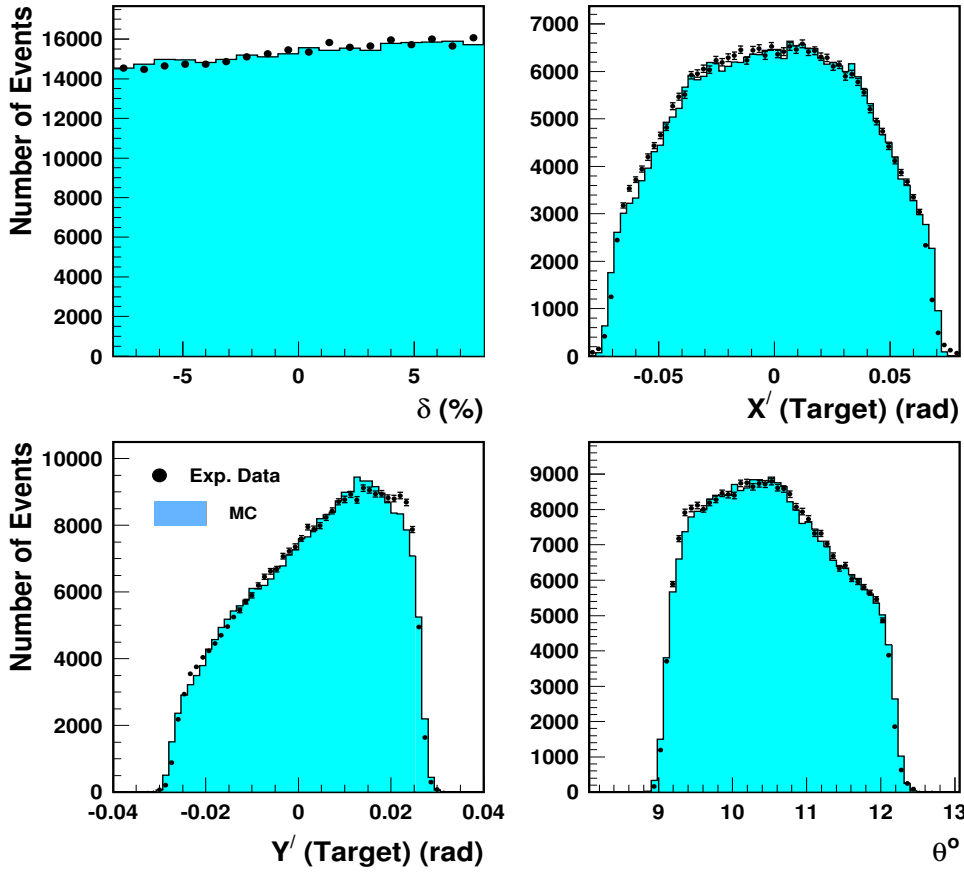


Figure 4.30: Comparison between data (carbon, $E' = 3.07$ GeV, $\theta = 10.566^\circ$) and Monte Carlo yield (grey histogram).

4.31. The function $f(\delta)$, which has been parametrized as a polynomial (of order 5), can be used to calculate $h(\delta_{real})$,

$$\delta_{exp} = h(\delta_{real}) = \int \frac{1}{f(\delta)} d\delta . \quad (4.39)$$

In order to get $h(\delta_{real}) = 0$ at $\delta = 0$, the integration constant has been forced to zero, because the calibration of δ has been done at $\delta = 0$.

The difference between δ_{exp} and δ_{real} is shown in Fig. 4.32. The difference between δ_{exp} and δ_{real} is 0.055 % at maximum, which is within the value of the systematic uncertainty of δ_{exp} , see Sect. 4.2.4.

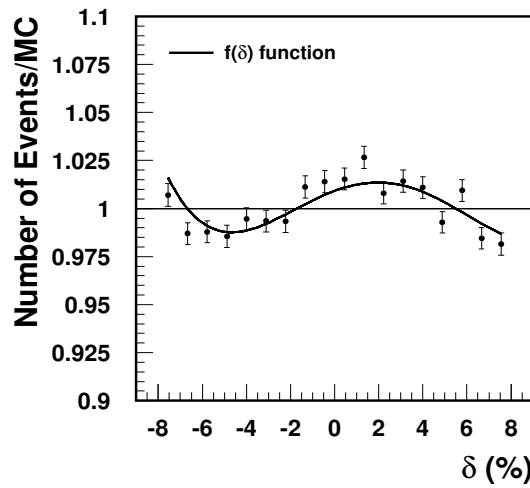


Figure 4.31: The average ratio of the data and the Monte Carlo at different δ bins.

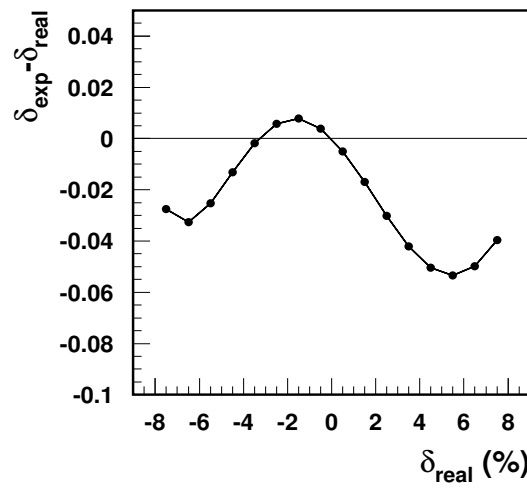


Figure 4.32: The difference between δ_{exp} and δ_{real} which causes the effect in Fig. 4.31.

During the analysis the parametrization of the δ effect has been used as a correction factor on a bin-by-bin basis in δ .

4.8 Extraction of the Cross Section

After calculating all corrections the differential cross section can be computed by the following formula

$$\frac{d^2\sigma}{d\Omega dE'} = \frac{PS \times CSB \times N^{e^-}}{Acceptance \times Charge \times \epsilon^{eff} \times \mathcal{L}^{times} \times T^{target} \times \Delta E'}, \quad (4.40)$$

where CSB represents the charge-symmetric background factor (see Sect. 4.3.2), PS the prescale factor, N^{e^-} the number of electrons. ϵ^{eff} the total efficiency: $\epsilon^{trigger} \times \epsilon^{tracking} \times \epsilon^{cerenkov} \times \epsilon^{calorimeter}$ (see Sect. 4.5), \mathcal{L}^{times} is the total live time: $\mathcal{L}^{computer} \times \mathcal{L}^{electronic}$ (see Sect. 4.4). $Acceptance$ is the Acceptance function (see Sect. 4.7), $Charge$ is the accumulated charge (see Sect. 3.1.3), $\Delta E'$ is the E' bin width and T^{target} is the target thickness¹⁵. For cryotargets the background from target walls must be subtracted first (see Sect. 4.3.4).

The bin centering correction is, apart from the radiative corrections, see Sect. 2.10, the last step that should be done, see the next Section.

4.9 Bin Centering Correction

The spectrometer acceptance (HMS) in θ is about $\pm 1.8^\circ$. Therefore, in order to determine the cross section at the central angle ($\theta^{central}$), a so-called bin centering correction must be applied. This correction is necessary due to the fact that the cross section rapidly varies with θ . As has been mentioned in Sect. 4.7 the data have been binned into small bins of E' and θ , corresponding to the δ and θ bins used to determine the spectrometer acceptance. In order to convert the cross section that has been measured in the interval $\pm 1.8^\circ$ around $\theta^{central}$ to the cross section at central $\theta^{central}$ the following procedure has been used for each (E', θ) bin:

For each $(E', \theta^{central})$ bin the Born cross section $\sigma^{model}(E, E', \theta^{central})$ (see Sect. 2.9) and the radiative correction factor $RC(E, E', \theta^{central})$ (see Sect. 2.10) have been calculated using certain models (see Sect. 2.9). The same procedure has been done for each (E', θ) bin, where θ is the central angle of the bin. The bin centering factor (BC) has been calculated for each (E', θ) bin as

$$BC(E, E', \theta) = \frac{\sigma^{model}(E, E', \theta^{central})}{RC(E, E', \theta^{central})} \Bigg/ \frac{\sigma^{model}(E, E', \theta)}{RC(E, E', \theta)}. \quad (4.41)$$

The Born cross sections have been divided by the radiative corrections in Eq. (4.41), because the radiative corrections can be different for different θ bins. Then, the experimental cross section at the central angle for each (E') bin has been determined by multiplying $\sigma(E, E', \theta)$ by the factor $BC(E, E', \theta)$

¹⁵For the cryotargets an additional correction must be applied, see Sect. 4.6

$$\sigma^{exp}(E, E', \theta^{central}) = \sigma(E, E', \theta) \times BC(E, E', \theta). \quad (4.42)$$

After applying the bin centering correction for each (E', θ) bin, the resulting cross sections at $(E', \theta^{central})$ have been averaged in order to arrive at the value of the cross section for $\theta^{central}$. In Fig. 4.33 (left) an example of the bin centering correction is shown. The effect

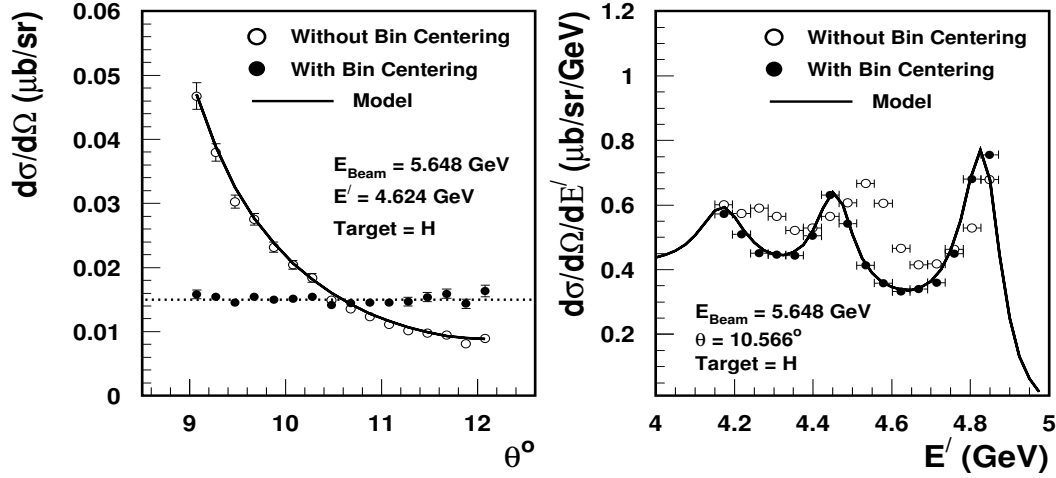


Figure 4.33: Left: Bin centering correction for one of the (E') bins. The cross sections at different angles (different θ bins, $\pm 1.8^\circ$ from $\theta^{central}$) have been converted to the central angle (10.566°). Right: the cross section for hydrogen in the resonance region with and without bin centering correction.

of this correction depends on E' and θ . If this procedure is applied in the resonance region, where the cross section rapidly changes with θ , the effect of the bin centering correction can be up to 60 % (for this experiment) as it is shown in Fig. 4.33 (right). When this procedure is applied in the DIS region the effect of this correction is much smaller.

The bin centering correction has been used during the analysis on a bin-by-bin basis in (E', θ) .

4.10 Calculation of the Radiative Corrections

As mentioned in Sect. 2.10, radiative processes have to be calculated and subtracted in order to determine the differential (Born) cross section . The measured cross section contains the following contributions, see Sect. 2.10,

$$\sigma_{meas} = \sigma_{Born} + \sigma_{el} + \sigma_{qel} + \sigma_{inel}^{rad} . \quad (4.43)$$

Each of these cross sections (σ_{el} , σ_{qel} , σ_{inel}^{rad}) can be divided into two parts: external and internal (e.g., $\sigma_{inel}^{rad} = \sigma_{inel}^{ext} + \sigma_{inel}^{int}$).

There are two ways of determining σ_{Born} : multiplicative and subtraction methods. In the multiplicative method σ_{Born} is calculated by multiplying σ_{meas} by a factor η ,

$$\sigma_{Born} = \eta \times \sigma_{meas} , \quad (4.44)$$

where η is

$$\eta = \frac{\sigma_{Born}^{model}}{\sigma_{el} + \sigma_{qel} + \sigma_{inel}} , \quad (4.45)$$

where σ_{inel} is the sum of the calculated radiative and non-radiated inelastic cross sections, σ_{Born}^{model} is the model of the Born cross section, which has been used in the iteration procedure, see Sect. 4.12, σ_{el} and σ_{qel} are the radiative elastic and quasi-elastic cross sections. However, since the elastic and quasi-elastic cross sections are not proportional to the Born cross section this formula will be correct only in case the Born cross section and the model cross section are exactly the same and even then it should not be used to calculate the uncertainties in σ_{Born} . Therefore, the multiplicative method should not be used for determining σ_{Born} .

In the full subtraction method the elastic σ_{el} , quasi-elastic σ_{qel} and inelastic σ_{inel}^{rad} radiative cross sections are subtracted from the measured cross section,

$$\sigma_{Born} = \sigma_{meas} - \sigma_{el} - \sigma_{qel} - \sigma_{inel}^{rad} . \quad (4.46)$$

Since the inelastic radiative cross section is largely proportional to the Born cross section, that part could better be treated multiplicatively, e.g.

$$\sigma_{Born} = \left(\sigma_{meas} - \sigma_{el} - \sigma_{qel} \right) \frac{\sigma_{Born}^{model}}{\sigma_{inel}} . \quad (4.47)$$

The usual calculation of radiative corrections only includes the emission of one hard photon. There is a possibility that the electron could emit two hard photons, and additional corrections (α^2 term) should be used for the elastic σ_{el} , quasi-elastic σ_{qel} and inelastic σ_{inel}^{rad} radiative cross sections.

There are two sets of programs available to calculate the radiative corrections: one based on the formalism of Mo and Tsai [91], and one based on the formalism of Bardin [98]. The

latter has a different treatment of multiple photon emission and incorporates an approximation for the emission of two hard-photons. The two hard-photon radiation is not included in the formalism of Mo and Tsai. On the other hand the program based on the Bardin formalism (*TERAD*) only calculates internal radiative corrections. Therefore, the following method has been used in order to calculate the radiative contributions to the measured cross section σ_{meas} .

The internal radiative corrections σ_{int} ($\sigma_{int} = \sigma_{el}^{int} + \sigma_{qel}^{int} + \sigma_{inel}^{int}$) have been calculated using the formalism of Bardin. The external radiative corrections σ_{ext} ($\sigma_{ext} = \sigma_{el}^{ext} + \sigma_{qel}^{ext} + \sigma_{inel}^{ext}$) have been calculated using the formalism of Mo and Tsai. Since two formalisms are used, it is necessary to take into account the possible difference between them, therefore, the following formula has been used in order to calculate σ_{Born} ,

$$\sigma_{Born} = \sigma_{meas} - \sigma_{Bardin}^{int} \left(\frac{\sigma^{int} + \sigma^{ext}}{\sigma^{int}} \right)_{Mo, Tsai}. \quad (4.48)$$

In using this formula is assumed that the ratio of external and internal radiative contributions is the same in the formalism of Bardin and Mo-Tsai. As has been mentioned above, a correction due to two hard-photon emission (α^2 term) should be included in the radiative contributions. Unfortunately, the higher α terms ($\alpha^3, \alpha^4 \dots$) are not known and may start to be non-negligible at low values of E' . Therefore, the decision has been made to calculate σ_{Born} with and without the α^2 term (σ_{Bardin}^{int} has been calculated with and without the α^2 term), and the final differential Born cross section has been calculated as the average of these two cross sections. The half difference between the two cross sections has been taken as the uncertainty of the final Born cross section and has been included in the systematic uncertainties. This has been done in order to include possible influences of the higher order α terms on the final differential Born cross section,

$$\sigma_{Born} = \frac{\sigma_{Born}^{\alpha^2=True} + \sigma_{Born}^{\alpha^2=False}}{2} \quad \delta_{\sigma_{Born}}^{\alpha^2} = \frac{\sigma_{Born}^{\alpha^2=False} - \sigma_{Born}^{\alpha^2=True}}{2}. \quad (4.49)$$

To compute the elastic and inelastic radiative contributions to the measured cross sections the following models have been used: for the elastic hydrogen contribution the model from Ref. [90] has been used, the model from Ref. [95] has been used for deuterium and the models from Ref. [96] have been used for heavy targets. The inelastic contribution has been computed using models that have been mentioned in Sect. 2.9. The models used for the calculation of the inelastic contribution are changed later on during the iteration procedure, see Sect. 4.12.

In the $A > 1$ targets a contribution arises also from quasi-elastic scattering. The radiative contribution from quasi-elastic scattering vanishes at $Q^2 \rightarrow 0$, by virtue of the orthogonality of the bound and the scattering wave functions [92]. A calculation of Arenhovel [94] has been used in order to calculate the quasi-elastic cross section on deuterium. The effect of the orthogonality requirement has been incorporated by a suppression factor given by Bernabeu

[93]. The calculation of the quasi-elastic cross section on heavier targets ($A > 2$) differs from the calculation for deuterium, since also Pauli blocking was taken into account. The y -scaling model [97] has been used for the calculation of the quasi-elastic cross section for the heavy targets.

As an example, the deuterium cross sections before and after subtraction of the radiative processes are shown in Fig. 4.34. In the same figure the cross sections for the various radiative

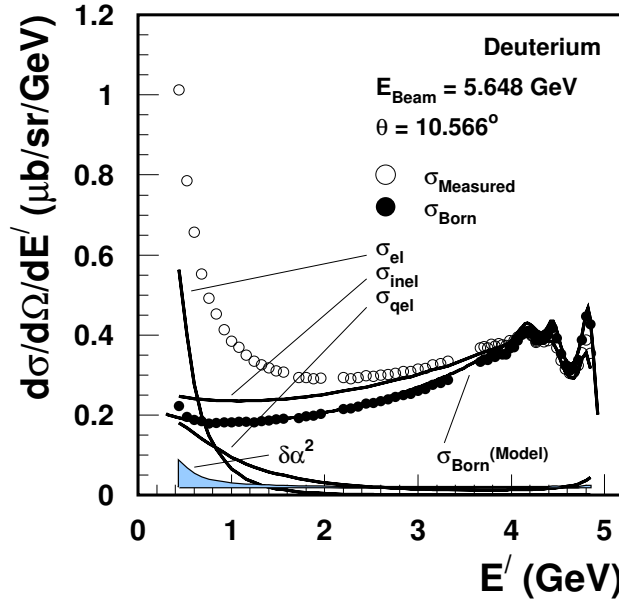


Figure 4.34: Measured and extracted Born cross section for deuterium for $\theta = 10.566^\circ$ at 5.648 GeV beam energy. The contributions from radiative processes (elastic, quasi-elastic and inelastic) are also shown. The uncertainty from the α^2 term ($\delta\alpha^2$) is shown as an error band.

processes (elastic, quasi-elastic and inelastic) are shown. Obviously, even a small error in the calculation of the elastic radiative tail will dramatically increase the uncertainty of σ_{Born} at low values of E' .

Since the external radiative processes depend on the target thickness they could be checked by comparing the final radiatively corrected cross sections for the same nucleus with different target thicknesses. During the data taking two carbon (1 % and 3 % radiation length thicknesses) and two copper (2 % and 3 % radiation length thicknesses) targets have been used with different thicknesses. The ratio of these cross sections $\sigma_C^{3\%}/\sigma_C^{1\%}$ and $\sigma_{Cu}^{3\%}/\sigma_{Cu}^{2\%}$, after subtraction of the radiative processes, for all beam energies, angles and scattered electron energies is constant within the experimental error bars, indicating that the external radiative

Target	$\delta_{\sigma_{el}}(\%)$	$\delta_{\sigma_{qel}}(\%)$	$\delta_{\sigma_{inel}}(\%)$
Hydrogen	1.5	-	1
Deuterium	1.5	2	1
Carbon	1.5	3	1
Aluminium	2	3	1
Copper	2	3	1
Gold	2	3	1

Table 4.4: The systematic uncertainties of radiative processes due to different input models.

corrections are treated correctly.

The systematic uncertainties resulting from the subtraction of the radiative processes have been estimated by changing the input models for the elastic, quasi-elastic and inelastic cross sections and comparing the resulting Born cross section with the Born cross section calculated using the models mentioned above. The systematic uncertainties for the elastic, quasi-elastic and inelastic cross sections are listed in the Table 4.4.

4.11 Extraction of R and F_2

In order to calculate R ($R = \sigma_L/\sigma_T$) the Rosenbluth separation technique (1^{st} method) has been used. Eq. (2.12) can be written in the following form

$$\frac{1}{\Gamma} \frac{d^2\sigma}{d\Omega dE'} = \sigma_T + \epsilon \sigma_L . \quad (4.50)$$

Hence, the left hand part linearly depends on ϵ . So, in order to determine σ_T and σ_L and from these R , the cross sections at the same (x, Q^2) but different ϵ are plotted, as shown in Fig. 4.35. After calculating σ_T and σ_L the structure functions R and F_2 can be determined by the following formulas

$$R = \frac{\sigma_L}{\sigma_T} , \quad (4.51)$$

$$F_2 = \frac{\nu K (\sigma_T + \sigma_L)}{4\pi^2 \alpha \left(1 + \frac{Q^2}{4M^2 x^2}\right)} . \quad (4.52)$$

For this experiment nine overlap regions (the same (x, Q^2) , but different ϵ) are available for carrying out a Rosenbluth separation.

Also, there is another possibility to calculate R (2^{nd} , model dependent, method). Using Eq. (2.8) and the formula

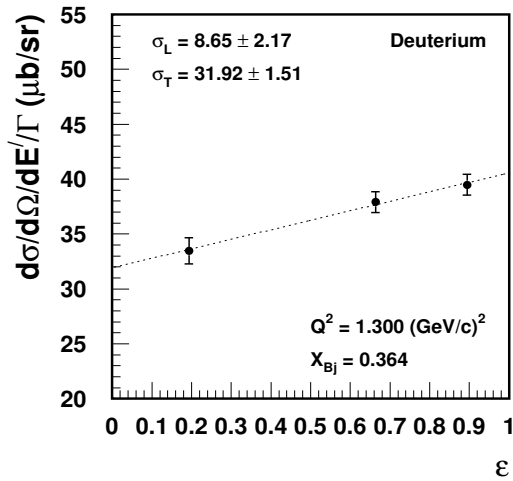


Figure 4.35: Rosenbluth separation technique.

$$F_1(x, Q^2) = \frac{F_2}{2x(R+1)} \left(1 + \frac{4M^2 x^2}{Q^2} \right), \quad (4.53)$$

one can derive

$$\frac{d^2\sigma}{d\Omega dE'} = \sigma_{Mott} \frac{2MxF_2}{Q^2\epsilon} \left(\frac{1+\epsilon R}{1+R} \right). \quad (4.54)$$

By using a model for the structure function $F_2(x, Q^2)$ and the experimental cross section σ^{exp} , R can be computed from Eq. (4.54).

4.12 Iteration procedure

In order to minimize the model dependence during the calculation of the radiative corrections and bin centering corrections the following *iteration* procedure has been used.

1. Born cross sections have been computed, see Sect. 4.8, by using models (as input models) for calculating radiative corrections, see Sect. 4.10 and bin centering corrections, see Sect. 4.9. Using differential Born cross sections the Rosenbluth separation technique, see Sect. 4.11, has been used in order to compute R and F_2 .

2. Since the computed values of F_2 based on the Rosenbluth separation technique are in agreement with the model of F_2 within a few percent, the difference between the measured Born cross section and the model cross section is only due to the difference between the measured values of R and the model R . As the model of F_2 is approximately correct it is allowed to calculate R using the 2nd method of extraction R , see Sect. 4.11.
3. Using the values of R which have been measured by means of the Rosenbluth separation technique and a 2nd method of extraction of R , see Sect. 4.11, a new model of R^{e99118} (output model) has been created.
4. Using the new model for R^{e99118} the steps 1, 2 and 3 have been repeated until the input and output models for R are in agreement within 1 %.

4.13 Systematic Uncertainty

The total systematic uncertainty in the differential cross section is taken as the sum in quadrature of all systematic errors of the quantities that make up the cross section. These uncertainties have been discussed in detail in the present chapter and a summary is given in Table 4.5.

Section	Quantity	Uncertainty	$\delta_\sigma \%$ (RES ¹⁶)	$\delta_\sigma \%$ (DIS)
4.2.4	Beam Energy	0.05 %	0.4 %	0.25 %
4.2.4	Scattered e' Energy	0.06 %	0.1 %	0.025 %
4.2.4	Scattered e' Angle	~ 0.2 mrad	0.5 %	0.3 %
3.2	Target Thickness	Tables 3.2-3.3	Tables 3.2-3.3	Tables 3.2-3.3
4.6	Target Density	0.1 %	0.1 %	0.1 %
4.4.1	Beam Charge	$0.2 \mu\text{A}$	0.8 % (25 μA)	0.8 % (25 μA)
4.4.1	Elect. Dead Time Correction	25 %	0.25 %	0.25 %
4.4.2	Comp. Dead Time Correction	0.2 %	0.2 %	0.2 %
4.5.1	Trigger Efficiency	0.07 %	0.07 %	0.07 %
4.5.2	Tracking Efficiency	0.3 %	0.3 %	0.3 %
4.5.3	Čerenkov Efficiency	0.15 %	0.15 %	0.15 %
4.5.4	Calorimeter Efficiency	0.05 - 0.2 %	0.05 %	0.2 %
4.3.2	Charge Symmetric Background	0.4 %	-	0.4 %
4.7	Acceptance	0.6 %	0.6 %	0.6 %
4.10	Radiative Correction	Sect. 4.10	Sect. 4.10	Sect. 4.10

Table 4.5: Systematic uncertainties in the experimental parameters (column 2 and 3) and the corresponding systematic uncertainties in the differential cross section in the resonance region (column 4) and DIS region (column 5).

The largest uncertainties are at low values of E' due to uncertainties in the radiative corrections. The total systematic uncertainty not including the one from the radiative corrections is 1.3 % - 1.7 % in the DIS region and 1.4 % - 1.8 % in the resonance (RES) region (depending on the target). In the Rosenbluth separation one has to distinguish between correlated (such as target thickness and the possible offset in the charge integration) and uncorrelated uncertainties. The uncorrelated systematic uncertainties amount to about 0.9 - 1.1 % (excluding systematic uncertainties in the radiative corrections). The influence of the uncertainties in the radiative corrections is discussed in detail in the next chapter.

¹⁶For $W^2 > 1.4 \text{ GeV}^2$.

Chapter 5

Results

In this chapter the results of the experiment are presented:

- The comparison of the cross sections of the elastic runs to the results of a Monte-Carlo simulation.
- The final extracted differential Born cross sections after model iteration, see Sect. 4.12, for all targets.
- F_2 and R via the Rosenbluth separation technique and via the model dependent method.
- The ratios σ_D/σ_H , F_2^D/F_2^H , R^D/R^H and F_1^D/F_1^H .
- The ratios σ_A/σ_D , F_2^A/F_2^D , R^A/R^D and F_1^A/F_1^D .

5.1 σ_{exp}/σ_{MC} for ${}^1\text{H}(\text{e}, \text{e})$

Several elastic runs have been taken at different E , θ and E' combinations, which have provided information about the experimental offsets δE , $\delta\theta$ and $\delta E'$, see Sect. 4.2.4.

The elastic data have also been used as an additional test for the accuracy of the experimental yields and the Monte-Carlo simulation (MC). Data for elastic scattering have been taken in nine different kinematic settings, which were modeled in the MC. The ratio of the experimental cross sections to the simulated ones is shown in Fig. 5.1. Over the whole Q^2 range between 0.4 and 3.4 (GeV/c)² the ratio scatters around unity with $\sigma = 2\%$, which is consistent with the estimated total uncertainty in the experimental cross section, see Sect. 4.13, and the uncertainty in the model cross section [90] that has been used in the Monte-Carlo simulation.

The result indicates that all corrections (dead times, efficiencies, radiative corrections) used to calculate experimental cross sections are well understood and that the Monte Carlo program simulates the experimental conditions and acceptances very well.

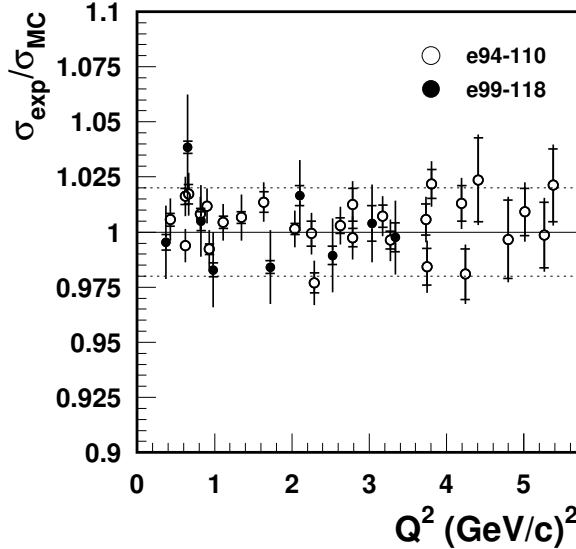


Figure 5.1: Ratios of experimental cross sections and MC for elastic scattering on ${}^1\text{H}$ for two experiments, the present one and the earlier experiment e94-110 [89] at JLAB (TJNAF), which measured values of R for hydrogen in the resonance region. The statistical and total (statistical plus systematical) error bars are shown. The dotted lines indicate the spread (1σ) calculated for the average of all shown data.

5.2 Cross Sections

After calculating the radiative contributions twice, with and without the α^2 term, see Sect. 4.10, the differential Born cross section has been calculated as the average of the cross sections evaluated with and without the α^2 term in the radiative corrections. Half the difference between the two cross sections has been taken as a contribution to the uncertainty in the final Born cross section and has been included in the systematic uncertainties, see Sect. 4.13.

Then, after applying the model iterations described in Sect. 4.12, the final differential Born cross sections have been extracted from the experimental data. The total systematic uncertainty has been obtained by adding the individual ones quadratically (including the error due to the α^2 term). The systematic uncertainty is much larger than the statistical one, so the total uncertainty is nearly equal to the systematic uncertainty.

The final Born cross sections for the hydrogen target for all beam energies and angles, as well as the total systematic uncertainties are shown in Figs. 5.2-5.4. The curves in the figures represent the model for the cross section, which has been calculated via $F_2(\text{ALLM97})$, see Sect. 2.9.1, and R_H^{e99118} , see Sect. 5.4.2.

The strength of the three structures due to the excitation of nucleon resonances strongly

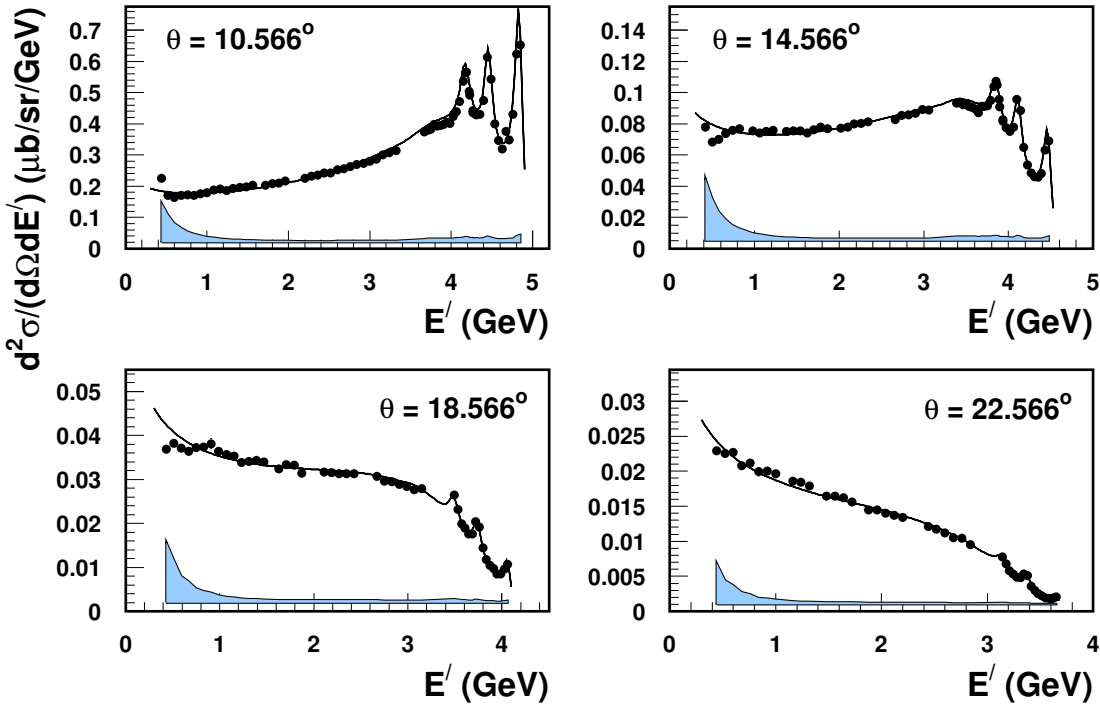


Figure 5.2: Cross sections for hydrogen at 5.648 GeV beam energy and different angles. The statistical error bars are smaller than the symbol size. The error band on the bottom of each plot represents the total systematic uncertainty. The curves represent the cross section model that has been used for the last iteration procedure, see text for details.

decreases as a function of Q^2 . This effect is caused by the strong decrease of the form factor of these resonances with increasing Q^2 , on top of the decrease of the Mott cross section.

The cross section for deuterium behaves similar to the hydrogen cross section apart from the resonance region, where the three resonance structures become wider due to Fermi motion. The total systematic uncertainty for deuterium is smaller than for hydrogen, since the elastic radiative contribution σ_{el} , and therefore its α^2 term, to the experimental cross section is larger for hydrogen. An example of the Born cross sections for deuterium at 5.648 GeV beam energy and different angles is shown in Fig. 5.5.

The final differential Born cross sections for hydrogen and deuterium are at all employed beam energies and scattering angles in agreement with the cross section models within the total systematic uncertainty. It has to be mentioned that the total systematic uncertainty becomes very large at low E' , where the radiative corrections and the uncertainties due to the α^2 term get very large.

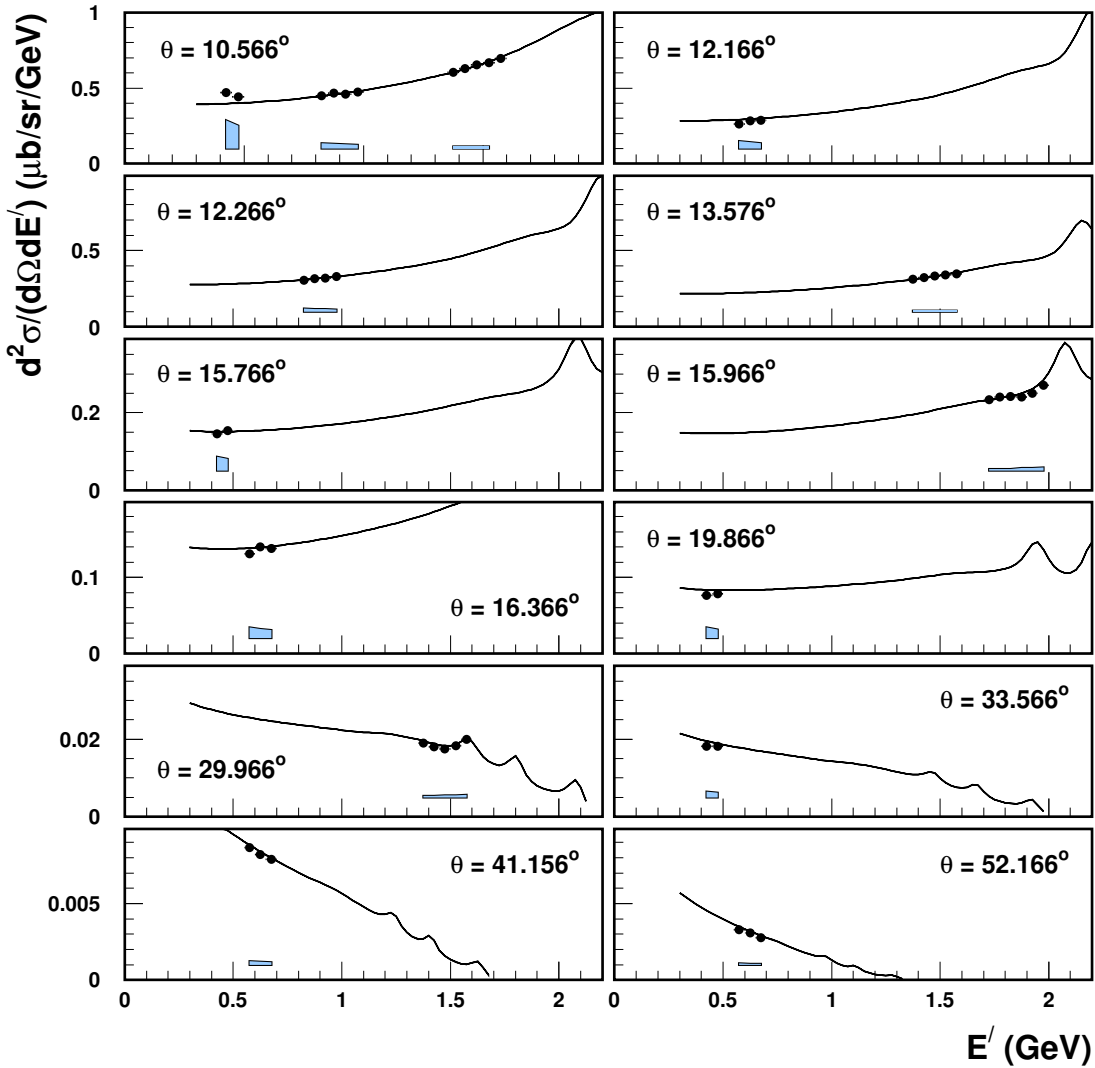


Figure 5.3: As Fig. 5.2, but at 3.419 GeV beam energy.

An example of the Born cross sections for aluminium is shown in Fig. 5.6. The aluminium cross sections agree only with the model at high E' and at high θ . At low and intermediate E' (and low scattering angle θ) the cross sections disagree with the model more than the total systematic uncertainty (including the error due to the α^2 term), which becomes very large at low values of E' . In some cases at low values of E' the aluminium cross section even becomes negative. The curve in Fig. 5.6 represents the cross section model that has been calculated through the parametrizations, see Sect. 2.9.3. An example of the strange behaviour of the

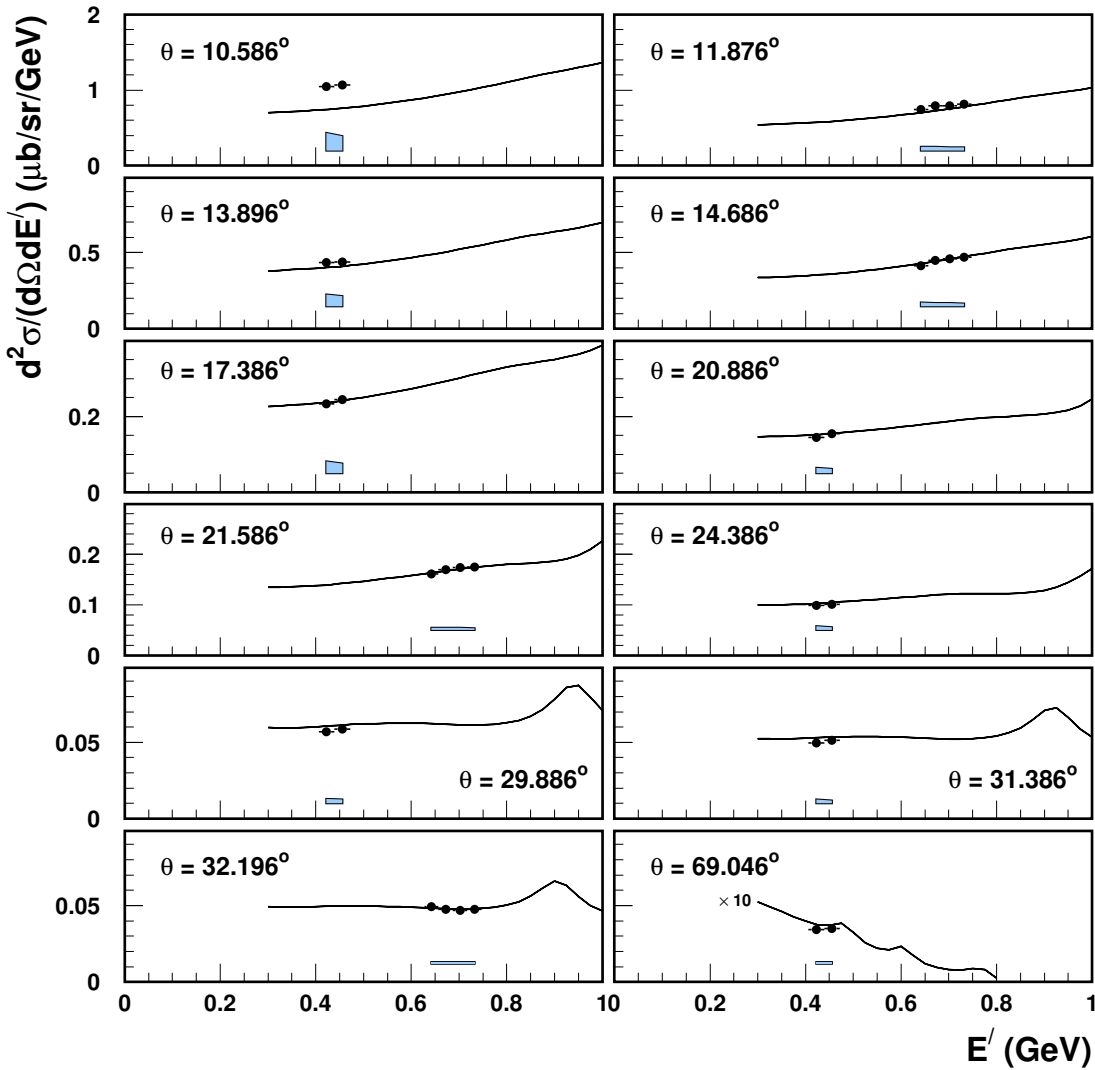


Figure 5.4: As Fig. 5.2, but at 2.301 GeV beam energy.

aluminium cross sections is shown in Fig. 5.7, where the Rosenbluth separation technique has been used: σ_L seems to be negative.

This strange behaviour of the aluminium cross section is still not understood. It looks as if the elastic radiative cross section is calculated too high, but the calculation and the used parametrizations have been checked, and the formalism for calculating the radiative corrections is entirely the same as the one employed for the other complex nuclei.

The cross sections for carbon, copper and gold look very similar at high and intermediate

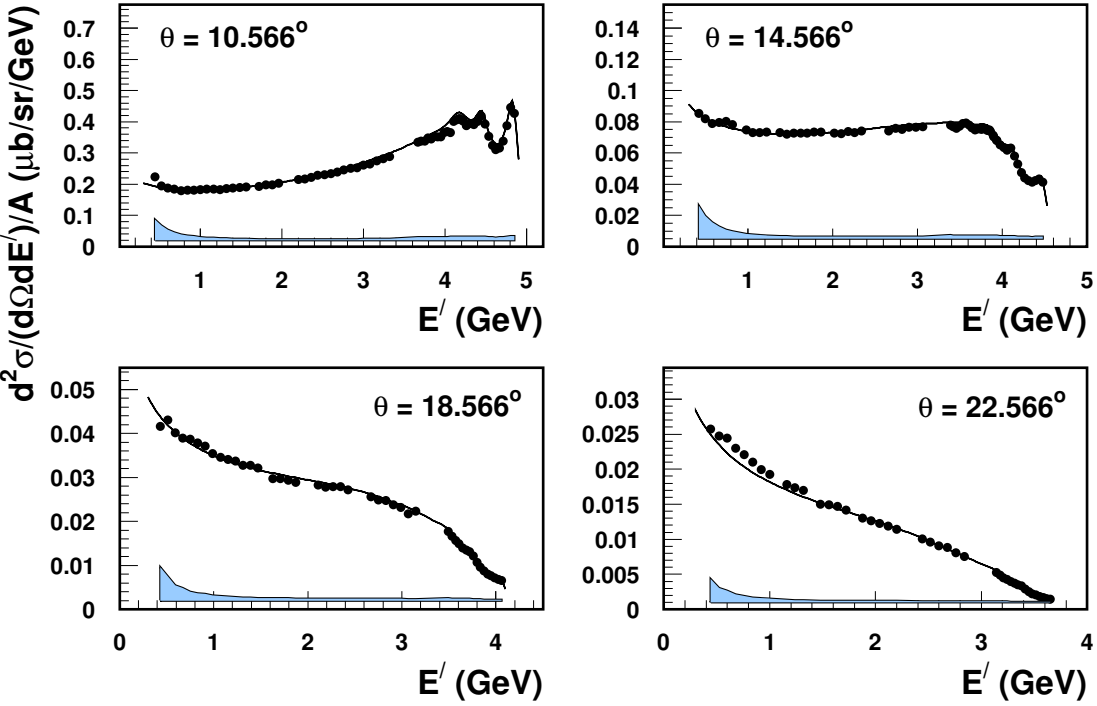


Figure 5.5: Cross sections for deuterium at 5.648 GeV beam energy and different angles. The statistical error bars are smaller than the symbol size. The error band on the bottom of each plot represents the total systematic uncertainty. The curves represent the cross section model that has been used for the last iteration procedure, see text for details.

values of E' . As an example, the final Born cross sections for copper for all beam energies and angles are shown in Figs. 5.8-5.10 (in order to facilitate the comparison the Born cross section is always plotted per nucleon). The curves in the figures represent the cross section model, which has been calculated through the parametrizations, discussed in Sect. 2.9.3, and R_{e99118}^{Cu} , see Sect. 5.6.2. At high and intermediate values of E' the Born cross section is in agreement with the model within the total systematic uncertainty. At low values of E' the cross sections disagree with the model and in some cases the cross section for copper become negative. The cross section for gold at low values of E' looks completely different from the cross section for copper: the cross section for gold increases rapidly as shown in Fig. 5.11. Moreover, at low values of E' ($E' < 1$ GeV), the cross section for gold completely disagrees with the model and this disagreement does not disappear at high angles like it happens for the copper cross sections. Therefore, the data for gold have not been analyzed for low values of E' ($E' < 1$ GeV). The error bar due to the α^2 term becomes very large since the elastic

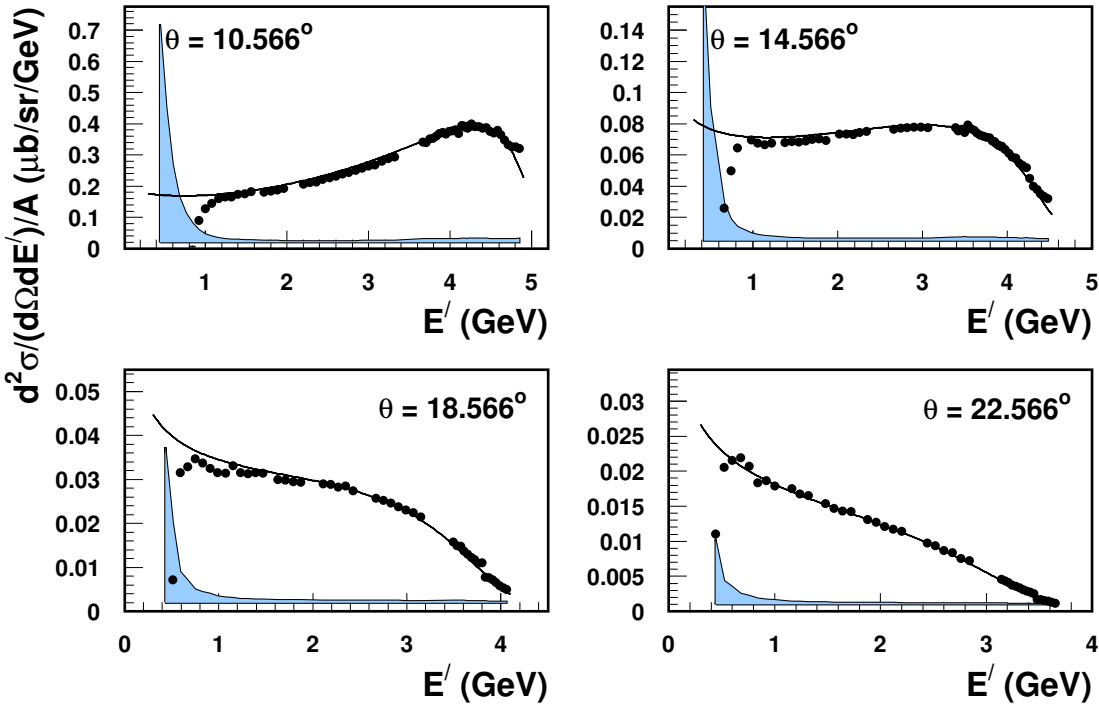


Figure 5.6: Cross sections for aluminium at 5.648 GeV beam energy and different angles. In some cases the cross section at low values of E' becomes negative. The statistical error bars are smaller than the symbol size. The error band on the bottom of each plot represents the total systematic uncertainty. The curves represent the cross section model that has been used for the last iteration procedure, see text for details.

radiative cross section becomes very large.

The strange behaviour of the cross sections observed for all nuclei, though most obvious in the heavier ones at lowest E' , is a puzzle. It can not be explained only by the α^2 term, since there is no value of the α^2 term that will change the behaviour of the Born cross section in such a way that it will behave smoothly. Presumably higher order α terms ($\alpha^3, \alpha^4 \dots$), which are not known, start to be non-negligible at the lowest values of E' . Another possibility is that the disagreement is due to Coulomb corrections in the elastic radiative tail and the Born cross section, which were not taken into account. So unfortunately the uncertainty in the radiative corrections at low values of E' precludes using several data points, depending on the target, and introduces large uncertainties in several points that were kept in the further analysis.

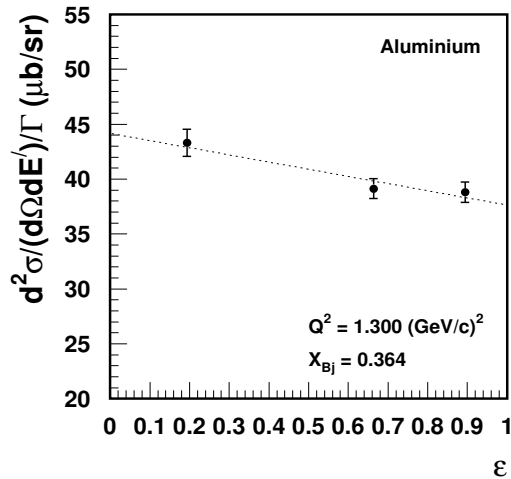


Figure 5.7: An example of the Rosenbluth separation for aluminium, compare with Fig. 4.35.

5.3 Averaging Data and Calculation of the Uncertainty due to the α^2 Term

Since in the following sections often cross sections have been averaged, and uncertainties, especially the one due to the α^2 term, were handled in a specific way, first these points are discussed.

5.3.1 Averaging Data

As has been mentioned in Sect. 4.7 the experimental cross section has been binned into small bins of E' and θ , corresponding to the δ and θ bins used to determine the spectrometer acceptance. By applying the *Bin Centering* correction, see Sect. 4.9, the cross section has been converted to the one at the central scattering angle. In order to average cross section ratios the following procedure has been applied:

The actual average value (for example σ^D/σ^H) has been calculated from the separate data points, where as a weight factor the total uncertainties (experimental uncertainties, uncertainties due to radiative corrections and uncertainty due to the α^2 term) have been used. The statistical uncertainty in the (averaged) ratio has been calculated using the statistical uncertainties from each data point involved in the averaging. The smallest systematical uncertainty of the data points involved in the averaging procedure has been chosen as the systematic uncertainty of the averaged value of (σ^D/σ^H) .

This method has been used for all cases where data have been averaged.

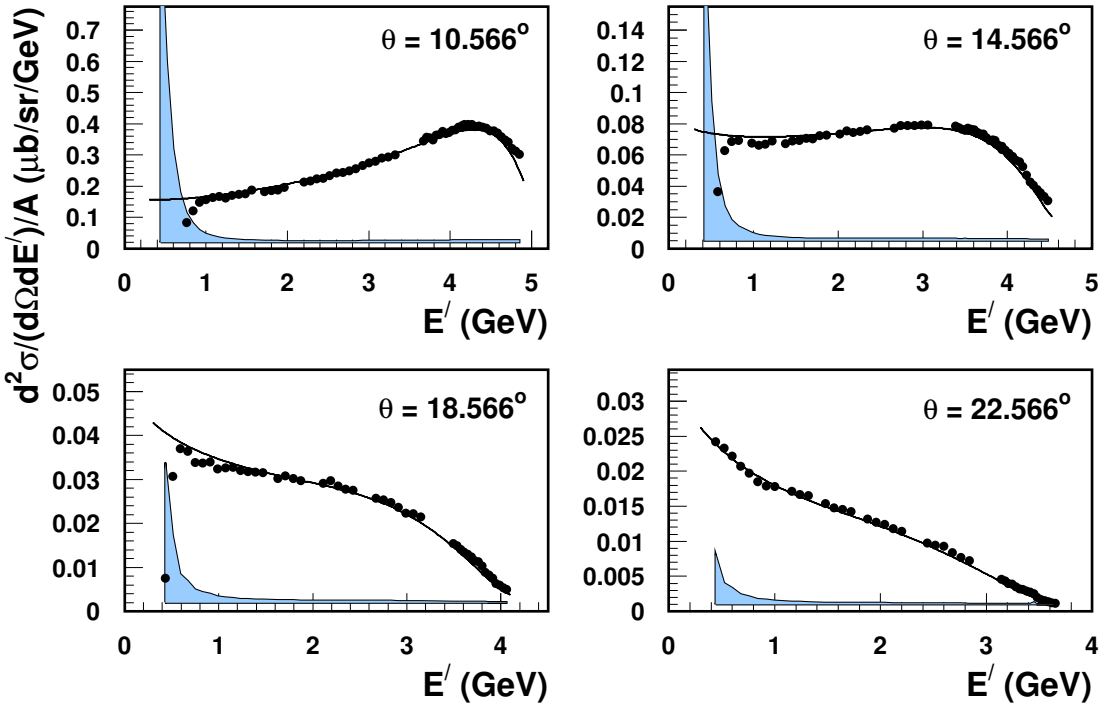


Figure 5.8: Cross sections for copper at 5.648 GeV beam energy. In some cases the cross section at low values of E' becomes negative. The statistical error bars are smaller than the symbol size. The error band on the bottom of each plot represents the total systematic uncertainty. The curves represent the cross section model that has been used for the last iteration procedure, see text for details.

5.3.2 Calculation of the Uncertainty due to the α^2 Term

Since the influence of the α^2 term in the radiative corrections is similar in both cross sections used in the ratio σ^A/σ^D (or σ^D/σ^H), or in the Rosenbluth separation procedure, or in the ratio of the structure functions, *i.e.*, it is a correlated error, the following method has been used:

First, the actual values of the ratio σ^A/σ^D or other physical quantities mentioned above have been calculated from the final differential Born cross sections, which have been extracted from the experimental data. These cross sections have been calculated as the average of the two cross sections calculated with and without the α^2 term in the radiative corrections. The uncertainty due to the α^2 term is at first not included in the uncertainty of the differential Born cross sections, but treated separately in the following way. The values of σ^A/σ^D have been calculated using the differential Born cross sections calculated with and without the α^2

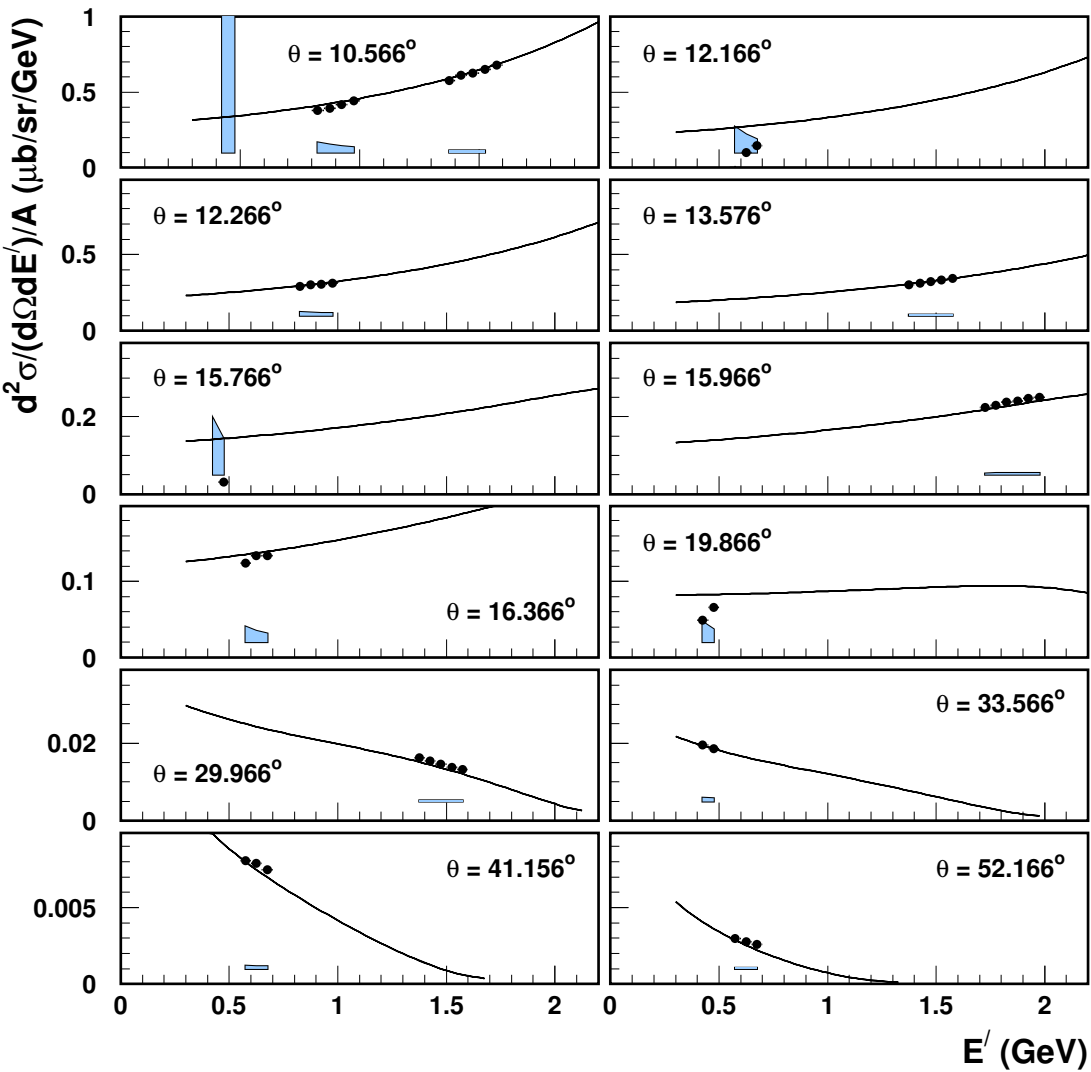


Figure 5.9: As Fig. 5.8, but at 3.419 GeV beam energy. In some cases the data at low E' are off-scale and therefore not visible.

term. The half difference between these results is used as the uncertainty in the ratio due to the α^2 term and then added to the other uncertainties (experimental uncertainties and uncertainties due to radiative corrections without the α^2 term) quadratically.

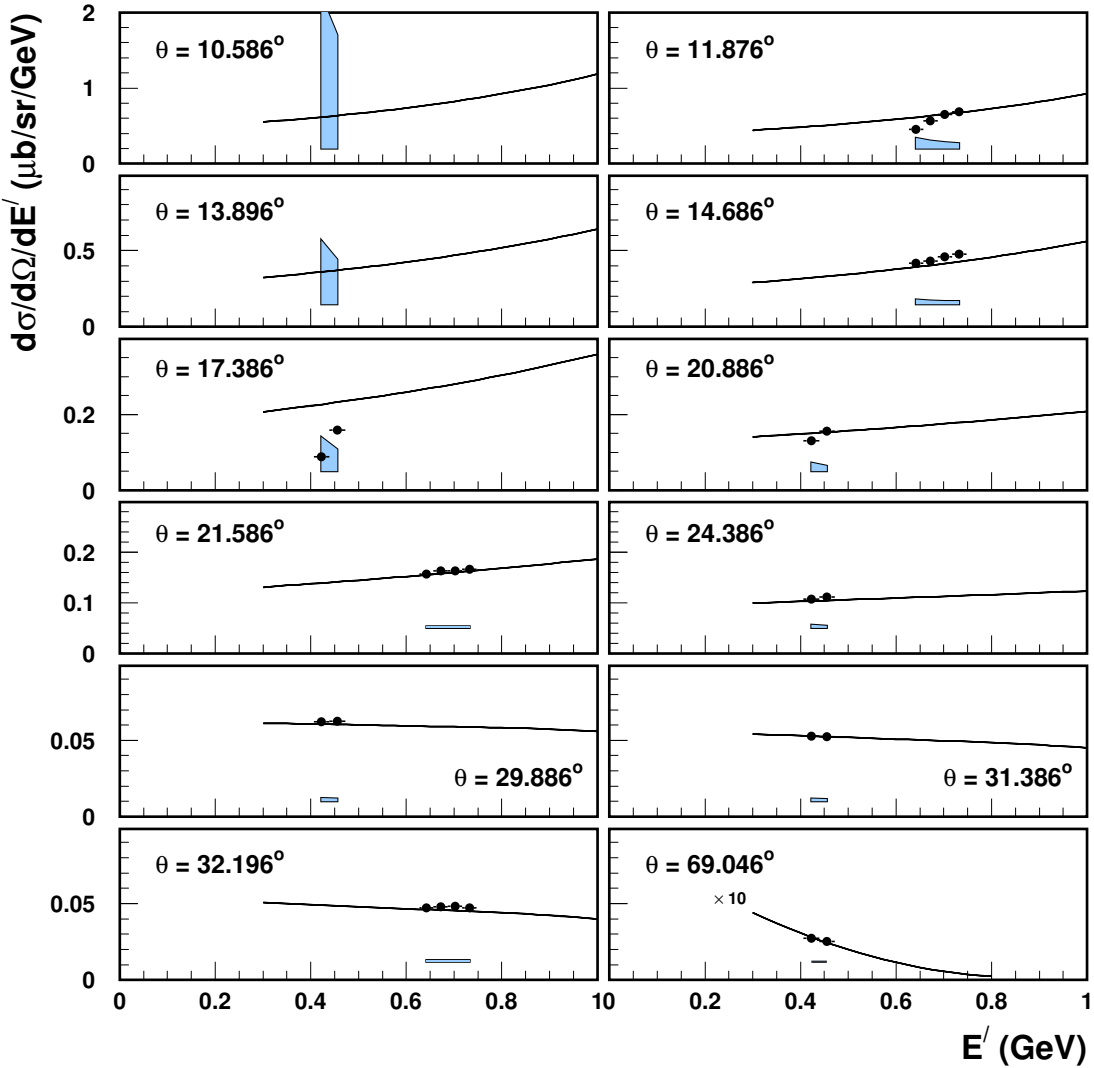


Figure 5.10: As Fig. 5.8, but at 2.301 GeV beam energy. In some cases the data at low E' are off-scale and therefore not visible.

5.4 Results for F_2 , F_1 and R for Hydrogen

In this section the results for hydrogen are presented: the structure functions $F_2(x, Q^2)$, $F_1(x, Q^2)$ and the ratio of the longitudinal and transverse virtual-photon cross sections $R(x, Q^2)$ determined via the Rosenbluth separation method, see Sect. 4.11. Also values are presented for $R(x, Q^2)$ and the structure function $F_2(x, Q^2)$ calculated via the model

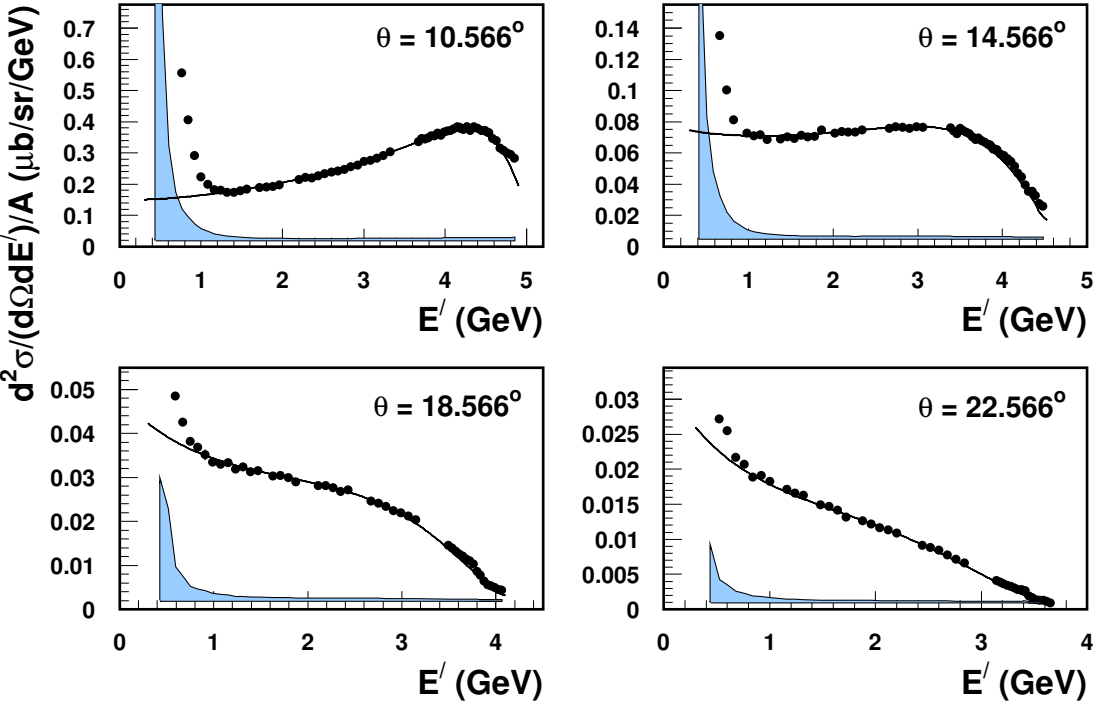


Figure 5.11: Cross sections for gold at 5.648 GeV beam energy and different angles. The statistical error bars are smaller than the symbol size. The error band on the bottom of each plot represents the total systematic uncertainty. In some cases the data at low E' are off-scale and therefore not visible. The curves represent the cross section model that has been used for the last iteration procedure, see text for details.

dependent method, see Eq. (4.52) and Eq. (4.54). All data points (at different E') within a given run (at a certain central E' spectrometer setting) were averaged using the procedure explained in Sect. 5.3.1, so each data point corresponds to one spectrometer setting. The uncertainty due to the α^2 term has been determined in the way explained in Sect. 5.3.2. Since the averaging procedure has been applied for all data points (binned in E') in a certain run, the systematic uncertainties and the uncertainty due to the α^2 term remain mainly the same, and only the statistical uncertainty of the averaged value becomes smaller. The uncertainty due to the α^2 term is shown separately as an error band for the results, where the Rosenbluth separation method has been used.

The numerical values of $F_2(x, Q^2)$, $F_1(x, Q^2)$ and $R(x, Q^2)$ for hydrogen that have been determined via the Rosenbluth separation and the model dependent methods are listed in Appendix A.

5.4.1 Results for F_1 and F_2 from the Rosenbluth Separation Method

In order to calculate $F_2(x, Q^2)$, $F_1(x, Q^2)$ and $R(x, Q^2)$ ($R = \sigma_L/\sigma_T$) knowledge of the longitudinal (σ_L) and transverse (σ_T) virtual-photon cross sections is needed, see Eq. (2.19) and Eq. (2.20). These cross sections can be determined by using the Rosenbluth separation technique, see Sect. 4.11, which requires at least two measurements of the cross section at the same (x, Q^2) , but different ϵ . An example of the Rosenbluth separation technique is shown in Fig. 4.35. Linear extrapolation to $\epsilon = 0$ gives σ_T (or $F_1(x, Q^2)$), and linear extrapolation to $\epsilon = 1$ gives $\sigma_T + \sigma_L$ (or $F_2(x, Q^2)$). Thus, the value of $F_2(x, Q^2)$ mainly depends on the cross section measured at higher ϵ (high E and E') and therefore, since the radiative corrections are smaller at high E' , the uncertainty in $F_2(x, Q^2)$ is smaller compared to the one in $F_1(x, Q^2)$.

The $F_2^H(x, Q^2)$ and $F_1^H(x, Q^2)$ structure functions for hydrogen are shown in Figs. 5.12-5.13 for nine different (x, Q^2) regions where the Rosenbluth separation has been performed. The error bars represent the combined statistical and systematic uncertainties without the one due to the α^2 term in the radiative corrections. The uncertainty due to the α^2 term is shown separately as an error band. The results for $F_2^H(x, Q^2)$ have been compared with the parametrization of the structure function $F_2(x, Q^2)^{Model}$, see Sect. 2.9.1 and the results for $F_1^H(x, Q^2)$ have been compared with a model $F_1(x, Q^2)^{Model}$ that has been calculated through the parametrizations of $F_2(x, Q^2)^{Model}$ and R_H^{e99118} , see Sect. 5.4.2. The calculated value of the structure functions $F_2^H(x, Q^2)$ and $F_1^H(x, Q^2)$ via the Rosenbluth separation technique are in a good agreement with the parametrizations for all Q^2 regions: on average within 4.2 % with a maximum deviation of 7.4 % for F_1 , and within 0.6 % with a maximum deviation of 2.8 % for F_2 .

5.4.2 R for Hydrogen

As has been mentioned above, the Rosenbluth separation technique gives access to the longitudinal (σ_L) and transverse (σ_T) virtual-photon cross sections. Therefore, $R(x, Q^2)$, which is the ratio of σ_L and σ_T , can be determined. The longitudinal cross section σ_L , and hence also R , has a relatively large error bar since it results from the difference of two (or more) cross sections used in the Rosenbluth separation technique. The values for R determined in this way are shown as the squares in Fig. 5.14.

As has been mentioned in Sect. 4.11, apart from the Rosenbluth separation method there is another possibility to calculate $R(x, Q^2)$, by using the final differential Born cross section and a model for the structure function $F_2^{Model}(x, Q^2)$ (model dependent method):

$$R(x, Q^2) = \frac{(\sigma_{exp} Q^2 \epsilon) - (2MxF_2 \sigma_{Mott})}{(2MxF_2 \epsilon \sigma_{Mott}) - (\sigma_{exp} Q^2 \epsilon)} . \quad (5.1)$$

Since the values of $F_2(x, Q^2)$ from the Rosenbluth separation, see Sect. 5.4.1, are in good agreement with the ALLM97 prediction $F_2^{Model}(x, Q^2)$, this parametrization has been used for the calculation of the R via the model dependent method. The difference between

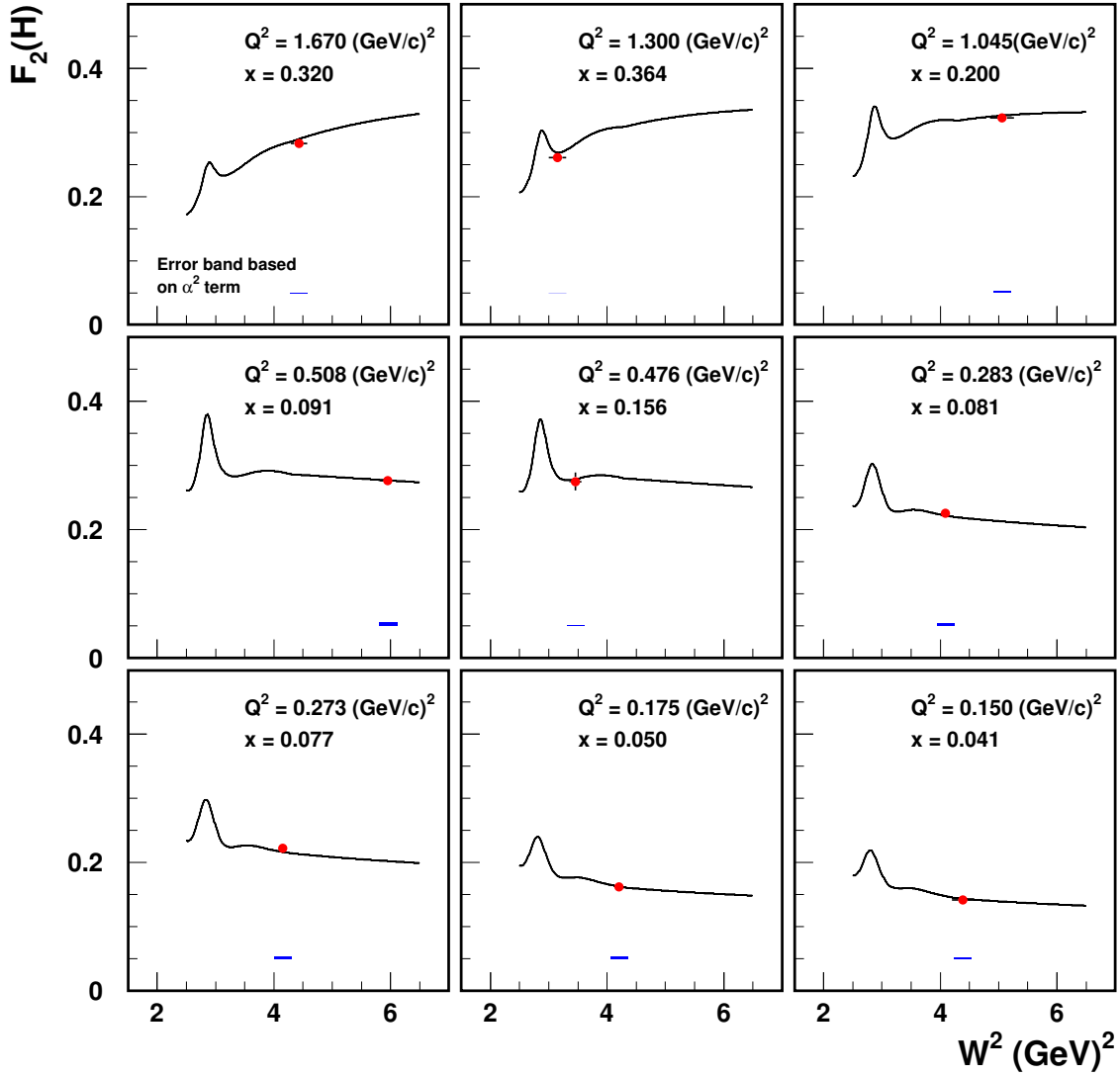


Figure 5.12: Values of $F_2^H(x, Q^2)$ for hydrogen from the present experiment determined through the Rosenbluth separation technique. The error bars represent the statistical and the systematic uncertainties without the one due to the α^2 term, which is shown separately as the error band, see text for details. The curve on each plot represents the parametrization of F_2^H (ALLM97), see Sect. 2.9.1.

$F_2^{Model}(x, Q^2)$ and the measured $F_2(x, Q^2)$ of on average 2 % has been included in the systematic uncertainties of $R(x, Q^2)$ that has been calculated.

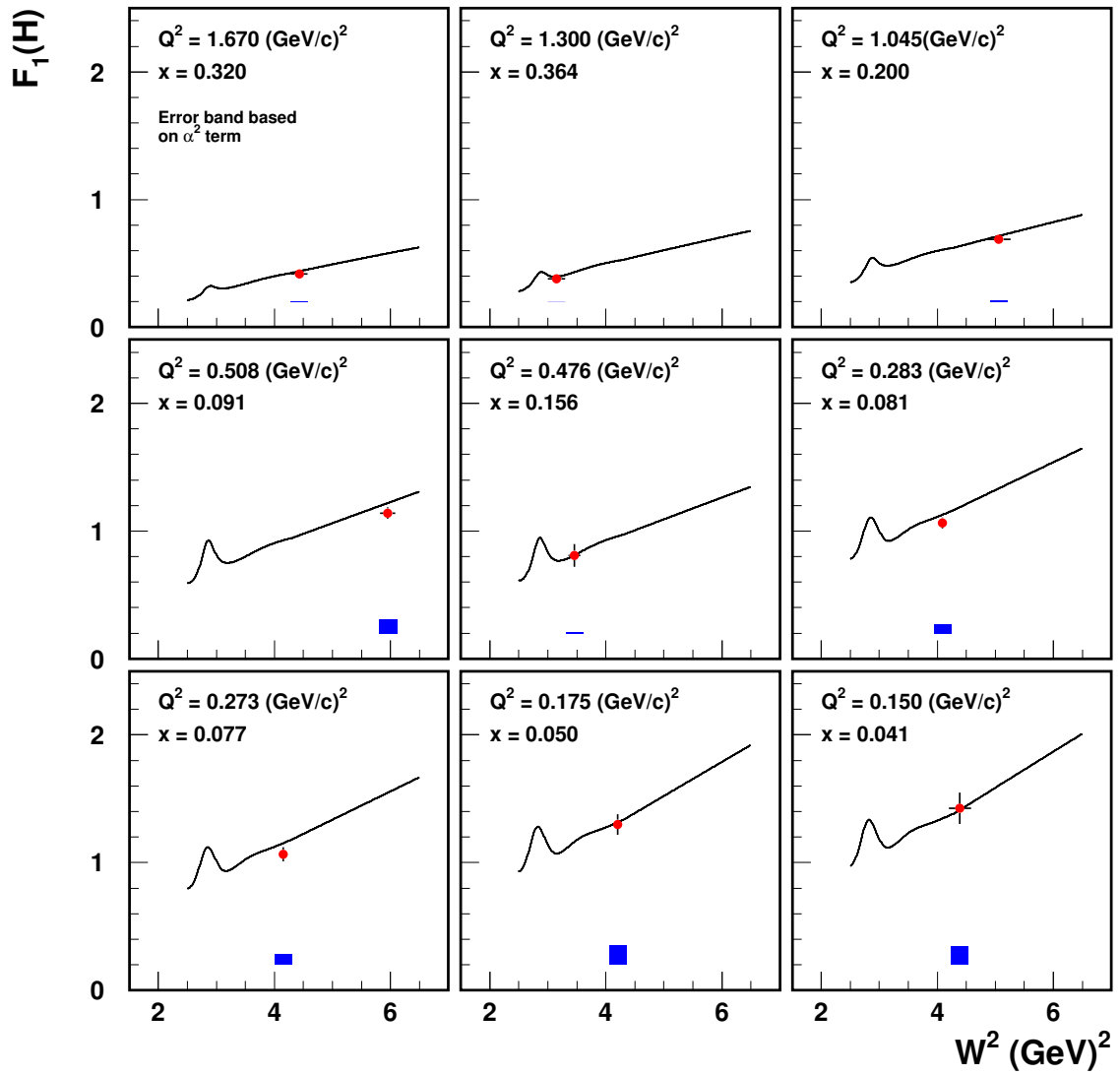


Figure 5.13: Values of $F_1^H(x, Q^2)$ for hydrogen from the present experiment determined through the Rosenbluth separation technique. The error bars represent the statistical and the systematic uncertainties without the one due to the α^2 term, which is shown separately as the error band, see text for details. The curve on each plot represents a model, which has been calculated through the parametrization of F_2^H (ALLM97), see Sect. 2.9.1 and the parametrization of R_{e99118}^H , see Sect. 5.4.2.

The values of $R(x, Q^2)$ for hydrogen from this method are also shown in Fig. 5.14, and compared to the results of previous measurements, SLAC [9], JLAB [89], EMC [100], NMC [101] and BCDMS [103], for different x values. The inner error bars represent the combined statistical and systematic uncertainties without the one due to α^2 term in the radiative corrections. The total error bars represent the total uncertainties including the uncertainty due to the α^2 term, which has been included quadratically. The results of all experiments, including the present one, are in mutual agreement within the (large) error bars.

As was mentioned in Sect. 2.6 the ratio R should approach zero as Q^2 goes to zero. According to the results of the present experiment this behaviour is not observed. Only at very low x there is a hint that R goes to zero, see Fig. 5.14. This means that the transition to zero occurs below a value of Q^2 of about 0.2 - 0.3 (GeV/c)².

Since, due to the large error bars, it is impossible to parametrize the values of $R(x, Q^2)$ from the present experiment as a function of both x and Q^2 , the following method has been used in order to create a parametrization for hydrogen that is valid for low values of Q^2 ($Q^2 < 1$ (GeV/c)²) and at the same time works for higher values of Q^2 ($Q^2 > 1$ (GeV/c)²).

First, R_H^H has been parametrized as a function of Q^2 only, and both the results from the Rosenbluth separation technique and the model dependent method have been used. The parametrization function has been chosen in such a way that it satisfies the condition that R must vanish at $Q^2 \rightarrow 0$:

$$R_H(Q^2) = A \left(1 - e^{-bQ^2} \right). \quad (5.2)$$

The value of b was found to be 9.212 (GeV/c)⁻². Since the parametrization R_{1990} , see Sect. 2.9.4, is based on measurements at relatively high Q^2 values ($Q^2 > 1$ (GeV/c)²), $R_H(Q^2)$ and $R_{1990}(x, Q^2)$ were connected at $Q^2 = 2$ (GeV/c)² by requiring (after b was determined) that $A(x) = R_{1990}(x, Q^2 = 2$ (GeV/c)²).

This parametrization ($R_{e99118}^H(x, Q^2)$), which uses $R_H(x, Q^2) = A(x)(1 - e^{-bQ^2})$ for $Q^2 < 2$ (GeV/c)², and $R_{1990}(x, Q^2)$ for $Q^2 > 2$ (GeV/c)² is shown in Fig. 5.14 as a function of Q^2 for different x bins.

This model R_{e99118}^H has been used in the last iteration to determine the radiative corrections, see Sect. 4.12.

5.4.3 Results for F_2 from a Model Dependent Method

Since a new parametrization of R ($R_{e99118}^H(x, Q^2)$) is available now it is possible to turn the method around, see Eq. (5.1), and determine F_2 (model dependently) for all x and Q^2 where the measured cross sections from the present experiment are available. Thus the structure function $F_2(x, Q^2)$ is calculated through the knowledge of the final differential Born cross section and the model of R^{model} via

$$F_2(x, Q^2) = \sigma \left(\frac{Q^2 \epsilon}{2 M x \sigma_{Mott}} \right) \left(\frac{1 + R^{model}}{1 + \epsilon R^{model}} \right). \quad (5.3)$$

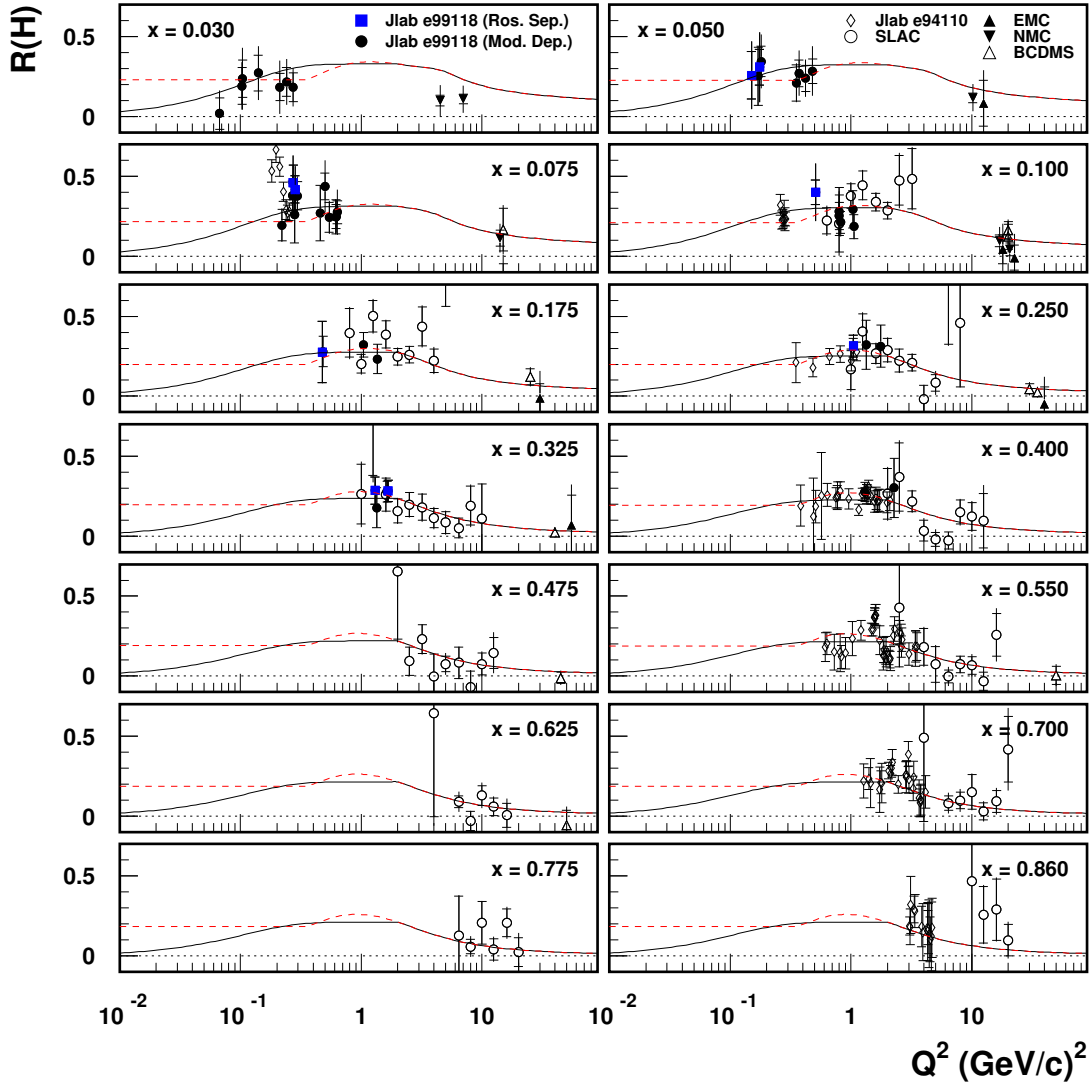


Figure 5.14: Comparison of the values of $R(x, Q^2)$ for hydrogen from the present experiment to the results of other experiments. The data points from the present experiment that have large error bars (> 0.2) have not been included in the figure. Data are shown from SLAC [9], JLAB [89], EMC [100], NMC [101] and BCDMS [103]. The solid curve represents the parametrization $R_{e99118}^H(x, Q^2)$ discussed in this section and the dashed curve represents the parametrization $R^{1990}(x, Q^2)$ that has been kept constant for $Q^2 < 0.35$ (GeV/c) 2 , see Sect. 2.9.4.

For R^{model} the parametrization $R_{e99118}^H(x, Q^2)$, which uses all available data, has been used, see the previous section. The uncertainty of the parametrization of $R_{e99118}^H(x, Q^2)$, which is about 0.075, has been included in the calculation of the uncertainty of the structure function. Values of $F_2(x, Q^2)$ for hydrogen determined in this way are shown for different x bins as a function of Q^2 in Fig. 5.15 together with the Rosenbluth results. Each point in the figure corresponds to one spectrometer setting. The total uncertainty, including the one due to the α^2 term, is shown. The curves on the figures represent the parametrization *ALLM97* of the structure function that has been discussed in Sect. 2.9.1. The structure function $F_2(x, Q^2)$ for hydrogen deduced from the present experiment has been compared with the structure function determined at SLAC [9]. The resulting structure functions deduced via the Rosenbluth separation method and via the model dependent method are in good agreement with the data from SLAC and with the parametrization of the structure function within the error bars even at very low Q^2 . In most cases the deviations of F_2 data from the model are less than 3 % and consistent within the error bars. It has to be mentioned that the large deviations come from the data points that have large systematic uncertainties. This conclusion is not self-evident since the parametrization of F_2 (*ALLM97*) for hydrogen is based on data that have been taken at much higher values of Q^2 (plus data at the photon point), see Fig. 2.12.

5.5 Results for F_2 , F_1 and R for Deuterium

In this section the results for deuterium are presented: the structure functions $F_2(x, Q^2)$ and $F_1(x, Q^2)$, and the ratio of the longitudinal and transverse virtual-photon cross sections $R(x, Q^2)$ determined via the Rosenbluth separation method, see Sect. 4.11. Also values are presented for $R(x, Q^2)$ and for the structure function $F_2(x, Q^2)$ calculated via the model dependent method, see Eq. (4.52) and Eq. (4.54). All data points for deuterium have been averaged per run using the procedure explained in Sect. 5.3.1, in the same way as it has been done for the hydrogen, so each data point corresponds to one spectrometer setting. The uncertainty due to the α^2 term has been determined in the way explained in Sect. 5.3.2.

The numerical values of $F_2(x, Q^2)$, $F_1(x, Q^2)$ and $R(x, Q^2)$ for deuterium that have been determined via the Rosenbluth separation and the model dependent methods are listed in Appendix A.

5.5.1 Results for F_1 and F_2 from the Rosenbluth Separation Method

The $F_2^D(x, Q^2)$ and $F_1^D(x, Q^2)$ structure functions for deuterium are shown in Figs. 5.16-5.17. The error bars represent the combined statistical and systematic uncertainties without the one due to the α^2 term in the radiative corrections. The uncertainty due to the α^2 term is shown separately as an error band. The results for $F_2^D(x, Q^2)$ have been compared with the parametrization of the structure function $F_2(x, Q^2)^{Model}$, see Sect. 2.9.2 and the results for $F_1^D(x, Q^2)$ have been compared with a model $F_1(x, Q^2)^{Model}$ that has been calculated through the parametrizations of $F_2(x, Q^2)^{Model}$ and R_{e99118}^D , see Sect. 5.5.2. The values of the structure functions $F_2^D(x, Q^2)$ and $F_1^D(x, Q^2)$ determined via the Rosenbluth separation

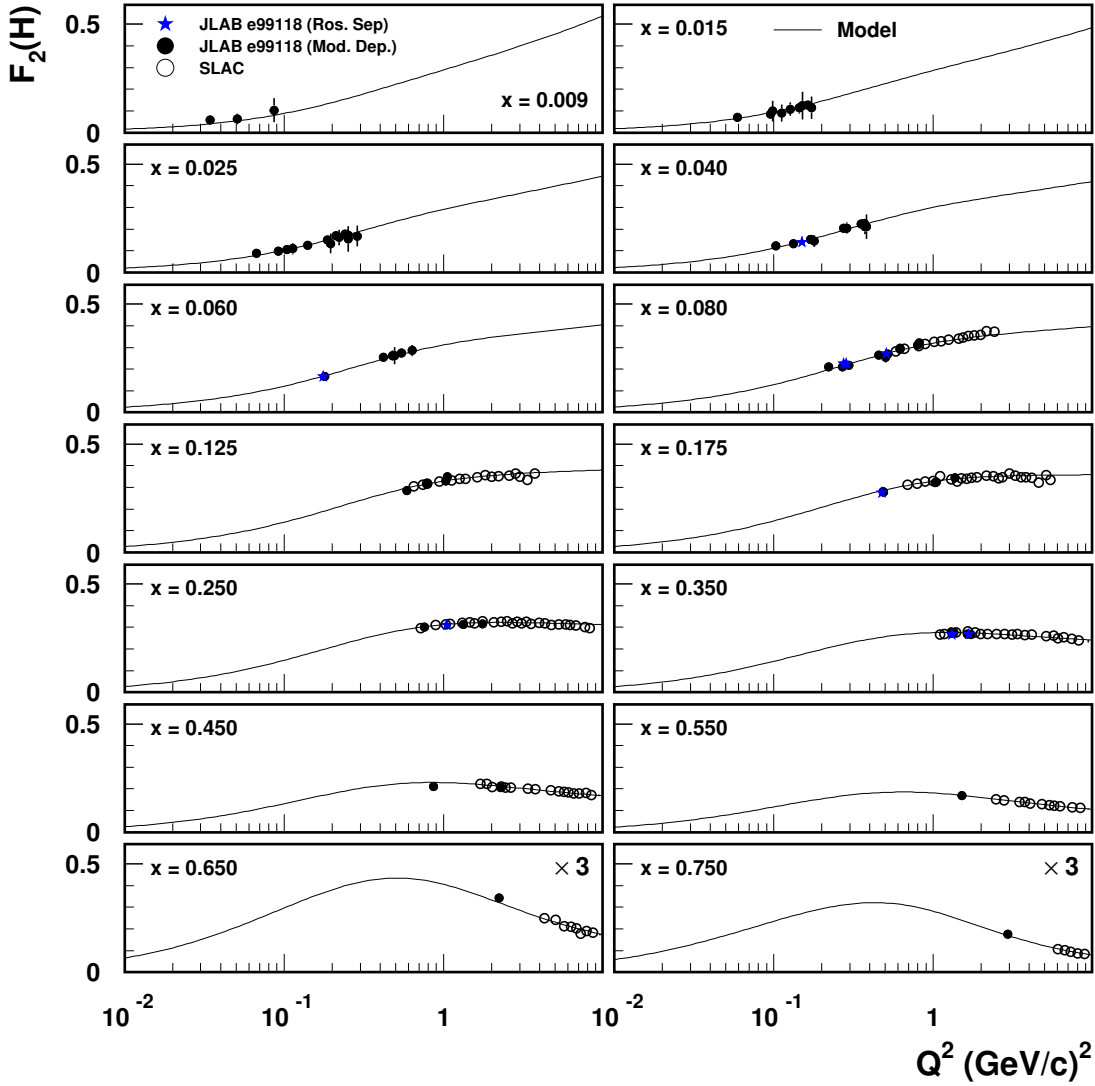


Figure 5.15: Values of $F_2(x, Q^2)$ for hydrogen determined via the Rosenbluth separation method (stars) and by using $R_{e99118}^H(x, Q^2)$ (closed circles). The total error bar is shown, including the one due to α^2 that has been added quadratically. The data from SLAC [9] are also shown (open circles). The curve represents the parametrization (ALLM97) of the structure function that has been discussed in Sect. 2.9.

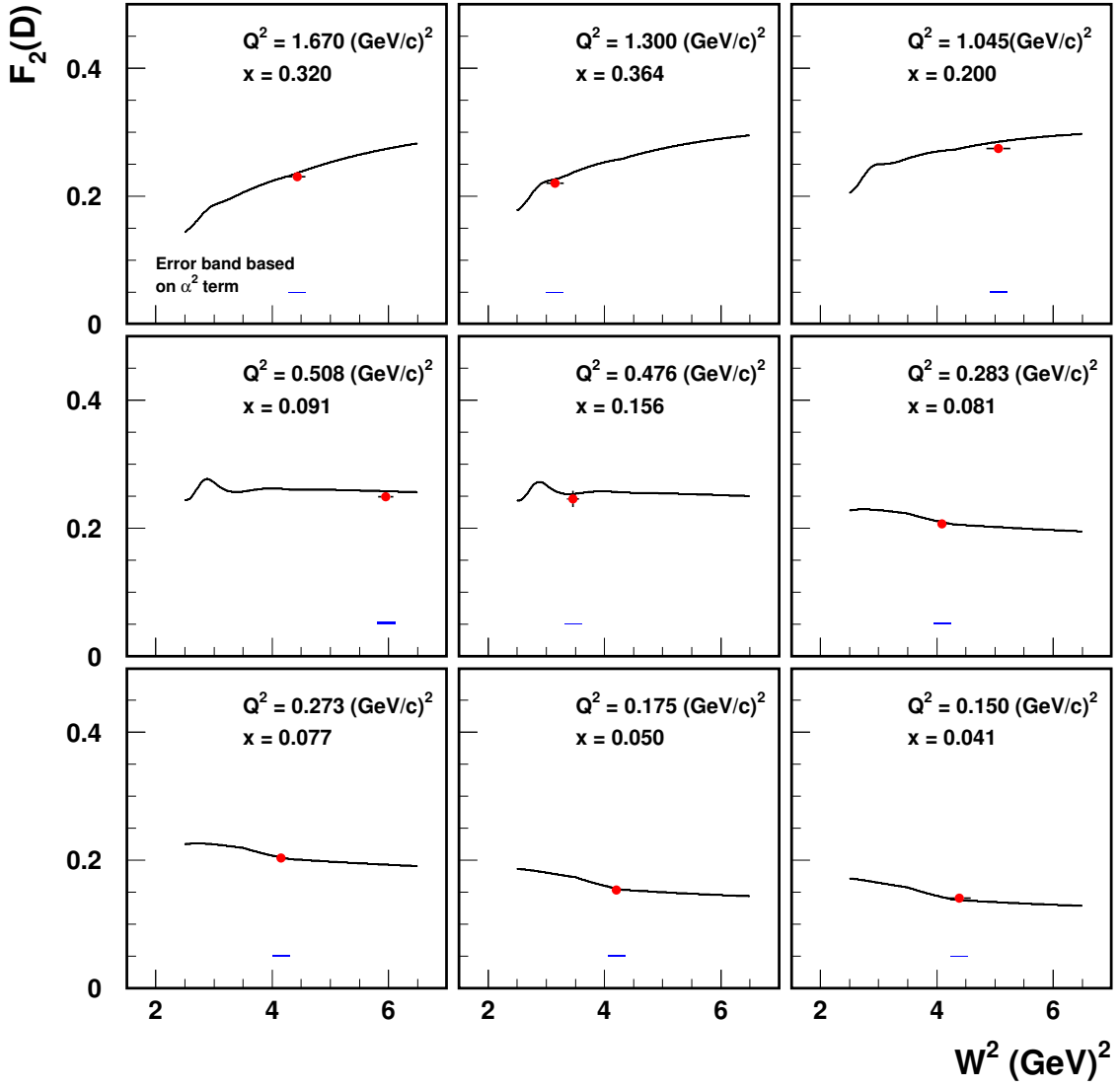


Figure 5.16: Values of $F_2^D(x, Q^2)$ for deuterium from the present experiment determined through the Rosenbluth separation technique. The error bars represent the statistical and the systematic uncertainties without the one due to the α^2 term, which is shown separately as the error band, see text for details. The curve on each plot represents the parametrization of F_2^D , see Sect. 2.9.2.

technique are in good agreement with the parametrizations for all Q^2 regions: on average within 1.6 % with a maximum deviation of 10.2 % for F_1 , and within 1.5 % with a maximum

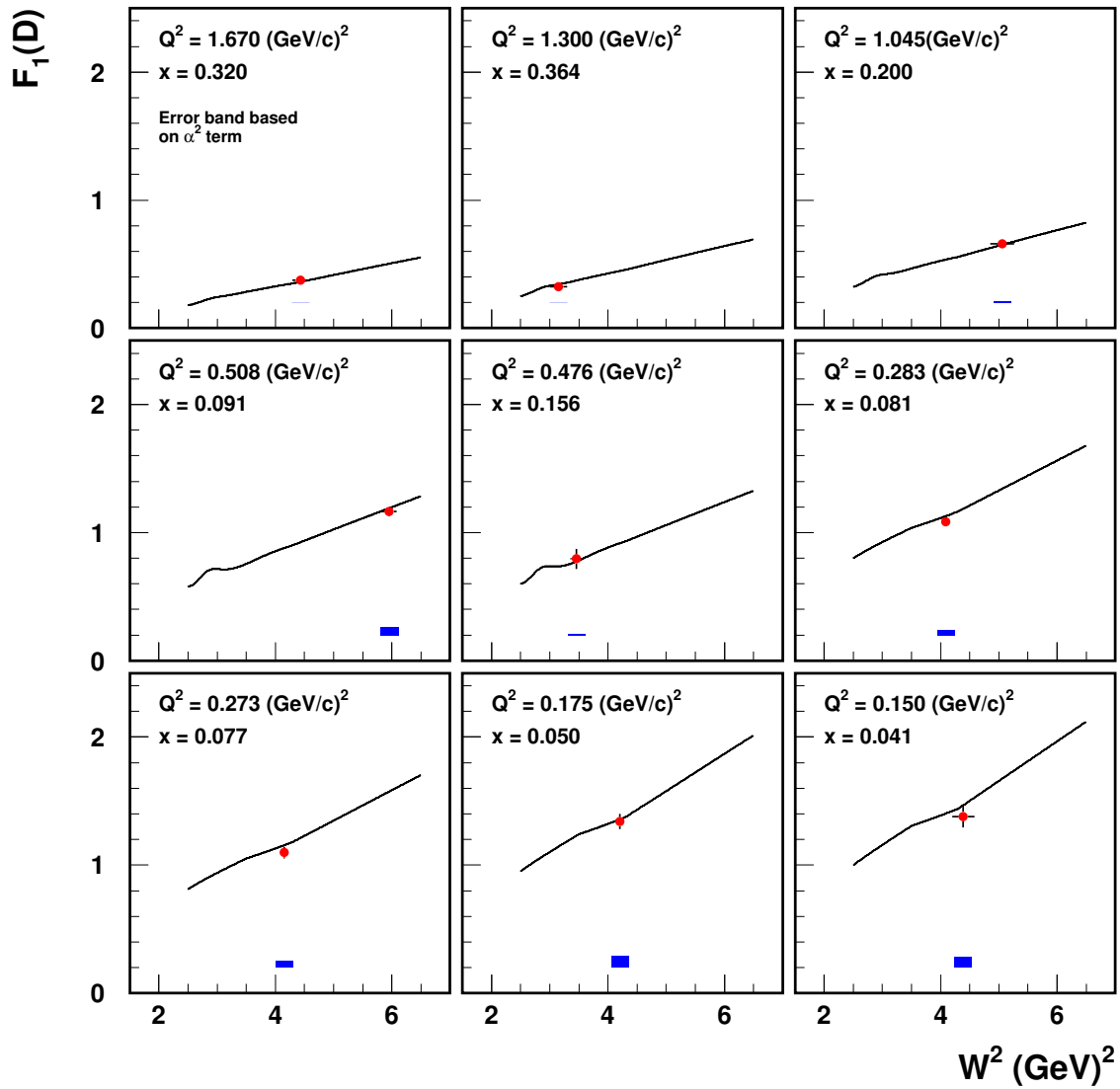


Figure 5.17: Values of $F_1^D(x, Q^2)$ for deuterium from the present experiment determined through the Rosenbluth separation technique. The error bars represent the statistical and the systematic uncertainties without the one due to the α^2 term, which is shown separately as the error band, see text for details. The curve on each plot represents a model, which has been calculated through the parametrization of F_2^D , see Sect. 2.9.2 and the parametrization of R_{e99118}^D , see Sect. 5.5.2

deviation of 3.5 % for F_2 .

5.5.2 R for Deuterium

The values for $R(x, Q^2)$ determined via the Rosenbluth separation technique are shown in Fig. 5.18.

Since the values of $F_2(x, Q^2)$ from the Rosenbluth separation, see Sect. 5.5.1, are in good agreement with $F_2^{Model}(x, Q^2)$, R can also be calculated via the model dependent method, see Sect. 5.4.2. The average difference between $F_2^{Model}(x, Q^2)$ and the measured $F_2(x, Q^2)$ has been included in the systematic uncertainties of $R(x, Q^2)$.

The values of $R(x, Q^2)$ for deuterium from the present experiment, determined by both the Rosenbluth and the model dependent method, are shown in Fig. 5.18, and compared to the results of previous measurements, SLAC [9] and BCDMS [103], for different x values. The inner error bars represent the combined statistical and systematic uncertainties without the one due to the α^2 term in the radiative corrections. The total error bars represent the total uncertainties including the uncertainty due to the α^2 term, which has been included quadratically. The results from all experiments, including the present one, are globally in agreement within the (large) error bars.

Since, due to the large error bars, it is impossible to parametrize the values of $R(x, Q^2)$ from the present experiment as a function of both x and Q^2 , the following method has been used in order to create a parametrization for deuterium that is valid for low values of Q^2 ($Q^2 < 1$ (GeV/c) 2) and at the same time works for higher values of Q^2 ($Q^2 > 1$ (GeV/c) 2).

First, R_D has been parametrized as a function of Q^2 only, using the same parametrization function as for hydrogen, see Eq. (5.2), and both the results from the Rosenbluth separation technique and the model dependent method have been used. The value of b was found to be 8.045 (GeV/c) $^{-2}$.

Since the parametrization R_{1990} , see Sect. 2.9.4, is based on measurements at relatively high Q^2 values ($Q^2 > 1$ (GeV/c) 2), $R_D(Q^2)$ and $R_{1990}(x, Q^2)$ were connected to each other, but in a different way than for hydrogen, see Sect. 5.5.2, because the deuterium data points are lower than the parametrization R_{1990} . Therefore, the connection point (Q_{conn}^2) between $R_D(Q^2)$ and $R_{1990}(x, Q^2)$ has not been taken constant like in the case of hydrogen, but was taken x -dependent in such a way that the overall description was optimal:

$$Q_{conn}^2(x) = \left(2 - \ln \left(\frac{x}{0.3} \right) \right) / 0.693 \text{ (GeV/c)}^2 . \quad (5.4)$$

The final parametrization $R_{e99118}^D(x, Q^2)$, which uses $R_D(x, Q^2) = A(x)(1 - e^{-bQ^2})$ and $R_{1990}(x, Q^2)$ depending on the connection point, is shown in Fig. 5.18 as a function of Q^2 for different x bins.

This model R_{e99118}^D has been used in the last iteration to determine the radiative corrections, see Sect. 4.12.

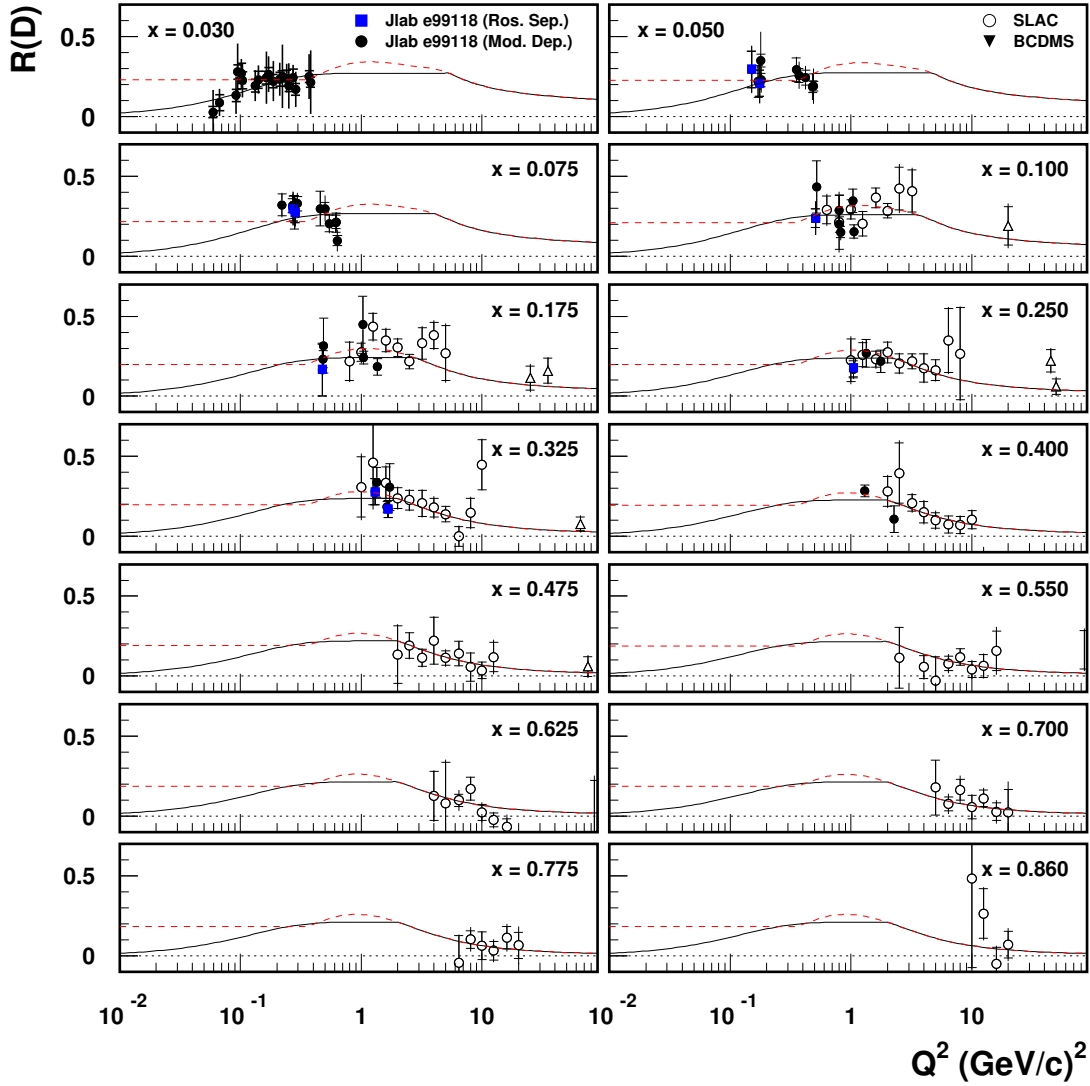


Figure 5.18: Comparison of the values of $R(x, Q^2)$ for deuterium from the present experiment to the results of other experiments. The data points from the present experiment that have large error bars (> 0.2) have not been included in the figure. Data are shown from SLAC [9] and BCDMS [103]. The solid curve represents the parametrization $R_{e99118}^D(x, Q^2)$ discussed in this section and the dashed curve represents the parametrization $R_{1990}(x, Q^2)$ kept constant for $Q^2 < 0.35$ $(\text{GeV}/c)^2$, see Sect. 2.9.4.

5.5.3 Results for F_2 from a Model Dependent Method

Values of $F_2(x, Q^2)$ for deuterium determined with the model dependent method, see Sect. 5.4.3, using R_{e99118}^D are shown for different x bins as a function of Q^2 in Fig. 5.19 together with the Rosenbluth results. Each point in the figure corresponds to one spectrometer setting. The total uncertainty, including the one due to the α^2 term, is shown. The curves on the figures represent the parametrization of the structure function that has been discussed in Sect. 2.9.2. The calculated structure function $F_2(x, Q^2)$ for deuterium from the present experiment has been compared with the structure function determined at SLAC [9]. The resulting structure functions calculated via Rosenbluth separation method and via the model dependent method for deuterium are in a good agreement with the data from SLAC and with the parametrization of the structure functions within the error bars even at very low Q^2 . In most cases the deviations of F_2 data from the model are less than 3 % and consistent within the error bars. It has to be mentioned that the large deviations come from the data points that have large systematic uncertainties.

5.6 Results for F_2 , F_1 and R for Carbon, Copper and Gold

In this section the results for carbon, copper and gold are presented: the structure functions $F_2(x, Q^2)$, $F_1(x, Q^2)$ and the ratio of the longitudinal and transverse virtual-photon cross sections $R(x, Q^2)$ determined via the Rosenbluth separation method, see Sect. 4.11. Also values are presented for $R(x, Q^2)$ and for the structure function $F_2(x, Q^2)$ calculated via the model dependent method, see Eq. (4.52) and Eq. (4.54). The data points have been averaged using the procedure explained in Sect. 5.3.1, in the way as it has been done for hydrogen. The uncertainty due to the α^2 term has been determined in the way explained in Sect. 5.3.2.

5.6.1 Results for F_1 and F_2 from the Rosenbluth Separation Method for Carbon, Copper and Gold

The $F_2(x, Q^2)$ and $F_1(x, Q^2)$ structure functions for carbon, copper and gold are shown in Fig. 5.20-5.23. Unfortunately, due to the limited beam time, less carbon data have been collected than for the other targets. As a result, only one region (x, Q^2) was available for carbon for the Rosenbluth separation. For copper all nine regions (x, Q^2) were available and for gold only cross sections at $E' > 1$ GeV have been used for the Rosenbluth separation, see Sect. 5.2, so only one region (x, Q^2) for gold was available for the Rosenbluth separation.

The results for $F_2^A(x, Q^2)$, where $A = C, Cu, Au$, have been compared with the parametrization of the structure function $F_2(x, Q^2)^{Model}$, see Sect. 2.9.3, and the results for $F_1(x, Q^2)$ have been compared with a model $F_1(x, Q^2)^{Model}$ that has been calculated through the parametrizations of $F_2(x, Q^2)^{Model}$ and R_{e99118}^A , see Sect. 5.6.2. The parametrizations are in good agreement with the values of the structure functions $F_2^A(x, Q^2)$ and $F_1^A(x, Q^2)$ that have been calculated via the Rosenbluth separation technique: within 3.2 % for F_1 , and 4.3 % for F_2 for carbon: within 8.4 % for F_1 , and 0.3 % for F_2 for copper: and within 13.3 % for F_1 , and 0.7 % for F_2 for gold.

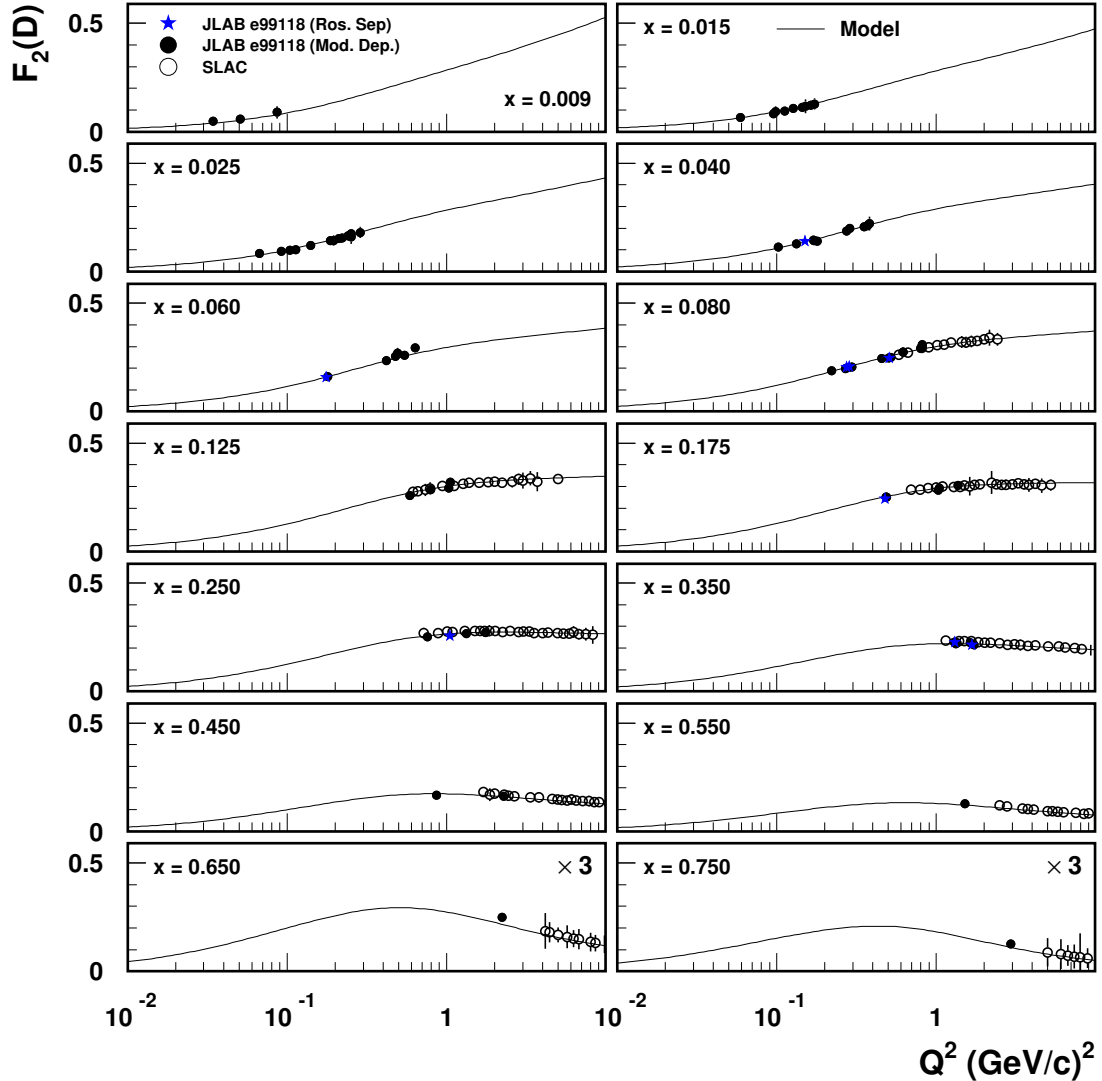


Figure 5.19: Values of $F_2(x, Q^2)$ for deuterium determined via the Rosenbluth separation method (stars) and by using $R_{e99118}^D(x, Q^2)$ (closed circles). The total error bar is shown, including the one due to α^2 that has been added quadratically. The data from SLAC [9] are also shown (open circles). The curve represents the parametrization of the structure function that has been discussed in Sect. 2.9.2.

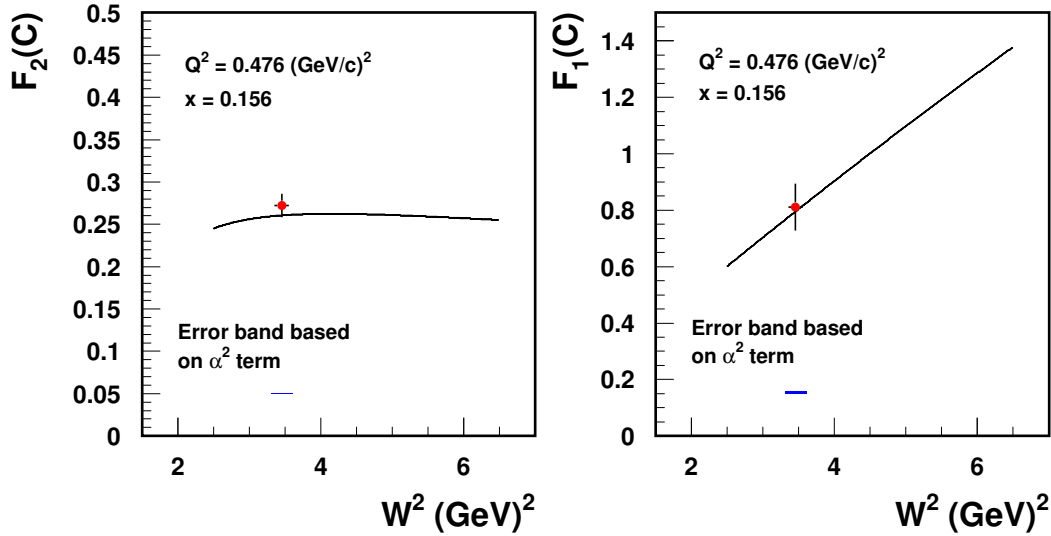


Figure 5.20: Left: $F_2^C(x, Q^2)$ for carbon from the present experiment determined through the Rosenbluth separation technique. The curve on the plot represents the parametrization of F_2^C , see Sect. 2.9.3. Right: $F_1^C(x, Q^2)$ for carbon from the present experiment determined through the Rosenbluth separation technique. The curve on the plot represents a model, which has been calculated through the parametrization of F_2^C , see Sect. 2.9.3 and the parametrization of R_{e99118}^C , see Sect. 5.6.2, which have been used in the last iteration procedure. The error bars on both plots represent the statistical and the systematic uncertainties without the one due to the α^2 term, which is shown separately as the error band, see text for details.

5.6.2 R for Carbon, Copper and Gold

Since the value of $F_2(x, Q^2)$ from the Rosenbluth separation, see Sect. 5.6.1, is in agreement with $F_2^{Model}(x, Q^2)$, the latter one has been used for the calculation of the R via the model dependent method, see Sect. 5.4.2. The difference between $F_2^{Model}(x, Q^2)$ and the measured $F_2(x, Q^2)$ has been included in the systematic uncertainties of $R(x, Q^2)$ that has been calculated.

The values of $R(x, Q^2)$ for carbon, copper and gold from the present experiment determined by both methods are shown in Fig. 5.24 and compared to the results of previous measurements, SLAC [53, 104]. The inner error bars represent the combined statistical and systematic uncertainties without the one due to the α^2 term in the radiative corrections. The total error bars represent the total uncertainties including the uncertainty due to the α^2 term, which has been included quadratically.

Due to the large error bars, it is impossible to parametrize the values of $R(x, Q^2)$ from the

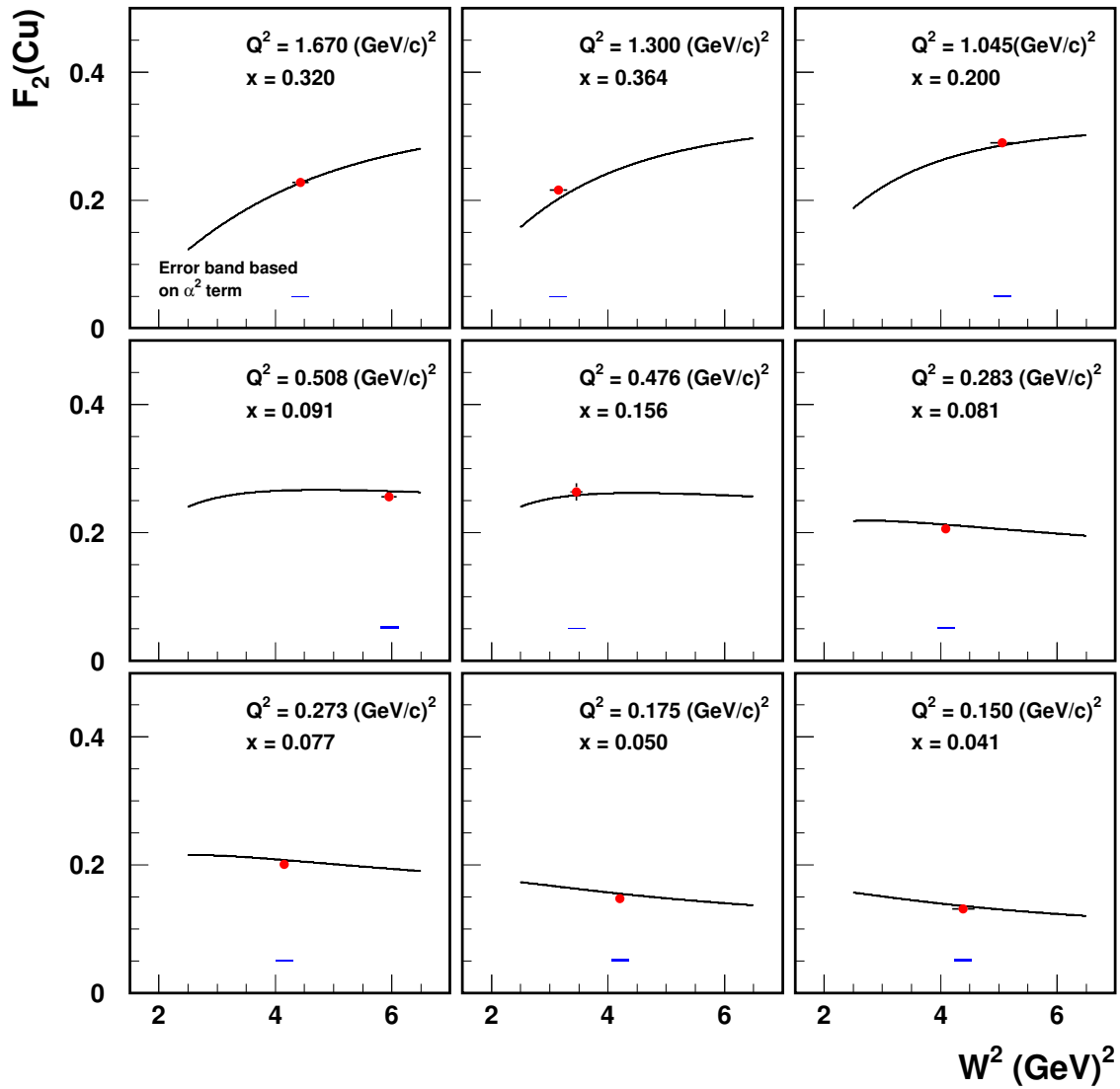


Figure 5.21: The values of $F_2^{Cu}(x, Q^2)$ for copper from the present experiment calculated through the Rosenbluth separation technique. The error bars represent the statistical and the systematic uncertainties without the one due to the α^2 term which is shown separately as the error band, see text for details. The curve on each plot represents the parametrization of F_2^{Cu} , see Sect. 2.9.3.

present experiment as a function of both x and Q^2 and there are not sufficient data available from other experiments for creating a parametrization in a similar way as for hydrogen or

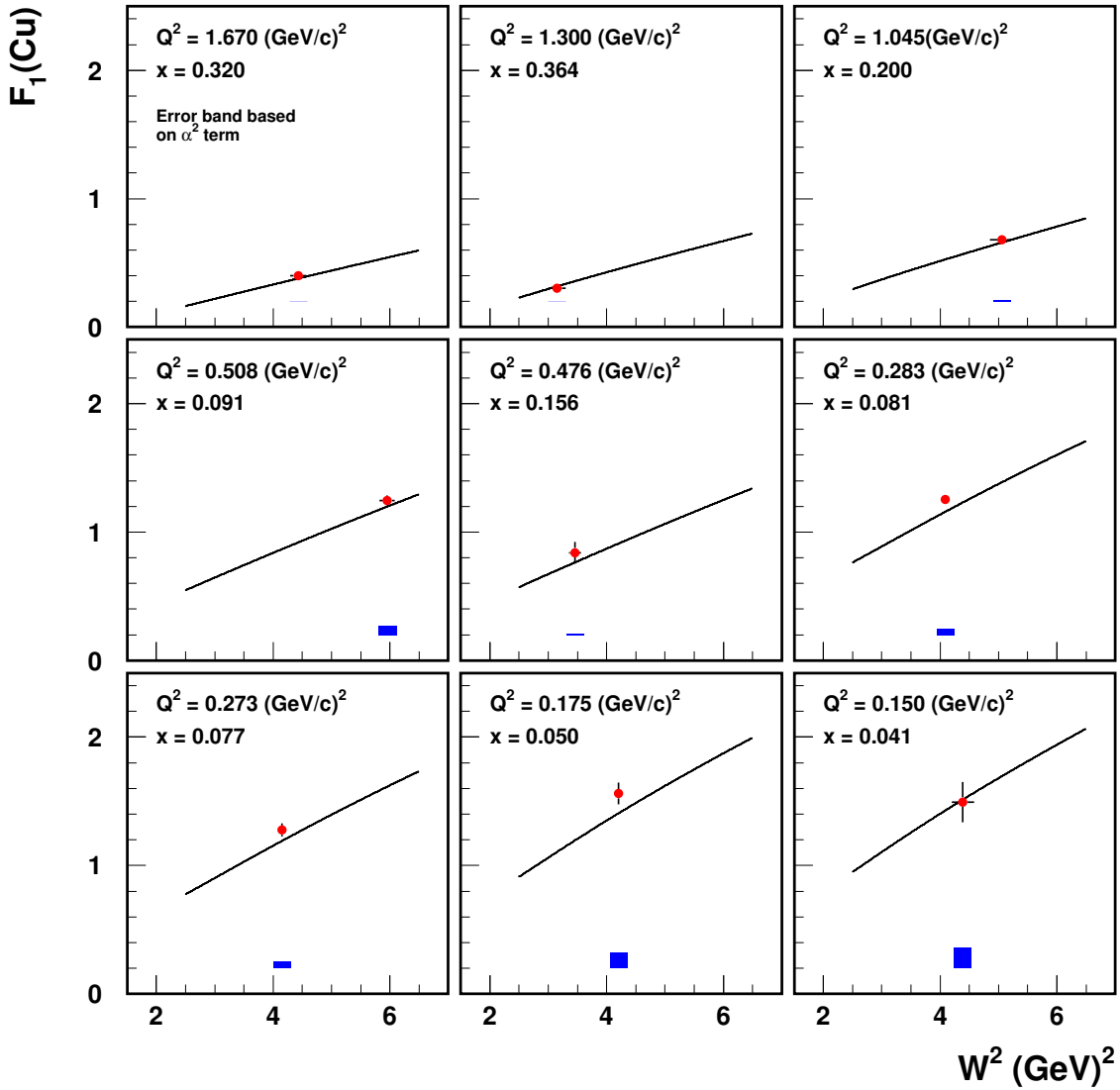


Figure 5.22: The values of $F_1^{Cu}(x, Q^2)$ for copper from the present experiment calculated through the Rosenbluth separation technique. The error bars represent the statistical and the systematic uncertainties without the one due to the α^2 term which is shown separately as the error band, see text for details. The curve on each plot represents a model, which has been calculated through the parametrization of F_2^{Cu} , see Sect. 2.9.3 and parametrization of R_{e99118}^{Cu} , see Sect. 5.6.2.

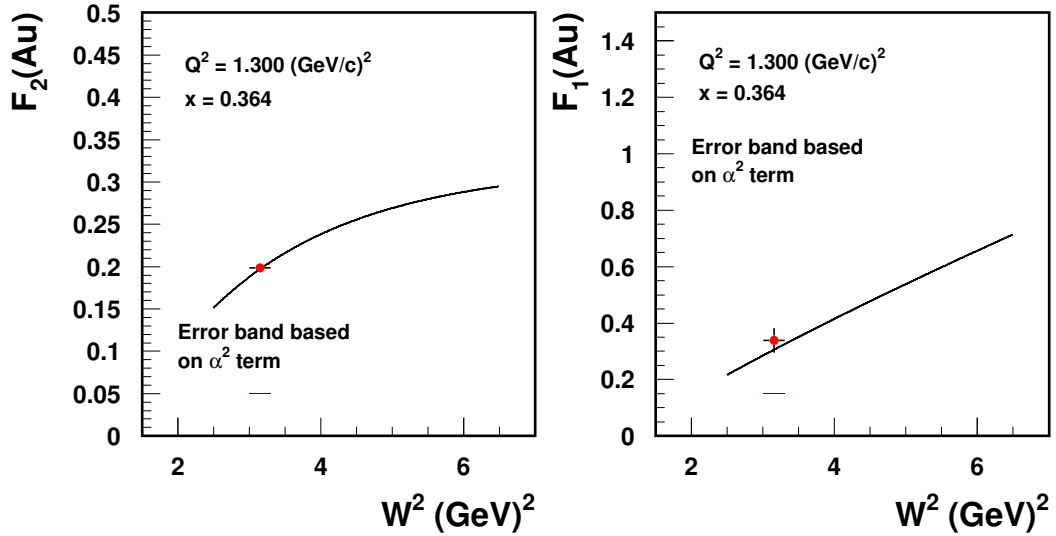


Figure 5.23: Left: $F_2^{Au}(x, Q^2)$ for gold from the present experiment determined through the Rosenbluth separation technique. The curve on the plot represents the parametrization of F_2^{Au} , see Sect. 2.9.3. Right: $F_1^{Au}(x, Q^2)$ for gold from the present experiment determined through the Rosenbluth separation technique. The curve on the plot represents a model, which has been calculated through the parametrization of F_2^{Au} , see Sect. 2.9.3 and the parametrization of R_{e99118}^{Au} , see Sect. 5.6.2 in the last iteration procedure. The error bars on the both plots represent the statistical and the systematic uncertainties without the one due to the α^2 term, which is shown separately as the error band, see text for details.

deuterium. Since also all existing and present data for different values of A agree with each other within the (large) error bars, R for carbon, copper and gold has been taken the same and has been parametrized only as a function of Q^2 (all previous measurements [9] have not observed a significant x dependence), see Fig. 5.25. The data from previous measurements [53, 104] have been included in this parametrization. The x range for the JLAB data is $0.02 < x < 0.4$ and the x ranges for the SLAC data are $0.03 < x < 0.1$ (carbon) and $0.2 < x < 0.5$ (copper). The data have been fitted by using the function

$$R_{e99118}^{A>2}(Q^2) = \left(\frac{A \times Q^2}{Q^4 + B} \right) . \quad (5.5)$$

The resulting parameters are: $A = 0.4503 \pm 0.0349 (\text{GeV}/c)^2$, $B = 0.5982 \pm 0.0868 (\text{GeV}/c)^4$.

In order to estimate the uncertainty in the parametrization, also a fit was done by adding a constant C in Eq. (5.5). The value of C came out close to zero. The uncertainty in

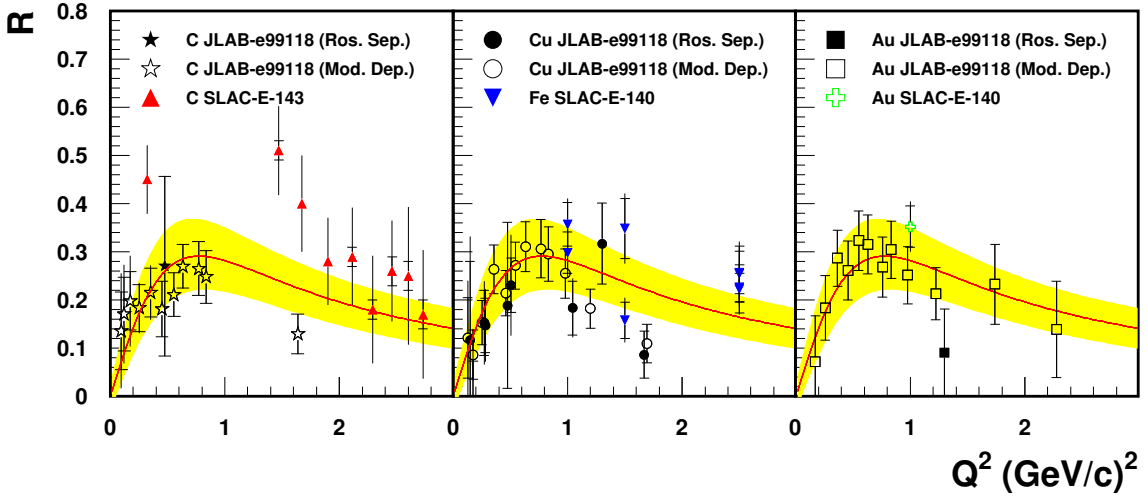


Figure 5.24: Values of R as a function of the Q^2 from the present experiment for carbon, copper and gold calculated via two different methods (Rosenbluth separation method and Model Dependent method). Also, data from SLAC [53, 104] are shown. The curves on each figure represent the parametrization, see text for details, and the shaded bands represent the error band of the parametrization.

the parametrization was then determined by varying the parameters A and B within their uncertainties, plus including the uncertainty of C (around the value $C = 0$, as otherwise the constraint on R at $Q^2 = 0$ would be violated).

This parametrization has been used later in order to calculate F_2^A via the model dependent method, see Sect. 5.6.3.

The values of R determined via the Rosenbluth separation and the model dependent method for the heavier nuclei suggest that R^A goes to zero below $Q^2 = 0.5$ (GeV/c) 2 . However, in view of the large uncertainties taken into account already, plus possible extra ones due to the mentioned problems with the radiative corrections at low E' , no conclusions can be drawn.

5.6.3 Results for F_2 from a Model Dependent Method for Carbon, Copper and Gold

Values of $F_2(x, Q^2)$ for carbon, copper and gold determined using the model dependent method (using the $R_{e99118}^{A>2}(Q^2)$ parametrization and its uncertainty), see Sect. 5.4.3, are shown for different x bins as a function of Q^2 in Fig. 5.26-5.28 together with the Rosenbluth separation results, plus the results of other experiments.

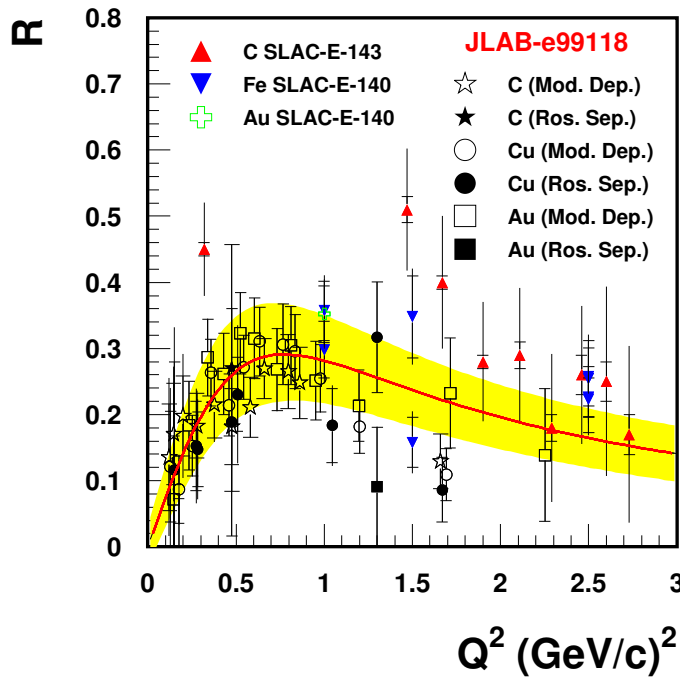


Figure 5.25: Values of R as a function of the Q^2 from the present experiment for carbon, copper and gold calculated via two different methods (the Rosenbluth separation method and the model Dependent method). The values of R calculated via the Model Dependent method have been averaged over some x bins, see text for details. The data from SLAC [53, 104] that have also been used for the creating the parametrization are also shown. The solid curve represents the parametrization of R for the heavy targets and the shaded band represents the correlated error band of the parametrization, see text for details.

The structure functions calculated via the Rosenbluth separation method and via the model dependent method are in good agreement with data from other experiments and with the parametrization of the structure functions within the error bars even at very low Q^2 .

5.7 The Ratios σ_D/σ_H , F_2^D/F_2^H and R^D/R^H

In this section the ratios of the cross sections, structure functions and R for deuterium over hydrogen are presented. The inner error bars in the figures represent the combined statistical and systematic uncertainties without the one due to the α^2 term in the radiative corrections. The total error bars represent the total uncertainties including the uncertainty due to the α^2

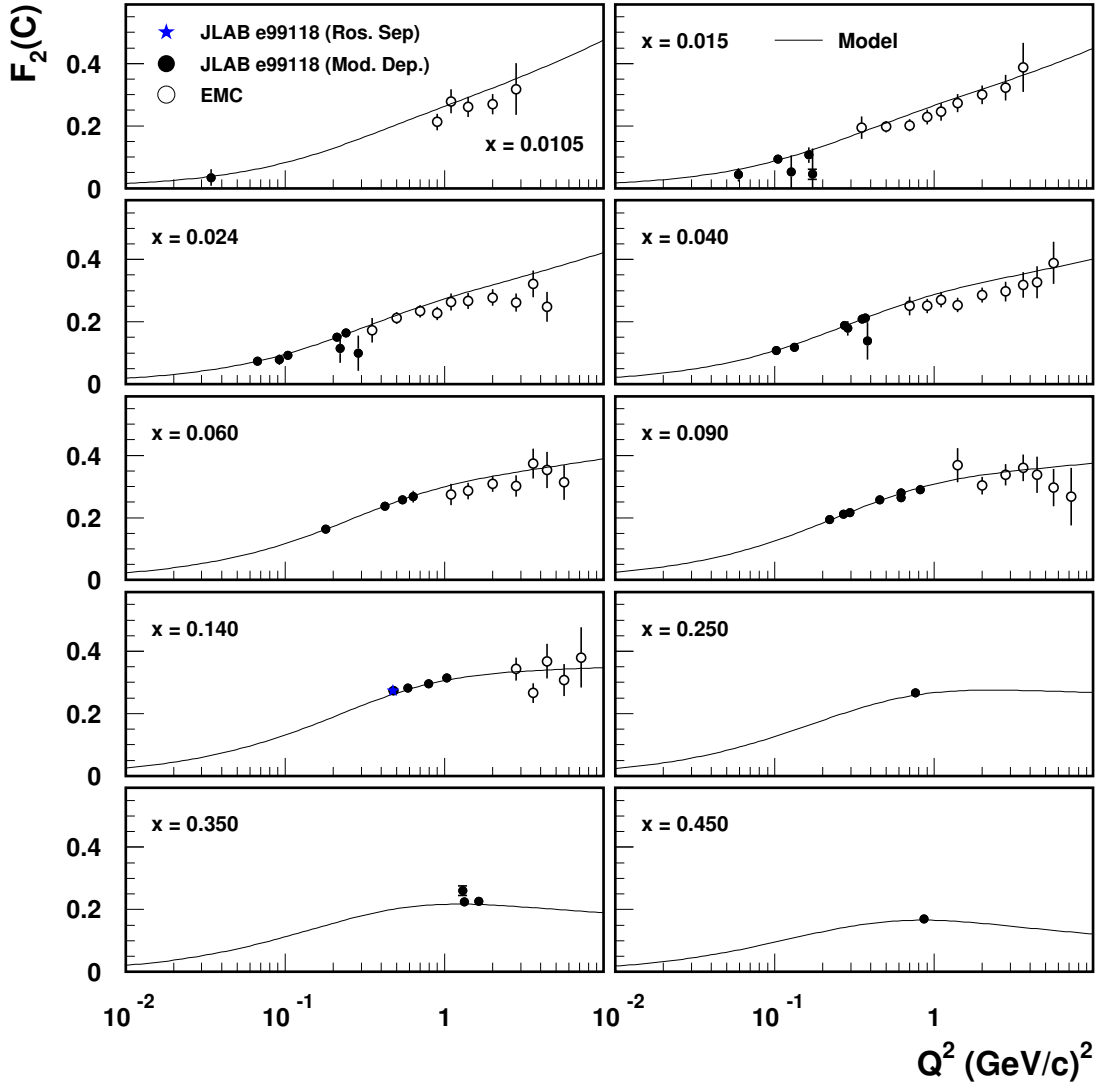


Figure 5.26: Values of $F_2(x, Q^2)$ for carbon determined via the Rosenbluth separation method and by using $R_{e99118}^{A>2}(Q^2)$, see text for details. The total uncertainty is shown, including the one due to the α^2 that has been added quadratically. The data from EMC [102] are also shown. The curve represents the parametrization of the structure function that has been discussed in Sect. 2.9.3.

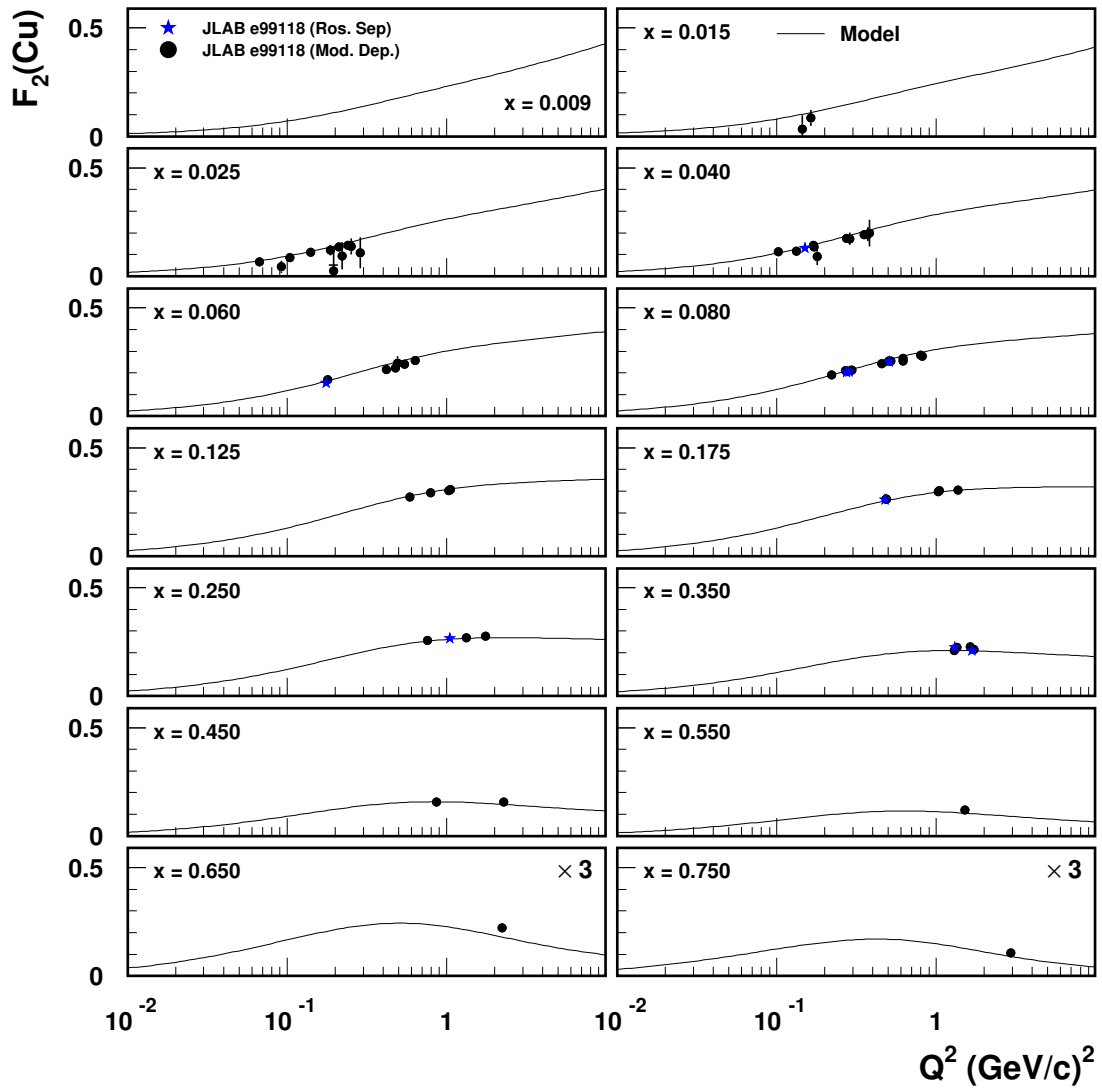


Figure 5.27: The same as Fig. 5.26, but for copper.

term.

The numerical values of the ratios as well as the total uncertainties are listed in Appendix B and Appendix C.

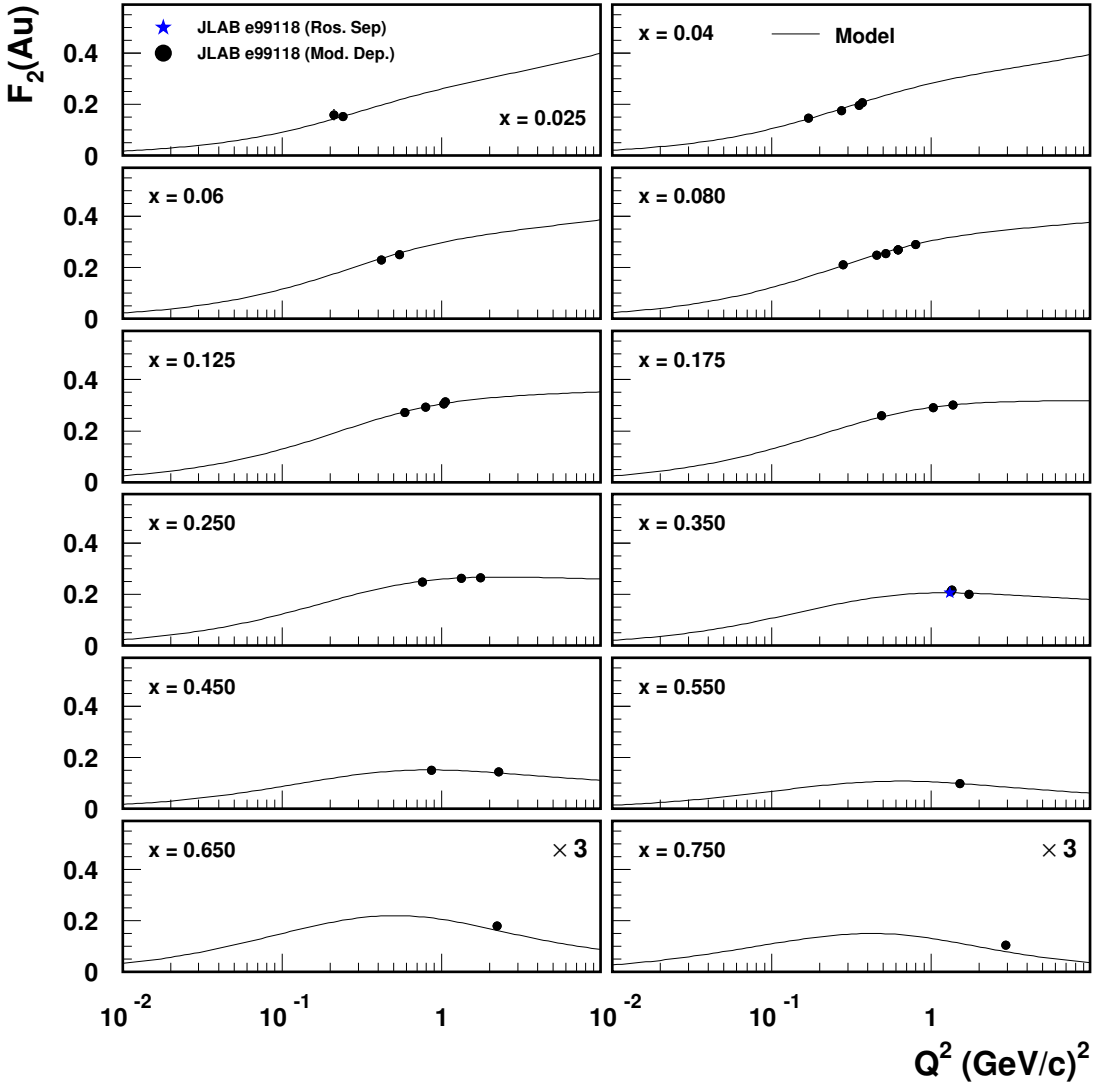


Figure 5.28: The same as Fig. 5.26, but for gold.

5.7.1 x Dependence of σ^D/σ^H

The cross section ratios σ^D/σ^H as a function of x , averaged over all beam energies and angles, are shown in Fig. 5.29 (open circles). The dot-dashed curve on the plot represents the parametrization of the ratio F_2^D/F_2^H as a function of x , see Sect. 2.9.2. This parametrization is based on previous data, which generally have been taken at high Q^2 [63]. Since all previous data [13] indicated that $R^H = R^D$ within the (large) error bars, or have been taken at high

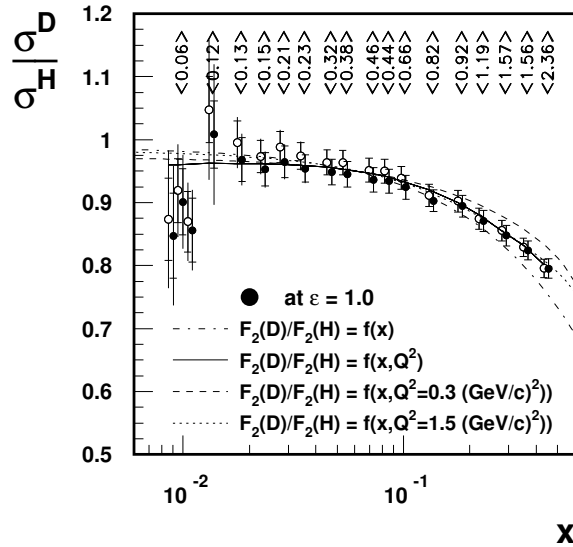


Figure 5.29: Comparison of σ^D/σ^H from the present experiment to the parametrizations of the world data. The inner error bars represent the combined statistical and systematic uncertainties without the one due to the α^2 term in the radiative corrections. The total error bars represent the total uncertainties. The average values of Q^2 in $(\text{GeV}/c)^2$ are shown at the top of the plot. The closed circles represent values of σ^D/σ^H corrected for the difference between R^H and R^D , see text for details. The dot-dashed curve represents a parametrization that depends only on x , see Sect. 2.9.2. The dashed and dotted curves represent parametrizations of the world's data σ^D/σ^H , including the data from the present experiment as a function of x and Q^2 , see Sect. 5.7.2. These curves are shown for $Q^2 = 0.3 (\text{GeV}/c)^2$ and $Q^2 = 1.5 (\text{GeV}/c)^2$. The solid curve represents the same parametrization that depends on x and Q^2 , but for the actual values of Q^2 corresponding to the data points.

ϵ , for those data the ratio of the cross sections σ^D/σ^H is equal to the ratio of the structure functions F_2^D/F_2^H . The data from the present experiment indicate that there is a difference between R^H and R^D ($R^D/R^H \neq 1$), see Sect. 5.7.4. In order to account for the influence of the different R^H and R^D on the ratio σ^D/σ^H , the data from the present experiment have been corrected for this difference using the formula

$$\left(\frac{\sigma^D}{\sigma^H}\right)_{corr} = \left(\frac{\sigma^D}{\sigma^H}\right)_{exp} \frac{(1 + \epsilon R_H)(1 + R_D)}{(1 + R_H)(1 + \epsilon R_D)} = \frac{F_2^D}{F_2^H}. \quad (5.6)$$

For R_H and R_D the parametrizations, see Sect. 5.4.2 and Sect. 5.5.2, have been used. Thus, the ratio of the cross sections $(\sigma^D/\sigma^H)_{corr}$ can be identified with the ratio of the structure functions F_2^D/F_2^H . The result is shown in Fig. 5.29 (closed circles). The corrected ratio σ^D/σ^H (F_2^D/F_2^H) is smaller by up to a few percent (depending on ϵ and the difference between R_H and R_D) compared to the uncorrected ratio of the cross sections (open circles), since $R_H > R_D$.

The dashed, dotted and solid curves in Fig. 5.29 represent a parametrization, see next section, of the world data σ^D/σ^H , including the data from the present experiment, as a function of both x and Q^2 , see Sect. 5.7.2. The parametrization is shown for $Q^2 = 0.3$ (GeV/c) 2 (dashed), $Q^2 = 1.5$ (GeV/c) 2 (dotted) and for the different values of Q^2 corresponding to the data points (solid curve). The Q^2 -dependence is small, but clearly visible. The corrected ratio σ^D/σ^H from the present experiment shows an excellent agreement with the parametrization. Moreover, the ratio σ^D/σ^H that has been corrected for the difference between R_H and R_D (closed circles) is clearly in better agreement with the parametrization than the uncorrected ratio (open circles).

5.7.2 Q^2 Dependence of σ^D/σ^H

In order to study a possible Q^2 dependence and the consistency of the ratio σ^D/σ^H with the results from previous experiments, the corrected ratio σ^D/σ^H has been plotted as a function of Q^2 for different x regions in Figs. 5.30-5.31. The results from the present experiment are in agreement within the error bars with all other experiments shown.

In order to make a parametrization of the ratio σ^D/σ^H that depends on both x and Q^2 the following function [99] has been used in order to fit the data σ^D/σ^H

$$\frac{\sigma^D}{\sigma^H}(x, Q^2) = A(x) + B(x) \ln(Q^2(\text{GeV}/c)^2) . \quad (5.7)$$

The parameters A and B are shown in Fig. 5.32 as functions of x , where their values are shown with and without the data from the present experiment used in the fit. The data from the present experiment do not influence much the parameters $A(x)$ and $B(x)$, since the number of data from the other experiments is much larger than from the present one.

One of the goals of the present experiment was to extend the range (to lower values of Q^2) in which the Q^2 dependence of the ratio can be studied. As shown in Fig. 5.33, the data from the present experiment are in excellent agreement with the parametrization and have relatively small error bars.

The values of A and B have been fitted with the following functions

$$A(x) = a_1 + x(a_2 + x(a_3 + x(a_4 + x a_5))) , \quad (5.8)$$

yielding $a_1 = 0.98051$, $a_2 = -0.50435$, $a_3 = 0.18717$, $a_4 = 0.5813$ and $a_5 = -0.84747$, and

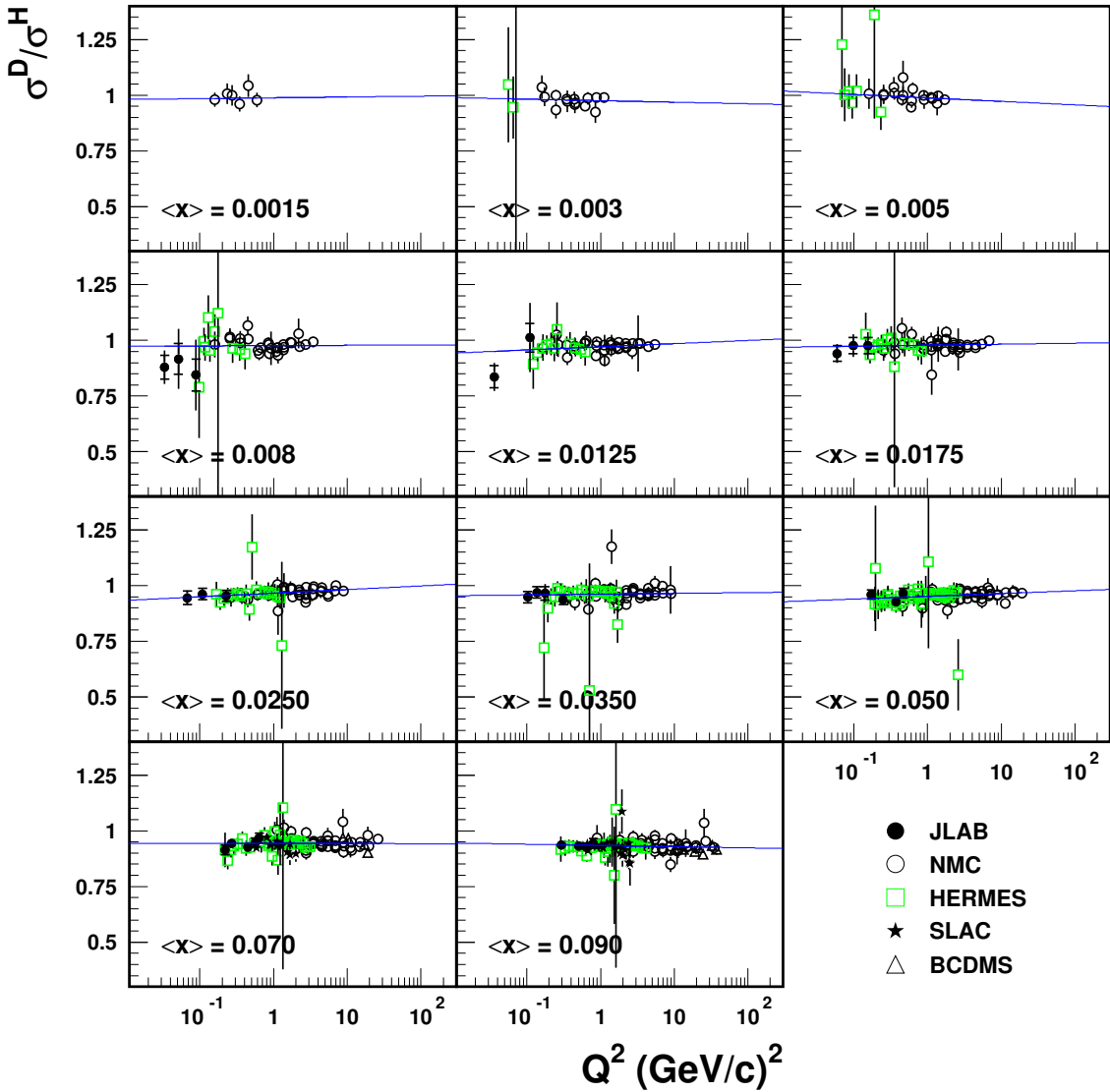


Figure 5.30: Q^2 dependence of the cross section ratio σ^D/σ^H for different x bins. The average x value for each x bin is listed in each panel. The results from other experiments are also shown.

$$B(x) = b_1 + b_2x + b_3x^2 , \quad (5.9)$$

with $b_1 = 0.006789$, $b_2 = -0.11536$ and $b_3 = 0.14625$. This parametrization, see Eq. (5.7),

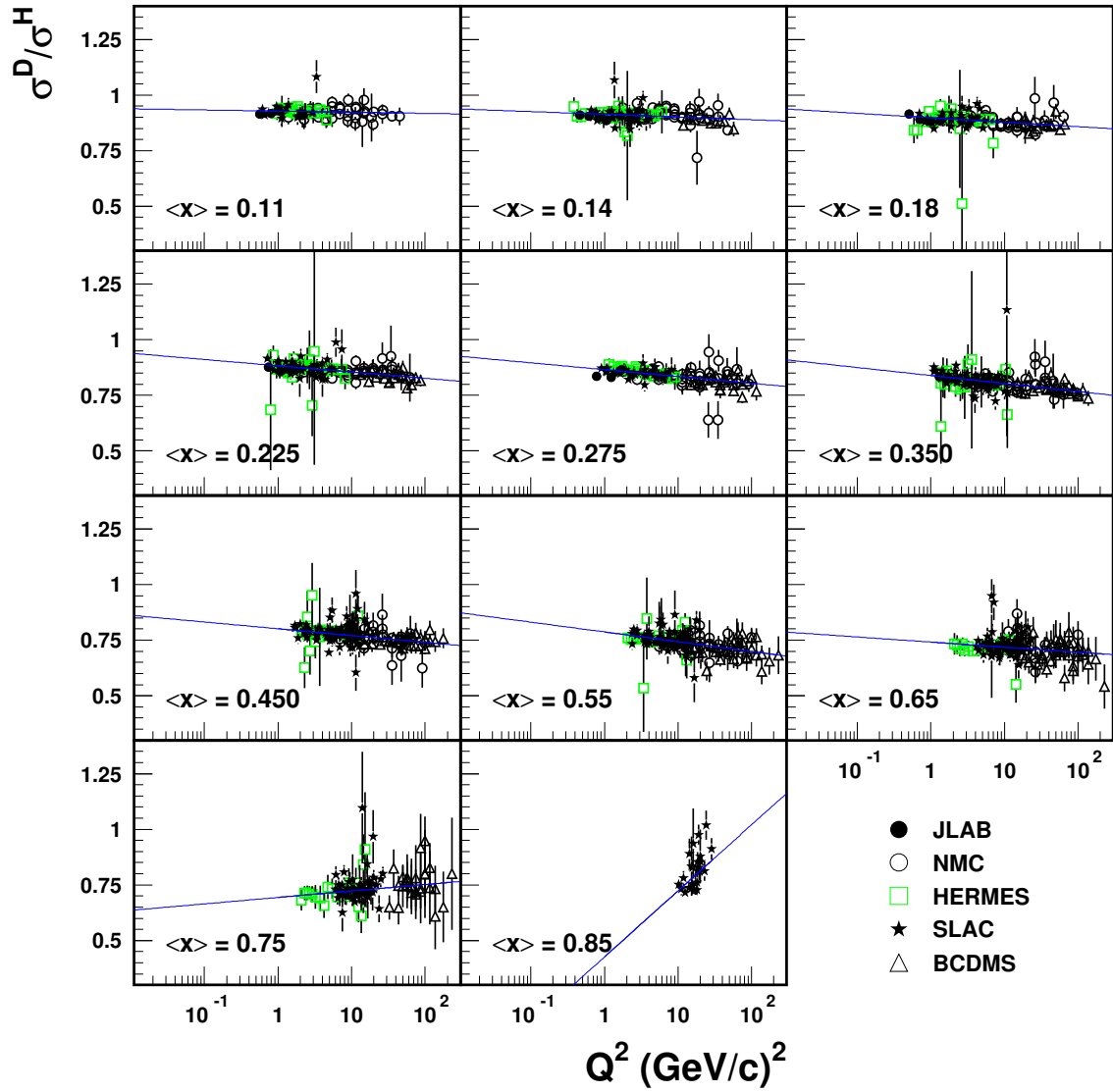


Figure 5.31: As Fig. 5.30, but for higher x bins.

of the ratio is shown in Figs. 5.30-5.31. The parametrization describes the measured ratios well. It is the parametrization that has been used already in Fig. 5.29, see Sect. 5.7.1.

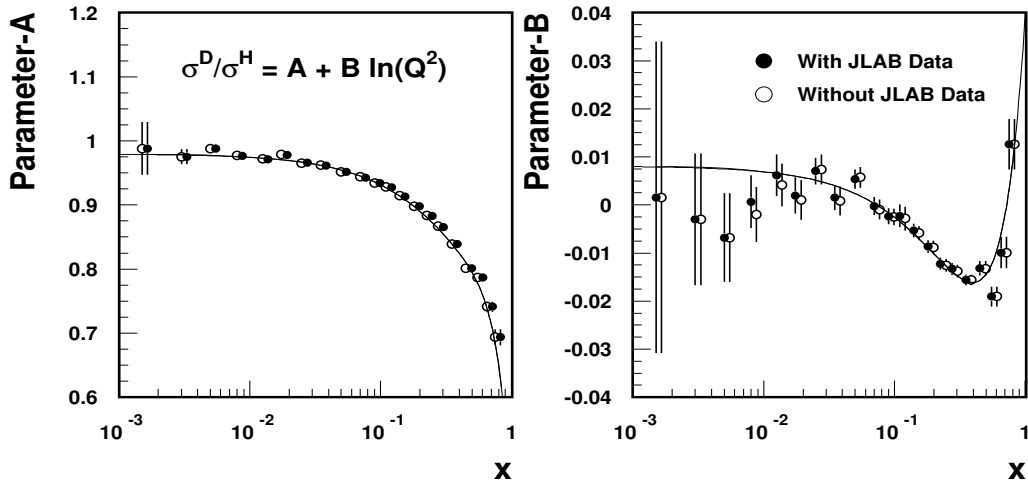


Figure 5.32: Left: Values of the parameter $A(x)$ from the fit based on Eq. (5.7). The curve represents a fit of the parameter $A(x)$, see text for details. Right: values of the parameter $B(x)$ from the fit based on Eq. (5.7). The curve represents a fit of the parameter $B(x)$, see text for details.

5.7.3 Ratio of the Structure Functions F_2^D/F_2^H

Using the values of the structure functions F_2^D and F_2^H , see Sect. 5.4 and Sect. 5.5, that have been calculated using the Rosenbluth separation and the model dependent method the ratio of the structure functions F_2^D/F_2^H has been computed as shown in Fig. 5.34. These ratios are in agreement with the parametrization that has been made using the corrected ratio σ^D/σ^H , see Sect. 5.7.1.

5.7.4 The Ratio R^D/R^H

The ratio R^D/R^H has been calculated using the results from the Rosenbluth separation and model dependent method, see Sect. 5.4 and Sect. 5.5. This ratio is shown in Fig. 5.35 for two x regions. The ratio R^D/R^H calculated through two different methods indicates that $R^D/R^H \neq 1$. However, it has to be mentioned the error bars are large. The data from SLAC [105] are shown, which also indicate that $R^D/R^H \neq 1$ at low values of Q^2 . The results from both experiments (JLAB and SLAC) are in mutual agreement within the error bars. At high values of Q^2 the data from Ref. [9, 105] suggest that $R^D \approx R^H$.

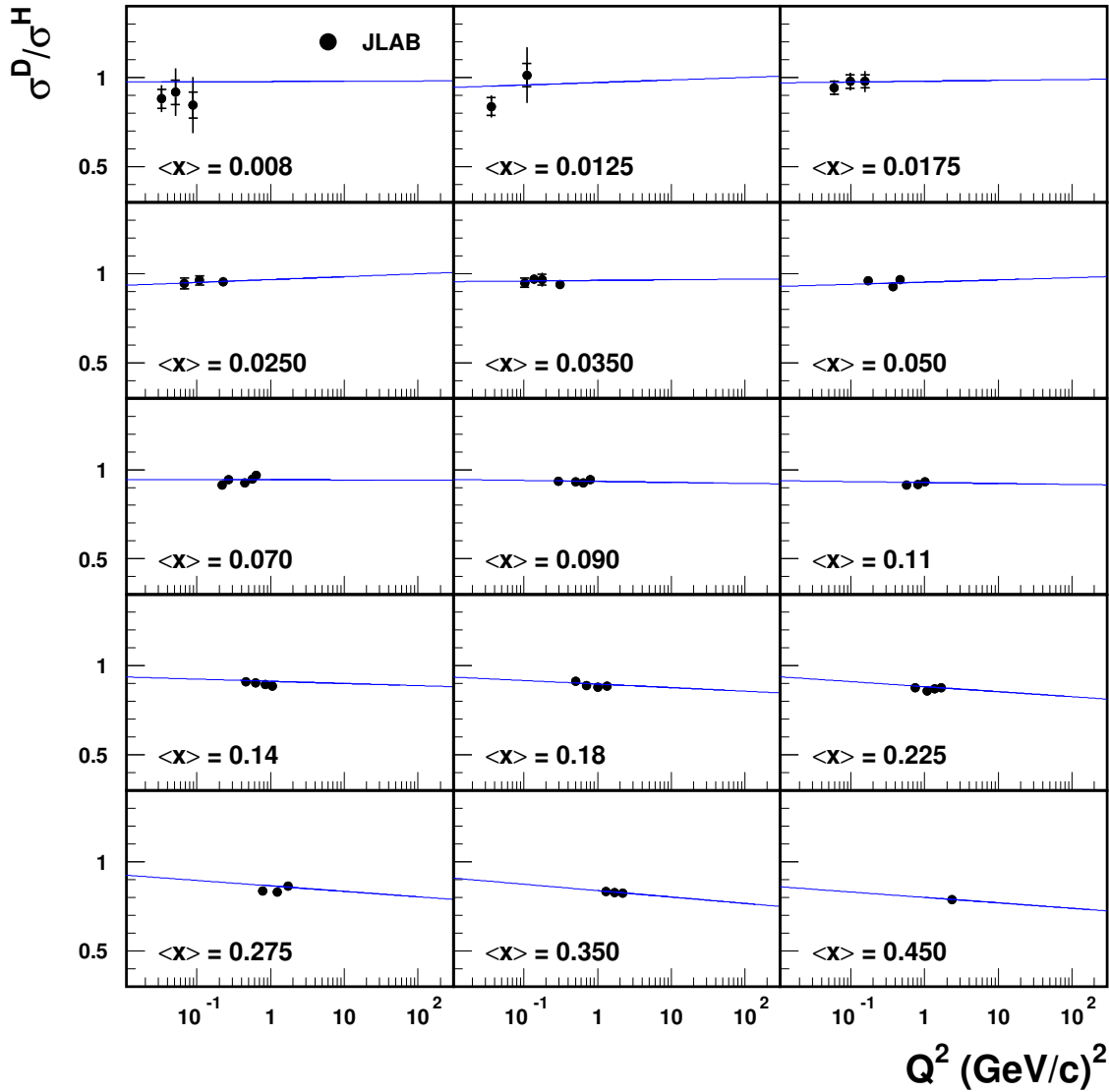


Figure 5.33: As Fig. 5.30, but only JLAB data shown.

5.8 The Ratios σ_A/σ_D , F_2^A/F_2^D and R^A/R^D

The ratios of the cross sections $(\sigma^A/\sigma^D)_{is}$, structure functions $(F_2^A/F_2^D)_{is}$ and the ratios of $(R^A/R^D)_{is}$ are presented in this section. These ratios have been obtained from the ratio of the measured cross sections σ^A/σ^D per nucleon by correcting for the excess neutrons, see Sect 2.9.3. This correction increases the data by a few percent in the high x region.

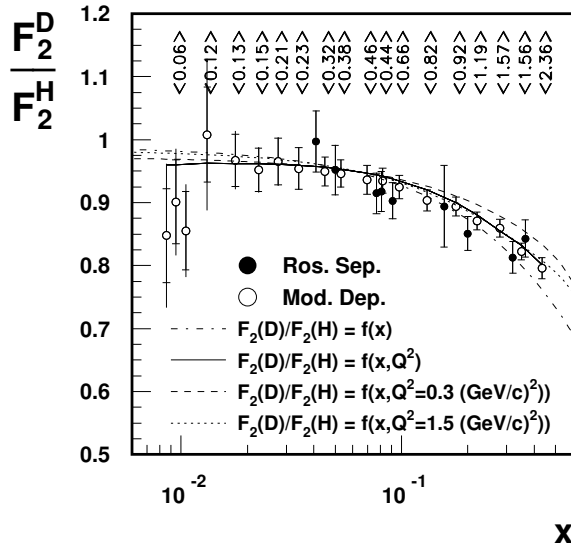


Figure 5.34: Comparison of F_2^D/F_2^H that has been calculated via the model dependent method and the Rosenbluth separation from the present experiment, to the parametrizations of the world data. The dot-dashed curve represents a parametrization that depends only on x , see Sect. 2.9.2. The dashed and dotted curves represent parametrizations of the world data σ^D/σ^H , including the data from the present experiment as a function x and Q^2 , see Sect. 5.7.2. These curves are shown for $Q^2 = 0.3 \text{ (GeV/c)}^2$ and $Q^2 = 1.5 \text{ (GeV/c)}^2$ and the solid curve represents the same parametrization that depends on x and Q^2 but for the values of the Q^2 corresponding to the data points.

In the figures the inner error bars represent the combined statistical and systematic uncertainties without the one due to the α^2 term in the radiative corrections. The total error bars represent the total uncertainty including the uncertainty due to the α^2 term.

5.8.1 Ratio of the Cross Sections σ^A/σ^D

The averaged cross-section ratios $(\sigma^A/\sigma^D)_{is}$ as a function of x for all beam energies and angles are shown in Fig. 5.36. The results from other experiments SLAC [65], NMC [66, 67], EMC [51]) are also shown. For clarity the data points from the present experiment that have large error bars (> 0.1) have not been included in the figure. Since, all previous measurements, as well as the current one, see Sect. 5.8.3, indicate that $R^A = R^D$ within the large error bars [13], the ratio of the cross sections was assumed to be equal to the ratio of the structure functions and no correction similar to the one for the σ^D/σ^H ratio was applied. The results from the present experiment are in agreement within the error bars with all other experiments

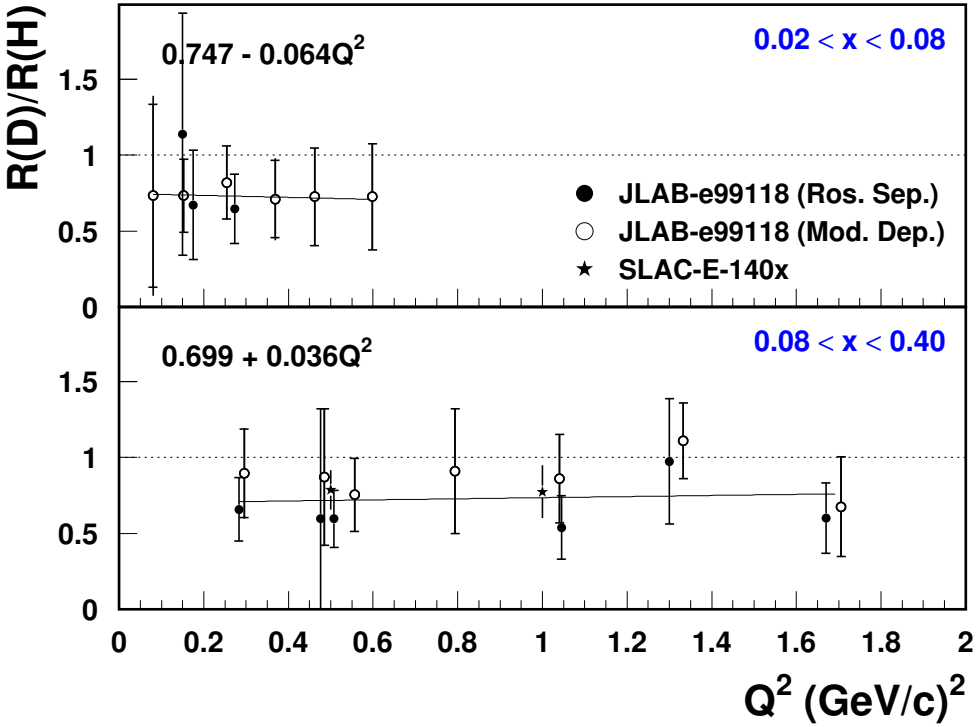


Figure 5.35: The ratio of R^D/R^H from the present experiment for two x regions. The values of R have been calculated via a Rosenbluth separation and via the model dependent method. The data from SLAC [105] are also shown. Systematic uncertainties are not included in the SLAC data.

shown. The curves on the plots represent the parametrizations discussed in Sect. 2.9.3.

5.8.2 Ratio of the Structure Functions F_2^A/F_2^D

Since the data from the present experiment, see Sect. 5.8.3, and the data from the other experiments [13], indicate that $R^A = R^D$ within the large error bars, see next section, the ratio of the structure functions F_2^A/F_2^D are exactly the same according to the Eq. (2.43) as the ratio of the cross sections σ^A/σ^D . Hence, ratios of the structure functions calculated via the model dependent method, see Sect. 5.6.3 do not contain any additional (new) information. Therefore, only ratios of the structure functions F_2^A/F_2^D that have been calculated via the Rosenbluth separation method are shown in Fig. 5.36. The ratio of the structure functions F_2^A/F_2^D are in agreement within the error bars, which are large, with the parametrizations of the ratios, see Sect. 2.9.3.

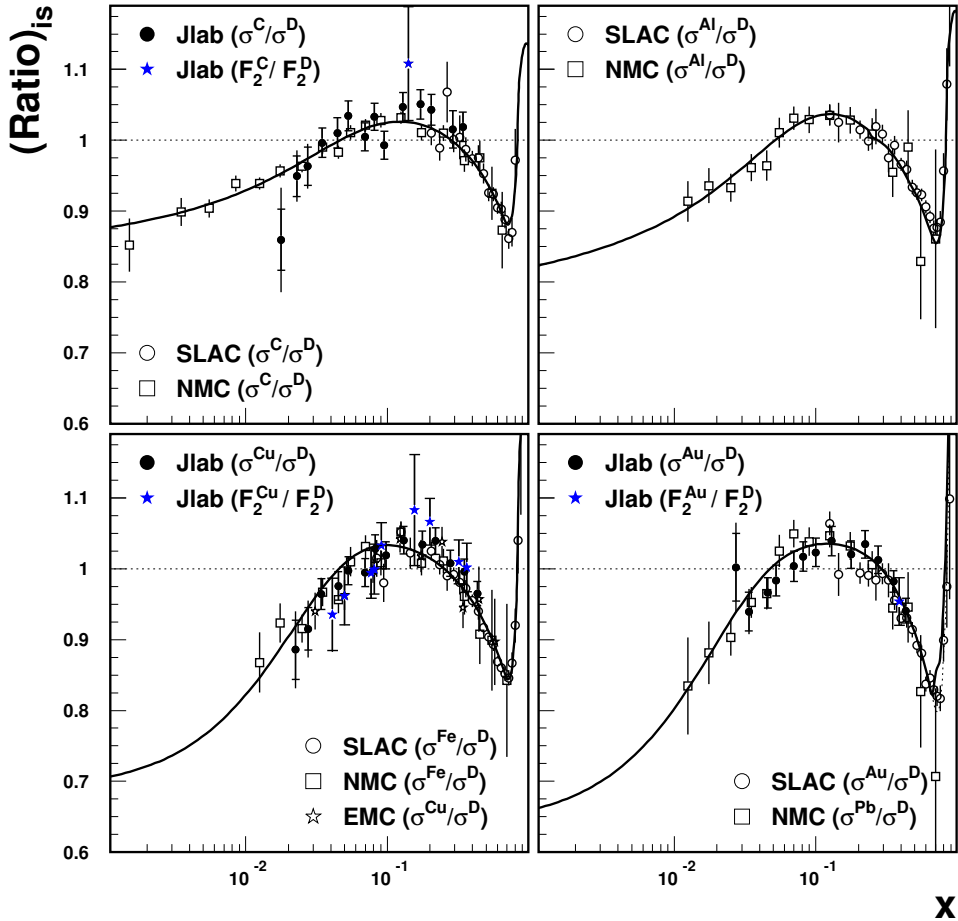


Figure 5.36: Comparison of $(\sigma^A/\sigma^D)_{is}$ from the present experiment (full circles) to the results of other experiments. Data are shown from SLAC (open circles) for C, Al, Fe and Au [65], from NMC (open squares) for C, Al, Fe, Pb [66, 67] and data from EMC for Cu [51]. The curves on the plots represent the parametrizations discussed in Sect. 2.9. The ratios of the structure functions are also shown, see Sect. 5.8.2.

5.8.3 The Ratio R^A/R^D

The ratio $(R^A/R^D)_{is}$ has been calculated using the results from the Rosenbluth separation and the model dependent method, see Sect. 5.6.1 and Sect. 5.6.3. The ratio $(R^A/R^D)_{is}$ from the present experiment together with other experiment results is shown in Fig. 5.37 for different x regions as a function of Q^2 .

The ratio $(R^A/R^D)_{is}$ is compatible with unity for all experiments. Thus, no A -dependence of $R(x, Q^2)$ was observed, neither in the experiments that were done at high values of Q^2 .

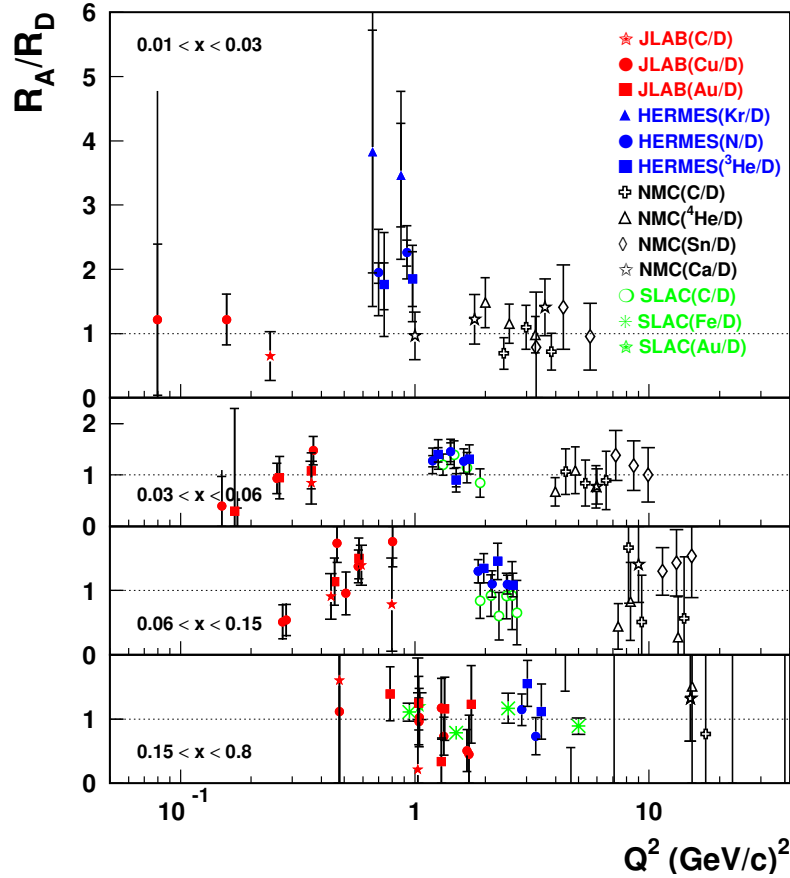


Figure 5.37: The ratio R_A/R_D from different experiments [9, 13, 53, 54] for several nuclei with respect to deuterium as a function of Q^2 for four different x bins.

($Q^2 \gtrsim 1$ (GeV/c) 2), nor in the present experiment, which was done at low values of Q^2 . Of course, the error bars for all experiments are rather large and therefore no final conclusion on the A -dependence of $R(x, Q^2)$ can be drawn.

Chapter 6

Summary and Conclusions

The goals of the investigation described in this thesis were to investigate the behaviour of the structure function F_2 and of the ratio R of the longitudinal and transverse virtual-photon cross sections at low values of Q^2 , *i.e.*, in the transition region from pQCD to non-pQCD, for nucleons and nuclei.

The data were taken in summer 2000 at Jefferson Laboratory (Newport News, VA, USA) at various scattering angles between 10° and 60° degrees on the targets H, D, C, Al, Cu, Au with 2.301, 3.419 and 5.648 GeV electron beams ($I = 25 \mu\text{A}$) and the High-Momentum Spectrometer in Hall C. The data were taken at values of Q^2 between 0.03 and 2.8 $(\text{GeV}/c)^2$, which allowed to investigate the behaviour of the cross sections, structure functions ($F_{1,2}$), ratios of the longitudinal and transverse virtual-photon cross sections (R) including their A -dependence, at low Q^2 , where no data were available at all.

During the data analysis a rate dependence (due to the track selection procedure) was found, which led to a detailed investigation of the track reconstruction procedure and a change in the tracking code used in Hall C. Since data were taken at rather low values of E' (lowest $E' \approx 0.4$ GeV) new methods for calculating the efficiency of the Čerenkov and calorimeter detector were developed and used. Backgrounds such as charge symmetric background, background from target walls and pion contamination were determined and subtracted.

Since the measured cross sections get a large contribution due to the elastic, quasi-elastic and inelastic radiative tails, special attention was paid to the radiative corrections. Also, an additional correction was taken into account due to the possibility that the electron could emit two hard photons (α^2 term). Since this α^2 contribution is open to some discussion, an additional uncertainty due to this term was included in the cross section uncertainty.

The differential Born cross sections were computed for H, D, C, Al, Cu, Au for the different beam energies and angles. When comparing the measured cross sections to model cross sections based on existing parametrizations of F_2 and R , the following results were obtained: the cross sections for hydrogen and deuterium were always in agreement with the cross section models within the total systematic uncertainty, which is dominated by the uncertainty due to the α^2 term at low E' . The cross sections for carbon, copper and gold looked very similar at high and intermediate values of E' and agreed with the model

cross section within the total systematic uncertainty. At low values of E' the cross sections disagreed with the model even outside the total systematic uncertainty, which is very large in that region. This strange behaviour of the cross sections, observed for all nuclei, though most obvious in the heavier ones at lowest E' , is a puzzle. It cannot be explained by simply scaling the α^2 term, since there is no value of the scaling factor that will change the behaviour of the Born cross section in such a way that it will behave smoothly. Presumably, higher order terms ($\alpha^3, \alpha^4 \dots$), which are not known, start to be non-negligible at the lowest values of E' . Also Coulomb corrections could play a role.

The data that were taken at the same values of (x, Q^2) , but different values of the virtual-photon polarization parameter ϵ , were used in a Rosenbluth separation, *i.e.* determine the longitudinal (σ_L) and transverse (σ_T) virtual-photon cross sections and from these values of R ($R = \sigma_L/\sigma_T$) and of the structure functions F_1 and F_2 . Since the values of $F_2(x, Q^2)$ from the Rosenbluth separation were in good agreement (on average deviations of less than 2 % percent for all targets) with the model structure function, R also was calculated using the measured cross sections and the model value of the structure function F_2 (model dependent method).

The values of R for hydrogen and deuterium determined in the present experiment via the Rosenbluth separation method and via the model dependent method were compared to the results of previous measurements (SLAC, EMC, NMC, BCDMS, JLAB) for different x and Q^2 regions. The comparison showed a good agreement in the regions of x and Q^2 where the data overlap. At low values of Q^2 the values of R , according to the theory, should go to zero as Q^2 goes to zero. In the data from the present experiment this behaviour was not yet observed. Only at very low x there is a hint that R goes to zero. This means that for hydrogen and deuterium the transition to zero occurs below a value of Q^2 of about 0.2 - 0.3 $(\text{GeV}/c)^2$.

The ratio R^D/R^H was calculated using the results from the Rosenbluth separation and the model dependent method. The ratio R^D/R^H that was determined in this experiment indicates that $R^D < R^H$ at low Q^2 values. All previous experiments, except one at SLAC, also at low values of Q^2 , found that (at relatively large values of Q^2) $R^D/R^H \approx 1$ within the generally large error bars.

The values of R determined via the Rosenbluth separation and the model dependent method for the heavier nuclei suggest that R^A goes to zero below $Q^2 = 0.5 (\text{GeV}/c)^2$. However, in view of the large uncertainties taken into account already, plus possible extra ones due to the mentioned problems with the radiative corrections at low E' , no conclusions can be drawn.

The ratios R^A/R^D from the present experiment, as well as the ratios from other experiments, indicate that $R^A/R^D \approx 1$. Thus, no A -dependence of $R(x, Q^2)$ was observed, neither in the experiments that were done at high values of Q^2 ($Q^2 \gtrsim 1 (\text{GeV}/c)^2$), nor in the present experiment, which was done at low values of Q^2 . Of course, the error bars for all experiments are rather large and therefore no final conclusion on the A -dependence of $R(x, Q^2)$ can be drawn.

Since there were many available data for hydrogen and deuterium at higher values of Q^2 ($Q^2 > 1 (\text{GeV}/c)^2$), which have been parametrized (the so called R_{1990} parametrization), the

data from the present experiment were joined to the parametrization R_{1990} making a new parametrization (R_{e99118} , different for hydrogen and deuterium) that is valid for all Q^2 .

For the heavy targets there are not sufficient data available from other experiments for creating a parametrization in a similar way as for hydrogen and deuterium. Since also all existing and present data for different values of A agreed with each other within the large error bars, R for carbon, copper and gold was taken the same and was parametrized only as a function of Q^2 (all previous measurements did not observe a significant x dependence).

Since now new parametrizations of R were available for all targets the model dependent method was turned around, and the structure functions F_2 were determined (model dependently) for all x and Q^2 and all targets, where measured cross sections from the present experiment were available. The resulting structure functions calculated via the Rosenbluth separation method and via the model dependent method were in good agreement with the data from the other experiments, and with the parametrization of the structure function within the error bars, even at very low Q^2 .

The x and Q^2 dependencies were studied for the ratio of the cross sections σ^D/σ^H . First, the x dependence of the ratio σ^D/σ^H from the present experiment was compared with the parametrization of F_2^D/F_2^H of the world data. Since all previous data indicated that $R^H = R^D$ within the (large) error bars, or were taken at high ϵ , for those data the ratio of the cross sections σ^D/σ^H was equal to the ratio of the structure functions F_2^D/F_2^H . The data from the present experiment indicated that there was a difference between R^H and R^D ($R^D/R^H \neq 1$). In order to account for the influence of the different R^H and R^D on the ratio σ^D/σ^H , the data from the present experiment were corrected for the difference between R^H and R^D . The corrected ratio was in better agreement with the parametrization than the uncorrected ratio.

Also, the ratios of the structure functions F_2^D/F_2^H and F_2^A/F_2^D that were determined via the Rosenbluth separation technique were compared as a function of x with the world data parametrization. The comparison showed a reasonable agreement with the data from other experiments.

One of the goals of the present experiment was to extend the range (to lower values of Q^2) in which the Q^2 dependence of the ratio (σ^D/σ^H) can be studied. Therefore, the Q^2 dependence of the corrected ratio σ^D/σ^H from the present experiment was compared with the world data and the parametrization of F_2^D/F_2^H . The data from the present experiment were in excellent agreement with the parametrization and had relatively small error bars.

The ratios of the cross section σ^A/σ^D were compared to the world data parametrizations (based on SLAC and NMC data) and the data from the present experiment showed a reasonable agreement with the data from other experiments and with the parametrizations.

Succes or not? That is the question that the reader of this thesis may ask. On the one hand some of the goals were reached, *i.e.*, the behaviour of the structure function F_2 at low values of Q^2 , for nucleons and nuclei, plus accurate ratios of cross sections, were determined. On the other hand due to the large error bars resulting from the uncertainties in the calculation of the radiative corrections, a final conclusion about the behaviour of the ratio R of the longitudinal and transverse virtual-photon cross sections and the ratios R^D/R^H and R^A/R^D can not yet be drawn.

Chapter 7

Samenvatting

Het doel van het onderzoek beschreven in dit proefschrift was om het gedrag van de structuurfunctie F_2 en de verhouding R van longitudinale en transversale werkzame doorsneden voor zowel nucleonen als kernen te bepalen als de impulsoverdracht Q^2 klein is. Hierdoor kan de overgang in de Quantum Chromo Dynamica van het gebied waar storingstheorie werkt (pQCD) naar het gebied waar deze niet toepasbaar is (non-pQCD) onderzocht worden.

De meetgegevens werden in de zomer van het jaar 2000 verzameld in Hall C van het Jefferson Laboratory in Newport News (V.S.). Bundels van $25 \mu A$ electronen met energieën van 2.301, 3.419 of 5.648 GeV werden verstrooid aan waterstof (H), deuterium (D), koolstof (C), aluminium (Al), koper (Cu) en goud (Au) trefplaten. De verstrooide electronen werden gedetecteerd in de High Momentum Spectrometer voor strooihoeken tussen de 10° en 60° . De resulterende waarde van Q^2 varieerde tussen de 0.03 en 2.8 (GeV/c)². Dit maakte het mogelijk het gedrag van de werkzame doorsneden, de structuurfuncties (F_1 en F_2), en de groothed R te bestuderen bij kleine Q^2 , alsmede een mogelijke afhankelijkheid van deze grootheden van het aantal nucleonen A in de gebruikte trefplaat. Tot nu toe waren er geen meetgegevens beschikbaar in dit gebied.

Tijdens de analyse van de meetgegevens werd een afhankelijkheid van de telsnelheid gevonden, die veroorzaakt bleek te worden door de wijze waarop deeltjessporen in de spectrometer geselecteerd werden. Dit leidde tot een nauwgezet onderzoek van de procedure die gebruikt werd om deze sporen te reconstrueren, en mondde uiteindelijk uit in een gewijzigde selectieprocedure. Aangezien de energie E' van de gemeten verstrooide electronen heel laag (0.4 GeV) kan zijn, werden ook nieuwe methodes ontwikkeld om de efficiency van de gebruikte Cerenkov en calorimeter detectoren te bepalen.

Stralingsstaarten van elastische, quasi-elastische en inelastische electron-kern verstrooiingen dragen sterk bij aan de gemeten werkzame doorsneden. Dit vereiste extra aandacht om deze bijdrages af te trekken. Een bijkomende onnauwkeurigheid werd veroorzaakt doordat het proces waarin het electron twee fotonen met hoge energie uitzendt niet goed bekend is. Deze bijdrage schaalt met α^2 en draagt bij tot de totale onzekerheid van de gemeten werkzame doorsneden.

Door te corrigeren voor de stralingseffecten, waarbij gebruik gemaakt werd van parametrisaties van F_2 en R , konden de zogenaamde Born werkzame doorsnedes berekend wor-

den. De gemeten doorsnedes voor de H en D trefplaten waren binnen de foutenvlag, die wordt gedomineerd door de α^2 bijdrage bij lage E' , in overeenstemming met de berekende doorsnedes. De gemeten doorsnedes voor C, Cu, en Au zijn zowel bij hoge en gemiddelde E' vergelijkbaar en komen goed overeen met het gebruikte model. Bij lage E' treedt een duidelijke afwijking van het model op, groter dan de (grote) systematische foutenvlag. De oorzaak van deze vreemde discrepantie, die gezien wordt voor alle kernen zwaarder dan D, is onbekend. Een herschaling van de onbekende α^2 bijdrage kan de discrepantie niet verklaren. Het is mogelijk dat hogere orde α^3 en α^4 bijdrages of Coulomb correcties hier een rol spelen.

Sommige werkzame doorsnedes zijn bepaald bij constante waarden van Q^2 en de Bjorken variabele x (x kan geassocieerd worden met de fractie van de impuls die gedragen wordt door het quark waaraan het electron verstoot), maar verschillende waarden van de polarisatie van het uitgewisselde foton (ϵ). Deze doorsnedes werden gebruikt in een *Rosenbluth separatie*, waarmee men de longitudinale en transversale werkzame doorsnedes apart kan bepalen. Hieruit haalt men dan de waarden van R , F_1 en F_2 . Doordat de waarden voor F_2 bepaald via de Rosenbluth separatie goed overeenkwamen met het gebruikte model, kon R ook bepaald worden door de gemeten werkzame doorsnedes te combineren met de F_2 van het model. Dit wordt verder de modelafhankelijke methode genoemd.

De gevonden waarden voor R voor H en D konden vergeleken worden met de resultaten van eerdere metingen door SLAC, EMC, NMC, BCDMS en JLab. Dit gold zowel voor de waarden bepaald via de Rosenbluth methode als de modelafhankelijke methode. Er werd goede overeenstemming gevonden voor gebieden in x en Q^2 waar de meetgegevens overlappen. Volgens de theorie moet R naar nul gaan bij kleine waarde van Q^2 . Dit gedrag werd nog niet waargenomen in onze meetgegevens, hoewel er enige aanwijzing lijkt te zijn bij de laagste waarden van x . Dit houdt in dat de verwachte overgang van R naar nul voor Q^2 kleiner dan 0.2-0.3 (GeV/c)² moet plaats vinden, althans voor de H en D kernen.

Ook de verhouding van R voor D en H (R^D/R^H) werd zowel bepaald via de Rosenbluth methode als de modelafhankelijke methode. Deze verhouding is kleiner dan 1 voor lage Q^2 . Alle eerdere experimenten vonden dat deze verhouding binnen de (vrij grote) foutenvlaggen gelijk aan 1 was, maar deze experimenten zijn bij hogere waarden van Q^2 gedaan. Een experiment op SLAC vond bij vergelijkbare waarden van Q^2 als in ons experiment ook een verhouding kleiner dan 1.

De gevonden waarden van R voor de zwaardere kernen lijken aan te geven dat R voor zware kernen naar nul gaat als $Q^2 < 0.5$ (GeV/c)². Dit geldt zowel voor de Rosenbluth methode als de modelafhankelijke methode. Aangezien dit precies het gebied is waar de foutenvlaggen groot zijn, deels door de eerder genoemde problemen met stralingsstaarten, lijkt een definitieve conclusie over dit gedrag echter nog voorbarig.

De verhouding van R voor de zwaardere kernen en D (R^A/R^D) gevonden in dit experiment is binnen de foutenvlaggen gelijk aan 1. Dit is in overeenstemming met eerdere experimenten. De conclusie is dat er nog geen meetbare afhankelijkheid van R als functie van A is gevonden. Dit geldt zowel voor het $Q^2 > 1$ (GeV/c)² gebied gemeten in eerdere experimenten als voor het lage Q^2 gebied van dit experiment.

De grote hoeveelheid meetgegevens voor de H en D kernen bij hoge Q^2 (> 1 (GeV/c)²) waren eerder geparametriseerd in R_{1990} . De resultaten van het huidige experiment werden

gecombineerd in een nieuwe parametrisatie: R_{e99118} . Deze parametrisatie is verschillend voor H en D, en geldt voor alle waarden van Q^2 .

Voor de zwaardere kernen zijn er niet genoeg meetgegevens beschikbaar om een soortgelijke parametrisatie te maken. Omdat er tot nu toe geen aanwijzingen bestaan voor een afhankelijkheid van A van R , hebben we de meetgegevens voor C, Cu en Au gecombineerd in een globale parametrisatie. Deze parametrisatie is alleen als functie van Q^2 gedaan, omdat geen enkele meting tot nu toe een grote afhankelijkheid van x liet zien.

Met de parametrisaties voor R konden de structuurfuncties F_2 nu voor alle x , Q^2 en A via de modelafhankelijke methode uit de werkzame doorsneden bepaald worden. De resulterende structuurfuncties zijn zowel in overeenstemming met de structuurfuncties bepaald via de Rosenbluth methode als met die bepaald in andere experimenten, en zijn zelfs tot lage Q^2 binnen de foutenvlaggen in overeenstemming met parametrisaties van F_2 .

De afhankelijkheid van de verhouding van werkzame doorsneden voor H en D (σ^D/σ^H) werd ook bestudeerd. Als functie van x werd deze verhouding vergeleken met de verhouding F_2^D/F_2^H van eerdere experimenten. Deze vergelijking is mogelijk omdat deze eerdere experimenten of beperkt waren tot hoge ϵ , of vonden dat $R^D = R^H$, zodat σ essentieel gelijk was aan F_2 . Aangezien dit experiment vond dat er een verschil is tussen R^D en R^H werd hiervoor gecorrigeerd in de σ^D/σ^H verhouding. Deze correctie zorgde voor een betere overeenstemming met de verhouding F_2^D/F_2^H van de andere experimenten.

De verhoudingen F_2^D/F_2^H en F_2^A/F_2^D , bepaald via de Rosenbluth methode, werden als functie van x ook met de parametrisaties van eerdere experimenten vergeleken. Er werd een goede overeenstemming gevonden.

Een belangrijk doel van dit experiment was het gebied in Q^2 waarover de verhouding σ^D/σ^H is bepaald uit te breiden tot lagere Q^2 . De afhankelijkheid van deze (gecorrigeerde) verhouding als functie van Q^2 werd vergeleken met de resultaten van eerdere experimenten en de globale parametrisatie van F_2^D/F_2^H . De resultaten van dit experiment waren in uitstekende overeenkomst met deze parametrisatie, met relatief kleine foutenvlaggen.

De verhouding σ^A/σ^D werd ook vergeleken met de resultaten van eerdere experimenten van SLAC en NMC. Er werd een redelijke overeenstemming gevonden.

Was dit experiment nu een succes of niet? Dit is een vraag die de lezer van dit proefschrift mogelijk zal stellen. Enerzijds werden de doelen van dit experiment bereikt. Het gedrag van de F_2 structuurfuncties werd zowel voor nucleonen als kernen bepaald bij lage Q^2 , alsmede nauwkeurige kennis omtrent de verhoudingen van werkzame doorsneden. Anderzijds maakte de onzekerheid in de berekening van de stralingsstaarten een definitieve conclusie over het gedrag van R bij lage Q^2 en de verhoudingen R^D/R^H en R^A/R^D onmogelijk.

Appendix A

Tables of F_2 , F_1 and R

The first error in all tables represents the combined statistical and systematic uncertainties without the one due to the α^2 term and the second one represents the total uncertainty.

$\langle Q^2 \rangle$	$\langle x \rangle$	$\langle W^2 \rangle$	F_2^H	F_2^D
1.670	0.320	4.429	$0.282 \pm 0.006 (\pm 0.006)$	$0.229 \pm 0.005 (\pm 0.005)$
1.300	0.364	3.151	$0.261 \pm 0.006 (\pm 0.006)$	$0.220 \pm 0.005 (\pm 0.005)$
1.045	0.200	5.060	$0.322 \pm 0.007 (\pm 0.007)$	$0.274 \pm 0.006 (\pm 0.006)$
0.508	0.091	5.954	$0.275 \pm 0.006 (\pm 0.008)$	$0.249 \pm 0.005 (\pm 0.006)$
0.476	0.156	3.455	$0.274 \pm 0.014 (\pm 0.014)$	$0.245 \pm 0.012 (\pm 0.012)$
0.283	0.081	4.091	$0.225 \pm 0.005 (\pm 0.006)$	$0.207 \pm 0.005 (\pm 0.005)$
0.273	0.077	4.152	$0.222 \pm 0.005 (\pm 0.006)$	$0.203 \pm 0.004 (\pm 0.005)$
0.175	0.050	4.205	$0.161 \pm 0.005 (\pm 0.006)$	$0.153 \pm 0.004 (\pm 0.004)$
0.150	0.041	4.388	$0.141 \pm 0.005 (\pm 0.005)$	$0.141 \pm 0.004 (\pm 0.004)$

$\langle Q^2 \rangle$	$\langle x \rangle$	$\langle W^2 \rangle$	F_2^C	F_2^{Cu}
1.670	0.320	4.429	-	$0.228 \pm 0.004 (\pm 0.004)$
1.300	0.364	3.151	-	$0.216 \pm 0.005 (\pm 0.005)$
1.045	0.200	5.060	-	$0.289 \pm 0.006 (\pm 0.006)$
0.508	0.091	5.954	-	$0.255 \pm 0.005 (\pm 0.006)$
0.476	0.156	3.455	$0.272 \pm 0.013 (\pm 0.013)$	$0.263 \pm 0.013 (\pm 0.013)$
0.283	0.081	4.091	-	$0.205 \pm 0.005 (\pm 0.005)$
0.273	0.077	4.152	-	$0.201 \pm 0.005 (\pm 0.005)$
0.175	0.050	4.205	-	$0.147 \pm 0.004 (\pm 0.005)$
0.150	0.041	4.388	-	$0.131 \pm 0.006 (\pm 0.006)$

Table A.1: The values of F_2 for hydrogen, deuterium, carbon and copper determined via the Rosenbluth separation that are shown in Figs. 5.12, 5.16, 5.20, 5.21.

$\langle Q^2 \rangle$	$\langle x \rangle$	$\langle W^2 \rangle$	F_1^H	F_1^D
1.670	0.320	4.429	$0.418 \pm 0.015 (\pm 0.015)$	$0.373 \pm 0.010 (\pm 0.010)$
1.300	0.364	3.151	$0.381 \pm 0.018 (\pm 0.018)$	$0.323 \pm 0.015 (\pm 0.015)$
1.045	0.200	5.060	$0.687 \pm 0.026 (\pm 0.029)$	$0.660 \pm 0.020 (\pm 0.022)$
0.508	0.091	5.954	$1.140 \pm 0.044 (\pm 0.119)$	$1.165 \pm 0.037 (\pm 0.076)$
0.476	0.156	3.455	$0.810 \pm 0.088 (\pm 0.089)$	$0.795 \pm 0.077 (\pm 0.077)$
0.283	0.081	4.091	$1.065 \pm 0.042 (\pm 0.083)$	$1.086 \pm 0.034 (\pm 0.054)$
0.273	0.077	4.152	$1.065 \pm 0.056 (\pm 0.097)$	$1.096 \pm 0.045 (\pm 0.065)$
0.175	0.050	4.205	$1.298 \pm 0.079 (\pm 0.171)$	$1.339 \pm 0.060 (\pm 0.106)$
0.150	0.041	4.388	$1.424 \pm 0.122 (\pm 0.190)$	$1.380 \pm 0.088 (\pm 0.121)$

$\langle Q^2 \rangle$	$\langle x \rangle$	$\langle W^2 \rangle$	F_1^C	F_1^{Cu}
1.670	0.320	4.429	-	$0.399 \pm 0.011 (\pm 0.011)$
1.300	0.364	3.151	-	$0.301 \pm 0.014 (\pm 0.014)$
1.045	0.200	5.060	-	$0.679 \pm 0.021 (\pm 0.023)$
0.508	0.091	5.954	-	$1.247 \pm 0.038 (\pm 0.080)$
0.476	0.156	3.455	$0.811 \pm 0.083 (\pm 0.083)$	$0.839 \pm 0.084 (\pm 0.084)$
0.283	0.081	4.091	-	$1.252 \pm 0.037 (\pm 0.058)$
0.273	0.077	4.152	-	$1.276 \pm 0.050 (\pm 0.071)$
0.175	0.050	4.205	-	$1.560 \pm 0.083 (\pm 0.149)$
0.150	0.041	4.388	-	$1.494 \pm 0.156 (\pm 0.222)$

Table A.2: The values of F_1 for hydrogen, deuterium, carbon and copper determined via the Rosenbluth separation that are shown in Figs. 5.13, 5.17, 5.20, 5.22.

$\langle Q^2 \rangle$	$\langle x \rangle$	$\langle W^2 \rangle$	F_2^{Au}	F_1^{Au}
1.300	0.364	3.151	$0.198 \pm 0.005 (\pm 0.005)$	$0.339 \pm 0.043 (\pm 0.043)$

Table A.3: The values of F_2 and F_1 for gold determined via the Rosenbluth separation that are shown in 5.23

$\langle x \rangle$	$\langle Q^2 \rangle$	F_2^H	F_2^D
0.009	0.034	$0.056 \pm 0.004 (\pm 0.011)$	$0.048 \pm 0.003 (\pm 0.006)$
0.009	0.050	$0.063 \pm 0.006 (\pm 0.024)$	$0.057 \pm 0.004 (\pm 0.012)$
0.009	0.086	$0.102 \pm 0.012 (\pm 0.055)$	$0.088 \pm 0.007 (\pm 0.027)$
0.015	0.059	$0.070 \pm 0.005 (\pm 0.011)$	$0.066 \pm 0.003 (\pm 0.006)$
0.015	0.095	$0.086 \pm 0.006 (\pm 0.013)$	$0.082 \pm 0.004 (\pm 0.007)$
0.015	0.098	$0.098 \pm 0.011 (\pm 0.048)$	$0.092 \pm 0.007 (\pm 0.024)$
0.015	0.111	$0.090 \pm 0.009 (\pm 0.039)$	$0.095 \pm 0.006 (\pm 0.019)$
0.015	0.126	$0.108 \pm 0.009 (\pm 0.031)$	$0.106 \pm 0.006 (\pm 0.016)$
0.015	0.144	$0.113 \pm 0.008 (\pm 0.025)$	$0.112 \pm 0.006 (\pm 0.014)$
0.015	0.151	$0.124 \pm 0.013 (\pm 0.063)$	$0.117 \pm 0.008 (\pm 0.031)$
0.015	0.163	$0.127 \pm 0.008 (\pm 0.020)$	$0.122 \pm 0.006 (\pm 0.011)$
0.015	0.171	$0.114 \pm 0.012 (\pm 0.051)$	$0.127 \pm 0.008 (\pm 0.026)$
0.025	0.067	$0.089 \pm 0.004 (\pm 0.006)$	$0.082 \pm 0.003 (\pm 0.003)$
0.025	0.092	$0.098 \pm 0.006 (\pm 0.012)$	$0.094 \pm 0.004 (\pm 0.007)$
0.025	0.104	$0.105 \pm 0.005 (\pm 0.007)$	$0.098 \pm 0.003 (\pm 0.005)$
0.025	0.113	$0.109 \pm 0.008 (\pm 0.026)$	$0.101 \pm 0.006 (\pm 0.013)$
0.025	0.140	$0.126 \pm 0.005 (\pm 0.008)$	$0.120 \pm 0.004 (\pm 0.005)$
0.025	0.186	$0.149 \pm 0.008 (\pm 0.017)$	$0.142 \pm 0.006 (\pm 0.010)$
0.025	0.195	$0.133 \pm 0.011 (\pm 0.044)$	$0.142 \pm 0.008 (\pm 0.023)$
0.025	0.211	$0.169 \pm 0.008 (\pm 0.014)$	$0.153 \pm 0.006 (\pm 0.009)$
0.025	0.222	$0.161 \pm 0.012 (\pm 0.036)$	$0.155 \pm 0.008 (\pm 0.020)$
0.025	0.240	$0.177 \pm 0.008 (\pm 0.012)$	$0.164 \pm 0.006 (\pm 0.008)$
0.025	0.252	$0.171 \pm 0.011 (\pm 0.029)$	$0.173 \pm 0.009 (\pm 0.017)$
0.025	0.252	$0.155 \pm 0.014 (\pm 0.060)$	$0.158 \pm 0.010 (\pm 0.031)$
0.025	0.287	$0.168 \pm 0.013 (\pm 0.048)$	$0.180 \pm 0.010 (\pm 0.026)$
0.040	0.102	$0.121 \pm 0.005 (\pm 0.006)$	$0.112 \pm 0.004 (\pm 0.004)$
0.040	0.132	$0.131 \pm 0.007 (\pm 0.013)$	$0.127 \pm 0.005 (\pm 0.008)$
0.040	0.170	$0.153 \pm 0.004 (\pm 0.004)$	$0.145 \pm 0.003 (\pm 0.003)$
0.040	0.171	$0.151 \pm 0.008 (\pm 0.015)$	$0.142 \pm 0.006 (\pm 0.009)$
0.040	0.178	$0.145 \pm 0.010 (\pm 0.026)$	$0.139 \pm 0.007 (\pm 0.014)$
0.040	0.273	$0.204 \pm 0.008 (\pm 0.011)$	$0.186 \pm 0.006 (\pm 0.007)$
0.040	0.286	$0.204 \pm 0.012 (\pm 0.025)$	$0.198 \pm 0.009 (\pm 0.015)$
0.040	0.352	$0.223 \pm 0.007 (\pm 0.008)$	$0.206 \pm 0.005 (\pm 0.006)$
0.040	0.370	$0.226 \pm 0.011 (\pm 0.017)$	$0.212 \pm 0.009 (\pm 0.011)$

Table A.4: The values of F_2 for hydrogen and deuterium determined via the model dependent method that are shown in Fig. 5.15 and Fig. 5.19.

$\langle x \rangle$	$\langle Q^2 \rangle$	F_2^H	F_2^D
0.040	0.371	$0.211 \pm 0.014 (\pm 0.033)$	$0.214 \pm 0.011 (\pm 0.020)$
0.040	0.379	$0.211 \pm 0.016 (\pm 0.056)$	$0.221 \pm 0.013 (\pm 0.031)$
0.060	0.180	$0.166 \pm 0.009 (\pm 0.013)$	$0.160 \pm 0.007 (\pm 0.008)$
0.060	0.420	$0.254 \pm 0.012 (\pm 0.015)$	$0.234 \pm 0.009 (\pm 0.010)$
0.060	0.479	$0.262 \pm 0.015 (\pm 0.023)$	$0.254 \pm 0.011 (\pm 0.016)$
0.060	0.491	$0.262 \pm 0.017 (\pm 0.038)$	$0.268 \pm 0.014 (\pm 0.024)$
0.060	0.543	$0.273 \pm 0.010 (\pm 0.011)$	$0.258 \pm 0.008 (\pm 0.009)$
0.060	0.633	$0.285 \pm 0.017 (\pm 0.026)$	$0.293 \pm 0.014 (\pm 0.018)$
0.080	0.220	$0.210 \pm 0.008 (\pm 0.008)$	$0.188 \pm 0.006 (\pm 0.006)$
0.080	0.268	$0.209 \pm 0.011 (\pm 0.013)$	$0.197 \pm 0.008 (\pm 0.009)$
0.080	0.280	$0.220 \pm 0.005 (\pm 0.005)$	$0.203 \pm 0.004 (\pm 0.004)$
0.080	0.295	$0.218 \pm 0.011 (\pm 0.013)$	$0.204 \pm 0.008 (\pm 0.009)$
0.080	0.455	$0.263 \pm 0.006 (\pm 0.006)$	$0.243 \pm 0.005 (\pm 0.005)$
0.080	0.500	$0.254 \pm 0.015 (\pm 0.023)$	$0.247 \pm 0.012 (\pm 0.015)$
0.080	0.517	$0.269 \pm 0.006 (\pm 0.006)$	$0.249 \pm 0.005 (\pm 0.005)$
0.080	0.617	$0.292 \pm 0.010 (\pm 0.010)$	$0.273 \pm 0.008 (\pm 0.008)$
0.080	0.618	$0.295 \pm 0.014 (\pm 0.017)$	$0.275 \pm 0.011 (\pm 0.012)$
0.080	0.799	$0.311 \pm 0.013 (\pm 0.013)$	$0.292 \pm 0.010 (\pm 0.010)$
0.080	0.818	$0.321 \pm 0.017 (\pm 0.019)$	$0.309 \pm 0.013 (\pm 0.014)$
0.125	0.588	$0.286 \pm 0.005 (\pm 0.005)$	$0.259 \pm 0.005 (\pm 0.005)$
0.125	0.797	$0.316 \pm 0.009 (\pm 0.009)$	$0.285 \pm 0.007 (\pm 0.007)$
0.125	1.031	$0.330 \pm 0.011 (\pm 0.011)$	$0.292 \pm 0.008 (\pm 0.008)$
0.125	1.056	$0.348 \pm 0.016 (\pm 0.016)$	$0.320 \pm 0.012 (\pm 0.012)$
0.175	0.483	$0.279 \pm 0.011 (\pm 0.011)$	$0.251 \pm 0.008 (\pm 0.008)$
0.175	0.487	$0.277 \pm 0.006 (\pm 0.006)$	$0.249 \pm 0.004 (\pm 0.004)$
0.175	1.029	$0.322 \pm 0.007 (\pm 0.007)$	$0.282 \pm 0.005 (\pm 0.005)$
0.175	1.045	$0.324 \pm 0.017 (\pm 0.018)$	$0.291 \pm 0.013 (\pm 0.013)$
0.175	1.364	$0.344 \pm 0.013 (\pm 0.013)$	$0.305 \pm 0.010 (\pm 0.010)$
0.250	0.759	$0.300 \pm 0.005 (\pm 0.005)$	$0.251 \pm 0.004 (\pm 0.004)$
0.250	1.332	$0.312 \pm 0.008 (\pm 0.008)$	$0.265 \pm 0.006 (\pm 0.006)$
0.250	1.761	$0.314 \pm 0.010 (\pm 0.010)$	$0.272 \pm 0.007 (\pm 0.007)$
0.350	1.298	$0.277 \pm 0.016 (\pm 0.016)$	$0.227 \pm 0.011 (\pm 0.011)$
0.350	1.329	$0.271 \pm 0.005 (\pm 0.005)$	$0.218 \pm 0.003 (\pm 0.004)$
0.350	1.340	$0.277 \pm 0.008 (\pm 0.008)$	$0.225 \pm 0.005 (\pm 0.005)$

Table A.5: Continuation of the Table A.4.

$\langle x \rangle$	$\langle Q^2 \rangle$	F_2^H	F_2^D
0.350	1.635	$0.268 \pm 0.015 (\pm 0.015)$	$0.224 \pm 0.010 (\pm 0.010)$
0.350	1.720	$0.266 \pm 0.006 (\pm 0.006)$	$0.215 \pm 0.004 (\pm 0.004)$
0.450	0.864	$0.211 \pm 0.003 (\pm 0.003)$	$0.166 \pm 0.002 (\pm 0.002)$
0.450	2.275	$0.206 \pm 0.005 (\pm 0.005)$	$0.162 \pm 0.003 (\pm 0.003)$
0.550	1.511	$0.168 \pm 0.003 (\pm 0.003)$	$0.128 \pm 0.002 (\pm 0.002)$
0.650	2.221	$0.118 \pm 0.002 (\pm 0.002)$	$0.080 \pm 0.001 (\pm 0.001)$
0.750	2.937	$0.064 \pm 0.001 (\pm 0.001)$	$0.042 \pm 0.001 (\pm 0.001)$

Table A.6: Continuation of the Table A.5.

$\langle x \rangle$	$\langle Q^2 \rangle$	F_2^C	F_2^{Cu}
0.009	0.034	$0.056 \pm 0.004 (\pm 0.011)$	-
0.009	0.050	$0.063 \pm 0.006 (\pm 0.024)$	-
0.009	0.086	$0.102 \pm 0.012 (\pm 0.055)$	-
0.015	0.059	$0.070 \pm 0.005 (\pm 0.011)$	-
0.015	0.095	$0.086 \pm 0.006 (\pm 0.013)$	-
0.015	0.098	$0.098 \pm 0.011 (\pm 0.048)$	-
0.015	0.111	$0.090 \pm 0.009 (\pm 0.039)$	-
0.015	0.126	$0.108 \pm 0.009 (\pm 0.031)$	-
0.015	0.144	$0.113 \pm 0.008 (\pm 0.025)$	$0.034 \pm 0.019 (\pm 0.064)$
0.015	0.151	$0.124 \pm 0.013 (\pm 0.063)$	-
0.015	0.163	$0.127 \pm 0.008 (\pm 0.020)$	$0.084 \pm 0.013 (\pm 0.036)$
0.015	0.171	$0.114 \pm 0.012 (\pm 0.051)$	-
0.025	0.067	$0.089 \pm 0.004 (\pm 0.006)$	$0.065 \pm 0.006 (\pm 0.010)$
0.025	0.092	$0.098 \pm 0.006 (\pm 0.012)$	$0.043 \pm 0.011 (\pm 0.027)$
0.025	0.104	$0.105 \pm 0.005 (\pm 0.007)$	$0.087 \pm 0.006 (\pm 0.010)$
0.025	0.113	$0.109 \pm 0.008 (\pm 0.026)$	-
0.025	0.140	$0.126 \pm 0.005 (\pm 0.008)$	$0.110 \pm 0.005 (\pm 0.007)$
0.025	0.186	$0.149 \pm 0.008 (\pm 0.017)$	$0.120 \pm 0.010 (\pm 0.025)$
0.025	0.195	$0.133 \pm 0.011 (\pm 0.044)$	$0.023 \pm 0.028 (\pm 0.111)$
0.025	0.211	$0.169 \pm 0.008 (\pm 0.014)$	$0.135 \pm 0.008 (\pm 0.016)$
0.025	0.222	$0.161 \pm 0.012 (\pm 0.036)$	$0.094 \pm 0.018 (\pm 0.063)$
0.025	0.240	$0.177 \pm 0.008 (\pm 0.012)$	$0.143 \pm 0.007 (\pm 0.011)$

Table A.7: The values of F_2 for carbon and copper determined via the model dependent method that are shown in Fig. 5.26 and Fig. 5.27.

$\langle x \rangle$	$\langle Q^2 \rangle$	F_2^C	F_2^{Cu}
0.025	0.252	$0.171 \pm 0.011 (\pm 0.029)$	$0.137 \pm 0.013 (\pm 0.037)$
0.025	0.252	$0.155 \pm 0.014 (\pm 0.060)$	-
0.025	0.287	$0.168 \pm 0.013 (\pm 0.048)$	$0.108 \pm 0.018 (\pm 0.071)$
0.040	0.102	$0.121 \pm 0.005 (\pm 0.006)$	$0.114 \pm 0.005 (\pm 0.006)$
0.040	0.132	$0.131 \pm 0.007 (\pm 0.013)$	$0.114 \pm 0.008 (\pm 0.015)$
0.040	0.170	$0.153 \pm 0.004 (\pm 0.004)$	$0.142 \pm 0.003 (\pm 0.003)$
0.040	0.171	$0.151 \pm 0.008 (\pm 0.015)$	$0.135 \pm 0.008 (\pm 0.017)$
0.040	0.178	$0.145 \pm 0.010 (\pm 0.026)$	$0.091 \pm 0.013 (\pm 0.041)$
0.040	0.273	$0.204 \pm 0.008 (\pm 0.011)$	$0.173 \pm 0.007 (\pm 0.009)$
0.040	0.286	$0.204 \pm 0.012 (\pm 0.025)$	$0.173 \pm 0.011 (\pm 0.027)$
0.040	0.352	$0.223 \pm 0.007 (\pm 0.008)$	$0.191 \pm 0.006 (\pm 0.006)$
0.040	0.370	$0.226 \pm 0.011 (\pm 0.017)$	$0.190 \pm 0.009 (\pm 0.014)$
0.040	0.371	$0.211 \pm 0.014 (\pm 0.033)$	$0.194 \pm 0.012 (\pm 0.031)$
0.040	0.379	$0.211 \pm 0.016 (\pm 0.056)$	$0.199 \pm 0.018 (\pm 0.061)$
0.060	0.180	$0.166 \pm 0.009 (\pm 0.013)$	$0.168 \pm 0.008 (\pm 0.011)$
0.060	0.420	$0.254 \pm 0.012 (\pm 0.015)$	$0.216 \pm 0.009 (\pm 0.012)$
0.060	0.479	$0.262 \pm 0.015 (\pm 0.023)$	$0.223 \pm 0.011 (\pm 0.019)$
0.060	0.491	$0.262 \pm 0.017 (\pm 0.038)$	$0.244 \pm 0.014 (\pm 0.031)$
0.060	0.543	$0.273 \pm 0.010 (\pm 0.011)$	$0.239 \pm 0.008 (\pm 0.009)$
0.060	0.633	$0.285 \pm 0.017 (\pm 0.026)$	$0.256 \pm 0.013 (\pm 0.019)$
0.080	0.220	$0.210 \pm 0.008 (\pm 0.008)$	$0.190 \pm 0.006 (\pm 0.007)$
0.080	0.268	$0.209 \pm 0.011 (\pm 0.013)$	$0.210 \pm 0.009 (\pm 0.010)$
0.080	0.280	$0.220 \pm 0.005 (\pm 0.005)$	$0.208 \pm 0.005 (\pm 0.005)$
0.080	0.295	$0.218 \pm 0.011 (\pm 0.013)$	$0.213 \pm 0.009 (\pm 0.010)$
0.080	0.455	$0.263 \pm 0.006 (\pm 0.006)$	$0.243 \pm 0.005 (\pm 0.005)$
0.080	0.500	$0.254 \pm 0.015 (\pm 0.023)$	$0.254 \pm 0.013 (\pm 0.016)$
0.080	0.517	$0.269 \pm 0.006 (\pm 0.006)$	$0.254 \pm 0.005 (\pm 0.005)$
0.080	0.617	$0.292 \pm 0.010 (\pm 0.010)$	$0.265 \pm 0.008 (\pm 0.008)$
0.080	0.618	$0.295 \pm 0.014 (\pm 0.017)$	$0.254 \pm 0.011 (\pm 0.013)$
0.080	0.799	$0.311 \pm 0.013 (\pm 0.013)$	$0.280 \pm 0.010 (\pm 0.010)$
0.080	0.818	$0.321 \pm 0.017 (\pm 0.019)$	$0.277 \pm 0.012 (\pm 0.014)$
0.125	0.588	$0.286 \pm 0.005 (\pm 0.005)$	$0.272 \pm 0.005 (\pm 0.005)$
0.125	0.797	$0.316 \pm 0.009 (\pm 0.009)$	$0.292 \pm 0.007 (\pm 0.007)$
0.125	1.031	$0.330 \pm 0.011 (\pm 0.011)$	$0.302 \pm 0.009 (\pm 0.009)$
0.125	1.056	$0.348 \pm 0.016 (\pm 0.016)$	$0.307 \pm 0.012 (\pm 0.012)$

Table A.8: Continuation of the Table A.7.

$\langle x \rangle$	$\langle Q^2 \rangle$	F_2^C	F_2^{Cu}
0.175	0.483	$0.279 \pm 0.011 (\pm 0.011)$	$0.263 \pm 0.009 (\pm 0.009)$
0.175	0.487	$0.277 \pm 0.006 (\pm 0.006)$	$0.263 \pm 0.005 (\pm 0.005)$
0.175	1.029	$0.322 \pm 0.007 (\pm 0.007)$	$0.297 \pm 0.005 (\pm 0.005)$
0.175	1.045	$0.324 \pm 0.017 (\pm 0.018)$	$0.302 \pm 0.013 (\pm 0.013)$
0.175	1.364	$0.344 \pm 0.013 (\pm 0.013)$	$0.305 \pm 0.010 (\pm 0.010)$
0.250	0.759	$0.300 \pm 0.005 (\pm 0.005)$	$0.256 \pm 0.004 (\pm 0.004)$
0.250	1.332	$0.312 \pm 0.008 (\pm 0.008)$	$0.269 \pm 0.006 (\pm 0.006)$
0.250	1.761	$0.314 \pm 0.010 (\pm 0.010)$	$0.275 \pm 0.007 (\pm 0.007)$
0.350	1.298	$0.277 \pm 0.016 (\pm 0.016)$	$0.210 \pm 0.010 (\pm 0.010)$
0.350	1.329	$0.271 \pm 0.005 (\pm 0.005)$	$0.222 \pm 0.003 (\pm 0.003)$
0.350	1.340	$0.277 \pm 0.008 (\pm 0.008)$	$0.225 \pm 0.005 (\pm 0.005)$
0.350	1.635	$0.268 \pm 0.015 (\pm 0.015)$	$0.225 \pm 0.010 (\pm 0.010)$
0.350	1.720	$0.266 \pm 0.006 (\pm 0.006)$	$0.214 \pm 0.004 (\pm 0.004)$
0.450	0.864	$0.211 \pm 0.003 (\pm 0.003)$	$0.158 \pm 0.002 (\pm 0.002)$
0.450	2.275	$0.206 \pm 0.005 (\pm 0.005)$	$0.157 \pm 0.003 (\pm 0.003)$
0.550	1.511	$0.168 \pm 0.003 (\pm 0.003)$	$0.118 \pm 0.002 (\pm 0.002)$
0.650	2.221	$0.118 \pm 0.002 (\pm 0.002)$	$0.074 \pm 0.001 (\pm 0.001)$
0.750	2.937	$0.064 \pm 0.001 (\pm 0.001)$	$0.035 \pm 0.001 (\pm 0.001)$

Table A.9: Continuation of the Table A.8.

$\langle x \rangle$	$\langle Q^2 \rangle$	F_2^{Au}
0.025	0.211	$0.159 \pm 0.008 (\pm 0.064)$
0.025	0.240	$0.153 \pm 0.007 (\pm 0.042)$
0.040	0.170	$0.146 \pm 0.003 (\pm 0.012)$
0.040	0.273	$0.176 \pm 0.007 (\pm 0.033)$
0.040	0.352	$0.197 \pm 0.006 (\pm 0.020)$
0.040	0.370	$0.206 \pm 0.009 (\pm 0.049)$
0.060	0.420	$0.230 \pm 0.009 (\pm 0.040)$
0.060	0.543	$0.250 \pm 0.008 (\pm 0.028)$
0.080	0.280	$0.210 \pm 0.005 (\pm 0.015)$
0.080	0.455	$0.248 \pm 0.005 (\pm 0.017)$
0.080	0.517	$0.255 \pm 0.005 (\pm 0.016)$

Table A.10: The values of F_2 for gold determined via the model dependent method that are shown in Fig. 5.28.

$\langle x \rangle$	$\langle Q^2 \rangle$	F_2^{Au}
0.080	0.617	$0.269 \pm 0.008 (\pm 0.025)$
0.080	0.618	$0.268 \pm 0.010 (\pm 0.042)$
0.080	0.799	$0.290 \pm 0.010 (\pm 0.032)$
0.125	0.588	$0.272 \pm 0.005 (\pm 0.015)$
0.125	0.797	$0.291 \pm 0.006 (\pm 0.021)$
0.125	1.031	$0.304 \pm 0.008 (\pm 0.026)$
0.125	1.056	$0.314 \pm 0.011 (\pm 0.037)$
0.175	0.487	$0.258 \pm 0.005 (\pm 0.015)$
0.175	1.029	$0.291 \pm 0.005 (\pm 0.017)$
0.175	1.364	$0.301 \pm 0.009 (\pm 0.029)$
0.250	0.759	$0.247 \pm 0.004 (\pm 0.012)$
0.250	1.332	$0.262 \pm 0.006 (\pm 0.019)$
0.250	1.761	$0.262 \pm 0.007 (\pm 0.021)$
0.350	1.329	$0.209 \pm 0.003 (\pm 0.011)$
0.350	1.340	$0.216 \pm 0.005 (\pm 0.016)$
0.350	1.720	$0.199 \pm 0.004 (\pm 0.012)$
0.450	0.864	$0.149 \pm 0.002 (\pm 0.008)$
0.450	2.275	$0.142 \pm 0.003 (\pm 0.009)$
0.550	1.511	$0.097 \pm 0.001 (\pm 0.005)$
0.650	2.221	$0.059 \pm 0.001 (\pm 0.003)$
0.750	2.937	$0.034 \pm 0.001 (\pm 0.002)$

Table A.11: Continuation of the Table A.10.

$\langle x \rangle$	$\langle Q^2 \rangle$	R^H	R^D
0.030	0.059	$0.034 \pm 0.100 (\pm 0.279)$	$0.027 \pm 0.035 (\pm 0.147)$
0.030	0.067	$0.017 \pm 0.099 (\pm 0.145)$	$0.088 \pm 0.051 (\pm 0.087)$
0.030	0.092	$0.219 \pm 0.105 (\pm 0.252)$	$0.133 \pm 0.038 (\pm 0.117)$
0.030	0.095	$0.360 \pm 0.133 (\pm 0.386)$	$0.289 \pm 0.046 (\pm 0.185)$
0.030	0.098	$0.152 \pm 0.143 (\pm 1.076)$	$0.118 \pm 0.039 (\pm 0.419)$
0.030	0.102	$0.190 \pm 0.115 (\pm 0.149)$	$0.266 \pm 0.062 (\pm 0.088)$

Table A.12: The values of R for hydrogen and deuterium determined via the model dependent method that are shown in Fig. 5.14 and Fig. 5.18. The data points that have total uncertainty greater than 0.2 are not shown on the figures.

$\langle x \rangle$	$\langle Q^2 \rangle$	R^H	R^D
0.030	0.104	$0.234 \pm 0.116 (\pm 0.194)$	$0.229 \pm 0.054 (\pm 0.107)$
0.030	0.111	$0.474 \pm 0.185 (\pm 1.300)$	$0.210 \pm 0.037 (\pm 0.358)$
0.030	0.113	$0.274 \pm 0.116 (\pm 0.465)$	$0.251 \pm 0.037 (\pm 0.230)$
0.030	0.126	$0.300 \pm 0.130 (\pm 0.608)$	$0.185 \pm 0.038 (\pm 0.256)$
0.030	0.132	$0.296 \pm 0.100 (\pm 0.205)$	$0.190 \pm 0.039 (\pm 0.094)$
0.030	0.140	$0.271 \pm 0.112 (\pm 0.167)$	$0.229 \pm 0.053 (\pm 0.088)$
0.030	0.144	$0.375 \pm 0.125 (\pm 0.494)$	$0.250 \pm 0.039 (\pm 0.218)$
0.030	0.151	$0.268 \pm 0.147 (\pm 1.219)$	$0.216 \pm 0.040 (\pm 0.442)$
0.030	0.163	$0.317 \pm 0.107 (\pm 0.336)$	$0.252 \pm 0.041 (\pm 0.169)$
0.030	0.171	$0.323 \pm 0.100 (\pm 0.217)$	$0.262 \pm 0.042 (\pm 0.110)$
0.030	0.171	$0.573 \pm 0.186 (\pm 1.370)$	$0.217 \pm 0.039 (\pm 0.328)$
0.030	0.178	$0.454 \pm 0.116 (\pm 0.393)$	$0.347 \pm 0.039 (\pm 0.180)$
0.030	0.186	$0.301 \pm 0.098 (\pm 0.251)$	$0.226 \pm 0.041 (\pm 0.127)$
0.030	0.195	$0.562 \pm 0.152 (\pm 0.857)$	$0.274 \pm 0.036 (\pm 0.272)$
0.030	0.211	$0.183 \pm 0.084 (\pm 0.166)$	$0.235 \pm 0.045 (\pm 0.105)$
0.030	0.222	$0.338 \pm 0.106 (\pm 0.430)$	$0.255 \pm 0.037 (\pm 0.203)$
0.030	0.240	$0.215 \pm 0.090 (\pm 0.144)$	$0.239 \pm 0.049 (\pm 0.089)$
0.030	0.252	$0.355 \pm 0.097 (\pm 0.332)$	$0.191 \pm 0.034 (\pm 0.143)$
0.030	0.252	$0.536 \pm 0.146 (\pm 0.956)$	$0.335 \pm 0.037 (\pm 0.329)$
0.030	0.273	$0.181 \pm 0.090 (\pm 0.120)$	$0.240 \pm 0.053 (\pm 0.078)$
0.030	0.286	$0.267 \pm 0.086 (\pm 0.224)$	$0.168 \pm 0.036 (\pm 0.110)$
0.030	0.287	$0.507 \pm 0.126 (\pm 0.629)$	$0.241 \pm 0.034 (\pm 0.218)$
0.030	0.371	$0.419 \pm 0.097 (\pm 0.310)$	$0.245 \pm 0.035 (\pm 0.136)$
0.030	0.379	$0.428 \pm 0.105 (\pm 0.521)$	$0.209 \pm 0.030 (\pm 0.195)$
0.050	0.150	$0.257 \pm 0.148 (\pm 0.212)$	$0.295 \pm 0.115 (\pm 0.147)$
0.050	0.170	$0.251 \pm 0.182 (\pm 0.186)$	$0.219 \pm 0.099 (\pm 0.102)$
0.050	0.175	$0.308 \pm 0.112 (\pm 0.218)$	$0.207 \pm 0.081 (\pm 0.125)$
0.050	0.180	$0.343 \pm 0.096 (\pm 0.169)$	$0.227 \pm 0.041 (\pm 0.080)$
0.050	0.352	$0.209 \pm 0.113 (\pm 0.121)$	$0.290 \pm 0.073 (\pm 0.081)$
0.050	0.370	$0.269 \pm 0.082 (\pm 0.142)$	$0.258 \pm 0.044 (\pm 0.086)$
0.050	0.420	$0.238 \pm 0.082 (\pm 0.116)$	$0.242 \pm 0.046 (\pm 0.072)$
0.050	0.479	$0.283 \pm 0.076 (\pm 0.155)$	$0.185 \pm 0.035 (\pm 0.082)$
0.050	0.491	$0.303 \pm 0.078 (\pm 0.243)$	$0.128 \pm 0.030 (\pm 0.108)$
0.075	0.220	$0.194 \pm 0.097 (\pm 0.104)$	$0.381 \pm 0.069 (\pm 0.076)$

Table A.13: Continuation of the Table A.12.

$\langle x \rangle$	$\langle Q^2 \rangle$	R^H	R^D
0.075	0.268	$0.379 \pm 0.090 (\pm 0.130)$	$0.316 \pm 0.044 (\pm 0.069)$
0.075	0.273	$0.461 \pm 0.107 (\pm 0.170)$	$0.298 \pm 0.079 (\pm 0.103)$
0.075	0.280	$0.259 \pm 0.174 (\pm 0.175)$	$0.275 \pm 0.104 (\pm 0.105)$
0.075	0.283	$0.417 \pm 0.085 (\pm 0.144)$	$0.275 \pm 0.066 (\pm 0.088)$
0.075	0.295	$0.378 \pm 0.089 (\pm 0.122)$	$0.338 \pm 0.045 (\pm 0.067)$
0.075	0.455	$0.269 \pm 0.173 (\pm 0.174)$	$0.298 \pm 0.107 (\pm 0.108)$
0.075	0.500	$0.437 \pm 0.083 (\pm 0.162)$	$0.297 \pm 0.037 (\pm 0.082)$
0.075	0.543	$0.242 \pm 0.094 (\pm 0.103)$	$0.205 \pm 0.052 (\pm 0.060)$
0.075	0.617	$0.247 \pm 0.106 (\pm 0.109)$	$0.208 \pm 0.059 (\pm 0.063)$
0.075	0.618	$0.248 \pm 0.076 (\pm 0.102)$	$0.214 \pm 0.041 (\pm 0.061)$
0.075	0.633	$0.275 \pm 0.071 (\pm 0.142)$	$0.098 \pm 0.031 (\pm 0.067)$
0.100	0.508	$0.400 \pm 0.076 (\pm 0.181)$	$0.238 \pm 0.059 (\pm 0.105)$
0.100	0.517	$0.388 \pm 0.257 (\pm 0.257)$	$0.433 \pm 0.164 (\pm 0.164)$
0.100	0.588	$0.649 \pm 0.488 (\pm 0.488)$	$0.673 \pm 0.301 (\pm 0.302)$
0.100	0.797	$0.280 \pm 0.151 (\pm 0.151)$	$0.283 \pm 0.091 (\pm 0.091)$
0.100	0.799	$0.252 \pm 0.085 (\pm 0.091)$	$0.199 \pm 0.048 (\pm 0.053)$
0.100	0.818	$0.212 \pm 0.067 (\pm 0.089)$	$0.120 \pm 0.035 (\pm 0.050)$
0.100	1.031	$0.293 \pm 0.116 (\pm 0.116)$	$0.339 \pm 0.072 (\pm 0.073)$
0.100	1.056	$0.185 \pm 0.074 (\pm 0.078)$	$0.122 \pm 0.041 (\pm 0.044)$
0.175	0.476	$0.275 \pm 0.191 (\pm 0.193)$	$0.167 \pm 0.164 (\pm 0.164)$
0.175	0.483	$0.279 \pm 0.095 (\pm 0.095)$	$0.235 \pm 0.053 (\pm 0.054)$
0.175	0.487	$0.288 \pm 0.272 (\pm 0.272)$	$0.320 \pm 0.171 (\pm 0.172)$
0.175	1.029	$0.402 \pm 0.279 (\pm 0.279)$	$0.436 \pm 0.175 (\pm 0.175)$
0.175	1.045	$0.321 \pm 0.075 (\pm 0.079)$	$0.234 \pm 0.040 (\pm 0.042)$
0.175	1.364	$0.232 \pm 0.091 (\pm 0.091)$	$0.183 \pm 0.051 (\pm 0.051)$
0.250	1.045	$0.314 \pm 0.068 (\pm 0.075)$	$0.178 \pm 0.057 (\pm 0.061)$
0.250	1.332	$0.321 \pm 0.154 (\pm 0.154)$	$0.282 \pm 0.092 (\pm 0.092)$
0.250	1.761	$0.313 \pm 0.131 (\pm 0.131)$	$0.215 \pm 0.069 (\pm 0.069)$
0.325	1.300	$0.285 \pm 0.086 (\pm 0.086)$	$0.277 \pm 0.082 (\pm 0.082)$
0.325	1.340	$0.177 \pm 0.124 (\pm 0.124)$	$0.336 \pm 0.093 (\pm 0.093)$
0.325	1.635	$0.279 \pm 0.065 (\pm 0.068)$	$0.183 \pm 0.034 (\pm 0.034)$
0.325	1.670	$0.282 \pm 0.066 (\pm 0.068)$	$0.169 \pm 0.052 (\pm 0.052)$
0.325	1.720	$0.400 \pm 0.276 (\pm 0.276)$	$0.306 \pm 0.147 (\pm 0.147)$
0.400	1.298	$0.276 \pm 0.058 (\pm 0.058)$	$0.283 \pm 0.035 (\pm 0.035)$
0.400	2.275	$0.302 \pm 0.185 (\pm 0.185)$	$0.106 \pm 0.083 (\pm 0.083)$

Table A.14: Continuation of the Table A.13.

$\langle Q^2 \rangle$	$\langle x \rangle$	R^C
0.096	0.027	$0.135 \pm 0.080 (\pm 0.119)$
0.121	0.026	$0.170 \pm 0.076 (\pm 0.102)$
0.174	0.030	$0.197 \pm 0.060 (\pm 0.093)$
0.252	0.044	$0.183 \pm 0.048 (\pm 0.052)$
0.353	0.047	$0.215 \pm 0.050 (\pm 0.056)$
0.450	0.096	$0.181 \pm 0.057 (\pm 0.057)$
0.557	0.093	$0.211 \pm 0.045 (\pm 0.045)$
0.634	0.082	$0.269 \pm 0.045 (\pm 0.045)$
0.770	0.103	$0.265 \pm 0.055 (\pm 0.055)$
0.836	0.111	$0.247 \pm 0.054 (\pm 0.054)$
1.635	0.311	$0.129 \pm 0.041 (\pm 0.041)$

Table A.15: The values of R for carbon determined via the model dependent method that are shown in Fig. 5.25.

$\langle Q^2 \rangle$	$\langle x \rangle$	R^{Cu}
0.128	0.027	$0.121 \pm 0.083 (\pm 0.119)$
0.174	0.032	$0.086 \pm 0.051 (\pm 0.053)$
0.252	0.043	$0.152 \pm 0.045 (\pm 0.046)$
0.356	0.046	$0.263 \pm 0.050 (\pm 0.050)$
0.461	0.081	$0.214 \pm 0.046 (\pm 0.046)$
0.543	0.087	$0.271 \pm 0.048 (\pm 0.048)$
0.634	0.085	$0.310 \pm 0.051 (\pm 0.051)$
0.766	0.110	$0.306 \pm 0.060 (\pm 0.060)$
0.834	0.109	$0.295 \pm 0.056 (\pm 0.056)$
0.978	0.153	$0.254 \pm 0.051 (\pm 0.051)$
1.199	0.213	$0.182 \pm 0.040 (\pm 0.040)$
1.692	0.293	$0.109 \pm 0.039 (\pm 0.039)$

Table A.16: The values of R for copper determined via the model dependent method that are shown in Fig. 5.25.

$\langle Q^2 \rangle$	$\langle x \rangle$	R^{Au}
0.171	0.047	$0.072 \pm 0.095 (\pm 0.096)$
0.258	0.043	$0.183 \pm 0.066 (\pm 0.067)$
0.364	0.048	$0.286 \pm 0.057 (\pm 0.058)$
0.455	0.088	$0.261 \pm 0.061 (\pm 0.061)$
0.550	0.094	$0.323 \pm 0.061 (\pm 0.061)$
0.630	0.092	$0.315 \pm 0.060 (\pm 0.061)$
0.757	0.148	$0.268 \pm 0.062 (\pm 0.062)$
0.835	0.116	$0.304 \pm 0.059 (\pm 0.059)$
0.977	0.144	$0.251 \pm 0.059 (\pm 0.059)$
1.222	0.212	$0.213 \pm 0.054 (\pm 0.054)$
1.739	0.297	$0.232 \pm 0.083 (\pm 0.083)$
2.275	0.403	$0.138 \pm 0.099 (\pm 0.099)$

Table A.17: The values of R for gold determined via the model dependent method that are shown in Fig. 5.25.

$\langle Q^2 \rangle$	$\langle x \rangle$	$\langle W^2 \rangle$	R^H	R^D
1.670	0.320	4.429	$0.283 \pm 0.066 (\pm 0.068)$	$0.170 \pm 0.052 (\pm 0.052)$
1.300	0.364	3.151	$0.278 \pm 0.084 (\pm 0.084)$	$0.271 \pm 0.080 (\pm 0.080)$
1.045	0.200	5.060	$0.332 \pm 0.072 (\pm 0.080)$	$0.179 \pm 0.057 (\pm 0.061)$
0.508	0.091	5.954	$0.405 \pm 0.077 (\pm 0.183)$	$0.241 \pm 0.059 (\pm 0.106)$
0.476	0.156	3.455	$0.282 \pm 0.196 (\pm 0.197)$	$0.169 \pm 0.166 (\pm 0.166)$
0.283	0.081	4.091	$0.414 \pm 0.084 (\pm 0.143)$	$0.273 \pm 0.065 (\pm 0.088)$
0.273	0.077	4.152	$0.460 \pm 0.107 (\pm 0.169)$	$0.297 \pm 0.079 (\pm 0.103)$
0.175	0.050	4.205	$0.308 \pm 0.112 (\pm 0.218)$	$0.207 \pm 0.081 (\pm 0.125)$
0.150	0.041	4.388	$0.259 \pm 0.150 (\pm 0.214)$	$0.295 \pm 0.115 (\pm 0.147)$

$\langle Q^2 \rangle$	$\langle x \rangle$	$\langle W^2 \rangle$	R^C	R^{Cu}
1.670	0.320	4.429	-	$0.086 \pm 0.048 (\pm 0.048)$
1.300	0.364	3.151	-	$0.316 \pm 0.084 (\pm 0.084)$
1.045	0.200	5.060	-	$0.183 \pm 0.055 (\pm 0.061)$
0.508	0.091	5.954	-	$0.230 \pm 0.056 (\pm 0.104)$
0.476	0.156	3.455	$0.270 \pm 0.186 (\pm 0.187)$	$0.188 \pm 0.171 (\pm 0.172)$

Table A.18: The values of R for hydrogen, deuterium, carbon and copper determined via the Rosenbluth separation that are shown in Figs. 5.14, 5.18, 5.25.

$\langle Q^2 \rangle$	$\langle x \rangle$	$\langle W^2 \rangle$	R^C	R^{Cu}
0.283	0.081	4.091	-	$0.147 \pm 0.056 (\pm 0.075)$
0.273	0.077	4.152	-	$0.152 \pm 0.067 (\pm 0.086)$
0.175	0.050	4.205	-	-
0.150	0.041	4.388	-	$0.116 \pm 0.163 (\pm 0.216)$

Table A.19: Continuation of the Table A.18.

$\langle Q^2 \rangle$	$\langle x \rangle$	$\langle W^2 \rangle$	R^{Au}
1.300	0.364	3.151	$0.091 \pm 0.091 (\pm 0.091)$

Table A.20: The values of R for gold determined via the Rosenbluth separation that are shown in Fig. 5.25.

Appendix B

Tables of the Cross Section Ratios

The first error in all tables represents the combined statistical and systematic uncertainties without the one due to the α^2 term and the second one represents the total uncertainty.

$\langle x \rangle$	$\langle Q^2 \rangle$	σ^D/σ^H
0.433	2.365	$0.795 \pm 0.015 (\pm 0.015)$
0.349	1.559	$0.824 \pm 0.014 (\pm 0.014)$
0.279	1.575	$0.847 \pm 0.016 (\pm 0.016)$
0.219	1.191	$0.871 \pm 0.016 (\pm 0.016)$
0.176	0.922	$0.894 \pm 0.017 (\pm 0.017)$
0.130	0.819	$0.902 \pm 0.017 (\pm 0.017)$
0.097	0.665	$0.924 \pm 0.018 (\pm 0.018)$
0.082	0.444	$0.934 \pm 0.018 (\pm 0.018)$
0.069	0.465	$0.936 \pm 0.019 (\pm 0.019)$
0.053	0.383	$0.944 \pm 0.020 (\pm 0.020)$
0.044	0.323	$0.948 \pm 0.020 (\pm 0.020)$
0.034	0.228	$0.954 \pm 0.021 (\pm 0.022)$
0.027	0.211	$0.964 \pm 0.025 (\pm 0.027)$
0.022	0.155	$0.952 \pm 0.026 (\pm 0.028)$
0.017	0.131	$0.968 \pm 0.034 (\pm 0.040)$
0.013	0.124	$1.008 \pm 0.053 (\pm 0.111)$
0.010	0.075	$0.856 \pm 0.050 (\pm 0.064)$
0.009	0.063	$0.901 \pm 0.052 (\pm 0.074)$
0.008	0.066	$0.847 \pm 0.067 (\pm 0.110)$

Table B.1: The values of the ratio σ^D/σ^H that are shown in Fig. 5.29.

$\langle x \rangle$	$\langle Q^2 \rangle$	σ^D / σ^H
0.008	0.033	$0.879 \pm 0.054 (\pm 0.075)$
0.008	0.050	$0.917 \pm 0.068 (\pm 0.133)$
0.008	0.088	$0.844 \pm 0.071 (\pm 0.158)$
0.012	0.035	$0.836 \pm 0.049 (\pm 0.063)$
0.012	0.109	$1.012 \pm 0.064 (\pm 0.155)$
0.017	0.059	$0.941 \pm 0.035 (\pm 0.041)$
0.017	0.097	$0.976 \pm 0.037 (\pm 0.049)$
0.017	0.155	$0.976 \pm 0.036 (\pm 0.059)$
0.025	0.067	$0.945 \pm 0.029 (\pm 0.033)$
0.025	0.108	$0.962 \pm 0.025 (\pm 0.028)$
0.025	0.228	$0.953 \pm 0.024 (\pm 0.027)$
0.035	0.102	$0.948 \pm 0.026 (\pm 0.027)$
0.035	0.136	$0.969 \pm 0.025 (\pm 0.027)$
0.035	0.176	$0.965 \pm 0.030 (\pm 0.040)$
0.035	0.309	$0.937 \pm 0.022 (\pm 0.023)$
0.050	0.171	$0.959 \pm 0.021 (\pm 0.021)$
0.050	0.371	$0.927 \pm 0.019 (\pm 0.020)$
0.050	0.464	$0.965 \pm 0.022 (\pm 0.023)$
0.070	0.219	$0.914 \pm 0.021 (\pm 0.021)$
0.070	0.269	$0.942 \pm 0.019 (\pm 0.019)$
0.070	0.446	$0.925 \pm 0.019 (\pm 0.019)$
0.070	0.562	$0.947 \pm 0.020 (\pm 0.021)$
0.070	0.639	$0.967 \pm 0.022 (\pm 0.023)$
0.090	0.293	$0.936 \pm 0.019 (\pm 0.019)$
0.090	0.499	$0.931 \pm 0.018 (\pm 0.018)$
0.090	0.632	$0.925 \pm 0.020 (\pm 0.020)$
0.090	0.794	$0.943 \pm 0.021 (\pm 0.021)$
0.110	0.564	$0.914 \pm 0.018 (\pm 0.018)$
0.110	0.807	$0.916 \pm 0.018 (\pm 0.018)$
0.110	1.013	$0.932 \pm 0.021 (\pm 0.021)$
0.140	0.464	$0.909 \pm 0.018 (\pm 0.018)$
0.140	0.620	$0.904 \pm 0.018 (\pm 0.018)$
0.140	0.840	$0.896 \pm 0.019 (\pm 0.019)$

Table B.2: The values of the ratio σ^D / σ^H that are shown in Fig. 5.30 and in Fig. 5.31.

$\langle x \rangle$	$\langle Q^2 \rangle$	σ^D / σ^H
0.140	1.062	$0.885 \pm 0.018 (\pm 0.018)$
0.180	0.503	$0.913 \pm 0.018 (\pm 0.018)$
0.180	0.706	$0.890 \pm 0.018 (\pm 0.018)$
0.180	0.998	$0.880 \pm 0.017 (\pm 0.017)$
0.180	1.339	$0.885 \pm 0.017 (\pm 0.017)$
0.225	0.740	$0.876 \pm 0.017 (\pm 0.017)$
0.225	1.081	$0.858 \pm 0.017 (\pm 0.017)$
0.225	1.365	$0.870 \pm 0.017 (\pm 0.017)$
0.225	1.673	$0.877 \pm 0.018 (\pm 0.018)$
0.275	0.774	$0.836 \pm 0.017 (\pm 0.017)$
0.275	1.236	$0.830 \pm 0.017 (\pm 0.017)$
0.275	1.710	$0.865 \pm 0.016 (\pm 0.016)$
0.350	1.300	$0.834 \pm 0.015 (\pm 0.015)$
0.350	1.710	$0.827 \pm 0.015 (\pm 0.015)$
0.350	2.184	$0.824 \pm 0.016 (\pm 0.016)$
0.450	2.366	$0.788 \pm 0.014 (\pm 0.014)$

Table B.3: Continuation of the Table B.2.

$\langle x \rangle$	σ^C / σ^D	σ^{Cu} / σ^D	σ^{Au} / σ^D
0.450	-	$0.965 \pm 0.017 (\pm 0.017)$	$0.940 \pm 0.017 (\pm 0.017)$
0.350	$1.018 \pm 0.020 (\pm 0.020)$	$0.996 \pm 0.017 (\pm 0.017)$	$0.982 \pm 0.015 (\pm 0.015)$
0.275	$1.015 \pm 0.026 (\pm 0.026)$	$1.007 \pm 0.018 (\pm 0.018)$	$1.012 \pm 0.019 (\pm 0.019)$
0.225	$1.043 \pm 0.021 (\pm 0.021)$	$1.039 \pm 0.018 (\pm 0.018)$	$1.034 \pm 0.019 (\pm 0.019)$
0.175	$1.050 \pm 0.020 (\pm 0.020)$	$1.034 \pm 0.019 (\pm 0.019)$	$1.020 \pm 0.019 (\pm 0.019)$
0.130	$1.047 \pm 0.020 (\pm 0.020)$	$1.040 \pm 0.019 (\pm 0.019)$	$1.039 \pm 0.020 (\pm 0.020)$
0.100	$0.992 \pm 0.019 (\pm 0.019)$	$1.018 \pm 0.018 (\pm 0.018)$	$1.023 \pm 0.020 (\pm 0.020)$
0.082	$1.032 \pm 0.019 (\pm 0.019)$	$1.028 \pm 0.019 (\pm 0.019)$	$1.017 \pm 0.020 (\pm 0.020)$
0.067	$1.004 \pm 0.019 (\pm 0.019)$	$0.994 \pm 0.019 (\pm 0.019)$	$1.003 \pm 0.021 (\pm 0.021)$
0.055	$1.034 \pm 0.020 (\pm 0.020)$	$0.997 \pm 0.019 (\pm 0.019)$	$0.983 \pm 0.021 (\pm 0.021)$
0.045	$1.010 \pm 0.021 (\pm 0.021)$	$0.975 \pm 0.019 (\pm 0.019)$	$0.966 \pm 0.021 (\pm 0.021)$
0.035	$0.996 \pm 0.020 (\pm 0.020)$	$0.964 \pm 0.021 (\pm 0.022)$	$0.939 \pm 0.027 (\pm 0.032)$

Table B.4: The values of the ratios σ^C / σ^D , σ^{Cu} / σ^D and σ^{Au} / σ^D that are shown in Fig. 5.36.

$< x >$	σ^C/σ^D	σ^{Cu}/σ^D	σ^{Au}/σ^D
0.027	$0.963 \pm 0.027 (\pm 0.031)$	$0.915 \pm 0.029 (\pm 0.040)$	$1.002 \pm 0.047 (\pm 0.063)$
0.022	$0.949 \pm 0.028 (\pm 0.036)$	$0.885 \pm 0.041 (\pm 0.054)$	-
0.017	$0.859 \pm 0.043 (\pm 0.073)$	-	-

Table B.5: Continuation of the Table C.1.

Appendix C

Tables of the Ratios of the Structure Functions and R

The first error in all tables represents the combined statistical and systematic uncertainties without the one due to the α^2 term and the second one represents the total uncertainty.

$< x >$	F_2^C/F_2^D	F_2^{Cu}/F_2^D	F_2^{Au}/F_2^D
0.364	-	$1.002 \pm 0.034 (\pm 0.034)$	$0.953 \pm 0.033 (\pm .033)$
0.320	-	$1.010 \pm 0.030 (\pm 0.030)$	-
0.200	-	$1.066 \pm 0.033 (\pm 0.032)$	-
0.156	$1.108 \pm 0.080 (\pm 0.080)$	$1.082 \pm 0.078 (\pm 0.078)$	-
0.091	-	$1.032 \pm 0.032 (\pm 0.032)$	-
0.081	-	$0.999 \pm 0.035 (\pm 0.035)$	-
0.077	-	$0.993 \pm 0.035 (\pm 0.035)$	-
0.050	-	$0.961 \pm 0.040 (\pm 0.041)$	-
0.041	-	$0.935 \pm 0.051 (\pm 0.053)$	-

Table C.1: The values of the ratios F_2^C/F_2^D , F_2^{Cu}/F_2^D and F_2^{Au}/F_2^D determined via the Rosenbluth separation that are shown in Fig. 5.36.

A	Method	$< Q^2 >$	$< x >$	R^A/R^D
C	Ros. Sep.	0.476	0.156	$1.599 \pm 1.921 (\pm 1.921)$
C	Mod. Dep.	1.029	0.195	$0.214 \pm 1.732 (\pm 1.732)$
C	Mod. Dep.	0.797	0.123	$0.781 \pm 0.725 (\pm 0.725)$

Table C.2: The values of the ratios R^C/R^D , R^{Cu}/R^D and R^{Au}/R^D determined via the Rosenbluth separation and via the model dependent method that are shown in Fig. 5.37.

A	Method	$\langle Q^2 \rangle$	$\langle x \rangle$	R^A/R^D
C	Mod. Dep.	0.591	0.086	$1.394 \pm 0.312 (\pm 0.312)$
C	Mod. Dep.	0.438	0.062	$0.910 \pm 0.354 (\pm 0.354)$
C	Mod. Dep.	0.361	0.046	$0.845 \pm 0.416 (\pm 0.421)$
C	Mod. Dep.	0.241	0.029	$0.650 \pm 0.378 (\pm 0.381)$
Cu	Ros. Sep.	1.670	0.320	$0.507 \pm 0.324 (\pm 0.324)$
Cu	Ros. Sep.	1.300	0.364	$1.168 \pm 0.465 (\pm 0.465)$
Cu	Ros. Sep.	1.045	0.200	$1.022 \pm 0.452 (\pm 0.452)$
Cu	Ros. Sep.	0.508	0.091	$0.955 \pm 0.332 (\pm 0.339)$
Cu	Ros. Sep.	0.476	0.156	$1.116 \pm 1.496 (\pm 1.496)$
Cu	Ros. Sep.	0.283	0.081	$0.540 \pm 0.244 (\pm 0.265)$
Cu	Ros. Sep.	0.273	0.077	$0.512 \pm 0.264 (\pm 0.284)$
Cu	Ros. Sep.	0.150	0.041	$0.393 \pm 0.576 (\pm 0.696)$
Cu	Mod. Dep.	1.705	0.303	$0.450 \pm 0.611 (\pm 0.611)$
Cu	Mod. Dep.	1.331	0.253	$0.731 \pm 0.293 (\pm 0.293)$
Cu	Mod. Dep.	1.040	0.165	$0.961 \pm 0.363 (\pm 0.363)$
Cu	Mod. Dep.	0.804	0.105	$1.761 \pm 0.390 (\pm 0.390)$
Cu	Mod. Dep.	0.574	0.085	$1.374 \pm 0.256 (\pm 0.256)$
Cu	Mod. Dep.	0.466	0.077	$1.733 \pm 0.296 (\pm 0.296)$
Cu	Mod. Dep.	0.368	0.042	$1.472 \pm 0.277 (\pm 0.278)$
Cu	Mod. Dep.	0.258	0.046	$0.928 \pm 0.293 (\pm 0.294)$
Cu	Mod. Dep.	0.157	0.030	$1.217 \pm 0.397 (\pm 0.399)$
Cu	Mod. Dep.	0.079	0.024	$1.217 \pm 1.175 (\pm 3.558)$
Au	Ros. Sep.	1.300	0.364	$0.334 \pm 0.348 (\pm 0.349)$
Au	Mod. Dep.	1.741	0.299	$1.226 \pm 0.602 (\pm 0.602)$
Au	Mod. Dep.	1.341	0.279	$1.156 \pm 0.491 (\pm 0.491)$
Au	Mod. Dep.	1.039	0.154	$1.246 \pm 0.419 (\pm 0.419)$
Au	Mod. Dep.	0.785	0.155	$1.390 \pm 0.419 (\pm 0.419)$
Au	Mod. Dep.	0.577	0.088	$1.498 \pm 0.317 (\pm 0.317)$
Au	Mod. Dep.	0.454	0.096	$1.140 \pm 0.367 (\pm 0.367)$
Au	Mod. Dep.	0.361	0.046	$1.077 \pm 0.349 (\pm 0.356)$
Au	Mod. Dep.	0.264	0.046	$0.945 \pm 0.415 (\pm 0.415)$
Au	Mod. Dep.	0.170	0.046	$0.293 \pm 2.000 (\pm 2.003)$

Table C.3: Continuation of the Table C.2.

Bibliography

- [1] R. P. Feynman, Photo-Hadron Interactions, W. A. Benjamin Inc. Reading, MA (1976).
- [2] K. Hagiwara et al., Phys. Rev. D 66 (2002).
- [3] V. N. Gribov and L. N. Lipatov. Deep Inelastic ep Scattering in Perturbation Theory. Yad. Fiz., 15, 781, (1972)
- [4] Y. L. Dokshitzer, Sov. Phys. JETP, 46, 1977, 641
- [5] G. Altarelli and G. Parisi. Asymptotic Freedom in Parton Language. Nucl. Phys., B126, 298, (1977).
- [6] B. Badelek and J. Kwiecinski, Warsaw University Preprint, IFD, 1, (1994).
- [7] M. Arneodo, et al., (NMC), Phys. Lett. B 309, 222, (1993).
- [8] M. Arneodo, Nuclear Effects in Structure Functions, Phys. Reports 240, 301-393, (1994).
- [9] L. W. Whiltow, Ph.D Thesis, Deep Inelastic
- [10] K. Ackerstaff et al., Phys. Lett. B 475, 386, (2000); Erratum, A. Airapetian et al., hep-ex/0210067.
- [11] Jeroen J. van Hunen, Deep-Inelastic Scattering of 14N, Ph.D Thesis, 1999.
- [12] Measurement of $R = \sigma_L/\sigma_T$ in Deep-Inelastic Scattering on Nuclei, HERMES Collaboration, ISSN 0418-9833, (2002).
- [13] A. Airapetian, et al., Measurements of $R = \sigma_L/\sigma_T$ in Deep - Inelastic Scattering on Nuclei, hep-ex/0210068, v1, (2002).
- [14] F. E. Close, An Introduction to Quarks and Partons, (1979).
- [15] F. Halzen, A. D. Martin, Quarks and Leptons, (1984).
- [16] J. Freidman and H. Kendall, Ann. Rev. Nul. Sci. 22, 203, (1972).
- [17] J. P. Bjorken, Phys. Rev. 120, 1547, (1963)
- [18] S. Dasu et al., Phys. Rev. Lett. 60 (1988) 2591; 61, 1061, (1988).

- [19] J. J. Aubert et al., Nucl. Phys. B 259 (1985) 189; B 293, 740, (1987) .
- [20] A. C. Benvenuti et al., Phys. Lett. B 223 (1989) 485; B237, 592, (1990).
- [21] P. Berge et al., Preprint CERN-EP/89-103 (1989), submitted to Z. Phys. C.
- [22] M. Gluck, E. Reya, M. Stratmann and W. Vogelsang, Phys. Rev. D 53, 4775, (1996).
- [23] k. Wilson, Phys. Rev. 179, 1499, (1969).
- [24] A. Buras et al., Rev. Mod. Phys. 52, 199, (1980).
- [25] J. L. Miramontes and J. Sanchez Guillen, Z. Phys. C 41, 247, (1988).
- [26] H. Georgi and H. Politzer, Phys. Rev. D 14, 1829, (1976).
- [27] O. Nachtmann, Nucl. Phys., B 63, 237, (1973).
- [28] U. K. Yang and A. Bodek, Phys. Rev. Lett. 82, 2467, (1999).
- [29] U. K. Yang and A. Bodek, hep-ex/9908058, v3, (1999).
- [30] J. J. Sakurai, Phys. Rev. Lett. 22, 981, (1969).
- [31] T. H. Bauer et al., Rev. Mod. Phys. 50, 261, (1978).
- [32] M. Staszek, J. Rozynek and G. Wilk, Phys. Rev. D29, 2638, (1984).
- [33] E. L. Berger, F. Coester and R. B. Wiringa, Phys. Rev. D 29, 398, (1984).
- [34] E. L. Berger and F. Coester, Phys. Rev. D 32, 1071, (1985).
- [35] B. L. Friman, V. R. Pandharipande and R. B. Wiringa, Phys. Rev. Lett. 51, 763, (1983).
- [36] D. M. Alde et al., Phys. Rev. Lett. 64, 2479, (1990).
- [37] V. Barone et al., Preprint DFTT-14/92, University of Torino, Dept. of Theoretical Physics, Preprint 53 - 92, University of Perugia, Dept. of Physics (1992), to appear in Z. Phys. C.
- [38] F. E. Close, R. G. Roberts and G. C. Ross, Phys. Lett. 129 B, 346, (1983).
- [39] R. L. Jaffe et al., Phys. Lett. 134 B, 449, (1984).
- [40] F. E. Close et al., Phys. Rev. D 31, 1004, (1985).
- [41] SLAC E139, R. G. Arnold et al., Phys. Rev. Lett. 52, 727, (1984). R. G. Arnold et al., SLAC Report SLAC-PUB-3257 (1983).
- [42] A. W. Hendry, D. B. Lichtenberg and E. Predazzi, Phys. Lett. 136 B, 433 (1984).
- [43] Ingo Sick, Phys. Lett. 157 B, 13, (1985).

- [44] R. L. Jaffe, Phys. Rev. Lett. 50, 228, (1983).
- [45] D. Sivers et al., Phys. Rep. 23, (1976).
- [46] D. Sivers, Annu. Rev. Nucl. Part. Sci. 32, 149, (1982).
- [47] C. E. Carlson and T. J. Havens, Phys. Rev. Lett. 51, 261, (1983).
- [48] L. Stodolsky, Phys. Rev. Lett. 18, 135, (1967).
- [49] N. N. Nikolaev and V. I. Zakharov, Phys. Lett. 55 B, 397, (1975).
- [50] E. L. Berger and J. Qiu, Phys. Lett. B 206, 141, (1988).
- [51] CERN NA2'/EMC, J. Ashman et al., Phys. Lett. B 202, 603, (1988).
- [52] CERN NA2'/EMC, J. Ashman et al., Z. Phys. C 57, 211, (1993).
- [53] S. Dasu et al., Phys. Rev. D49, 5641, (1994).
- [54] Amaudruz, et al., (NMC), Phys. Lett. B 294, 120, (1992); and M. Arneodo et. al., (NMC), Phys. Lett. B 481, 23, (1996).
- [55] U. K. Yang et al., Phys. Rev. Lett. 87, 251802, (2001).
- [56] G. A. Miller, S. J. Brodsky and M. Karliner, hep-ph/0002156, v3, (2000).
- [57] M. Ericson and S. Kumano, hep-ph/0212001, v1, (2002).
- [58] S. Kumano, hep-ph/0307105, v1, (2003).
- [59] H. Abramowicz and A. Levy, hep-ph/9712415, v1, (1997).
- [60] A. Donnachie, P. V. Landshoff, Z. Phys. C 61, 139 - 145, (1994).
- [61] C. E. Keppel, Ph. D. Thesis, American University, (1994).
- [62] J. Gomez et al., Measurement of the A-Dependence of Deep-Inelastic Electron Scattering, SLAC-PUB-5813, (2001).
- [63] M. Arneodo, et al., (NMC), Nucl. Phys. B 487, 3, (1997).
- [64] M. A. Niculescu, Ph.D Thesis, Inclusive Resonance Electroproduction Data from Hydrogen and Deuterium and Studies of Quark-Hadron Duality, (1999).
- [65] J. Gomez et al. Measurement of the A dependence of deep-inelastic electron scattering, Phys. Rev. D 49, 4348, (1994).
- [66] M. Arneodo, et al., The Structure Function ratios F_2^{Li}/F_2^D and F_2^C/F_2^D at small x , Nucl. Phys. B 441, 12-30, (1995).

- [67] M. Arneodo, et al., The A Dependence of the Nuclear Structure Function ratios, Nucl. Phys. B 481, 3-22, (1996).
- [68] E. G. Floratov, D. S. Ross, C. T. Sachrada, Nucl. Phys. B129, 66, (1977). E. G. Floratov, D. S. Ross, C. T. Sachrada, Nucl. Phys. B139, 545, (1978) A. Gonzales-Arrayo, C. Lopez, F. J. Yndurain, Nucl. Phys. B153, 161, (1979)
- [69] G. Altarelli and G. Martinelli, Phys. lett. B 76, 89, (1978).
- [70] R. K. Ellis, W. Futmanski and R. Petronzio, Nucl. Phys. B 207, 1, (1982). Structure Functions For Electron Scattering on Hydrogen, Deuterium and Iron, (1990).
- [71] Antje Bruell, private communication.
- [72] P. Amaudruz et al., Z. Phys. C 51, 387, (1991).
- [73] L. L. Frankfurt and. M. I. Strikman, Phys. Rep. 160, 235, (1988).
- [74] L. L. Frankfurt and. M. I. Strikman, Preprint LNPI-886, Academy of Sciences of the USSR, Leningrad Nuclear Physics Institute (1983); Soviet J. Nucl. Phys. 41, 1585, (1985).
- [75] A. H. Muller and J. Qiu, Nucl. Phys. B 268, 427, (1986).
- [76] O. K. Baker, et al., Nuc. Instrum. Methods, A367, 92 (1995).
- [77] J. R. Arrington, Ph.D Thesis, (1998).
- [78] Trigger Supervisor Users Guide, Internal CEBAF document.
- [79] D. Abbott et al., Proc. of the IEEE Conference on Real-Time Computer Applications in Nuclear, Particle, and Plasma Physisc, edited by R. Fox (Michigan State University - NSCL, East Lansisng, 1995), p.147.
- [80] CODA-CEBAF On-line Data Acquisition User's Manual.
- [81] P. Gueye, M Tiefenback, C. Yan, Hall C Beam Energy Measurement, CEBAF Internal Report.
- [82] C. Yan et al., Nucl. Instrum. Methods, A365, 261 (1995).
- [83] P. Gueye, Status of the Actual Beam Position Monitors in the Hall C Beamlne, CEBAF Internal Report.
- [84] K. B. Unser, The Parametric Current Transformer, a Beam Current Monitor Developed for LEP, CERN SL/91-42 (unpublished.).
- [85] M. Berz, COSY Infinity Version and Reference Manual, NSCL Technical Report MSUCL-977, Michigan State University, (1995).

- [86] K. A. Assamagan, D. Dutta and P. Welch, Hall C Matrix Element Optimization Package, CEBAF Internal Report, (1996), unpublished,
- [87] M. E. Christy, Determining Kinematic Offsets From HMS Single Arm Elastics, Hall C Internal Report (2000).
- [88] J. Volmer, Ph.D Thesis, The Pion Charge Form Factor via Pion Electroproduction on the Proton, (2000).
- [89] Yongguang Liang, Ph.D. Thesis, Measurement of $R = \sigma_L/\sigma_T$ in the Nucleon Resonance Region.
- [90] J. Arrington, Implications of the discrepancy between proton form factor measurements, nucl-ex/0309011 v3, (2003).
- [91] Radiative Corrections to Elastic and Inelastic Scattering, L. W. Mo and Y. S. Tsai, Rev. Mod. Phys. 41, 205, (1969).
- [92] J. V. Noble, Phys. Rev. C 17, 6, 2155, (1978).
- [93] J. Bernabeu, Nucl. Phys. B49, 186, (1972).
- [94] Arenhoven, private communication.
- [95] Phenomenology of the Deuteron Electromagnetic Form Factors, The European Physical Journal, A7, 421-427, (2000).
- [96] H. de Vries, C. W. de Jager and C. de Vries, Atomic Data and Nuclear Data Tables, Vol. 36, N3, May, (1987).
- [97] C. C. Atti and G. B. West, Preprint NUCL-TH/9702009, (1997).
- [98] A. A. Akhundov, D. Yu. Bardin and N. M. Shumeiko, Sov. J. Nucl. Phys., 26, (1977); D. Yu. Bardin and N. M. Shumeiko, Sov. J. Nucl. Phys., 29, (1979); and A. A. Akhundov et al., Sov. J. Nucl. Phys., 44, (1986).
- [99] J. Visser, Ph.D Thesis, Deep Inelastic Scattering of Hydrogen and Deuterium, (2002).
- [100] Aubert et al., Nucl. Phys. B 259, 189, (1985).
- [101] Arneodo et al., Nucl. Phys. B 483, 3, (1997).
- [102] Arneodo et al., Nucl. Phys. B 333, 1, (1989).
- [103] Benvenuti et al., Phys. Lett. B 223, 485 (1989).
- [104] Abe et al., Phys. Lett. B 452, 194 (1999).
- [105] Tao et al., Z. Phys. C 70, 387-390, (1996).

Acknowledgements

This is probably the most difficult *chapter* for me, since during the 4 years of my Ph.D. work I received help from many people at VU, NIKHEF and JLAB. I hope I will not forget to mention anyone. Therefore, let's start from the beginning ...

First, I would like to thank Moskov for giving me my first lessons in experimental physics. His enthusiasm and capability to work 24 hours a day always gave me a great example to follow.

I want to thank the colleagues from the Vrije Universiteit, and in particular my promotor Jo, for giving me the priceless opportunity to be a Ph.D. student at the Vrije Universiteit.

Dear Gerard, it was a big pleasure for me to be a member of the Hermes group. Your supervision allowed the group to work successfully for many years. Apart from work, the Hermes group was always known at NIKHEF as friendly and joyful. A salute to all the Ph.D. students of the Hermes group. Special thanks to Erika Garutti from me, my wife and daughter. Dear Erika your support and *Italian* help in very difficult times for me was important. You showed what it means to be a good friend, and I wish you to be surrounded all your life by friends like you. A very big kiss to you from small Erika. I would like to thank Louk and Jos for their support and clear explanations of physical problems. Dear Louk, I am grateful for all calculations that you have done for me.

Special thanks to Barbara Spruit from the Vrije Universiteit, Teus and Ed from NIKHEF for helping me with dealing with bureaucratic life. Dear friends, your help to foreign students was really great and important.

My thesis would have been incomplete without the help from Rolf, Thia, Beni and Eric. Your comments and great help were always useful. Special thanks to Antje and Peter for their comments, explanations and calculations. Thanks to colleagues from JLAB John, Vardan, Hamlet, Steve and Dave, you were always helpful.

Dear Henk, thank you so much for all your lessons and patience. In these four years I learned a lot from you, and now being a PostDoc I am trying to use your methods to help young Ph.D. students. I will never forget the main rule that you tried to teach me: *Vladas, use your brain first and only then do your calculations on the computer*; I will! Also, I would like to thank you for being patient with me. Of course I perfectly understand how hard it was for you, since we have two different cultures, but nevertheless I believe that you did your job on a very high level! THANK YOU!

Of course thanks to my wife Karina for helping, loving and understanding me during my work. Special thanks to my daughter Erika for allowing me to sleep during the nights and being the source of joy in my life. Finally, I would like to thank my parents Bronus and Nina for giving me life.